The NEXT experiment: DAQ, backgrounds and medical applications

DOCTORADO EN FÍSICA

José María Benlloch Rodríguez

Directores: Juan José Gómez Cadenas
Paola Ferrario
Javier Muñoz Vidal

Tutor: José Díaz Medina

VNIVERSITAT DE VALÈNCIA

Departamento de Física Atómica, Molecular y Nuclear

Septiembre de 2020

The work in this thesis has been carried out at the *Instituto de Física Corpuscular* (IFIC), affiliated with the Universitat de València and CSIC.

INFORME DEL DIRECTOR

Juan José Gómez Cadenas, profesor Ikerbasque del Donostia International Physics Center,

Paola Ferrario, Ikerbasque Research Associate del Donostia International Physics Center, y

Javier Muñoz Vidal, investigador postdoctoral del Consejo Superior de Investigaciones Científicas,

CERTIFICAN:

Que los trabajos aquí detallados han sido realizados por el estudiante en el Instituto de Física Corpuscular bajo su dirección y que el presente texto constituye el trabajo de tesis doctoral por la que el estudiante opta al grado de Doctor en Física por la Universidad de Valencia.

Paterna, a 15 de septiembre de 2020,

Juan José Gómez Cadenas Paola Ferrario Javier Muñoz Vidal

Agradecimientos

En primer lugar a Juanjo, por acogerme en su grupo desde el día en que llamé a su puerta pidiendo un trabajo fin de máster. Por todo lo que vino después. Guardo un especial recuerdo de aquellos viajes a Ginebra y de los baños en el río después de las mañanas de trabajo. Por haber hecho posible esta tesis.

A Paola por haber dirigido este trabajo desde el primer día. Ha llovido mucho desde aquel primer correo con las instrucciones para compilar nexus e Irene. Siempre que hubo algún problema solo tenía que ir al despacho de enfrente para encontrar la solución.

A Javi, por las visitas ineludibles a la cafetería cada mañana. Por los días peleándonos con la simulación de NEXT-100 hasta que conseguimos aclarar el problema. Y, cómo no, por resolver todas mi dudas sobre aviones, aeropuertos y control de tráfico aéreo.

A Raúl, trabajador incansable, ingeniero competente como pocos, por estar desde las `0x0F96` de la mañana hasta las `0xFAFA` de la madrugada. Por nuestras largas charlas en hexadecimal, por ese lenguaje que has creado y que probablemente solo tenga dos hablantes.

A Josh, por la detallada revisión de todo el texto, thank you for dismantling the *scheme* and everything else.

A Carmen por escuchar incansablemente mis historias en L'Anglassé. A Alberto por acogerme en su casa con su familia. Cuando los eternos shifts ya me pesaban demasiado, los que tuve con vosotros fueron mucho más agradables. A los demás con los que he ido compartiendo despacho: Ryan, Miryam, Marija, Ander, Miquel, Gonzalo, Brais, no habría sido lo mismo sin vosotros. También recuerdo a Alejandro Botas y nuestra excursión en bici por el lago Léman.

Al resto del equipo de software de NEXT en el IFIC: Andrew, Michel, Justo, Neus y Pau por todas las veces que me habéis echado una mano o resuelto algún problema. A todos los ingenieros del *zulo*: Javi, Marc, Sara, Alberto, Vicente, por hacernos la vida más fácil y por vuestra eterna paciencia atendiendo a nuestras desesperadas llamadas desde Canfranc. A José Vicente por su gran trabajo, a veces en la sombra, encargándose de toda la infraestructura informática, sin él NEXT no sería posible. Por supuesto, a Jose Pérez por resolver rápidamente cualquier cuestión que pudiera surgir.

Al equipo de la Fira Experimenta, en especial a Chantal y Jordi, por todos los buenos ratos pasados organizando la feria. Ver la felicidad de tantos estudiantes con sus proyectos, te hacía recuperar la fe en la humanidad en los momentos bajos en los que la ciencia era más humana y menos divina. A María Jesús y a Ariadna por las comidas y cenas que tantas veces servían para desconectar de los problemas de la tesis.

A Mario, por ser un profesor como nunca he conocido. Nunca olvidaré la pasión que transmitías en aquellas clases de computabilidad y complejidad. Por ser un investigador excelente y siempre dispuesto a ayudar a aquellos interesados en continuar aprendiendo. Gracias a ti la balanza se inclinó en esta dirección y hoy existe esta tesis.

A JoseRa por haber dirigido mi primera incursión en esto que llaman investigación. Por haber aparecido como un oasis cuando en la ETSII yo buscaba alguna forma de hacer algún trabajo relacionado con la física cuántica. Por tus gaditanísimas maneras.

A Perea, por hacer más llevaderas aquellas prácticas de bases de datos, de ingeniería de software o de lo que se terciara. Por todas aquellas ocasiones en las que podíamos hablar de física y no de las cosas que se hacían en el LSI.

A Juan y Piury, por todas las veces que hemos quedado en Sevilla y habéis soportado mis alegrías y mis penas. A Jose y Gloria por Ginebra, Barcelona, Sevilla y lo que nos quede. Los periódicos viajes a Ginebra siempre eran más agradables sabiendo que allí estaríais vosotros.

A Jorge por las comidas, las cenas, Benasque, Ibi, Córdoba, Benicasim, Ginebra... Por haber compartido estos años de luces y de sombras. Por la amistad. Por todo lo que vendrá.

A Ignacio por ser como un hermano. Por todas nuestras aventuras que llamaron locuras. Porque tu sabes lo que ha costado esta tesis y las veces que estuvo a punto de no ser.

A toda mi familia de Castellón por tantos fines de semana.

A mi madre y mi hermano porque gracias a ellos he llegado aquí. A mis tíos de Cádiz porque la familia siempre está para lo que haga falta.

Gracias a todos vosotros esta tesis ha visto la luz.

Valencia, Septiembre de 2020

Contents

Resum **9**

Resumen **21**

1 The nature of neutrinos **33**
1.1 Brief history of neutrinos 33
1.2 Massive neutrinos 39
1.2.1 Neutrino mass experimental measurement . . . 42
1.3 Dirac and Majorana neutrinos 45
1.3.1 The see-saw mechanism 46
1.3.2 The missing antimatter 48
1.3.3 Observables sensitive to the neutrino nature . . 49

2 Neutrinoless double beta decay **51**
2.1 Introduction to double beta decay 51
2.2 Standard neutrinoless double beta decay mechanism . 53
2.3 The black box theorem 55
2.4 Design of double beta decay experiments 55
2.4.1 Isotope 58
2.4.2 Energy resolution 58
2.4.3 Background rate 59
2.4.4 Detection efficiency 61
2.4.5 Exposure 61
2.5 Current experiments 62
2.5.1 KamLAND-Zen 62
2.5.2 EXO 63
2.5.3 GERDA 65
2.5.4 CUORE 67

2.5.5 SNO+ 67
2.6 The future of neutrinoless double beta decay experiments 70

3 The NEXT Experiment 73
3.1 Introduction 73
3.2 Xenon gas as a detector medium 74
3.2.1 Primary signals in xenon: scintillation and ionization 74
3.2.2 Detection of the ionization and scintillation signals 76
3.2.3 Intrinsic energy resolution of xenon gas 78
3.3 The SOFT concept 82
3.4 NEXT detectors 85
3.4.1 R&D prototypes 85
3.4.2 NEXT-White 88
3.4.3 NEXT-100 106
3.5 Future generation detectors 109

4 Data Acquisition System 111
4.1 NEXT-White Data Acquisition System 111
4.2 DATE online system 112
4.3 NEXT data format 115
4.4 Trigger system 123
4.5 Decoding software 127
4.5.1 File structure 129
4.5.2 Database structure 131
4.5.3 Automated testing and quality control 132
4.6 Huffman compression 134
4.7 NEXT-White setup in Canfranc 137
4.8 Towards NEXT-100's DAQ 140

5 Neutrinoless $\beta\beta$ searches with NEXT-100 143
5.1 Radiogenic backgrounds in NEXT-100 145
5.2 The NEXT-100 detector simulation 151
5.3 Simulation and classical reconstruction 154
5.3.1 Geometrical and lifetime corrections 159
5.3.2 Analysis cuts 159
5.3.3 Topological optimization 162
5.4 FANAL 164

5.5 The problem of diffusion 166
5.6 Dual cut analysis 169
5.7 Richardson-Lucy deconvolution 174
5.8 Results 178
5.9 Conclusions 187

6 Medical applications of NEXT technology 189
6.1 Positron Emission Tomography 189
6.2 The PETALO concept 192
6.3 The Cherenkov radiation 193
6.3.1 Using Cherenkov light in PET scanners 194
6.4 Monte Carlo simulation 195
6.4.1 CRT calculation 199
6.5 Analysis and results 201
6.5.1 Speed of Cherenkov photons 201
6.5.2 Intrinsic CRT 202
6.5.3 Effect of the sensor and front-end electronics jitter 204
6.6 Summary and outlook 206

7 Conclusions and prospects 207

Bibliography 211

Resum

El Model Estàndard de la física de partícules és una teoria que descriu amb gran precisió l'estructura i el comportament de la matèria. Va ser desenvolupat als anys 70 i ha pogut explicar amb èxit l'observació de noves partícules al llarg de les últimes dècades. Segons aquest model, els neutrins són partícules sense càrrega i sense massa. No obstant això, l'observació experimental d'oscil·lacións de neutrins demostra que aquestes partícules han de tenir una massa no nul·la, ja que aquest fenomen ocorre per la diferència entre els estats de sabor i de massa parametritzada en la matriu de mescla U_{PMNS}. Per aquest motiu, el Model Estàndard ha de ser ampliat.

Hi ha diversos mecanismes per dotar de massa al neutrins. Una possibilitat és que el neutrí siga una partícula de Majorana, és a dir, partícules idèntiques a les seues antipartícules, al contrari que la resta de fermions. El neutrí de Majorana permetria interaccions que violen la conservació del nombre leptònic. En aquest cas, els neutrinos podrien explicar, mitjançant la leptogènesis, part de l'asimetria matèria-antimatèria observada en l'univers. Així mateix, es podria explicar la seua petita massa a través del mecanisme de "see-saw".

La principal tècnica experimental per discernir si el neutrí és una partícula de Majorana és la recerca de desintegracions doble beta sense neutrins ($0\nu\beta\beta$). Es tracta d'una hipotètica i extremadament rara desintegració radioactiva en la qual un nucli de nombre atòmic Z i nombre màssic A es transforma en el seu isòbar de nombre atòmic $Z+2$ emetent dos electrons,

$$ {}^{\mathrm{A}}_{\mathrm{Z}}\mathrm{X} \rightarrow {}^{\mathrm{A}}_{\mathrm{Z+2}}\mathrm{X} + e^- + e^- \,. \tag{1} $$

Aquest procés encara no ha sigut observat per cap experiment. Encara que qualsevol mecanisme que impliqui la violació del nombre leptònic

podria induir la desintegració $0\nu\beta\beta$ i contribuir a la seua amplitud, el *teorema de la caixa negra* garanteix que, si s'observa una desintegració $0\nu\beta\beta$, llavors els neutrins són partícules de Majorana.

El mecanisme més simple per induir $0\nu\beta\beta$ seria l'intercanvi d'un neutrí lleuger de tipus Majorana. La semivida d'aquest procés ve donada per

$$\left(T^{0\nu}_{1/2}\right)^{-1} = G^{0\nu} \left|M^{0\nu}\right|^2 \left(\frac{m_{\beta\beta}}{m_e}\right)^2 , \tag{2}$$

on $G^{0\nu}$ és una integral d'espai de fases, $M^{0\nu}$ és l'element de matriu nuclear del procés, m_e és la massa de l'electró i $m_{\beta\beta}$ és l'anomenada massa efectiva de Majorana. Aquesta es defineix com

$$m_{\beta\beta} \equiv \left| \sum_{i=1}^{3} U_{ei}^2 \, m_i \right| , \tag{3}$$

on U_{ei} són els elements de la primera fila de la matriu de mescla i m_i són les masses dels neutrins. Per tant, l'observació del procés oferiria una mesura indirecta de l'escala absoluta de masses dels neutrins, inobservable en experiments d'oscil·lacions.

Detectar aquesta desintegració és una tasca complexa. La tècnica consisteix en mesurar la suma de les energies dels dos electrons emesos al procés. En una desintegració doble beta sense neutrins, aquesta suma seria sempre igual al valor Q del procés, és a dir, a la diferencia de masses entre els àtoms inicial i final,

$$Q_{\beta\beta} \equiv M(A, Z) - M(A, Z+2) . \tag{4}$$

Aquesta mesura és crucial per distingir aquest procés de la desintegració doble beta amb neutrins ($2\nu\beta\beta$), permesa al Model Estàndard, a la qual l'energia dels dos electrons segueix un espectre continu per sota de $Q_{\beta\beta}$. La resolució energètica finita de qualsevol detector donaria com a resultat una distribució gaussiana al voltant de $Q_{\beta\beta}$ en el cas d'esdeveniments $0\nu\beta\beta$. Per aquest motiu, podria passar que algun altre procés contribuïra al soroll de fons dipositant energia al detector al voltant d'aquest valor, fent més difícil la mesura. Per minimitzar la quantitat de soroll, els detectors es construïxen amb materials *radiopurs* i s'operen en laboratoris subterranis per disminuir l'efecte dels raigs còsmics.

Hi ha diverses aproximacions tecnològiques per cercar les desintegracions $0\nu\beta\beta$. Per poder comparar el seu rendiment potencial, s'utilitza la sensibilitat a $m_{\beta\beta}$ donada per

$$\mathcal{S}(m_{\beta\beta}) \propto \sqrt{1/\varepsilon}\,\left(\frac{b\,\Delta E}{M\,t}\right)^{1/4}, \tag{5}$$

on ε és l'eficiència de detecció de l'experiment, M és la massa de l'isòtop $0\nu\beta\beta$ usada en l'experiment, t és el temps de mesura, ΔE és la resolució energètica del detector i b és la taxa de soroll de l'experiment en la finestra de energia d'interès (ROI) (expressada, normalment, en comptes per keV, kilogram i any).

Entre els experiments de la generació actual, la cota més estricta per a la semivida de la desintegració $0\nu\beta\beta$ del ^{136}Xe l'ha establerta l'experiment KamLAND-Zen, amb un valor de $T^{0\nu}_{1/2}(^{136}\mathrm{Xe}) > 1.07 \times 10^{26}$ anys (90% CL), resultant una massa menor de $61 - 165$ meV. En el cas de l'isòtop ^{76}Ge, l'experiment GERDA ha establert la cota $T^{0\nu}_{1/2}(^{76}\mathrm{Ge}) > 1.8 \times 10^{26}$ anys (90% CL), corresponent a una massa efectiva menor de $80 - 182$ meV.

L'experiment NEXT

La col·laboració NEXT (Neutrino Experiment with a Xenon TPC) proposa l'ús d'una càmera de projecció temporal (TPC) amb xenó gasós a alta pressió per a la recerca de desintegracions doble beta sense neutrins. L'experiment usarà xenó enriquit al 90% en l'isòtop ^{136}Xe, ja que aquest es pot desintegrar doble beta. A més, en aquest procés s'allibera una energia alta (2458 keV), facilitant l'eliminació de gran part del fons radiactiu natural.

La propagació dels electrons en el xenó gasós deixa un patró característic d'energia dipositada. Els electrons perden energia per ionització de forma gairebé constant fins que deixen de ser relativistes. En aquest punt, el ritme amb què perden l'energia creix, degut principalment al *scattering* múltiple, i les partícules perden la resta de la seua energia en una distància petita, produint una gran deposició d'energia, anomenada *blob*.

En el cas d'esdeveniments doble beta sense neutrins, es produirien en el detector dos electrons amb una energia total de ^{136}Xe $Q_{\beta\beta}$

(2458 keV) procedents del mateix vèrtex. Per tant, els electrons deixarien una única traça en el detector amb dos *blobs*, un a cada extrem. La rellevància de les potencials fonts de fons radioactiu depèn de la seua probabilitat per generar una traça similar a la produïda per un esdeveniment de senyal amb una energia al voltant de ^{136}Xe $Q_{\beta\beta}$.

En principi, les partícules carregades (muons, betes, etc.) que entren al detector poden ser rebutjades amb una eficiència alta definint una petita regió de vet (alguns centímetres) al voltant de les vores del detector. D'altra banda, les traces completament contingudes produïdes per partícules neutres externes, com gammes d'alta energia, o per les impureses del gas poden donar lloc a una traça única amb energia $Q_{\beta\beta}$. Aquests esdeveniments, però, poden ser rebutjats mitjançant l'anàlisi de la topologia de la seva deposició energètica. Atès que la majoria d'ells són esdeveniments amb un únic electró, crearan una traça amb un *blob* en només un dels seus extrems.

Aquesta diferència entre el comportament dels esdeveniments de senyal i de fons es pot aprofitar per rebutjar esdeveniments de fons establint una energia mínima per als *blobs* en ambdós extrems de cada traça. Aquesta idea és una de les claus de l'experiment NEXT, dissenyat per tenir una excel·lent resolució energètica i ser capaç de reconstruir aquesta informació topològica. Els requisits perquè els sensors puguin complir aquestes tasques són prou diferents, de manera que cadascun dels plànols de la TPC de NEXT està especialitzat en un tipus de mesura diferent. Aquest concepte es coneix com Separated Optimized Function TPC (SOFT).

L'experiment NEXT es basa en una TPC asimètrica en la qual un dels plans, el pla d'energia, està instrumentat amb tubs fotomultiplicadors (PMTs) per aconseguir una mesura precisa de l'energia de l'esdeveniment. En l'altre extrem de la TPC es troba al pla de *tracking*, instrumentat amb una matriu de fotomultiplicadors de silici (SiPMs) per aconseguir la reconstrucció topològica de l'esdeveniment. Per aconseguir la resolució energètica òptima, NEXT amplifica el senyal mitjançant electroluminescència. Això requereix d'un intens camp elèctric per provocar l'emissió de llum a través de l'excitació dels àtoms de xenó.

El procés de detecció en NEXT funciona de la següent manera: una o diverses partícules carregades interactuen amb el xenó a alta pressió, transferint la seva energia mitjançant excitació i ionització.

L'excitació produeix un centelleig primari (S1) emetent llum ultravio-lada ($\sim$ 178 nm). Els electrons arrencats en la ionització són arrossegats per un camp elèctric moderat que evita la seva recombinació. Aquests electrons continuen la seva deriva cap a l'ànode de la TPC, on un camp elèctric de més intensitat accelera els electrons proporcionant energia suficient per excitar els àtoms de xenó. D'aquesta forma, es generen més fotons ultraviolats, donant lloc al centelleig secundari (S2). Per operar a la regió òptima dels sensors, la llum ultraviolada es converteix en llum blava ($\sim$ 430 nm) mitjançant l'ús d'un canviador de longitud d'ona (tetrafenil butadiè, o TPB).

El pla d'energia és capaç de mesurar la llum emesa pel centelleig primari, marcant el començament de l'esdeveniment. Mesurant la llum emesa en el centelleig secundari és possible aconseguir una mesura molt precisa de l'energia de l'esdeveniment. La diferència temporal entre el S1 i el S2 proporciona la posició longitudinal de l'esdeveniment a la TPC.

D'altra banda, el pla de *tracking* utilitza la llum emesa en el S2 per determinar amb precisió les dues coordenades transversals dels electrons de ionització. Combinant aquesta informació amb l'obtinguda pel pla d'energia és possible aconseguir una reconstrucció tridimensional detallada de cada esdeveniment.

Seguint aquests principis, la col·laboració NEXT està construint el detector NEXT-100 per a la recerca de desintegracions $0\nu\beta\beta$ del ^{136}Xe. El detector consisteix en una càmera de projecció temporal (TPC) electroluminescent capaç de contenir 100 kg de xenó enriquit al 91% en ^{136}Xe a 15 bar de pressió. El detector es construirà i operarà al Laboratori Subterrani de Canfranc. Les seues característiques principals són una excel·lent resolució energètica (fins 0.3% FHWM a $Q_{\beta\beta}$) i la possibilitat de realitzar una reconstrucció topològica dels esdeveniments per discriminar senyal i soroll. A més a més, presenta altres avantatges com escalabilitat a grans masses, la facilitat per purificar el gas xenó eliminant impureses o el cost del seu enriquiment en comparació a altres isòtops.

Dins del programa d'investigació de NEXT, com a prototip s'ha construït el detector NEXT-White amb la finalitat de provar les solucions tecnològiques ideades per NEXT-100. Aquest detector té $\sim$ 5 kg de xenó i és una versió a escala 1:2 de NEXT-100. NEXT-White està operant al Laboratori Subterrani de Canfranc des de l'any 2016 en con-

dicions de baix fons radioactiu. El programa de física de NEXT-White inclou la caracterització del fons radioactiu del laboratori, així com la mesura de la semivida de la desintegració $2\nu\beta\beta$ del ^{136}Xe.

Aquesta tesi doctoral s'ha realitzat dins de la col·laboració NEXT amb els següents objectius:

- **Desenvolupament del sistema d'adquisició de dades de NEXT-White**. Escriptura i manteniment del software necessari per poder descodificar la informació llegida pels sensors i enviada als servidors per l'electrònica d'adquisició. Aquest software ha de traduir les dades a un format d'alt nivell adequat per al software d'anàlisi. El sistema desenvolupat ha de ser escalable per a la seva futura utilització en el detector NEXT-100.

- **Estudi de el fons radioactiu de NEXT-100**. Realitzar mitjançant simulacions detallades del detector i del seu comportament una anàlisi sobre el nivell de soroll esperat en el detector NEXT-100, tenint en compte les últimes mesures disponibles sobre la radiopuresa dels materials emprats en els components del detector. Estudiar el possible impacte de la difusió del núvol d'electrons durant el seu arrossegament i, si escau, possibles algoritmes per pal·liar-ne els efectes.

- **Estudi de possibles aplicacions mèdiques de la tecnologia desenvolupada en NEXT**. Avaluació mitjançant simulació d'un escàner de Tomografia per Emissió de Positrons (PET) emprant xenó líquid i fotomultiplicadors de silici.

Sistema d'adquisició de dades

En aquest treball es presenta el sistema de adquisició de dades (DAQ) de NEXT-White. El sistema està basat en l'arquitectura ATCA-SRS dissenyada per NEXT, el CERN i IFIN-HH en el marc de la col·laboració RD51. El DAQ es compon de tres subsistemes: (a) el pla d'energia amb 12 PMTs, (b) el pla de *tracking* compost per 1792 SiPMs agrupats en 28 *Front-End Boards*, i (c) el sistema de *trigger*. Els PMTs són digitalitzats amb una freqüència de 40 MHz utilitzant 12 bits per mostra. En el cas dels SiPMs la freqüència de digitalització és d'1 MHz, també amb 12 bits per mostra.

El software utilitzat per al sistema *online* és DATE, de la col·laboració ALICE del CERN. DATE és un software capaç de gestionar fluxos de dades en paral·lel procedents de diferents subsistemes del detector. El sistema utilitza Gigabit Ethernet i el protocol UDP per comunicar les diferents màquines implicades en el procés d'adquisició.

L'arquitectura del sistema inclou dos nivells de servidors: concentradors locals de dades (LDC) i concentradors globals de dades (GDC). El primer nivell està format pels LDC, que reben subevents amb les dades d'un subconjunt de sensors de detector. D'aquí, són enviats als GDC per al procés final de construcció de l'esdeveniment. Per aconseguir això, els LDC i GDC estan connectats via xarxa. Els GDC poden implementar mecanismes de balanceig de càrrega per millorar la freqüència de trigger del sistema. El més simple d'ells és un algoritme *Round Robin* que envie un esdeveniment a cada GDC seguint un ordre circular.

Per poder transferir i emmagatzemar de forma eficient la informació relativa als esdeveniments presos, la col·laboració NEXT ha definit un format binari de dades específic per complir els requisits del sistema. Aquest format ha de ser conegut per l'electrònica que processa la informació recollida dels sensors, així com pel software de reconstrucció i anàlisi. Amb aquesta finalitat, s'ha desenvolupat un software de decodificació que tradueix els fitxers creats pel DAQ en format binari a un altre format de més alt nivell, HDF5, utilitzat pel software de reconstrucció. El desenvolupament d'aquest software ha estat la principal contribució al DAQ d'aquesta tesi. Per assegurar la qualitat del mateix, s'ha implementat un sistema de proves automàtiques que avaluen el correcte funcionament del software.

El sistema de detecció d'esdeveniments de NEXT és capaç de detectar amb alta eficiència una gran varietat d'esdeveniments. Els esdeveniments de calibratge de baixa energia procedents d'una font de ^{83m}Kr produeixen senyals petits, mentre que les fonts d'alta energia (^{222}Rn, ^{232}Th), esdeveniments de fons o muons produeixen esdeveniments amb topologies molt diferents segons la direcció de les partícules en el gas.

El sistema de trigger de NEXT-White ofereix una gran flexibilitat per a la selecció dels esdeveniments. La manera normal d'operació inclou un trigger dual. El trigger 1 es configura per als esdeveniments de baixa energia (calibratge de Kr), mentre que el trigger 2 es reserva

per als esdeveniments d'alta energia, normalment prop de $Q_{\beta\beta}$. Això permet que el sistema puga ser calibrat en tot moment usant els esdeveniments de baixa energia. Per minimitzar la probabilitat de perdre un esdeveniment d'interès, el trigger 2 té prioritat sobre el trigger 1, que és molt més freqüent que el trigger 2.

El rendiment del sistema s'ha millorat mitjançant la implementació d'un algoritme de compressió basat en codis de Huffman. Amb aquest procediment s'aconsegueixen taxes de compressió superiors al 85%, permetent una reducció significativa del temps mort del detector. NEXT-White ha pres satisfactòriament més de 1600 milions d'esdeveniments, demostrant la robustesa del sistema. Per a NEXT-100 s'utilitzarà la mateixa arquitectura amb petis canvis al sistema.

Estudi del fons en NEXT-100

El detector NEXT-100 compta amb dos plans instrumentats, estant cadascun d'ells optimitzat per a una funció diferent. Els electrons procedents de la desintegració $\beta\beta$ produïxen centelleig i ionització en el xenó. La llum de centelleig és registrada per un conjunt de tubs fotomultiplicadors (PMT) situats al càtode, que marquen el temps d'inici de l'esdeveniment (t_0). Els electrons d'ionització són derivats cap a l'ànode per un camp elèctric moderat fins a la regió de electroluminescència. En aquest punt són accelerats per un camp elèctric més intens capaç de produir un centelleig secundari proporcional al nombre de electrons que hi arriben. Els PMTs registren aquesta llum donant com a resultat una mesura precisa de l'energia de l'esdeveniment. D'altra banda, al costat de l'ànode es troba el pla de *tracking* instrumentat amb fotomultiplicadors de silici (SiPM) formant una matriu amb un espaiat regular d'1 cm. Mitjançant aquests sensors és possible aconseguir una reconstrucció detallada de la trajectòria de les partícules que han travessat el detector.

El patró de deposició d'energia és diferent per als esdeveniments de senyal i els de fons. En un esdeveniment de senyal es produïxen dos electrons que parteixen del mateix vèrtex i es mouen dipositant la seua energia. Al final de la seua trajectòria dipositen energia a major ritme (a cause de el pic de Bragg), deixant un patró característic consistent en una traça allargada amb dues grans deposicions d'energia (*blob*) als seus extrems. En el cas de l'esdeveniments de fons, la traça només

tindrà un *blob* en un dels seus extrems, però no en l'altre. Mitjançant un tall en l'energia mínima dels extrems de la traça és possible aconseguir una major separació de senyal i fons.

En estudis previs s'han avaluat els diferents possibles fons que podrien afectar NEXT-100. La contribució dominant (97%) prové de fonts radiogèniques, això és, de la contaminació radioactiva dels materials amb què es construeix el detector. Els isòtops més problemàtics són el ^{214}Bi i el ^{208}Tl presents en las cadenes de desintegració natural de l'urani i del tori, respectivament. Les seues gammes de desintegració tenen una energia molt propera al valor $Q_{\beta\beta}$ del ^{136}Xe.

En aquesta tesi es presenta un estudi actualitzat de la contribució dels fons d'origen radiogènic a NEXT-100 utilitzant les últimes mesures de radiopuresa obtingudes en la col·laboració. Els estudis previs van ser realitzats amb una simulació Monte Carlo simplificada que no tenia els detalls implementats en el software més recent de la col·laboració NEXT. El present estudi inclou una simulació detallada de la deriva del núvol d'electrons, així com de l'efecte de l'electrònica i la reconstrucció.

L'anàlisi estàndard en la col·laboració, anomenat *anàlisi clàssic*, inclou correccions geomètriques i de vida mitjana dels electrons. També s'ha realitzat una optimització dels paràmetres dels talls topològics. Els resultats obtinguts amb aquest anàlisi són significativament pitjors que el que ofereix una reconstrucció ideal: el soroll esperat es 2.75 vegades major. La difusió del núvol d'electrons a la TPC és el principal origen de l'escàs rendiment obtingut amb l'anàlisi clàssic.

Modificant els talls implementats en l'anàlisi clàssic és possible millorar el resultat, encara que no prou. La forma de solucionar el problema és mitjançant l'ús de l'algoritme Richardson-Lucy. Aquest procediment és capaç de recuperar una imatge subjacent alterada per una funció de dispersió de punt (PSF) coneguda. En el caso de NEXT, aquestes PSFs es poden construir mitjançant l'anàlisi d'esdeveniments puntuals de baixa energia procedents de una font de ^{83m}Kr. Mitjançant l'ús de diferents PSFs depenent de la posició longitudinal de l'esdeveniment, és possible deconvolucionar l'efecte de la difusió del núvol d'electrons. Aquest algoritme aconsegueix una millora significativa en els resultats, sent comparables als resultats obtinguts amb la reconstrucció ideal.

El fons esperat trobat usant la deconvolució R-L és 4.29×10^{-4}

cts keV^{-1} kg^{-1} yr^{-1}. Aquests resultats posen de manifest la importància crítica que té la difusió del núvol d'electrons en detectors grans. Algoritmes com Richardson-Lucy són una de les eines per tractar aquest problema. Més enllà de solucions basades en millores del procediment de reconstrucció, la investigació sobre additius per al gas xenó que disminueixen la difusió és també una opció de gran interès.

Dels resultats obtinguts també es dedueix que reemplaçar els PMTs per SiPMs produiria una rebaixa important del nivell de fons del detector, ja que el pla de PMTs és la major font d'esdeveniments de fons.

Aplicacions mèdiques de NEXT

Per acabar, la tecnologia desenvolupada per als detectors NEXT té també aplicacions més enllà de la física fonamental, concretament en imatge mèdica. L'ús del xenó com a medi de detecció de radiacions, amb fotomultiplicadors de silici per registrar la seua resposta, permet el desenvolupament d'un nou sistema de tomografia per emissió de positrons (PET).

El sistema PET és una tècnica d'imatge mèdica no invasiva emprada per observar els processos metabòlics del cos. No mostra trets anatòmics com una Ressonància Magnètica o un TAC, sinó l'activitat de les cèl·lules. Els escàners PET s'usen en investigació clínica i preclínica per estudiar les bases moleculars de la malaltia i els seus tractaments.

El principi d'operació consisteix a injectar al pacient una molècula amb alguna activitat biològica, modificada per incloure un radioisòtop, anomenada traçador. Un traçador comú és la fluorodeoxiglucosa, que consisteix en una molècula de glucosa en la qual un oxigen ha estat reemplaçat per un ^{18}F, emissor β^+. El radionucli es desintegra dins el pacient i el positró emès s'aniquila amb un electró després de travessar una curta distància en els teixits propers. Aquesta aniquilació produeix dos fotons de 511 keV en direccions oposades. La trajectòria dels fotons defineix una línia de resposta (LOR) que pot ser reconstruïda mitjançant la mesura de la direcció de les dues partícules. Això s'aconsegueix observant la interacció d'aquestes partícules amb un detector situat al voltant del cos del pacient. La intersecció de moltes LOR mostra el punt d'emissió del radiotraçador. La mesura de la diferència

temporal entre l'arribada dels dos fotons (*time-of-flight*, TOF), permet millorar la sensibilitat del sistema.

El projecte PETALO planteja la construcció d'un escàner PET basat en xenó líquid instrumentat amb SiPMs. Aquesta nova tecnologia presenta importants avantatges: (a) una resposta de centelleig molt ràpida i amb una gran quantitat de llum; (b) el xenó líquid ofereix un medi continu amb resposta uniforme; (c) potencialment, la identificació i reconstrucció d'esdeveniments Compton.

En aquesta tesi es presenta un estudi mitjançant simulació de la llum Cherenkov produïda en el xenó líquid. L'interès d'aquest tipus de resposta és que és extremadament ràpida, per la qual cosa el seu ús podria permetre el disseny de sistemes PET amb informació del temps de vol (TOF) amb una resolució temporal de coincidències (CRT) extraordinària. L'anàlisi de la simulació implementada mostra com un CRT de $\sim$ 30 ps seria possible amb sensors i electrònica suficientment ràpids.

Conclusions

Els objectius d'aquesta tesi s'han complert satisfactòriament. S'ha desenvolupat un sistema d'adquisició de dades escalable que ha demostrat sobradament la seua fiabilitat i rendiment durant diversos anys d'operació del detector NEXT-White al Laboratori Subterrani de Canfranc. L'ús de la compressió mitjançant codis de Huffman ha permès una millora notable de el temps mort de l'detector.

Les simulacions detallades realitzades del fons radioactiu natural de NEXT-100 han mostrat la importància crucial de tractar el problema de la difusió del núvol d'electrons al llarg de la seva deriva en la TPC. L'algoritme de deconvolució Richardson-Lucy permet corregir aquest efecte aconseguint resultats similars als obtinguts en una simulació ideal sense incloure la difusió. Aquest resultat també posa de manifest l'interès de l'estudi de diferents additius per al gas que disminueixin la difusió.

Finalment, els resultats obtinguts en la simulació de sistema PETALO mostren la gran potencialitat d'un escàner PET basat en xenó líquid per obtenir una resolució temporal de coincidències extraordinària.

Resumen

El Modelo Estándar de la física de partículas es una teoría que describe con gran precisión la estructura y el comportamiento de la materia. Fue desarrollado en los años 70 y ha podido explicar con éxito la observación de nuevas partículas a lo largo de las últimas décadas. Según este modelo, los neutrinos son partículas sin carga y sin masa. Sin embargo, la observación experimental de oscilaciones de neutrinos demuestra que estas partículas tienen que tener una masa no nula, pues este fenómeno ocurre por la diferencia entre los estados de sabor y masa parametrizada en la matriz de mezcla U_{PMNS}. Por este motivo, el Modelo Estándar debe ser extendido.

Existen diversos mecanismos para dotar de masa a los neutrinos. Una posibilidad es que el neutrino sea una partícula de Majorana, esto es, partículas idénticas a sus antipartículas, al contrario que el resto de fermiones. El neutrino de Majorana permitiría interacciones que violan la conservación del número leptónico. En tal caso, los neutrinos podrían explicar, mediante la leptogénesis, parte de la asimetría materia-antimateria observada en el universo. Asimismo, se podría explicar su pequeña masa a través del mecanismo de "see-saw".

La principal técnica experimental para discernir si el neutrino es una partícula de Majorana, es la búsqueda de desintegraciones doble beta sin neutrinos ($0\nu\beta\beta$). Se trata de una hipotética y extremadamente rara desintegración radiactiva en la que un núcleo de número atómico Z y número másico A se transforma en su isóbaro de número atómico $Z+2$ emitiendo dos electrones,

$$ {}^{A}_{Z}\mathrm{X} \rightarrow {}^{A}_{Z+2}\mathrm{X} + e^- + e^- \, . \tag{6} $$

Este proceso no ha sido observado a día de hoy por ningún experimento. Aunque cualquier mecanismo que implique la violación del

número leptónico podría inducir la desintegración $0\nu\beta\beta$ y contribuir a su amplitud, el *teorema de la caja negra* garantiza que, si se observa una desintegración $0\nu\beta\beta$, entonces los neutrinos son partículas de Majorana.

El mecanismo más simple para inducir $0\nu\beta\beta$ sería el intercambio de un neutrino ligero de tipo Majorana. La semivida de dicho proceso viene dada por

$$\left(T^{0\nu}_{1/2}\right)^{-1} = G^{0\nu} \left|M^{0\nu}\right|^2 \left(\frac{m_{\beta\beta}}{m_e}\right)^2 , \tag{7}$$

donde $G^{0\nu}$ es una integral de espacio de fases, $M^{0\nu}$ es el elemento de matriz nuclear del proceso, m_e es la masa del electrón y $m_{\beta\beta}$ es la llamada masa efectiva de Majorana. Esta se define como

$$m_{\beta\beta} \equiv \left| \sum_{i=1}^{3} U_{ei}^2 \, m_i \right| , \tag{8}$$

donde U_{ei} son los elementos de la primera fila de la matriz de mezcla y m_i son las masas de los neutrinos. Por tanto, la observación del proceso aportaría una medida indirecta de la escala absoluta de masas de los neutrinos, inobservable en experimentos de oscilaciones.

Detectar esta desintegración es una tarea compleja. La técnica consiste en medir la suma de las energías de los dos electrones emitidos en el proceso. En una desintegración doble beta sin neutrinos, dicha suma sería siempre igual al valor Q del proceso, esto es, a la diferencia de masas entre los átomos inicial y final,

$$Q_{\beta\beta} \equiv M(A, Z) - M(A, Z+2) . \tag{9}$$

Esta medida es clave para distinguir este proceso de la desintegración doble beta con neutrinos ($2\nu\beta\beta$), permitida en el Modelo Estándar, en la que la energía de los dos electrones sigue un espectro continuo por debajo de $Q_{\beta\beta}$. La resolución energética finita de cualquier detector daría como resultado una distribución gaussiana en torno a $Q_{\beta\beta}$ en el caso de eventos $0\nu\beta\beta$. Por este motivo, podría ocurrir que algún otro proceso contribuyera al ruido de fondo depositando energía en el detector en torno dicho valor, haciendo más difícil la medida. Para minimizar la cantidad de ruido, los detectores se construyen con

materiales *radiopuros* y se operan en laboratorios subterráneos para disminuir el efecto de los rayos cósmicos.

Existen diversas aproximaciones tecnológicas para buscar las desintegraciones $0\nu\beta\beta$. Para poder comparar su rendimiento potencial se utiliza la sensibilidad a $m_{\beta\beta}$ dada por

$$\mathcal{S}(m_{\beta\beta}) \propto \sqrt{1/\varepsilon}\,\left(\frac{b\,\Delta E}{M\,t}\right)^{1/4}, \tag{10}$$

donde ε es la eficiencia de detección del experimento, M es la masa de isótopo $0\nu\beta\beta$ usada en el experimento, t es el tiempo de medida, ΔE es la resolución energética del detector y b es la tasa de ruido del experimento en la ventana de energía de interés (ROI) (expresada, normalmente, en cuentas por keV, kilogramo y año).

Entre los experimentos de la generación actual, la cota más estricta para la semivida de la desintegración $0\nu\beta\beta$ del ^{136}Xe ha sido establecida por el experimento KamLAND-Zen, con un valor de $T^{0\nu}_{1/2}(^{136}\mathrm{Xe}) > 1{,}07 \times 10^{26}$ años (90 % CL), resultando una masa menor de $61 - 165$ meV. En el caso del isótopo ^{76}Ge, el experimento GERDA ha establecido la cota $T^{0\nu}_{1/2}(^{76}\mathrm{Ge}) > 1{,}8 \times 10^{26}$ años (90 % CL), correspondiente a una masa efectiva menor de $80 - 182$ meV.

El experimento NEXT

La colaboración NEXT (Neutrino Experiment with a Xenon TPC) propone el uso de una cámara de proyección temporal (TPC) con xenón gaseoso a alta presión para la búsqueda de desintegraciones doble beta sin neutrinos. El experimento usará xenón enriquecido al 90 % en el isótopo ^{136}Xe, ya que este puede desintegrarse doble beta. Además, en dicho proceso se libera una energía alta (2458 keV), facilitando la eliminación de gran parte del fondo radiactivo natural.

La propagación de los electrones en el xenón gaseoso deja un patrón característico de energía depositada. Los electrones pierden energía por ionización de forma casi constante hasta que dejan de ser relativistas. En ese punto, el ritmo al que pierden la energía crece, debido principalmente al *scattering* múltiple, y las partículas pierden el resto de su energía en una distancia pequeña, produciendo una gran deposición de energía, denominada *blob*.

En el caso de eventos doble beta sin neutrinos, se producirían en el detector dos electrones con una energía total de ^{136}Xe $Q_{\beta\beta}$ (2458 keV) procedentes del mismo vértice. Por tanto, los electrones dejarían una única traza en el detector con dos *blobs*, uno en cada extremo. La relevancia de las potenciales fuentes de fondo radiactivo depende de su probabilidad para generar una traza similar a la producida por un evento de señal con una energía en torno a ^{136}Xe $Q_{\beta\beta}$.

En principio, las partículas cargadas (muones, betas, etc.) que entran al detector pueden ser rechazadas con una eficiencia alta definiendo una pequeña región de veto (algunos centímetros) alrededor de los bordes del detector. Por otra parte, las trazas completamente contenidas producidas por partículas neutras externas, como gammas de alta energía, o por las impurezas del gas pueden dar lugar a una traza única con energía $Q_{\beta\beta}$. Estos eventos, sin embargo, pueden ser rechazados mediante el análisis de la topología de su deposición energética. Dado que la mayoría de ellos son eventos con un único electrón, crearán una traza con un *blob* en solo uno de sus extremos.

Esta diferencia entre el comportamiento de los eventos de señal y de fondo se puede aprovechar para rechazar eventos de fondo estableciendo una energía mínima para los *blobs* en ambos extremos de cada traza. Esta idea es una de las claves del experimento NEXT, diseñado para tener una excelente resolución energética y ser capaz de reconstruir esta información topológica. Los requisitos para que los sensores puedan cumplir esas tareas son bastante diferentes, por lo que cada uno de los planos de la TPC de NEXT está especializado en un tipo de medida diferente. Este concepto se conoce como Separated Optimized Function TPC (SOFT).

El experimento NEXT se basa en una TPC asimétrica en la cual uno de los planos, el plano de energía, está instrumentado con tubos fotomultiplicadores (PMTs) para conseguir una medida precisa de la energía del evento. En en el otro extremo de la TPC se encuentra el plano de *tracking*, instrumentado con una matriz de fotomultiplicadores de silicio (SiPMs) para conseguir la reconstrucción topológica del evento. Para conseguir la resolución energética óptima, NEXT amplifica la señal mediante electroluminiscencia. Esto requiere un intenso campo eléctrico para provocar la emisión de luz a través de la excitación de los átomos de xenón.

El proceso de detección en NEXT funciona de la siguiente manera:

una o varias partículas cargadas interactúan con el xenón a alta presión, transfiriendo su energía mediante excitación e ionización. La excitación produce un centelleo primario (S1) emitiendo luz ultravioleta ($\sim$178 nm). Los electrones arrancados en la ionización son arrastrados por un campo eléctrico moderado que evita su recombinación. Estos electrones continúan su deriva hacia el ánodo de la TPC, donde un campo eléctrico de mayor intensidad acelera los electrones proporcionándoles energía suficiente para excitar los átomos de xenón. De esa forma, se generan más fotones ultravioleta, dando lugar al centelleo secundario (S2). Para operar en la región óptima de los sensores, la luz ultravioleta se convierte en luz azul ($\sim$430 nm) mediante el uso de un cambiador de longitud de onda (tetrafenil butadieno, o TPB).

El plano de energía es capaz de medir la luz emitida por el centelleo primario, marcando el comienzo del evento. Midiendo la luz emitida en el centelleo secundario es posible conseguir una medida muy precisa de la energía del evento. La diferencia temporal entre el S1 y el S2 proporciona la posición longitudinal del evento en la TPC.

Por otro lado, el plano de *tracking* utiliza la luz emitida en el S2 para determinar con precisión las dos coordenadas transversales de los electrones de ionización. Combinando esta información con la obtenida por el plano de energía es posible conseguir una reconstrucción tridimensional detallada de cada evento.

Siguiendo esos principios, la colaboración NEXT está construyendo el detector NEXT-100 para la búsqueda de desintegraciones $0\nu\beta\beta$ del ^{136}Xe. El detector consiste en una cámara de proyección temporal (TPC) eletroluminiscente capaz de contener $\sim$100 kg de xenon enriquecido al 91 % en ^{136}Xe a 15 bar de presión. El detector se operará en el Laboratorio Subterráneo de Canfranc. Sus características principales son su excelente resolución energética (hasta 0.3 % FHWM en $Q_{\beta\beta}$) y la posibilidad de realizar una reconstrucción topológica de los eventos para discriminar la señal y el ruido. Además de lo anterior presenta otras ventajas como escalabilidad a mayores masas, la facilidad para purificar el gas xenón eliminando impurezas o el coste de su enriquecimiento en comparación a otros isótopos.

Dentro del programa de investigación de NEXT, a modo de prototipo se ha construido el detector NEXT-White con el fin de probar las soluciones tecnológicas ideadas para NEXT-100. Este detector tiene $\sim$ 5 kg de xenón y es una versión a escala 1:2 de NEXT-100. NEXT-

White está operando en el Laboratorio Subterráneo de Canfranc desde el año 2016 en condiciones de bajo fondo radiactivo. El programa de física de NEXT-White incluye la caracterización del fondo radiactivo del laboratorio así como la medida de la semivida de la desintegración $2\nu\beta\beta$ del ^{136}Xe.

Esta tesis doctoral se ha realizado dentro de la colaboración NEXT con los siguientes objetivos:

- **Desarrollo del sistema de adquisición de datos de NEXT-White**. Escritura y mantenimiento del software necesario para poder decodificar la información leída por los sensores y enviada a los servidores por la electrónica de adquisición. Este software debe traducir los datos a un formato de alto nivel adecuado para el software de análisis. El sistema desarrollado debe ser escalable para su futura utilización en el detector NEXT-100.

- **Estudio del fondo radiactivo de NEXT-100**. Realizar mediante simulaciones detalladas del detector y su comportamiento un análisis sobre el nivel de ruido esperado en el detector NEXT-100, teniendo en cuenta las últimas medidas disponibles sobre la radiopureza de los materiales empleados en los componentes del detector. Estudiar el posible impacto de la difusión de la nube de electrones durante su arrastre y, en su caso, posibles algoritmos para paliar sus efectos.

- **Estudio de posibles aplicaciones médicas de la tecnología desarrollada en NEXT**. Evaluación mediante simulación de un escáner para Tomografía por Emisión de Positrones (PET) empleando xenón líquido y fotomultiplicadores de silicio.

Sistema de adquisición de datos

En este trabajo se presenta el sistema de adquisición de datos (DAQ) de NEXT-White. El sistema está basado en la arquitectura ATCA-SRS diseñada por NEXT, el CERN e IFIN-HH en el marco de la colaboración RD51. El DAQ se compone de tres subsistemas: (a) el plano de energía con 12 PMTs, (b) el plano de *tracking* compuesto por 1792 SiPMs agrupados en 28 *Front-End Boards*, y (c) el sistema de *trigger*. Los PMTs son digitalizados con una frecuencia de 40 MHz utilizando 12

bits por muestra. En el caso de los SiPMs la frecuencia de digitalización es de 1 MHz, también con 12 bits por muestra.

El software utilizado para el sistema *online* es DATE, de la colaboración ALICE del CERN. DATE es un software capaz de gestionar flujos de datos en paralelo procedentes de diferentes subsistemas del detector. El sistema utiliza Gigabit Ethernet y el protocolo UDP para comunicar las distintas máquinas implicadas en el proceso de adquisición.

La arquitectura del sistema incluye dos niveles de servidores: concentradores locales de datos (LDC) y concentradores globales de datos (GDC). El primer nivel esta formado por los LDC, que reciben subeventos con los datos de un subconjunto de sensores del detector. De ahí, son enviados a los GDC para el proceso final de construcción del evento. Para conseguir esto, los LDC y GDC están conectados via red. Los GDC pueden implementar mecanismos de balanceo de carga para mejorar la frecuencia de trigger del sistema. El más simple de ellos es un algoritmo *Round Robin* que envíe un evento a cada GDC siguiendo un orden circular.

Para poder transferir y almacenar de forma eficiente la información relativa a los eventos tomados, la colaboración NEXT ha definido un formato binario de datos específico para cumplir los requisitos del sistema. El formato empleado incluye diferentes cabeceras para los datos de los PMTs, de los SiPMs y los relacionados con la información del trigger. Este formato debe ser conocido por la electrónica que procesa la información recogida de los sensores así como por el software de reconstrucción y análisis. Con esta finalidad, se ha desarrollado un software de decodificación que traduce los ficheros creados por el DAQ en formato binario a otro formato de más alto nivel, HDF5, utilizado por el software de reconstrucción. El desarrollo de este software ha sido la principal contribución al DAQ de esta tesis. Para asegurar la calidad del mismo, se ha implementado un sistema de pruebas automáticas que evalúan el correcto funcionamiento del software.

El sistema de detección de eventos de NEXT es capaz de detectar con alta eficiencia una gran variedad de eventos. Los eventos de calibración de baja energía procedentes de una fuente de ^{83m}Kr producen señales pequeñas, mientras que las fuentes de alta energía (^{222}Rn, ^{232}Th), eventos de fondo o muones producen eventos con topologías muy diferentes según la dirección de las partículas en el

gas.

El sistema de trigger de NEXT-White ofrece una gran flexibilidad para la selección de los eventos. El modo normal de operación incluye un trigger dual. El trigger 1 se configura para los eventos de baja energía (calibración de Kr), mientras que el trigger 2 se reserva para los eventos de alta energía, normalmente cerca de $Q_{\beta\beta}$. Esto permite que el sistema pueda ser calibrado en todo momento usando los eventos de baja energía. Para minimizar la probabilidad de perder un evento de interés, el trigger 2 tiene prioridad sobre el trigger 1, que es mucho más frecuente que el trigger 2.

El rendimiento del sistema se ha mejorado mediante la implementación de un algoritmo de compresión basado en códigos de Huffman. Con este procedimiento se consiguen tasas de compresión superiores al 85 %, permitiendo una reducción significativa del tiempo muerto del detector. NEXT-White ha tomado satisfactoriamente más de 1600 millones de eventos, demostrando la robustez del sistema. Para NEXT-100 se utilizará la misma arquitectura con pequeños cambios en el sistema.

Estudio del fondo en NEXT-100

El detector NEXT-100 cuenta con dos planos instrumentados, estando cada uno de ellos optimizado para una función diferente. Los electrones procedentes de la desintegración $\beta\beta$ producen centelleo e ionización en el xenón. La luz de centelleo es registrada por un conjunto de tubos fotomultiplicadores (PMT) situados en el cátodo que marcan el tiempo de inicio del evento (t_0). Los electrones de ionización son derivados hacia el ánodo por un campo eléctrico moderado hasta la región de electroluminiscencia. En ese punto son acelerados por un campo eléctrico más intenso capaz de producir un centelleo secundario proporcional al número de electrones que llegan. Los PMTs registran esta luz dando como resultado una medida precisa de la energía del evento. Por otro lado, junto al ánodo se encuentra el plano de *tracking* instrumentado con fotomultiplicadores de silicio (SiPM) formando una matriz con un espaciado regular de 1 cm. Mediante estos sensores es posible conseguir una reconstrucción detallada de la trayectoria de las partículas que han atravesado el detector.

El patrón de deposición de energía es diferente para los eventos de señal y los de fondo. En un evento de señal se producen dos electrones que parten del mismo vértice y se mueven depositando su energía. Al final de su trayectoria depositan energía a mayor ritmo (debido al pico de Bragg), dejando un patrón característico consistente en una traza alargada con dos grandes deposiciones de energía (*blob*) en sus extremos. En el caso de los eventos de fondo, la traza solo tendrá un *blob* en uno de sus extremos, pero no en el otro. Mediante un corte en la energía mínima de los extremos de la traza es posible conseguir una mayor separación de la señal y el fondo.

En estudios previos se han evaluado los distintos posibles fondos que podrían afectar a NEXT-100. La contribución dominante (97 %) proviene de fuentes radiogénicas, esto es, de la contaminación radiactiva de los materiales con los que se construye el detector. Los isótopos más problemáticos son el ^{214}Bi y el ^{208}Tl presentes en las cadenas de desintegración natural del uranio y del torio, respectivamente. Sus gammas de desintegración tienen una energía muy próxima al valor $Q_{\beta\beta}$ del ^{136}Xe.

En esta tesis se presenta un estudio actualizado de la contribución de los fondos de origen radiogénico a NEXT-100 usando las últimas medidas de radiopureza obtenidas en la colaboración. Los estudios previos fueron realizados con una simulación Monte Carlo simplificada que carecía de los detalles implementados en el software más reciente de la colaboración NEXT. El presente estudio incluye una simulación detallada de la deriva de la nube de electrones, así como del efecto de la electrónica y la reconstrucción.

El análisis estándar en la colaboración, llamado *análisis clásico*, incluye correcciones geométricas y de vida media de los electrones. También se ha realizado una optimización de los parámetros de los cortes topológicos. Los resultados obtenidos con este análisis son significativamente peores que lo que ofrece una reconstrucción ideal: el ruido esperado es 2.75 veces mayor. La difusión de la nube de electrones en la TPC es el principal origen del escaso rendimiento obtenido con el análisis clásico.

Modificando los cortes implementados en el análisis clásico es posible mejorar el resultado, aunque no lo suficiente. La forma de solucionar el problema es mediante el uso del algoritmo Richardson-Lucy. Este procedimiento es capaz de recuperar una imagen subyacente

alterada por una función de dispersión de punto (PSF) conocida. En el caso de NEXT, estas PSFs se pueden construir mediante el análisis de eventos puntuales de baja energía procedentes de una fuente de ^{83m}Kr. Mediante el uso de distintas PSFs dependiendo de la posición longitudinal del evento, es posible deconvolucionar el efecto de la difusión de la nube de electrones. Este algoritmo consigue una mejora significativa en los resultados, siendo comparable a los resultados obtenidos con la reconstrucción ideal.

El fondo esperado encontrado usando la deconvolución R-L es $4{,}29 \times 10^{-4}$ cts keV^{-1} kg^{-1} yr^{-1}. Estos resultados ponen de manifiesto la importancia crítica que tiene la difusión de la nube de electrones en detectores grandes. Algoritmos como Richardson-Lucy son una de las herramientas para tratar este problema. Más allá de soluciones basadas en mejoras del procedimiento de reconstrucción, la investigación sobre aditivos para el gas xenón que disminuyan la difusión es también una opción de gran interés.

De los resultados obtenidos también se deduce que reemplazar los PMTs por SiPMs produciría una rebaja importante del nivel de fondo del detector, ya que el plano de PMTs es la mayor fuente de eventos de fondo.

Aplicaciones médicas de NEXT

Para terminar, la tecnología desarrollada para los detectores NEXT tiene también aplicaciones más allá de la física fundamental, concretamente en la imagen médica. El uso del xenón como medio de detección para radiaciones, con fotomultiplicadores de silicio para registrar su respuesta, permite el desarrollo de un nuevo sistema de tomografía por emisión de positrones (PET).

El sistema PET es una técnica de imagen médica no invasiva empleada para observar los procesos metabólicos del cuerpo. No muestra rasgos anatómicos como una Resonancia Magnética o un TAC, sino la actividad de las células. Los escáneres PET se usan en investigación clínica y preclínica para estudiar las bases moleculares de la enfermedad y sus tratamientos.

El principio de operación consiste en inyectar al paciente una molécula con alguna actividad biológica, modificada para incluir un radioisótopo, denominada trazador. Un trazador común es la fluoro-

deoxiglucosa, que consiste en una molécula de glucosa en la que un oxígeno ha sido reemplazado por un ^{18}F, emisor β^+. El radionúcleo se desintegra dentro del paciente y el positrón emitido se aniquila con un electrón después de atravesar una corta distancia en los tejidos cercanos. Esta aniquilación produce dos fotones de 511 keV en direcciones opuestas. La trayectoria de los fotones define una linea de respuesta (LOR) que puede ser reconstruida mediante la medida de la dirección de ambas partículas. Esto se consigue observando la interacción de dichas partículas con un detector situado alrededor del cuerpo del paciente. La intersección de muchas LOR muestra el punto de emisión del radiotrazador. La medida de la diferencia temporal entre la llegada de los dos fotones (*time-of-flight*, TOF), permite mejorar la sensibilidad del sistema.

El proyecto PETALO planea la construcción de un escáner PET basado en xenón líquido instrumentado con SiPMs. Esta nueva tecnología presenta importantes ventajas: (a) una respuesta de centelleo muy rápida y con una gran cantidad de luz; (b) el xenón líquido ofrece un medio continuo con respuesta uniforme; (c) potencialmente, la identificación y reconstrucción de eventos Compton.

En esta tesis se presenta un estudio mediante simulación de la luz Cherenkov producida en el xenón líquido. El interés de este tipo de respuesta es que es extremadamente rápida, por lo que su uso podría permitir el diseño de sistemas PET con información del tiempo de vuelo (TOF) con una resolución temporal de coincidencias (CRT) extraordinaria. El análisis de la simulación implementada muestra como un CRT de $\sim$ 30 ps sería posible con sensores y electrónica suficientemente rápidos.

Conclusiones

Los objetivos de esta tesis se han cumplido satisfactoriamente. Se ha desarrollado un sistema de adquisición de datos escalable que ha demostrado sobradamente su fiabilidad y rendimiento durante varios años de operación del detector NEXT-White en el Laboratorio Subterráneo de Canfranc. El uso de la compresión mediante códigos de Huffman ha permitido una mejora notable del tiempo muerto del detector.

Las simulaciones detalladas realizadas del fondo radiactivo natural de NEXT-100 han mostrado la importancia crucial de tratar el problema de la difusión de la nube de electrones a lo largo de su deriva en la TPC. El algoritmo de deconvolución Richardson-Lucy permite corregir ese efecto logrando resultados similares a los obtenidos en una simulación ideal sin incluir la difusión. Este resultado también pone de manifiesto el interés del estudio de diferentes aditivos para el gas que disminuyan la difusión.

Por último, los resultados obtenidos en la simulación del sistema PETALO muestran la gran potencialidad de un escáner PET basado en xenón líquido para obtener una resolución temporal de coincidencias extraordinaria.

1 The nature of neutrinos

1.1 Brief history of neutrinos

In the 1920s there was a problem with the energy spectrum of β-decays. Protons and electrons were considered to be elementary particles, with nuclei being bound states of them. In that framework, the emission of a single e^- with a fixed kinetic energy $Q = (M_{A,Z} - M_{A,Z+1}) - m_e$ was expected. Instead, experiments such as William Wooster's in 1927 [1] found a continuous β spectrum, with end-point energy equal to Q, as shown in Figure 1.1.

Moreover, molecular band spectra established [2] that the spin of ^{14}N is 1, implying the violation of angular momentum conservation too, as the process ${}^{14}_{6}\mathrm{C} \rightarrow {}^{14}_{7}\mathrm{N} + e^-$ would involve the spins $0 \rightarrow 1 + \frac{1}{2}$.

A desperate answer to those experimental facts was proposed by Niels Bohr, when he postulated that energy conservation was true only in a statistical sense [3]. Nevertheless, his proposal could not solve the problem of the angular momentum.

In 1930, Wolfgang Pauli addressed the problem in a famous letter sent the 4th of December to the participants of the Tübingen conference [4]. The solution came in the form of a new neutral 1/2-spin particle, with a mass less than 1% of the proton mass, invisible to the detectors of that time. Hence, the decay would be a three-body process with the energy shared between the electron and the new particle, showing a continuous spectrum for electron energy. The angular momentum problem could also be solved as the reaction would be ${}^{14}_{6}\mathrm{C} \rightarrow {}^{14}_{7}\mathrm{N} + e^- + \nu$, with spins $0 \rightarrow 1 + \frac{1}{2} + \frac{1}{2}$, an allowed transition.

Enrico Fermi made the next fundamental contribution to the neutrino history in 1934, as he built the first theory of the β-decay of nuclei [5] based on Pauli's assumptions and called the new particle

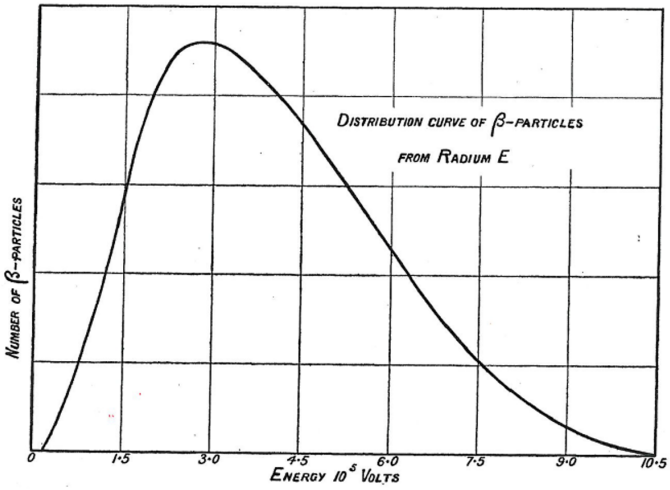

Figure 1.1: β decay electron energy spectrum from Wooster's experiment. Taken from Ref. [1]

the *neutrino*, because the neutron had been discovered by James Chadwick in 1932 [6]. He proposed a four-fermion coupling (Figure 1.2) describing the reactions

$$\begin{aligned} n &\to p + e^- + \bar{\nu}\,, \\ p &\to n + e^+ + \nu\,. \end{aligned} \tag{1.1}$$

As seen, his model for β decay required the existence of the (yet) unobservable neutrino to work.

In 1937, Ettore Majorana proposed a new theory for neutral, spin-1/2 particles, called today Majorana particles, in which particles and antiparticles are identical [7].

During the following years, physicists started to think about how the neutrino could be detected experimentally. Using Fermi's theory, Hans Bethe and Rudolf Peierls estimated in 1934 [8] the mean absorption length of neutrinos in solid matter, finding it to be a discouraging 10^{14} km. Neutrinos could traverse the Earth without interacting, leading them to conclude that "it is absolutely impossible to observe processes of this kind".

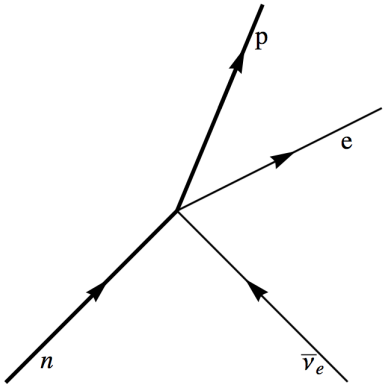

Figure 1.2: Four-fermion vertex in Fermi's β-decay theory.

Bruno Pontecorvo proposed the first technique for neutrino detection in 1946 [9]. He wrote *"The Object of this note is to show that the experimental observation of an inverse β process produced by neutrino is not out of the question with the modern experimental observation feasible"*. He considered a Cl-Ar reaction

$$\nu + {}^{37}\mathrm{Cl} \rightarrow e^- + {}^{37}\mathrm{Ar}\,, \tag{1.2}$$

as an appropiate candidate for neutrino detection. In a big sample of ^{37}Cl, long irradiated by neutrinos, a few atoms of ^{37}Ar could be produced. Since argon is a noble gas, atoms of ^{37}Ar could be easily extracted and placed in a proportional counter in which their decay would be detected.

The first neutrino detection was done in 1956 in an experiment by Fred Reines and Clyde Cowan [10]. They observed the process

$$\bar{\nu} + p \rightarrow e^+ + n \tag{1.3}$$

using the Savannah River reactor as a $\bar{\nu}$ source, and tanks filled with liquid scintillator (1.4×10^3 liters of cadmium chloride, $CdCl_2$) as target. They were able to detect the two 511 keV gammas from positron annihilation in coincidence with the nuclear gamma

$$n + {}^{108}\mathrm{Cd} \rightarrow {}^{109}\mathrm{Cd} + \gamma \tag{1.4}$$

due to the de-excitation of the ^{109}Cd nucleus after the neutron was captured by $CdCl_2$ molecules.

Their experiment not only discovered the antineutrino, but introduced a detection technique that is still being used in state-of-the-art detectors. Reines received the Nobel Prize in 1995 for the discovery.

By the time of the antineutrino discovery, two charged leptons were known: electrons and muons. The latter appears in pion decay, a process similar to β decay that involves also an antineutrino,

$$\pi^- \rightarrow \mu^- + \bar{\nu}. \tag{1.5}$$

Whether pion decays and beta decays have the same neutrinos, or not, was an open question until 1962. The Brookhaven neutrino experiment was the first one to measure antineutrinos from pion decays [11]. Leon Lederman, Melvin Schwartz and Jack Steinberger created the first neutrino beam by aiming a boosted proton beam against a target, producing pions and other hadrons that decay emitting neutrinos among other particles. A neutrino detector was placed behind the shield. If the charged-current interaction of the neutrinos with the target produced both electrons and muons, the experiment would have proven that there is a single type of neutrino. On the other hand, only muons were found in the detector, showing the existence of two different neutrino flavors. It established two families of leptons: (ν_e, e) and (ν_μ, μ).

This result suggested that the total electron and muon lepton numbers L_e and L_μ, which are called flavor lepton numbers, were conserved:

$$\sum_i L_e^{(i)} = const; \qquad \sum_i L_\mu^{(i)} = const \tag{1.6}$$

The third type of neutrino, ν_τ, the partner of the τ lepton, was discovered in 2000 by the DONUT Collaboration in Fermilab [12] with the measurement of τ appearance in the process

$$\nu_\tau + (A, Z) \rightarrow \tau + \ldots \tag{1.7}$$

All of these experiments detected artificially produced neutrinos, yet it was well-known that high fluxes of neutrinos, mainly produced in the Sun or the Earth's atmosphere, could be detected with this technology as well.

The first attempt to measure the solar neutrino flux came shortly after the discovery of the neutrinos by Reines and Cowan. Raymond Davis and collaborators started an experiment with chlorine-37 as proposed by Pontecorvo, but they only measured a third of the neutrino flux predicted by the theory [13]. At the beginning, those discrepancies were not taken too seriously due to a lack of confidence in the theory, and throughout the years, different experiments kept systematically observing less flux than predicted.

By the end of the 1980s Kamiokande-II, a solar neutrino experiment measuring the recoil electrons from the elastic scattering $\nu + e \rightarrow \nu + e$ from the solar reaction

$$^{8}\mathrm{Be} \rightarrow {}^{8}\mathrm{Be} + e^{+} + \nu_e \tag{1.8}$$

observed 46($\pm$13)% of the predicted flux of high energy neutrinos (>9.3 MeV). At the beginning of the nineties two new solar neutrino experiments based on gallium came to the same conclusion. GALLEX [14] and SAGE [15] detected ν_e's via the observation of radioactive ^{71}Ge atoms produced in the process

$$\nu_e + {}^{71}\mathrm{Ga} \rightarrow e^{-} + {}^{71}\mathrm{Ge}\,. \tag{1.9}$$

The fluxes measured were 62($\pm$10)% smaller than the predicted flux for energies > 0.233 MeV.

With all those experimental results, the solar neutrino problem was a real puzzle in the 1990s: all the experiments were seeing a deficit in the solar neutrino flux. Since it was different for different energies, it was unlikely to be an experimental issue. In that context, the most plausible solution was the hypothesis of neutrino oscillations, proposed by Pontecorvo in 1957 [9]. Neutrinos could have different flavor and mass eigenstates, leading to quantum mechanical oscillations.

In 1998, the Super-Kamiokande atmospheric neutrino experiment measured a significant up-down asymmetry in high-energy muon events, consistent with the oscillation picture, as shown in Figure 1.3. Neutrinos produced in the atmosphere above the detector (down-going) travel distances from 20 km to 500 km, while atmospheric neutrinos arriving to the detector through the Earth (up-going) travel distances from 500 km to 12000 km. Looking at high-energy muon

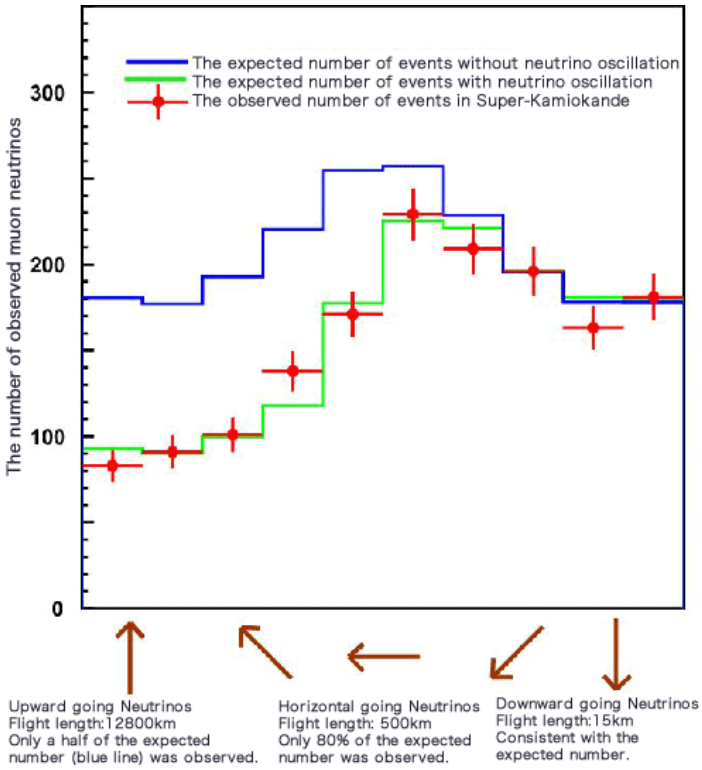

Figure 1.3: Super-Kamiokande observed and predicted number of muon neutrinos with and without oscillations as a function of the zenith angle. The difference between the experimental results and the prediction without oscillations increases with the traveled distance. Taken from Ref. [16].

neutrino events, Super-Kamiokande showed that the number of up-going neutrinos was about half of those down-going.

The next experimental breakthrough arrived in 2002 with the Sudbury Neutrino Observatory (SNO) experiment [17] measuring high-energy solar neutrinos from ^{8}Be decay both through charged currents (CC) and neutral currents (NC). The detection of CC events allowed them to measure the ν_e flux, while NC events were sensitive to all neutrino flavors (ν_e, ν_μ and ν_τ). The observed solar ν_e flux was a third of the flux of all three neutrinos combined. Therefore, it showed that ν_e's were changed to ν_μ and ν_τ on their way from the Sun to the Earth.

A few years later, in 2002-2004, the reactor neutrino experiment KamLAND, observed evidence of ν_e oscillations [18]. The detector measured neutrinos coming from 55 nuclear reactors at an average distance of 170 km. The total number of ν_e events was about 60% of the expected amount without oscillations.

Further confirmation of the oscillation paradigm using accelerator neutrinos was found by the K2K experiment in 2006 [19], and so the question of whether neutrinos undergo flavor oscillations has been answered using all major types of neutrino sources.

This historical consolidation of the neutrino oscillation picture has thus established some unique properties of these elusive particles. Even though there are further measurements needed to precisely determine all details of the oscillation model, a fundamental conclusion is already clear: neutrinos need to be massive particles in order to undergo oscillations, and their masses are direct evidence of physics beyond the Standard Model.

1.2 Massive neutrinos

The Standard Model (SM) of particle physics, illustrated in Figure 1.4, describes electromagnetic, weak and strong interactions. It was developed in the 1970s and has received extensive experimental support in the following decades. There are, though, some open questions in it, several of them related to the nature of neutrinos.

Neutrinos in the SM are massless particles that interact only through the weak force as they do not have electromagnetic charge nor color. All neutrinos are left-handed while antineutrinos are right-handed.

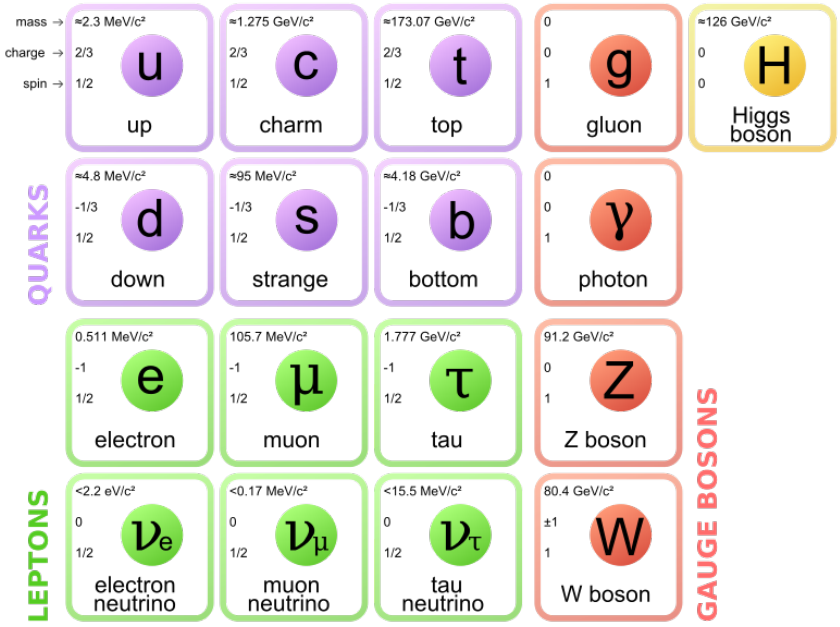

Figure 1.4: Elementary particles described in the Standard Model. Notice the mass scale of neutrinos compared with that of other fundamental particles. Taken from Ref. [20].

There are three types of neutrinos, one for each lepton family (e, ν_e), (μ, ν_μ), (τ, ν_τ) with their own lepton number conserved separately. Neutrinos and antineutrinos are distinct.

Neutrino oscillations, which have been experimentally confirmed, are only possible if neutrinos are massive, and they break the conservation of flavor lepton number: only the global lepton number L is conserved. Oscillations are a quantum mechanical effect arising from the fact that flavor eigenstates are a superposition of different mass eigenstates. When a neutrino is produced it has a well-defined flavor state that can be expressed as a combination of mass eigenstates:

$$|\nu_\alpha\rangle = \sum_k U^*_{\alpha k} |\nu_k\rangle \,, \tag{1.10}$$

where $|\nu_\alpha\rangle$ is a neutrino with flavor $\alpha = e$ (electron), μ (muon) or τ (tau), and $|\nu_k\rangle$ is a neutrino state with definite mass m_k ($k = 1, 2, 3$).

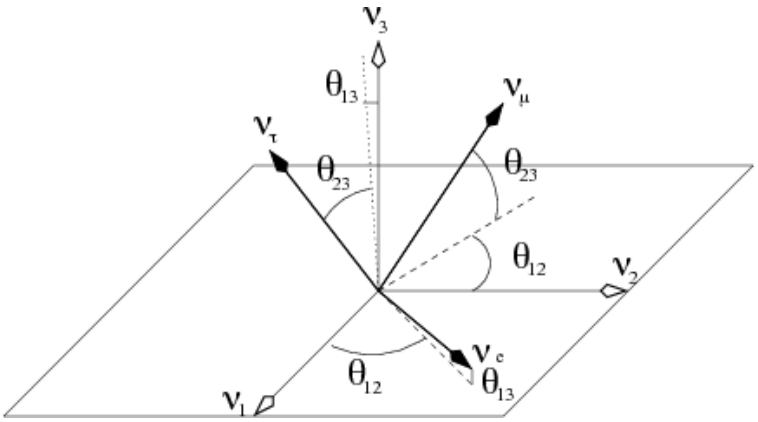

Figure 1.5: Representation of the three mass eigenstates and the three flavour eigenstates, with all the mixing angles involved in the rotation between them. Taken from Ref. [21].

Since neutrinos are relativistic particles their energy is $E = \sqrt{p^2 + m^2}$ and their propagation is expressed in terms of mass eigenstates as

$$e^{-iHt} |\nu_\alpha\rangle = \sum_k U^*_{\alpha k} e^{-iE_k t} |\nu_k\rangle \tag{1.11}$$

with a different phase for each massive neutrino. When a neutrino is detected it has a probability to be measured as each different flavor

$$P_{\alpha\beta}(t) = \left| \langle \nu_\beta | \, e^{-iHt} |\nu_\alpha\rangle \right|^2 . \tag{1.12}$$

The mixing matrix U governing the rotation between flavor and mass eigenstates bases is the Pontecorvo-Maki-Nakagawa-Sakata matrix, usually parametrized as

$$U_{\text{PMNS}} = \begin{bmatrix} c_{12}c_{13} & s_{12}c_{13} & s_{13}e^{-i\delta} \\ -s_{12}c_{23} - c_{12}s_{23}s_{13}e^{i\delta} & (c_{12}c_{23} - s_{12}s_{23}s_{13}e^{i\delta}) & s_{23}c_{13} \\ s_{12}s_{23} - c_{12}c_{23}e^{i\delta} & -c_{12}s_{23} - s_{12}c_{23}s_{13}e^{i\delta} & c_{23}c_{13} \end{bmatrix}, \tag{1.13}$$

where $c_{ij} \equiv \cos\theta_{ij}$ and $s_{ij} \equiv \sin\theta_{ij}$.

The oscillation probability depends on the three mixing angles θ_{ij} (illustrated in Figure 1.5), the CP phase δ and phase differences of the

mass eingenstates in Eq. (1.11). Since neutrinos are ultrarelativistic and their energy is

$$E_k \approx p + \frac{m_k^2}{2p}\,, \qquad m_k^2 \ll p^2\,, \tag{1.14}$$

these phase differences can be expressed as

$$\Delta E_{ij}\, t = \frac{\Delta m_{ij}^2 L}{2E}\,, \tag{1.15}$$

where $\Delta m_{ij}^2 \equiv m_i^2 - m_j^2$. Therefore, neutrino oscillations experiments can probe the U_{PMNS} matrix and the mass differences between neutrinos, but not their absolute mass scale.

Global analyses of neutrino oscillation data [22] have determined with good precision (at the few percent level) the value of the three mixing angles: the solar angle $\theta_{12} \simeq 34^\circ$, the atmospheric angle $\theta_{23} \simeq 50^\circ$ and the reactor angle $\theta_{13} \simeq 9^\circ$; each named according to the its main measurement channel. Experiments using solar and reactor neutrinos have measured one mass difference, the so-called *solar mass splitting*: $\Delta m^2_{\text{sol}} \simeq 7.4 \times 10^{-5}$ eV^2. Atmospheric and accelerator-based oscillation experiments have measured the other mass difference, the *atmospheric mass splitting*: $|\Delta m^2_{\text{atm}}| \simeq 2.5 \times 10^{-3}$ eV$^2 \gg \Delta m^2_{\text{sol}}$.

Due to the unknown sign of the atmospheric mass splitting, there are two possible orderings of the neutrino masses: normal and inverted, illustrated in Figure 1.6. In the normal ordering Δm^2_{sol} is the difference between the squared masses of the two lightest mass states, while in the inverted ordering it corresponds to the difference between the two heaviest states. Table 1.1 shows the latest values for neutrino mass differences and mixing angles.

1.2.1 Neutrino mass experimental measurement

Neutrino oscillations do not provide information regarding the absolute neutrino mass scale. This value is of utmost importance to understand the formation and evolution of the universe as well as to extend particle physics beyond the Standard Model. There are several processes that provide access to this information: single β-decay, electron capture and neutrinoless double decay (see Chapter § 2). Also,

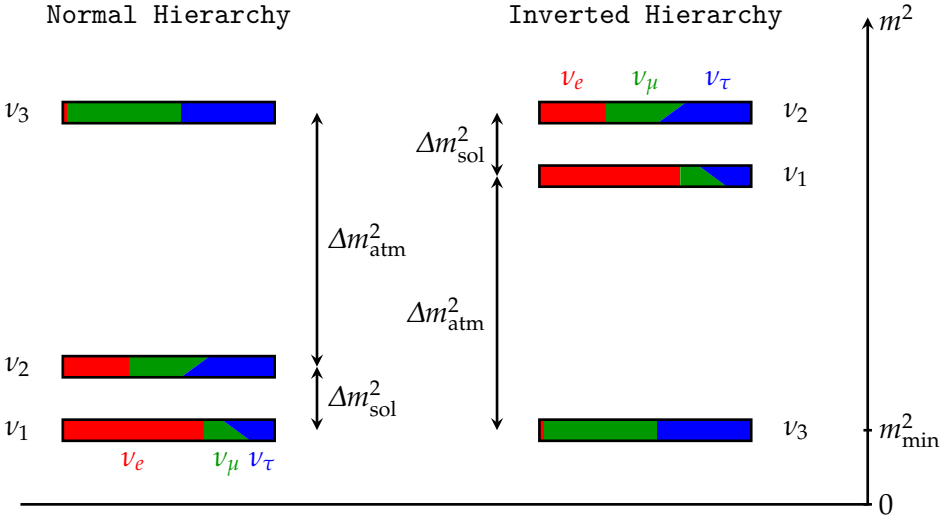

Figure 1.6: Possible neutrino mass orderings, with the mass eigenstates ν_k separated by the known atmospheric and solar mass splittings; the unknown absolute mass scale m_{min} is also shown. The colored areas show the flavor fraction $|U_{\alpha k}|^2$ of each ν_k for $\alpha = e$ (red), μ (green), τ (blue). The change in $|U_{\alpha k}|^2$ from the bottom to the top of the boxes corresponds to changing $\cos\delta$ from 1 to -1. Taken from Ref. [23].

cosmological observations can put bounds on the sum of all neutrino masses.

Conceptually, the simplest way to measure the absolute neutrino mass is to look at the high-end of the energy spectrum from a β-decay source, as shown in Figure 1.7. In a beta decay, an electron and an antineutrino are emitted, with the transition energy (Q_β) shared among their kinetic energies and masses. The difference between the maximum energy of the electron and Q_β can provide an estimation for the effective neutrino mass

$$m_\beta^2 = \sum_{i=1}^{3} |U_{ei}|^2 \, m_i^2 \, . \tag{1.16}$$

Given the very small value of this mass, such a measurement is very challenging. The most promising experiment using this approach

Table 1.1: Neutrino mixing parameters according to the most recent global oscillation analysis [22].

Parameter	Normal ordering		Inverted ordering	
	best fit $\pm$ 1σ	3σ range	best fit $\pm$ 1σ	3σ range
θ_{12} (°)	34.3±1.0	[31.4, 37.4]	34.3±1.0	[31.4, 37.4]
θ_{23} (°)	$48.79^{+0.93}_{-1.25}$	[41.63, 51.32]	$48.79^{+1.04}_{-1.30}$	[41.88, 51.3]
θ_{13} (°)	$8.58^{+0.11}_{-0.15}$	[8.16, 8.94]	$8.63^{+0.11}_{-0.15}$	[8.21, 8.99]
δ_{CP} (°)	216^{+41}_{-25}	[144, 360]	277^{+23}_{-24}	[205, 342]
Δm^2_{21} (10^{-5} eV^2)	$7.50^{+0.22}_{-0.20}$	[6.94, 8.14]	$7.50^{+0.22}_{-0.20}$	[6.94, 8.14]
$\lvert\Delta m^2_{31}\rvert$ (10^{-3} eV^2)	$2.56^{+0.03}_{-0.04}$	[2.46, 2.65]	2.46 ± 0.03	[2.37, 2.55]

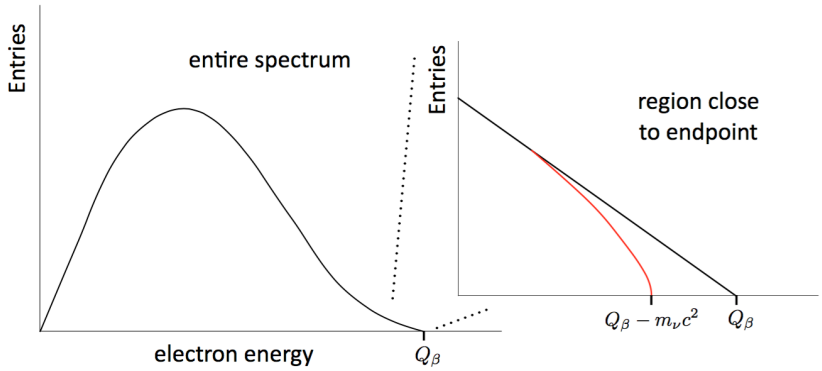

Figure 1.7: Energy spectrum of beta decay showing the endpoint region. The black line corresponds to zero neutrino mass and the red line to finite neutrino mass. Taken from Ref. [25].

is KATRIN, which using tritium as the source ($Q_\beta = 18570$ eV) is expected to reach a sensitivity of 0.2 eV (90% CL) on m_β. Their first results were published in 2019 with the upper limit $m_\beta < 1.1$ eV (90% CL) [24].

Massive neutrinos could have a big impact in cosmology too since

they are the most abundant population in the universe after photons. Neutrinos could produce a measurable effect on the universe's structure by having affected in the past the rate of expansion and the growth of cosmological perturbations [26].

The study of anisotropies in the Cosmic Microwave Background radiation (CMB), distribution of galaxies and the structure of the universe can set different limits on the sum of the three neutrino masses depending on the cosmological model used. In 2019 the Planck collaboration published its latest results [27]: combining Planck data with Baryon Acoustic Oscillations (BAO) the limit was set to

$$\sum_{\nu} m_{\nu} < 0.12 \text{ eV} \quad (95\% \text{ CL}). \tag{1.17}$$

1.3 Dirac and Majorana neutrinos

Despite the fact that neutrinos are massless in the Standard Model, it is known that they have to be massive due to observations like neutrino oscillations. This requires a modification to the SM lagrangian to include a neutrino mass term. Depending on how that is done two kinds of neutrinos are possible: Dirac and Majorana.

Dirac neutrinos get their mass in the same way as quarks and charged leptons: via a Yukawa coupling with the Higgs field [28, 29]. This interaction requires both left- and right-handed neutrinos, although only left-handed neutrinos have been observed experimentally. The lagrangian would include a term of the form

$$-\mathcal{L}_D = m_D(\bar{\nu}_L \nu_R + \bar{\nu}_R \nu_L) \tag{1.18}$$

adding therefore right-handed neutrinos that are *sterile*, i.e. they only interact through gravitation. This mechanism needs Yukawa couplings for neutrinos that are orders of magnitude smaller than the couplings of the other fermions, making it rather unnatural.

In addition to that approach, the neutrino masses can be added to the SM with a Majorana mass term. Ettore Majorana proposed the removal of two degrees of freedom of a massive Dirac spinor [7]. This can be achieved by applying the Majorana condition, i.e. making the neutrino field ν equal to its CP conjugate

$$\nu = \nu^c \tag{1.19}$$

where $\nu^c = C\bar{\nu}^T$, with C being the charge-conjugation operator. This condition implies that there is only one field to describe neutrino and antineutrino states. Decomposing the neutrino field into left- and right-handed components Eq. (1.19) implies

$$\nu_R = (\nu_L)^c \tag{1.20}$$

The relationship can be applied to the SM lagrangian contribution from Eq. (1.18) to obtain the Majorana mass term

$$-\mathcal{L}_L = \frac{1}{2} m_L (\overline{\nu_L}(\nu_L)^c + \overline{(\nu_L)^c}\nu_L)\,, \tag{1.21}$$

where m_L is a free parameter with mass dimensions. Once a Majorana term is generated for a left-handed neutrino, the same term can be built for the right-handed one

$$-\mathcal{L}_R = \frac{1}{2} m_R (\overline{\nu_R}(\nu_R)^c + \overline{(\nu_R)^c}\nu_R)\,. \tag{1.22}$$

The Majorana mass term coming from this new mechanism converts particles into their own antiparticles, thus violating the SM total lepton number $L \equiv L_e + L_\mu + L_\tau$ by two units ($|\Delta L| = 2$). Those mass terms are only possible for neutrinos, since all charged fermions would otherwise violate charge conservation.

The Majorana nature of the 3 light neutrinos would open the door to extra sources of CP violation in the lepton sector, which are usually parametrized by adding two extra phases to the PMNS matrix,

$$U_{PMNS} \mapsto U_{PMNS} \times \begin{bmatrix} 1 & 0 & 0 \\ 0 & e^{i\alpha/2} & 0 \\ 0 & 0 & e^{i\beta/2} \end{bmatrix} \tag{1.23}$$

These extra phases are unobservable in neutrino oscillations, but they affect all processes where the Majorana nature of neutrinos play a role.

1.3.1 The see-saw mechanism

The see-saw mechanism is a generic model used to understand why neutrino masses are orders of magnitude smaller than those of other

fermions [28]. After adding the Majorana mass term to the SM lagrangian, it can be expressed as

$$-\mathcal{L}_{D+R} = \frac{1}{2}\overline{\mathcal{N}_L^c} M \mathcal{N}_L + h.c., \tag{1.24}$$

written in terms of the neutrino-fields vector $\mathcal{N}_L = \left(\nu_L, \nu_R^c\right)$ and the mass matrix

$$M = \begin{pmatrix} 0 & m_D \\ m_D & m_R \end{pmatrix} \tag{1.25}$$

Therefore, the two components in $\mathcal{N}_L$ do not have a definite mass. To get definite-mass states the matrix has to be diagonalized, yielding two new fields ν_{1L} and ν_{2L} with their associated eigenvalues m_1 and m_2. A unitary matrix U can be computed satisfying

$$U^T M U = \begin{pmatrix} m_1 & 0 \\ 0 & m_2 \end{pmatrix}, \qquad \mathcal{N}_L = U n_L\,. \tag{1.26}$$

which diagonalizes the mass matrix and relates $\mathcal{N}_L$ to the vector of eigenstates $n_L = \left(\nu_{1L}, \quad \nu_{2L}\right)$.

Using this transformation, the lagrangian term (1.24) becomes

$$-\mathcal{L}_{D+R} = \frac{1}{2}\left(m_1 \overline{\nu_{1L}^c}\nu_{1L} + m_2 \overline{\nu_{2L}^c}\nu_{2L}\right) + h.c.\,, \tag{1.27}$$

in terms of definite-mass states. Using the approximation $m_D \ll m_R$ the mass states would be

$$m_1 \simeq \frac{m_D^2}{m_R}\,; \qquad m_2 \simeq m_R \tag{1.28}$$

with m_1 being much smaller than m_2, hence the name of the model.

The procedure described above can be generalized to 3 neutrino flavors, resulting in 3 light neutrinos and 3 heavy neutrinos. The light ones would correspond to the 3 neutrinos observed experimentally, while the heavy ones have not been observed due to the high energies required (close to the GUT scale [28]) and the fact that the mixing angles between light and heavy neutrinos are very small.

1.3.2 The missing antimatter

Our current cosmological models predict an equal amount of matter and antimatter at the beginning of the universe, but now only a matter universe is observed. Majorana neutrinos could contribute to explaining the origin of this asymmetry according to leptogenesis theories [30].

Heavy Majorana neutrinos could decay into leptons l_α and Higgs bosons ϕ and, since they are their own antiparticles, also into their corresponding antiparticles ($\bar{l}_\alpha$, $\bar{\phi}$). An unbalance in the decay rates of the two modes would directly translate into a lepton asymmetry which can be converted into a baryon asymmetry through a sphaleron process [31]. In order for a process to induce a non-vanishing contribution to baryogenesis, the Sakharov's conditions [32] must be met:

1. **Violation of the baryon number**. In the case of heavy Majorana neutrino decay the total lepton number is violated and, through a sphaleron process, baryon number conservation can be violated too.

2. **Violation of both** C **and** CP **symmetries**, which can also happen if there is more than one heavy Majorana neutrino field.

3. **The universe went through a stage of non-equilibrium**. This can be produced if the decay rate was slower than the expansion rate of the universe when the universe's temperature was of the of the order of the mass of the heavy neutrino.

The lepton flavor asymmetry is defined as

$$\epsilon_{\alpha\alpha} = \frac{\Gamma(N_1 \to \phi l_\alpha) - \Gamma(N_1 \to \bar{\phi}\overline{l_\alpha})}{\Gamma(N_1 \to \phi l_\alpha) + \Gamma(N_1 \to \bar{\phi}\overline{l_\alpha})}, \tag{1.29}$$

where Γ is the decay rate of the corresponding channel. To explain the baryon asymmetry observed in the universe the condition $|\epsilon_{\alpha\alpha}| > 10^{-7}$ must be met [31]. Majorana neutrinos would not necessarily imply the existence of this mechanism in nature, but would make it very likely.

1.3.3 Observables sensitive to the neutrino nature

The nature of neutrinos, whether they are Dirac or Majorana particles, is still unknown. If neutrinos are Majorana particles a series of lepton number violating (LNV) processes would be allowed. The simplest $|\Delta L| = 2$ process is

$$W^- W^- \to l_\alpha^- l_\beta^- \tag{1.30}$$

with $\alpha, \beta = e, \nu, \tau$. If light Majorana neutrino exchange is the only contribution to lepton violation, the matrix element for the previous process is

$$M_{\alpha\beta}^{\text{light}} = \left(U^* \text{diag}(m_1, m_2, m_3) U^\dagger \right)_{\alpha\beta} = \sum_{i=1}^{3} U_{\alpha i}^* U_{\beta i}^* m_i \,, \tag{1.31}$$

where U is the PMNS matrix, m_i are the light neutrino masses and M^{light} is the mass matrix for light neutrinos. This gives the effective neutrino mass for a given process and it is useful to compare $|\Delta L| = 2$ processes. Table 1.2 shows some LNV processes with their possible experimental techniques and the bounds found for each of their effective Majorana masses. Neutrinoless double beta decay is the most promising one in terms of putting a bound on the effective neutrino mass.

Table 1.2: Limits on the effective neutrino masses for total lepton number violating processes according to the flavors involved. Numbers taken or derived from [33, 34].

Flavors	**Exp. technique**	**Exp. bound**	**Mass bound (eV)**
(e,e)	$\beta\beta 0\nu$	$T_{1/2}(^{136}Ge \rightarrow ^{136}Se + 2e^-) > 9 \times 10^{25}$	$\lvert m_{ee}\rvert < 0.16$
(e,μ)	$\mu^- \rightarrow e^+$ conversion	$\Gamma(Ti + \mu^- \rightarrow e^+ + Ca_{\text{gs}})/$ $\Gamma(Ti + \mu^-\text{capture}) < 1.7 \times 10^{-12}$	$\lvert m_{e\mu}\rvert < 1.7 \times 10^{7}$
(e,τ)	Rare τ decays	$\Gamma(\tau^- \rightarrow e^+\pi^-\pi^-)/\Gamma_{\text{tot}} < 8.8 \times 10^{-8}$	$\lvert m_{e\tau}\rvert < 2.6 \times 10^{12}$
(μ,μ)	Rare kaon decays	$\Gamma(K^+ \rightarrow \pi^+\mu^+\mu^+)/\Gamma_{\text{tot}} < 1.1 \times 10^{-9}$	$\lvert m_{\mu\mu}\rvert < 2.9 \times 10^{8}$
(μ,τ)	Rare τ decays	$\Gamma(\tau^- \rightarrow \mu^+\pi^-\pi^-)/\Gamma_{\text{tot}} < 3.7 \times 10^{-8}$	$\lvert m_{\mu\tau}\rvert < 2.1 \times 10^{12}$
(τ,τ)	—	—	—

2 Neutrinoless double beta decay

2.1 Introduction to double beta decay

Double beta decay is a very rare process in which a nucleus with Z protons decays into another one with Z+2 or Z-2 protons and the same mass number. The ordinary mode, known as $2\nu\beta\beta$, emits two electrons and two antineutrinos in the process

$$(Z, A) \rightarrow (Z + 2, A) + 2e^{-} + 2\bar{\nu}_e \tag{2.1}$$

and was first proposed in 1935 by Maria Goeppert-Mayer [35]. Lepton number is conserved in this process and it is allowed by the Standard Model.

Although the first evidence for the process appeared in 1950 using geochemical techniques for the isotope ^{130}Te [36], it was not until 1987 that a direct observation was possible. The measurement was done for ^{82}Se using a time projection chamber and showed a half-life of 1.1×10^{20} years [37]. Such a long half-life makes the single β-decay of most nuclides an intense source of background for $2\nu\beta\beta$ detection. Only when single β-decay is forbidden or strongly suppressed is the detection of $2\nu\beta\beta$ possible. Figure 2.1 shows the mass parabola for isobars with $A = 136$; in the case of ^{136}Xe, single β-decay is forbidden due to energy conservation, so it can only decay through double beta to ^{136}Ba. The higher mass of the odd-odd isotopes is due to smaller value of the pairing term in their nuclear binding energy [38]. This condition is fulfilled for 35 naturally-occurring isotopes, with 12 of them already having a measurement of their half-life with typical values in the order of $10^{18} - 10^{21}$ years. Table 2.1 shows a list of the latest values.

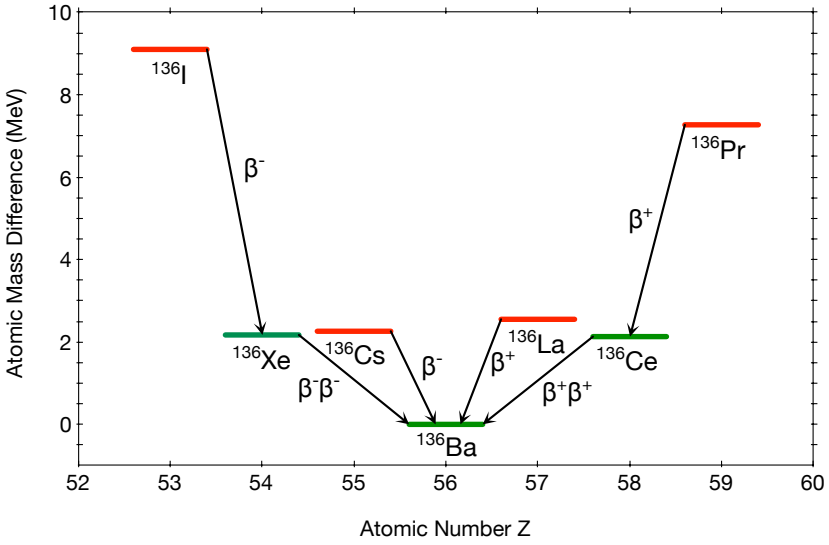

Figure 2.1: Atomic masses of isobars with $A = 136$ given as differences with respect to the most stable one, ^{136}Ba. The red levels indicate odd-odd nuclides, whereas the green indicate even-even ones. The arrows show the type of nuclear transition connecting the levels. $\beta\beta$ (either plus or minus) transitions are possible because the intermediate state ($\Delta Z = \pm 1$) is less stable, forbidding the β decay.

Besides the normal mode of the decay, in 1939 Wendell Furry proposed a neutrinoless process ($0\nu\beta\beta$) [39]

$$(Z, A) \rightarrow (Z + 2, A) + 2e^{-} \tag{2.2}$$

as a method to test the Majorana nature of the neutrinos [7]. This process would violate total lepton number and is, therefore, not allowed by the Standard Model: it would only be possible if neutrinos are Majorana particles. No experimental evidence of this decay has ever been found yet.

The nuclear recoil is negligible in both decay modes, so the emitted leptons share almost all the energy available. By looking at an energy spectrum of the sum of the two electrons, it would be possible to identify both decay modes. In the neutrinoless case, the sum of the kinetic energies of the two electrons would be a mono-energetic line

Table 2.1: Half-lives for two-neutrino double beta decay ($2\nu\beta\beta$) from the best direct measurements [33].

Isotope	$T^{2\nu}_{1/2}$ (10^{21} yr)	Experiment
^{48}Ca	$0.064^{+0.007+0.012}_{-0.006-0.009}$	NEMO-3
^{76}Ge	1.926 ± 0.094	GERDA
^{78}Kr	$9.2^{+5.5}_{-2.6} \pm 1.3$	BAKSAN
^{82}Se	$0.0939 \pm 0.0017 \pm 0.0058$	NEMO-3
^{96}Zr	$0.0235 \pm 0.0014 \pm 0.0016$	NEMO-3
^{100}Mo	$0.0068 \pm 0.00001^{+0.00038}_{-0.00040}$	NEMO-3
^{116}Cd	$0.0263^{+0.0011}_{-0.0012}$	AURORA
^{130}Te	$0.82 \pm 0.02 \pm 0.06$	CUORE-0
^{134}Xe	> 0.87	EXO-200
^{136}Xe	$2.165 \pm 0.016 \pm 0.059$	EXO-200
^{150}Nd	$0.00934 \pm 0.00022^{+0.00062}_{-0.00060}$	NEMO-3

at $Q_{\beta\beta}$, defined as the mass difference between the two nuclides,

$$Q_{\beta\beta} \equiv M(A,Z) - M(A,Z+2)\,, \tag{2.3}$$

while in the two neutrino mode, the spectrum is continuous, ranging from 0 to $Q_{\beta\beta}$ with a peak below $Q_{\beta\beta}/2$. Both cases are illustrated in Figure 2.2.

2.2 Standard neutrinoless double beta decay mechanism

The simplest way in which neutrinoless double beta decay can occur is from a diagram in which a parent nucleus emits a pair of virtual W bosons, which exchange a light Majorana neutrino to produce the outgoing electrons (see Figure 2.3). The lifetime for the $0\nu\beta\beta$ process mediated by a light Majorana neutrino can be expressed as [40]

$$\left(T^{0\nu}_{1/2}\right)^{-1} = G^{0\nu}(Q,Z)\left|M^{0\nu}\right|^2 \left(\frac{m_{\beta\beta}}{m_e}\right)^2, \tag{2.4}$$

where $G^{0\nu}$ is the phase-space factor that depends on the transition Q-value and on the atomic number Z of the parent nucleus and can be

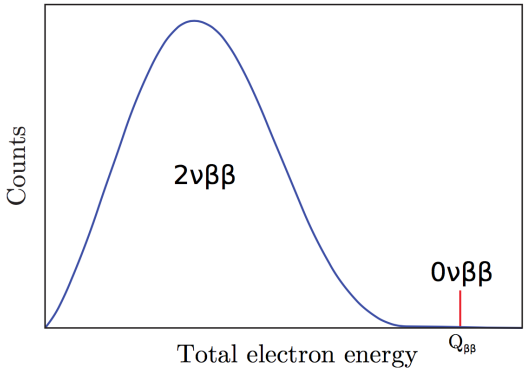

Figure 2.2: Illustration of the spectra for the sum of the kinetic energies of the two emitted electrons for $2\nu\beta\beta$ (blue) and $0\nu\beta\beta$ (red). The relative amplitudes are arbitrary.

computed accurately [41,42]; $M^{0\nu}$ is the nuclear matrix element (NME) and can be computed using different nuclear models, which will be discussed in Section 2.4.1; and $m_{\beta\beta}$ is an effective Majorana neutrino mass given by

$$m_{\beta\beta} = \left| \sum_i U_{ei}^2 \, m_i \right| , \tag{2.5}$$

where U is the PMNS matrix and m_i are the neutrino masses.

Following Eq. (2.4), a non-zero $0\nu\beta\beta$ rate measurement can provide a value for the effective Majorana neutrino mass, providing direct information on the absolute neutrino mass scale, although with uncertainties coming mainly from $M^{0\nu}$. In the same way, a non-observation of the $0\nu\beta\beta$ process by an experiment can lead to an upper bound on $m_{\beta\beta}$.

The information about the neutrino masses m_i that can be extracted from $m_{\beta\beta}$ is affected by the uncertainties in the oscillation parameters, on the unknown phase angles of the mixing matrix (Dirac and Majorana) and on the mass hierarchy. Furthermore, some additional unknown neutrino physics could be affecting this relationship too. Figure 2.4 shows the dependence between $m_{\beta\beta}$ and m_{light}.

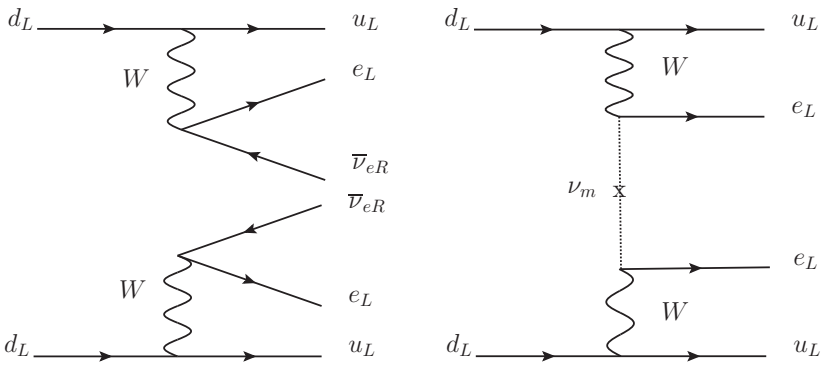

Figure 2.3: Feynman diagram for the $2\nu\beta\beta$ (left) and the $0\nu\beta\beta$ (right) decay modes.

2.3 The black box theorem

Beyond this standard mechanism, there are many other theories predicting LNV processes and all of them can lead to $0\nu\beta\beta$ decay. Irrespective of the mechanism, they imply neutrinos are Majorana particles, as was proven by Joseph Schechter and Jose Valle in 1982 [44]. This is known as the black box theorem and is due to the fact that any diagram that does not conserve the total lepton number would contribute to the Majorana mass matrix as illustrated in Figure 2.5.

Quantitatively, the diagram corresponds to a small mass generated at four-loop level and it is not enough to explain the mass splittings observed in neutrino oscillation experiments [45]. Therefore, other still unknown Dirac or Majorana mass contributions must exist. The theorem cannot clarify which physics mechanism is the dominant contribution to the $0\nu\beta\beta$ decay. The dominating mechanism could be directly or indirectly connected to oscillations or not related at all to neutrino oscillations phenomenology [46].

2.4 Design of double beta decay experiments

The observation of $0\nu\beta\beta$ events would be a major discovery in particle physics, as it would prove neutrinos are Majorana particles. Nevertheless, the design of detectors capable of measuring $0\nu\beta\beta$ events is a big

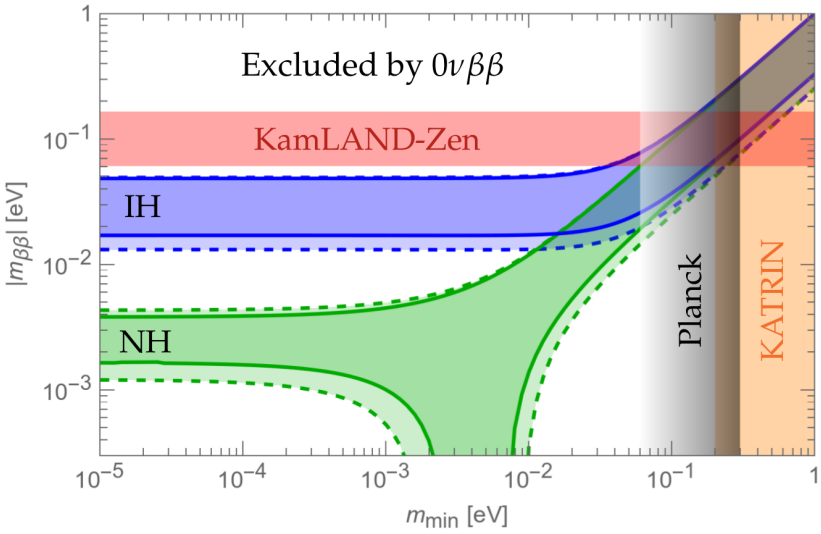

Figure 2.4: Effective Majorana neutrino mass, $m_{\beta\beta}$ as a function of the lightest neutrino mass, m_{light}, for both Normal (green) and Inverted (blue) Hierarchies. Solid lines show the limits for the best-fit configuration (Table 1.1), dashed lines show the limits changing the parameters in their 2σ ranges. Current experimental bounds are also shown for the $0\nu\beta\beta$ KamLAND-Zen bound [43] (red), β-decay KATRIN sensitivity [24] (orange), and cosmological Planck results [27] (gray). Taken from Ref. [23].

experimental challenge, since the lifetimes of the decays are extremely large. For instance, with a $m_{\beta\beta}$ of 50 meV the expected lifetime would be on the order of 10^{26} to 10^{27} years, depending on the isotope and the nuclear model.

Quantitatively, the number of events expected in an observation time much smaller than the half-life can be approximated as

$$N_{0\nu\beta\beta} = \log 2 \, \frac{M \, N_A}{W} \, \frac{t}{T^{0\nu}_{1/2}} \, \epsilon \, , \tag{2.6}$$

where M and W are the mass and the molar mass of the $\beta\beta$ emitter respectively, N_A is the Avogadro constant and ϵ is the detector efficiency.

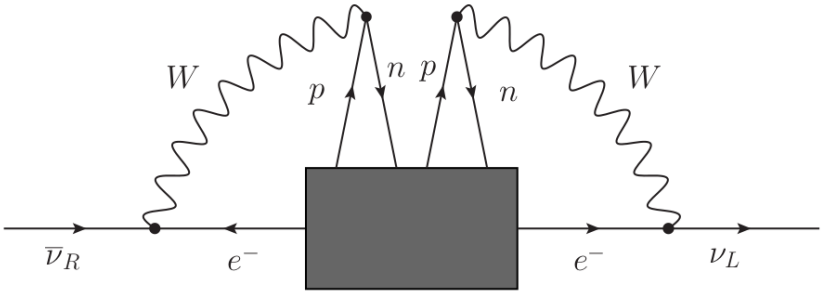

Figure 2.5: Diagram of the black box theorem showing how any neutrinoless double beta decay mechanism induces a transition from $\bar{\nu}$ to ν, which translates into an effective Majorana mass term.

Combining this number of events with the half-life in Eq. (2.4), the sensitivity of a $0\nu\beta\beta$ experiment can be defined as the upper limit on $m_{\beta\beta}$ that can be inferred from an experiment with no observations,

$$m_{\beta\beta} = K_1 \frac{1}{\sqrt{\epsilon M t}}, \tag{2.7}$$

where K_1 is a constant depending only on the $0\nu\beta\beta$ isotope. This is not realistic as experiments are affected by background, especially for such long half-lifes. If the background is intense enough, it can be added easily to the previous equation as

$$m_{\beta\beta} = K_2 \frac{\sqrt[4]{b}}{\sqrt{\epsilon M t}}, \tag{2.8}$$

where K_2 depends on the isotope and the proportionality of signal and background. Non-uniform backgrounds can be described in terms of the count rate c expected in the energy window ΔE around $Q_{\beta\beta}$ in a given exposure Mt, having then $b = cMt\Delta E$. In terms of this count rate, usually expressed in number of events per kilogram and keV in a year, the sensitivity reads:

$$m_{\beta\beta} = K_2 \frac{1}{\sqrt{\epsilon}} \sqrt[4]{\frac{c\,\Delta E}{M\,t}}. \tag{2.9}$$

The aim of a $0\nu\beta\beta$ experiments is to probe a $m_{\beta\beta}$ as small as possible. As seen, there are several key parameters involved in the $m_{\beta\beta}$ sensitivity, which we discuss in detail in the following.

2.4.1 Isotope

The selection of the isotope is of utmost importance for $\beta\beta$ experiments as it influences many factors. First of all, the half-life depends on the the nuclear matrix element, $M^{0\nu}$. This quantity can be computed using different nuclear models such as the Interacting Shell Model (ISM) [47], the Quasiparticle Random Phase Approximation (QRPA) [48,49], the Interacting Boson Model (IBM-2) [50] or the Energy Density Functional Method (EDF) [51,52]. There are large uncertainties and mismatches between values coming from different models. Figure 2.6 shows $M^{0\nu}$ for several different isotopes and models. It is clear from this that after measuring $T^{0\nu}_{1/2}$, the uncertainty from $M^{0\nu}$ would be transfered to $m_{\beta\beta}$, producing broad intervals. In the same way, using $M^{0\nu}$ to select the best isotope is not feasible due to this huge variability.

One critical parameter is the $Q_{\beta\beta}$, with higher values being more favorable. On one hand, higher energies have less background coming from natural radioactivity. On the other hand, the half-life $T^{0\nu}_{1/2}$ also depends inversely on the phase space factor $G^{0\nu}$, which varies as $Q^5_{\beta\beta}$ [42], making isotopes with large $Q_{\beta\beta}$ values strongly favored. The most commonly used isotopes in $0\nu\beta\beta$ experimental searches have $Q_{\beta\beta} > 2$ MeV.

The two-neutrino mode of the $\beta\beta$-decay can become a considerable background source for $0\nu\beta\beta$ if the rate is sufficiently high and the energy resolution is not good enough.

In addition to these physical properties, some other considerations must be taken into account, such as the procurement cost or the possibility of enriching the sample in the desired isotope.

2.4.2 Energy resolution

Good energy resolution is a critical characteristic of a $0\nu\beta\beta$ detector, since it is the only tool that allows one to discriminate between $0\nu\beta\beta$ and $2\nu\beta\beta$ events in the higher-energy end of the spectrum. A better energy resolution also improves the signal-to-noise ratio in the $Q_{\beta\beta}$

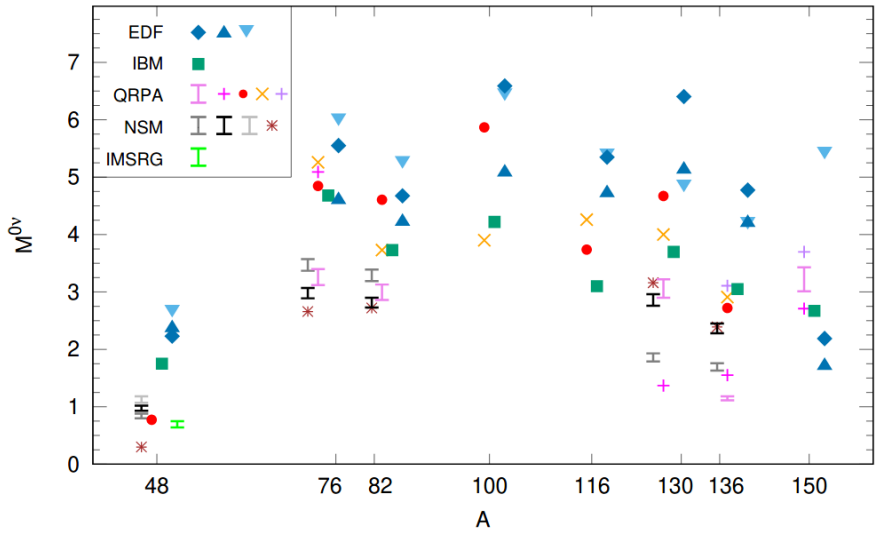

Figure 2.6: Nuclear matrix elements ($M^{0\nu}$) for $0\nu\beta\beta$ decay candidates given by their of mass number A. Taken from Ref. [53].

region. Figure 2.7 shows three different experiments with the same signal and background but different energy resolution. As seen, better energy resolution improves the discovery potential. Experiments with worse energy resolution must compensate with lower backgrounds or higher exposures.

2.4.3 *Background rate*

The main source of background in a $0\nu\beta\beta$-decay experiment is natural radioactivity, in most cases. Particularly notorious are ^{208}Tl from the Thorium series, and ^{214}Bi from the Uranium series, present at some level in any material. This requires extensive screening campaigns to select the most radiopure materials for use in detector construction.

Radon gas is also a concern since it is emanated from all materials and, being a noble gas, is chemically not very reactive and can therefore often end up in the active region of the detector. Furthermore, the byproducts of radon decay, also radioactive, can become attached to the detector's surface. Providing a radon-free environment becomes,

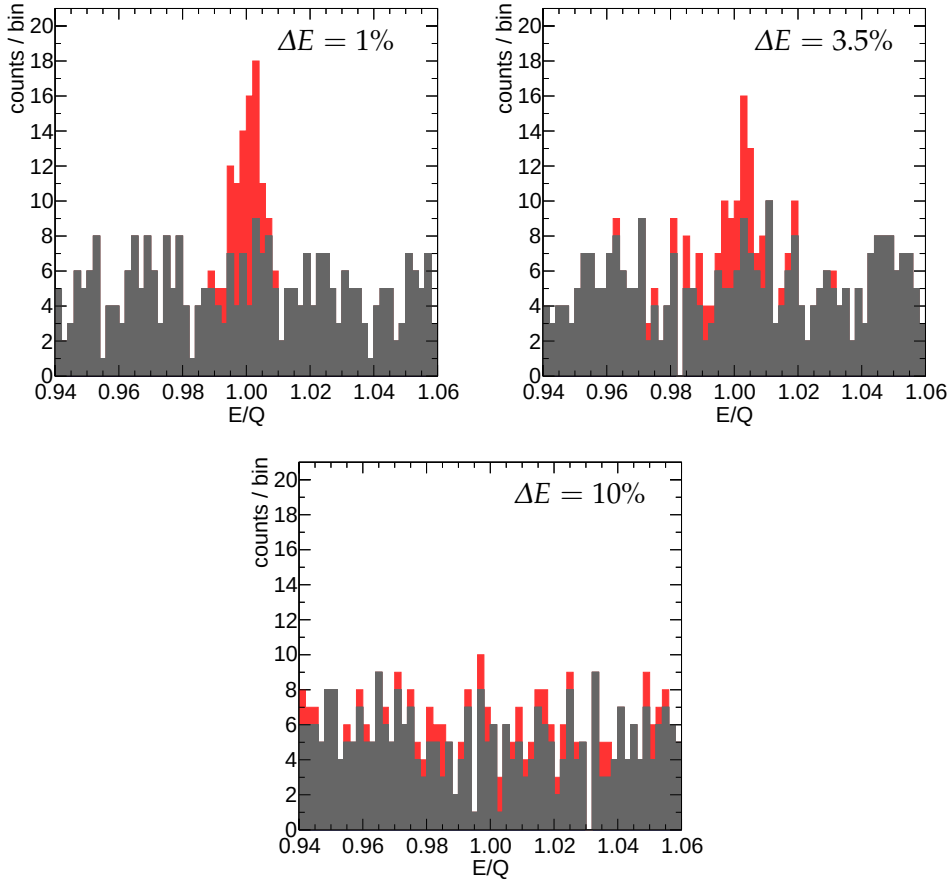

Figure 2.7: Signal (red) and background (gray) in the region of interest around $Q_{\beta\beta}$ for three Monte Carlo experiments with the same signal strength (50 counts) and background rate (1 count/keV), but different energy resolution (top: 1% FWHM; middle: 3.5% FWHM; bottom: 10% FWHM). The signal is distributed normally around $Q_{\beta\beta}$, while the background is assumed to be flat. Taken from Ref. [54].

therefore, another requirement for $0\nu\beta\beta$-decay experiments. Avoiding these backgrounds can be achieved by using radon traps in the air circulation system.

Cosmic rays also represent an important source of background. The easiest way to mitigate them is installing the experiment in an underground lab [55], shielding the detector and reducing the flux by several orders of magnitude compared to that of the Earth's surface.

By going underground cosmic backgrounds are strongly suppressed, but it is not enough, since natural radioactivity from the surrounding rock can produce high-energy gammas and neutrons that could interact in the detector. These backgrounds can be reduced by placing additional shielding around the detector, typically made of dense radiopure materials such as lead, copper or water.

In addition to material selection and shielding, some experiments employ active methods to reduce background such as using the event topology, pulse-shape discrimination and decay-product identification [56–58].

2.4.4 *Detection efficiency*

Detection efficiency is an important requirement for $0\nu\beta\beta$ experiments since the process they are looking for is very rare. Assuming the same level of background, the sensitivity to $m_{\beta\beta}$ achieved by doubling the efficiency would be equivalent to increasing the mass by a factor 4.

In general, simpler detection techniques achieve higher efficiencies. Experiments performing only calorimetry have better efficiency rates than more complex ones including features such as tracking reconstruction. Detectors using the same material as $0\nu\beta\beta$ source and as detection medium generally have higher efficiencies, although they lose some efficiency due to the use of a fiducial volume.

2.4.5 *Exposure*

To completely explore the inverted hierarchy of neutrino masses, thousands of kilograms of $\beta\beta$ source will be needed. Many experiments are already planning tonne-scale detectors for the future, although not all technologies can scale up easily. All $\beta\beta$ isotopes are rare on Earth and require isotopic enrichment to achieve those quantities,

making the process very expensive. The most cost-effective technique is centrifugal separation [59–61], but it is only possible for elements with a stable gas compound. Xenon, being a noble gas, is easier and cheaper to centrifugate, so ^{136}Xe is a strong candidate for a tonne-scale experiment.

2.5 Current experiments

Neutrinoless double beta decay is a very active field in particle physics, with several experiments already running and some newer ones being built now. As discussed in the previous section, there are several considerations to make when designing a $0\nu\beta\beta$ experiment, leading to different technologies for its detection. Below we present a review of the main ones and their results.

2.5.1 KamLAND-Zen

Located in Kamioka, the KamLAND-Zen experiment searches for $0\nu\beta\beta$ using ^{136}Xe [43]. The detector is a modification of KamLAND carried out in the summer of 2011. The $\beta\beta$ source and detector are 13 tons of Xe-loaded liquid scintillator (Xe-LS). The technique was first proposed by Ramaswamy Raghavan in 1994 [62]. The detector has an inner spherical balloon (IB) with a 3m diameter containing Xe-LS. The IB is made of transparent nylon film and is surrounded by 1 kiloton of LS in a 13m-diameter outer balloon (OB), used as an active shield for external gammas and as a detector for radiation coming from the IB. An oil buffer separates the OB from a stainless-steel containment tank instrumented with 1879 PMTs. Finally the whole detector is placed inside a 3.2-kton water Cherenkov tank which serves as a veto for cosmic-ray muons. A scheme of KamLAND-Zen is shown in Figure 2.8.

The detector took data in two phases, the first one with 345 kg of ^{136}Xe and the second with 383 kg. Overall, a background rate of 0.01 cts keV^{-1} kg^{-1} yr^{-1} [63] was achieved by making a tight selection cut in the fiducial volume and by Bi-Po tagging ^{214}Bi events [64].

The first phase began in 2011 and accumulated an exposure of 89.5 kg year with an energy resolution of 9.89 % FWHM at $Q_{\beta\beta}$, setting the bound $T^{0\nu}_{1/2}(^{136}\text{Xe}) > 1.9 \times 10^{25}$ yr at 90 % CL [65]. They were also

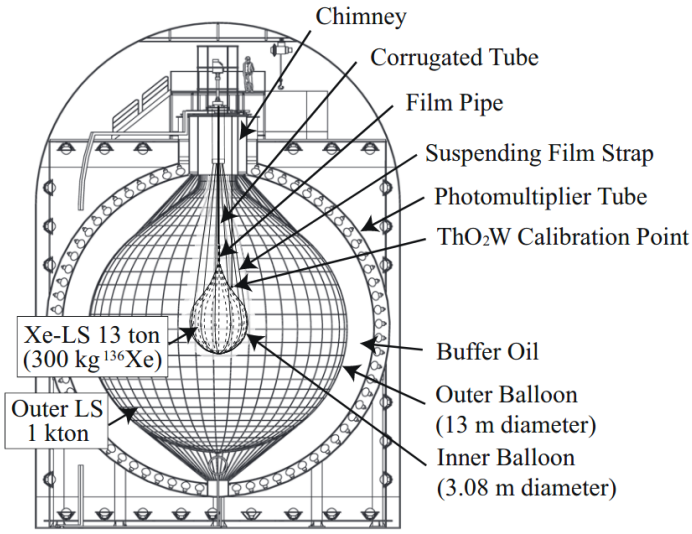

Figure 2.8: Schematic drawing of the KamLAND-Zen detector. Taken from Ref. [66].

able to measure the half-life of the two-neutrino mode with a value of $T^{2\nu}_{1/2}(^{136}\text{Xe}) = (2.38 \pm 0.02(\text{stat.}) \pm 0.13(\text{sys.})) \times 10^{21}$ yr.

The second phase took place between December 2013 and October 2015 and improved the bound to $T^{0\nu}_{1/2}(^{136}\text{Xe}) > 9.6 \times 10^{25}$ yr at 90 % CL, despite a worse resolution at $Q_{\beta\beta}$, 10.94 % FWHM. Combining the two data campaigns, the final result is $T^{0\nu}_{1/2}(^{136}\text{Xe}) > 1.07 \times 10^{26}$ yr at 90 % CL, implying an effective majorana mass below $61 - 165$ meV, depending on the NME [43].

2.5.2 EXO

The Enriched Xenon Observatory (EXO) is the other leading ^{136}Xe $0\nu\beta\beta$ experiment. The detector is a liquid xenon (LXe) Time Projection Chamber (TPC), located in the Waste Isolation Pilot Plant (WIPP) in New Mexico (USA), since May 2011. The first phase of the experiment, EXO-200 [67], uses 200 kg of xenon enriched to 80% in the ^{136}Xe isotope. Of the total mass, 175 kg are in liquid phase and 110 kg are in the active volume of detector.

The EXO detector, shown in Figure 2.9, consists of a symmetrical TPC with a central transparent cathode. The ionization signal is read by two wire planes, one on each end of the TPC, while the scintillation light is read by two arrays of large-area avalanche photodiodes (LAAPDs). The inner sides of the chamber are covered by teflon sheets to improve light collection efficiency. LXe is contained in a thin copper vessel inmersed in cryofluid at ~ 167 K, inside a double-walled copper cryostat. Lead blocks surrounding the cryostat are used as shielding and there is also an active muon veto made of plastic scintillator panels.

Due to the high density of LXe, electrons only travel a few millimeters. Therefore, $\beta\beta$ events are single-site (SS) events, typically. On the other hand, background events produce multi-site events (MS). This, combined with a cluster reconstruction that can achieve millimeter precision, allows EXO-200 to remove some extra background.

The energy resolution in LXe is worse than in xenon gas, reducing the sensitivity of the experiment. However, reading both ionization and scintillation signals allows for anti-correlation corrections [68]. The resolution obtained at $Q_{\beta\beta}$ is $(3.60 \pm 0.15)\%$ FWHM for SS events and $(3.88 \pm 0.12\%)$ FWHM for MS events [69].

The experiment measured a background rate of $(1.7 \pm 0.2) \times 10^{-3}$ cts keV^{-1} kg^{-1} yr^{-1}, which combined with a large exposure of $\sim$ 100 kg yr yields a very competitive result on $m_{\beta\beta}$ sensitivity.

For the two neutrino mode, EXO-200 had an efficiency of $(87.4 \pm 2.53)\%$ for events inside the fiducial volume. With an exposure of 23.14 kg yr, the half-life of the process was measured to be $T^{2\nu}_{1/2}(^{136}\mathrm{Xe}) = (2.165 \pm 0.016(\mathrm{stat.}) \pm 0.059(\mathrm{sys.})) \times 10^{21}$ years [70].

In the case of the neutrinoless $\beta\beta$-decay, with an exposure of 234.1 kg yr and a signal efficiency of $(96.4 \pm 3.0)\%$, the collaboration reported the limit $T^{0\nu}_{1/2} > 3.5 \times 10^{25}$ yr at 90% CL, which corresponds to an effective mass below $78 - 239$ meV, depending on the NME [71].

Finally, the EXO collaboration also published a limit on both $\beta\beta$-decay rates of ^{134}Xe, yielding the results (at 90% CL): $T^{2\nu}_{1/2}(^{134}\mathrm{Xe}) > 8.7 \times 10^{20}$ yr and $T^{0\nu}_{1/2}(^{134}\mathrm{Xe}) > 1.1 \times 10^{23}$ yr [72].

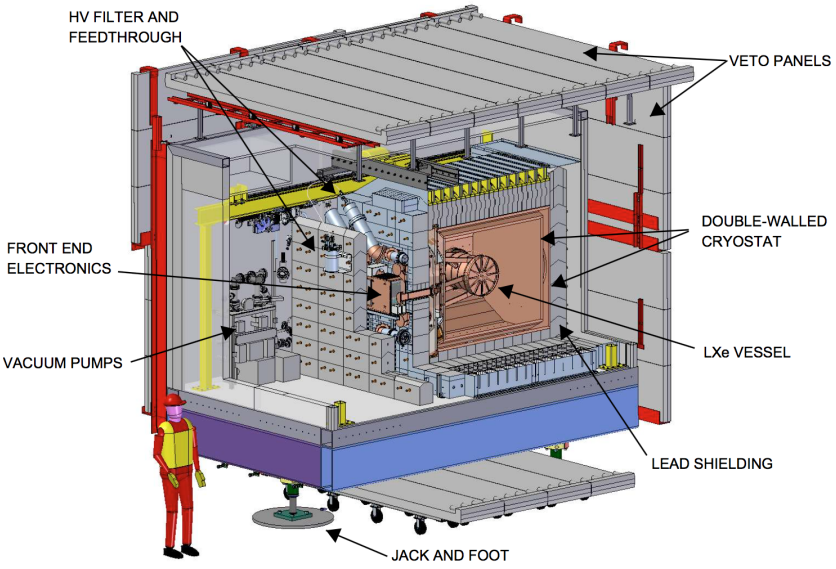

Figure 2.9: Drawing of the EXO-200 detector, cryostat and shielding. Taken from Ref. [67].

2.5.3 GERDA

The GERmanium Detector Array (GERDA) experiment, located at the Laboratori Nazionali del Gran Sasso (LNGS), searches for $0\nu\beta\beta$ using high-purity germanium (HPGe) diodes. They are made of large germanium crystals enriched to $\sim 86\%$ in ^{76}Ge that operate as source and detector for $0\nu\beta\beta$ decays. The detectors are placed in arrays suspended inside a cryostat filled with liquid argon (LAr), which serves as both a cooler and a shield. The inner surface of the cryostat is covered with 6 cm of pure copper to reduce background coming from the vessel. A water tank surrounds the cryostat providing extra shielding for external gammas and neutrons. It has 66 PMTs for the detection of Cherenkov light and also scintillator panels on the top that serve as a muon veto system. A schematic drawing of the detector is shown in Figure 2.10.

GERDA has run in two phases, improving the detector between

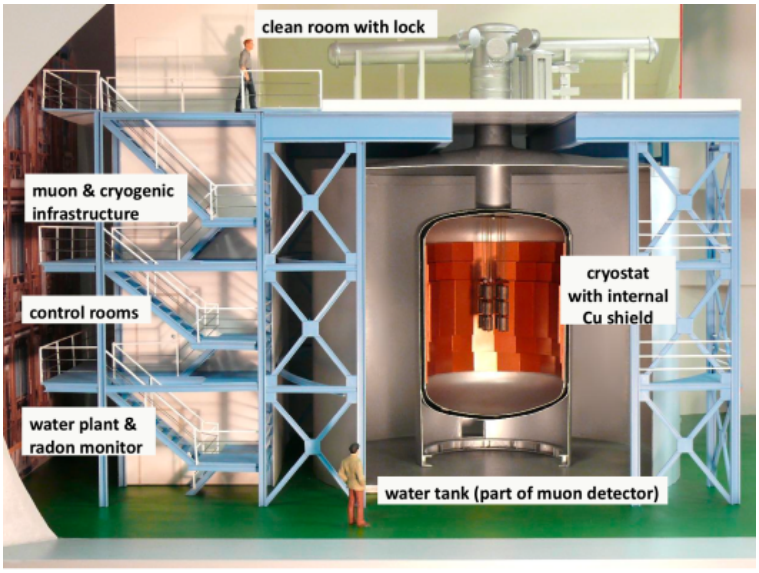

Figure 2.10: Artistic view of the GERDA detector at LNGS. Taken from Ref. [75].

them. The first one took place between November 2011 and March 2013 using 8 refurbished semi-coaxial HPGe detectors from the HdM and IGEX experiments. In July 2012, 5 broad-energy germanium (BEGe) diodes were added to the detector. The second phase included 7 HPGe and 30 BEGe diodes.

The use of BEGe diodes improved notably the performance of the detector, as they have much better resolution than HPGe detectors. The resolution measured at $Q_{\beta\beta}$ is (3.2 ± 0.2) keV $(0.23 \pm 0.01\%)$ for the BEGe detectors and 4.8 ± 0.2 keV $(0.16 \pm 0.01\%)$ for the HPGe ones [65]. Furthermore, the signals from single-site events (SS) and multi-site events are different (MS), so GERDA can also use pulse shape discrimination to separate SS (signal) and MS (background) events, enhancing the experiment's sensitivity to $m_{\beta\beta}$. The estimated background reported for Phase I is $(11 \pm 2) \times 10^{-3}$ cts keV^{-1} kg^{-1} yr^{-1} [73], while for Phase II it was improved to $(0.7^{+1.1}_{-0.5}) \times 10^{-3}$ cts keV^{-1} kg^{-1} yr^{-1} [74], reaching a nearly background-free regime.

The collaboration reported a measurement of the two neutrino mode with Phase I data, yielding a half-life of $(1.926 \pm 0.095) \times 10^{21}$ yr

with an exposure of 20.3 kg yr [76]. The $0\nu\beta\beta$ analysis with Phase I data resulted in the limit $T^{0\nu}_{1/2}(^{76}\text{Ge}) > 2.1 \times 10^{25}$ yr at 90% CL [73]. Combining Phase I and Phase II data, the limit was updated to $T^{0\nu}_{1/2}(^{76}\text{Ge}) > 1.8 \times 10^{26}$ yr at 90% CL [77], corresponding to an effective Majorana mass below $80 - 182$ meV, depending on the NME.

2.5.4 CUORE

The Cryogenic Underground Observatory for Rare Events (CUORE), located at LNGS, searches for neutrinoless double beta decay in ^{130}Te using TeO_2 crystal bolometers. A bolometer is a device capable of measuring small changes of temperature in the crystals. Particle interactions are detectable through small temperature increases due to the small heat capacity of the detector at 10 mK. With this method an outstanding energy resolution of 4.2 keV (0.2%) FWHM at $Q_{\beta\beta}$ has been achieved [78].

The CUORE detector, shown in Figure 2.11, is composed of 988 bolometers divided in 19 towers with a total isotope mass of 206 kg. Each bolometer has a TeO_2 crystal cube of $5 \times 5 \times 5$ cm^3 with a thermal sensor and a resistive heater. The towers are located inside a copper cryostat that can reach a temperature of 10 mK. The cryostat is surrounded by several layers of lead used to shield from external background.

The collaboration reported a background rate of $(1.38 \pm 0.07) \times 10^{-2}$ cts keV^{-1} kg^{-1} yr^{-1} in the $0\nu\beta\beta$ region. With an exposure of 372.5 kg yr they set the lower limit $T^{0\nu}_{1/2}(^{130}\text{Te}) > 3.2 \times 10^{25}$ yr at 90% CL [79], yielding an upper limit on the effective Majorana mass of $75 - 350$ meV, depending on the nuclear matrix elements.

2.5.5 SNO+

The SNO+ experiment is a follow-up of the Sudbury Neutrino Observatory (SNO) [81], reusing many of the components of its predecessor. SNO+, located in the SNO-LAB (Ontario, Canada), is a multipurpose liquid scintillator experiment. The detector, shown in Figure 2.12, consist of a 12m-diameter acrylic vessel filled with 780 tonnes of Te-loaded liquid scintillator, read out by 9500 8-inch PMTs providing a

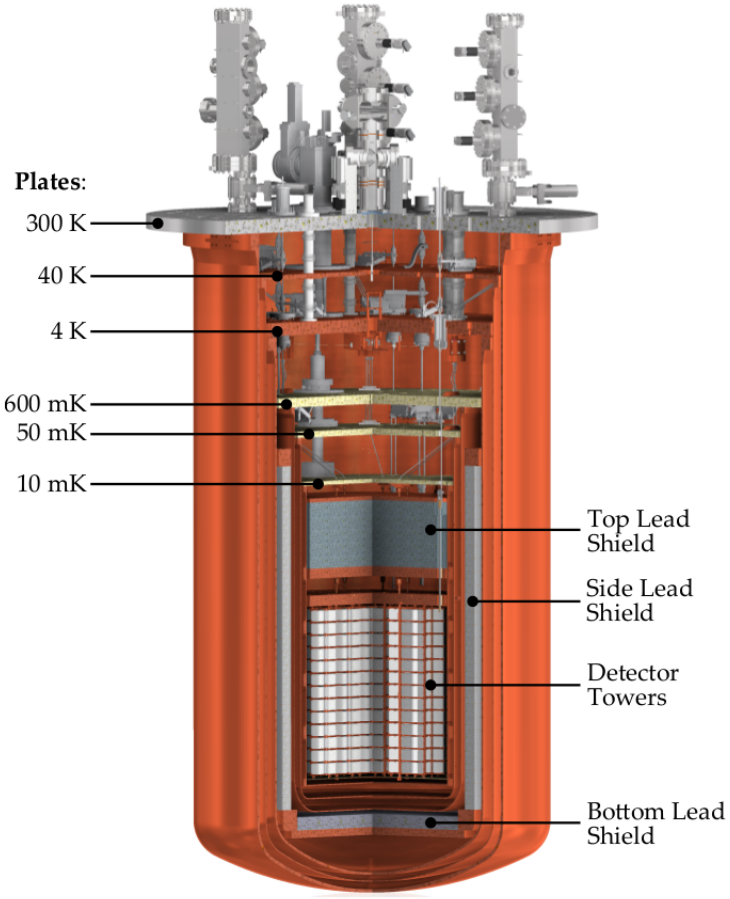

Figure 2.11: Schematic drawing of the CUORE detector. Taken from Ref. [80].

54% coverage. The space between the vessel and the cavern walls is filled with ultra pure water for background reduction.

The primary goal of SNO+ is searching for $0\nu\beta\beta$ decay of ^{130}Te. In Phase I the detector will be loaded with 1.3 tonnes of ^{130}Te, dissolved in the scintillator, but this quantity could be increased in further upgrades.

The SNO+ approach is similar to that of KamLAND-Zen, where large $\beta\beta$-emitter masses compensate for the poor energy resolution of detector, expected to be $\sim$ 10.8% FWHM at ^{130}Te $Q_{\beta\beta}$. Therefore, the two-neutrino mode of the $\beta\beta$-decay will be an important background. External background will come mainly from uranium and thorium in the liquid scintillator, but can be suppressed via Bi-Po tagging [82]. A tight fiducial cut will be set to reject external backgrounds. The expected sensitivity after 5 years of data taking is $T^{0\nu}_{1/2} > 1.9 \times 10^{26}$ yr at 90% CL, corresponding to a limit of $m_{\beta\beta} < 41 - 99$ meV, depending on the NME [83].

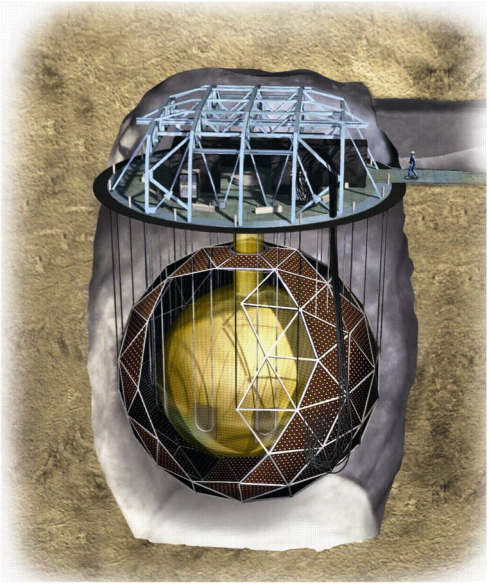

Figure 2.12: Artistic view of the SNO+ detector showing the acrylic vessel and the support structure of the photomultiplier tubes. Taken from Ref. [82].

2.6 The future of neutrinoless double beta decay experiments

To completely explore the $m_{\beta\beta}$ region corresponding to the inverted hierarchy, experiments at the tonne-scale will be needed. The next generation of experiments is already planning to reach those levels. It seems possible that in the future there will be a consolidation of experiments to one per isotope or technique due to the high costs required to scale up. A brief summary of different future experiments is presented in the following, more details can be found in Ref. [84].

LEGEND

One of the most promising experiments is LEGEND, resulting from the merge of the GERDA and MAJORANA [85] collaborations. The aim is to build a tonne-scale detector to search for the $0\nu\beta\beta$ decay of ^{76}Ge with discovery potential at a half-life beyond 10^{28} yr [86]. A first phase of the experiment, LEGEND-200, will reuse the existing GERDA infrastructure to run an experiment with about 200 kg of ^{76}Ge. LEGEND-200 will be operated to achieve an exposure of 1000 kg yr with a discovery potential of 10^{27} yr. The background in LEGEND-200 will be reduced to $< 2 \cdot 10^{-4}$ cts keV^{-1} kg^{-1} yr^{-1} which corresponds to a factor of 3 with respect to GERDA. LEGEND-200 is operating since February 2020 and the first calibration runs have been taken already [77].

In a subsequent stage, LEGEND-1000 will deploy up to 1000 kg of ^{76}Ge. The background index needs to be reduced by another factor of 10 with respect to LEGEND-200 to operate background-free for approximately 10 t yr. The goal is to achieve a discovery sensitivity beyond 10^{28} years. The underground laboratory for LEGEND-1000 will be decided at a later stage.

nEXO

The next-generation Enriched Xenon Observatory, nEXO, is designed to optimize the unique features of a massive monolithic and homogeneous detector using 5-tons of isotopically enriched liquid xenon. The implementation of LXe-based time projection chambers has already

been successfully demonstrated on a smaller scale by the predecessor EXO-200.

nEXO, as the evolution of EXO-200, will be a LXe single-phase TPC. The primary goal is the optimization of the energy resolution near the Q-value. The nEXO TPC is designed to read out both ionization and scintillation light, in order to exploit the anti-correlation between these two channels and to obtain the best possible energy resolution. Charge collection will be achieved at the top of the TPC. Scintillation readout will be obtained with VUV-sensitive Silicon Photomultipliers (SiPMs) installed behind the field-shaping rings. This arrangement will allow for larger coverage compared to that of EXO-200. The LXe TPC is at the center of different active and passive shielding layers, each containing components made of materials which are progressively lower in radioactive contamination the deeper they are in the detector.

nEXOs sensitivity reach is based on assumptions on the detector and analysis performance, and on using only measured radioassay inputs to build the background model. nEXO's expected median sensitivity on the $T^{2\nu}_{1/2}$ at 90% C.L. reaches 9.2×10^{27} yr in a 10 year run [87].

CUPID

CUPID (CUORE Upgrade with Particle IDentification) is a proposed next-generation $0\nu\beta\beta$ experiment based on scintillating bolometers to be installed in the cryogenic infrastructure currently hosting CUORE at LNGS [88]. The bolometer crystals will be grown from $Li_2{}^{100}MoO_4$ enriched to 95% in ^{100}Mo. The CUPID collaboration has designed cylindrical crystals with 50 mm diameter and 50 mm height, corresponding to a mass of 301 g each. The flat surfaces of the crystals will be exposed to bolometric light detectors fabricated from Ge wafers with 5 cm diameter, using an NTD Ge thermistor as a thermal sensor. The crystals will be stacked in detector towers conceptually similar to those of CUPID-0 [89] and CUPID-Mo [90], two smaller prototypes. With this design, about 1500 crystals will be hosted by the CUORE cryostat, corresponding to about 250 kg of ^{100}Mo.

The background goal is 10^{-4}cts keV^{-1} kg^{-1} yr^{-1}, yielding a 3σ discovery sensitivity on $m_{\beta\beta}$ of 12–20 meV in 10 yr live time. Further upgrades are possible to improve the background level of the experiment,

leading to two possible scenarios after CUPID. The first one is to operate the same CUPID detector in a zero-background mode, which corresponds to the background index of 2×10^{-5}cts keV^{-1} kg^{-1} yr^{-1}. The second, and more ambitious one, is CUPID-1T: a detector with 1.8 tons of Li_2MoO_4, or 1000 kg of ^{100}Mo. For such experiment, the background should be further reduced to the level of 5×10^{-6}cts keV^{-1} kg^{-1} yr^{-1}. The 3σ half-life discovery sensitivity of these two future searches would be 2×10^{27} yr and 8×10^{27} yr respectively in 10 yr live time.

Loaded liquid scintillators

Large volume liquid scintillator detectors loaded with a $\beta\beta$ isotope represent a cost-efficient way of scaling up an experiment to large isotope masses. KamLAND-Zen and SNO+ are experiments of this kind and are already planning future phases to increase their sensitivity. Both experiments plan to increase their photocathode coverage to achieve a better light collection. This improvement would allow them to reach an energy resolution of 4-5% FWHM at the $Q_{\beta\beta}$ of ^{136}Xe and ^{130}Te. Additionally, the isotope loading would be increased having, therefore, more $\beta\beta$ emitter mass. Nevertheless, the sensitivity of these approaches might ultimately be compromised by the intrinsic two-neutrino background.

Towards the normal hierarchy

If the neutrino hierarchy turns out to be normal, the search for $0\nu\beta\beta$ becomes even more complicated. Experiments would need to be in the background-free regime and their scalability to multi-tonne scale would become critical. For such large masses, modular detectors that can be split and placed in different laboratories would probably be the best option. Cost and availability of $\beta\beta$ emitters would also have an important role in the discussion.

3 The NEXT Experiment

3.1 Introduction

As explained in the previous chapter, measuring $0\nu\beta\beta$ is extremely challenging, given the very long half-life of the process. This search requires large $\beta\beta$-emitter masses, good energy resolution and background rejection capabilities. The NEXT[1] experiment searches for $0\nu\beta\beta$ in ^{136}Xe using a High-Pressure Xenon (HPXe) Time Projection Chamber (TPC). The experiment is located at the Laboratorio Subterráneo de Canfranc (LSC), under the Spanish Pyrenees [91] and offers an excellent energy resolution, topological signature for background rejection and scalability.

All radiation detectors are based on the same fundamental principle: the transfer of part or all of the radiation energy to the detector mass, where it is converted into some other form more adequate for human perception or electronic processing. Xenon is extensively used as a radiation detector medium since it has both scintillation and ionization signals, and, being a noble gas, it is easy to purify. Detectors using xenon can be found in medical imaging, dark matter experiments, X-ray astronomy and double beta decay experiments [92–96].

Xenon has two isotopes that can undergo $\beta\beta$-decay: ^{134}Xe and ^{136}Xe. The latter is preferred for $0\nu\beta\beta$ searches since it has a higher $Q_{\beta\beta}$, 2458 keV. ^{136}Xe represents only 8.86% of natural xenon, but the enrichment procedure is easy and cheap in comparison to other $\beta\beta$ isotopes.

The idea of using ^{136}Xe to search for $0\nu\beta\beta$ is already several decades old [97]. In the late 1980s, the Milano experiment at LNGS built a multi-wire proportional chamber filled with xenon gas enriched in

[1] Neutrino Experiment with a Xenon TPC

^{136}Xe [98]. Another pioneering experiment was the Gotthard TPC built by a Caltech-PSI-Neuchâtel collaboration and operated at the St. Gotthard road tunnel (Switzerland) in the 1990s. This TPC demonstrated the effectiveness of tracking in xenon to discriminate signal from background [99, 100]. In 2009 it was pointed out that xenon gas can provide very good energy resolution, better than 0.5% FWHM at the $Q_{\beta\beta}$ value of ^{136}Xe [101].

3.2 Xenon gas as a detector medium

3.2.1 Primary signals in xenon: scintillation and ionization

The energy released by the β particles in the $\beta\beta$ process can be transferred to xenon atoms in the form of heat, ionization or excitation. In the excitation process, one electron from the atom is raised to a higher energy level, while in ionization the transferred energy is high enough to remove an electron from the atom, creating an electron-ion pair. Atomic de-excitations and recombination of these ionization pairs lead to the emission of scintillation photons with a spectrum peaking at 172 nm (in the VUV region). All these processes are summarized in Figure 3.1.

The Platzman equation expresses the relation between radiation energy absorbed and the scintillation and ionization processes [102]:

$$E_\beta = N_i\langle E_i\rangle + N_{sci}\langle E_{sci}\rangle + N_i\langle\epsilon\rangle \tag{3.1}$$

where E_β is the energy absorbed by the gas, N_i is the number of electron-ion pairs ultimately produced with an average energy expenditure $\langle E_i\rangle$, N_{sci} is the number of atoms excited at an average energy expenditure $\langle E_{sci}\rangle$, and $\langle\epsilon\rangle$ is the average kinetic energy of sub-excitation electrons, with energy lower than the first excited level, which ultimately is released as heat.

Both the electron-ion pairs and the scintillation photons can provide information on the identity, energy and kinematics of the ionizing radiation. Therefore, the performance of a detector depends, among other things, on the properties of those signals. The ionization and scintillation amplitudes are usually expressed in terms of the average energies required to produce respectively, an electron-ion pair: W_i

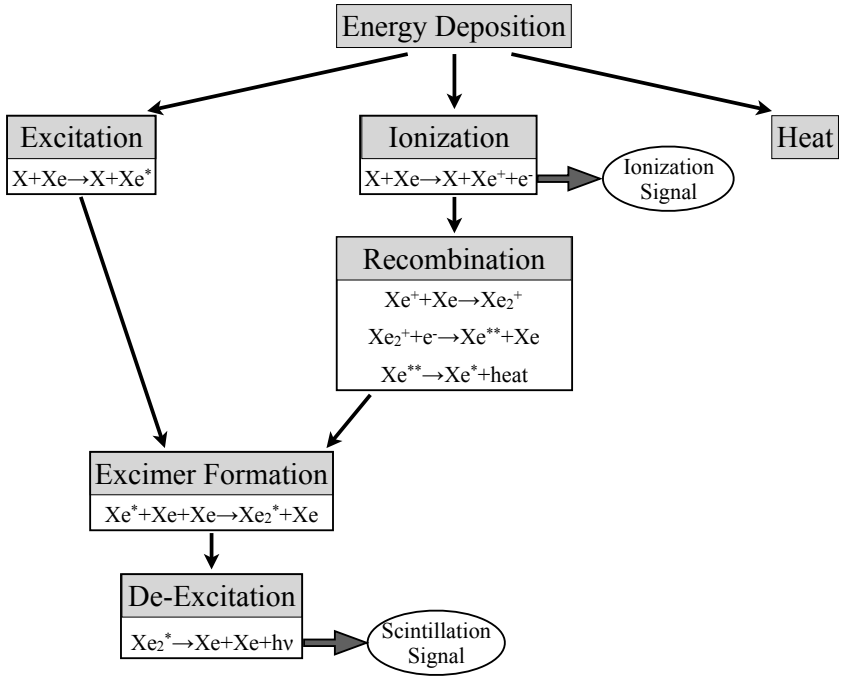

Figure 3.1: Main processes responsible for the ionization and scintillation signals in xenon. The symbol X indicates ionizing radiation. Taken from Ref. [103].

(so-called ionization W), and a scintillation photon: W_{sci} (so-called scintillation W). According to Equation (3.1), W_i and W_{sci} can be written as

$$W_i \equiv \frac{E_\beta}{N_i} = \langle E_i \rangle + \langle E_{sci} \rangle \frac{N_{sci}}{N_i} + \langle \epsilon \rangle \tag{3.2}$$

$$W_{sci} \equiv \frac{E_\beta}{N_{sci}} = \langle E_i \rangle \frac{N_i}{N_{sci}} + \langle E_{sci} \rangle + \langle \epsilon \rangle \frac{N_i}{N_{sci}} \tag{3.3}$$

Among all noble gases, ^{136}Xe has the smallest W_i value and, therefore, the largest ionization yield. In the gaseous phase $W_i = 21.9$ eV [104], while in the liquid phase $W_i = 15.6$ eV [105]. The energy available in $0\nu\beta\beta$ from ^{136}Xe is $Q_{\beta\beta} = 2458$ keV, therefore the average number of

primary ionization electrons is:

$$Gas.\ ^{136}\text{Xe}\ \bar{N}_i = \frac{Q_{\beta\beta}}{W_i} = \frac{2458\ keV}{21.9\ eV} = 112\,237\ electrons \tag{3.4}$$

$$Liq.\ ^{136}\text{Xe}\ \bar{N}_i = \frac{Q_{\beta\beta}}{W_i} = \frac{2458\ keV}{15.6\ eV} = 157\,564\ electrons \tag{3.5}$$

In the case of scintillation, the emission spectrum is the result of a complex system of discrete atomic lines, and bands originated from many excited states and from various collision and transfer processes [106, 107]. It is dominated by the vacuum-ultraviolet (VUV) region (20-200 nm). The value of W_{sci} is affected by the presence of an external electric field, as that can affect the recombination process [103, 107]. In the absence of an electric field, all ions and electrons recombine ($r \simeq 1$), while a very intense field prevents recombination at all ($r \simeq 0$). These two situations correspond, respectively, to the maximum and minimum scintillation yields and, therefore, to the minimum and maximum values of W_{sci}. In the literature there are several measurements of W_{sci} for xenon gas [108–110], but they are not in agreement with the theoretical predictions and present important discrepancies among them.

The NEXT collaboration made a measurement of W_{sci} based on the ratio of excited to ionized atoms produced in xenon gas by alpha particles in the NEXT-DEMO detector, yielding a result of $W_{sci} = 39.2 \pm 3.2$ eV [111]. For the liquid phase, Aprile et al. published a measurement of $W_{sci} = 13.8$ eV [107]. Taking those values, the average numbers of primary scintillation photons are equal to:

$$Gas.\ ^{136}\text{Xe}\ \bar{N}_{sci} = \frac{Q_{\beta\beta}}{W_{sci}} = \frac{2458\ keV}{39.2\ eV} = 62\,704\ primary\ photons \tag{3.6}$$

$$Liq.\ ^{136}\text{Xe}\ \bar{N}_{sci} = \frac{Q_{\beta\beta}}{W_{sci}} = \frac{2458\ keV}{13.8\ eV} = 178\,116\ primary\ photons \tag{3.7}$$

3.2.2 Detection of the ionization and scintillation signals

In order to detect the ionization signal, an external electric field has to be applied to transport the ionization pairs through the gas. This process, known as drift, accelerates electrons and ions in opposite

directions towards, respectively, the anode and the cathode. The acceleration is interrupted by collisions with the gas atoms, limiting the maximum average velocity the drifting charges can achieve. For low enough fields, the drift velocity of electrons, v_d, is proportional to the field strength. At high fields, the drift velocity saturates, becoming independent of the field. The drift velocity of ions is several orders of magnitude smaller than that of the electrons.

Diffusion also comes into play during the drift. Due to the collisions with gas atoms, ionization charges undergo gaussian deviations from the trajectories defined by the field lines in both the longitudinal and transverse directions. This effect limits the intrinsic position resolution of gaseous detectors. The magnitude of the spread is proportional to the drift time, t_d:

$$\sigma_L = \sqrt{D_L\, t_d}\,,\ \sigma_T = \sqrt{D_T\, t_d}\,, \tag{3.8}$$

where D_L and D_T are, respectively, the longitudinal and transverse diffusion coefficients of the gas.

Impurities in the gas can also degrade the performance of the detector as electron attachment can significantly decrease the ionization signal along the drift. This effect can be described, in general, by an exponential distribution:

$$N(t_d) = N(0)\ \exp(-t_d/\tau)\,, \tag{3.9}$$

where N is the number of drifting electrons, which is a function of the drift time, t_d, and τ is the electron lifetime in the gas, which becomes shorter with higher concentration of impurities. Achieving long enough electron lifetimes is possible by continuously circulating the gas through appropriate purifying filters.

In most applications, the total ionization charge collected is too low to be measured precisely by the electronics, leading to poor signal-to-noise ratios. Electroluminescence (EL) can improve this situation. The technique consists of amplifying the primary-electron signal using electric fields of higher intensity than those typically applied for the drift. If the amplification field is high enough to transfer energy to the electrons above the excitation threshold but below the ionization threshold, the electrons will excite gas atoms that will decay later emitting light, known as secondary scintillation. In this way, each primary

ionization electron produces a measurable, proportional optical signal (see Figure 3.2). If the amplification field is such that the energy gained by the electrons is above the ionization threshold, they will produce new electron-ion pairs while drifting. These secondary ionization electrons can also ionize further atoms, leading to a charge avalanche with an electron yield orders of magnitude higher than the number of primary ionization electrons. This charge signal is then large enough to be detected by the electronics.

NEXT detectors use EL for amplification and avoid the production of charge avalanches. The absolute electroluminescence gain η, under a uniform and constant $\bar{E}/p$, defined as the number of scintillation photons produced by a single ionization electron, is given by [112]:

$$\eta = 140\,(E/p - 0.83)\,p\,\Delta x\ (\text{UV photons}/e^-) \tag{3.10}$$

where E/p is given in kV cm^{-1} bar^{-1}, p in bar, and the separation Δx between the meshes generating the secondary drift field in cm.

The VUV scintillation photons emitted by noble gases are difficult to detect because they are strongly absorbed by most materials. Moreover, light sensors have their optimal efficiency in the visible or near-visible region, where highly transparent or reflective materials are also available. Therefore, the VUV light is shifted using photofluorescent coatings deposited on the surfaces exposed to the gas. Popular wavelength shifters used in xenon detectors are p-terphenyl (TPH) and tetraphenyl butadiene (TPB) [107].

3.2.3 *Intrinsic energy resolution of xenon gas*

The number of ionization electrons (N_i) is a good measure of the energy deposited in the medium. The resolution achievable is limited by stochastic fluctuations in the number of electron-ion pairs produced. Events of a given energy will deposit via ionization an average energy of $E = N_i W_i$, where W_i is the average energy needed to produce an ionization electron. Ugo Fano showed [113] that the fluctuations associated with N_i are well described by

$$\sigma_i^2 = F N_i = F\frac{E}{W_i}\,, \tag{3.11}$$

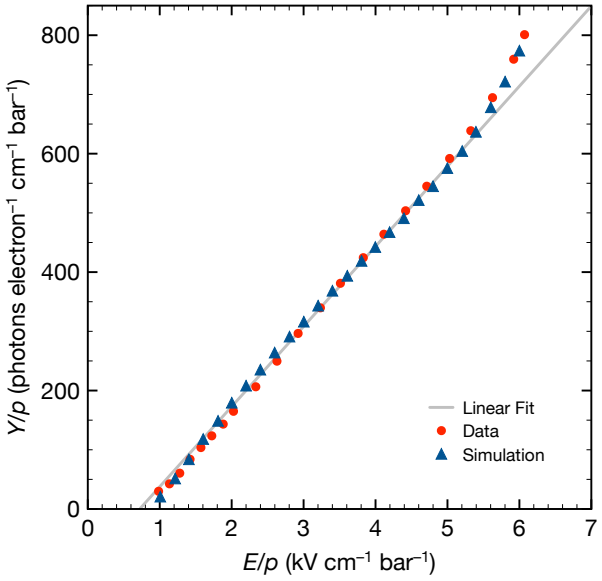

Figure 3.2: Reduced electroluminescence yield (Y/p) of gaseous xenon as a function of the reduced electric field, E/p. The results of Garfield / Magboltz microscopic simulations [104] are compared to the experimental measurements by Monteiro et al. (2007) [112]. A linear fit to the simulation data points is also shown. The EL yield is linearly proportional to the reduced electric field above a threshold of 0.83 kV cm^{-1} bar^{-1} and up to approximately 5.5 kV cm^{-1} bar^{-1}, where secondary-ionization effects become visible. Figure redrawn from Oliveira et al. (2011) [104].

where the number F depends on the medium and is known as the Fano factor. The best energy resolution (FWHM) achievable with an ionization detector is, therefore, given by

$$\frac{\delta E}{E} = 2.35\,\frac{\sqrt{F\,N_{\rm i}}W_i}{E} = 2.35\,\sqrt{\frac{FW_i}{E}} \tag{3.12}$$

The Fano factor of noble gases is well understood. For xenon gas different experimental measurements have shown values between 0.13 and 0.17 [114–116], in agreement with Monte Carlo computations [117]. On the other hand, the value found for liquid xenon is much higher $F > 20$ [68, 107], in contradiction with the theoretical calculations [118].

According to Eq. (3.12), the intrinsic energy resolution for HPXe detectors is much better than for those with LXe:

$$\begin{aligned}(\delta E/E)_{Gas\ ^{136}\mathrm{Xe}} &= 2.35\,\sqrt{0.15\cdot 21.9\ /\ Q_{\beta\beta}} = 0.38\%\ \mathrm{FWHM}\\ (\delta E/E)_{Liq\ ^{136}\mathrm{Xe}} &= 2.35\,\sqrt{20\cdot 15.6\ /\ Q_{\beta\beta}} \ = 2.65\%\ \mathrm{FWHM}\end{aligned} \tag{3.13}$$

Bolotnikov and Ramsey measured the energy resolution as a function of the xenon gas density using 662-keV gammas from a ^{137}Cs source (see Figure 3.3) [119]. For densities below $\rho_t \sim 0.55$ g/cm^3 ($P \sim 100bar$) the resolution is approximately constant, but quickly deteriorates for higher densities, transitioning to the values typical of liquid xenon. Below the transitioning point, in the regime corresponding to typical operation pressures in NEXT, the energy resolution measured at 662 keV is 0.6% FWHM, near the Fano limit (0.523% FWHM).

It has been suggested [101, 107] that the contribution of globs of liquid xenon coexisting with the gas could introduce anomalous fluctuations. The liquid phase fraction would grow for higher densities, and so would the impact of the fluctuations, reaching the maximum at the density of the liquid phase, while being practically non-existent below ρ_t.

Beyond all of the above, at a practical level, all detectors are affected by noises and fluctuations that may worsen the energy resolution. It can be assumed that any possible fluctuations associated with the signal $s_{\rm i}$ are uncorrelated with those intrinsic to the ionization process, described by Eq. (3.12). Therefore, both variances can be added in quadrature, with the overall variance being

$$\sigma_E^2 = \sigma_{\rm i}^2 + \sigma_G^2 = F\,N_{\rm i} + G\,N_{\rm i} = (F+G)\,N_{\rm i}\,, \tag{3.14}$$

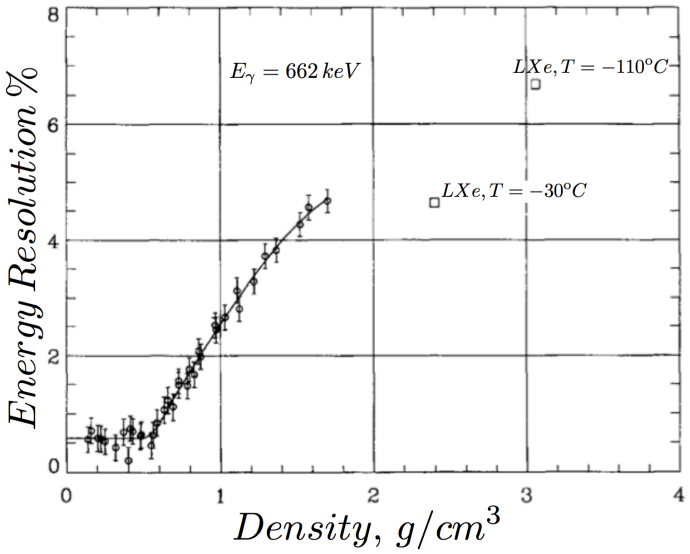

Figure 3.3: Density dependence of the energy resolution (% FWHM) measured in xenon using the ionization signal generated by 662-keV gamma rays from ^{137}Cs. Taken from Ref. [119].

where G is the variance of signal s_i. Therefore, the energy resolution (FWHM) of a gaseous detector, including the effect of detection fluctuations, is given by

$$\delta E/E = 2.35\sqrt{(F+G)\,W_i\,/\,E}\,. \tag{3.15}$$

The factors F and G are fundamentally different, despite the fact that they enter in the previous equation in the same way: F reflects a constraint on fluctuations in energy partitioning for a fixed total energy, while G reflects the impact of statistical fluctuations in the detection process for a single electron [101]. In the case of detectors using electroluminescence amplification, like NEXT, G includes factors such as fluctuations in the optical amplification process or in the photosensors themselves. All experimental approaches aim to have the smallest G possible. In the case where $F = G = 0.15$, the obtained

energy resolution at $Q_{\beta\beta}$ value in a HPXe detector would be:

$$\delta E/E = 0.42\% \text{ FWHM} \tag{3.16}$$

This value is in agreement with the one obtained in [120], where a HPXe TPC was used to measure the energy resolution of a 122 keV γ-ray source. An energy resolution of 2.2 % FWHM was obtained at this energy, so if an extrapolation as $E^{-1/2}$ is done, the energy resolution at $Q_{\beta\beta}$ of ^{136}Xe would be

$$\delta E/E = 0.49\% \text{ FWHM} \tag{3.17}$$

3.3 The SOFT concept

A xenon gas detector optimized for neutrinoless double beta decay searches can provide an excellent energy resolution and information on the event topology useful for background discrimination. The most adequate design is a Time Projection Chamber (TPC), invented by David Nygren in the 1970s [121, 122]. Its working principle is illustrated in Figure 3.4. A uniform electric field is applied along the symmetry axis of a cylindrical chamber filled with a gaseous (or liquid) detection medium. Charged particles traversing the cylinder create ionization electrons along their trajectory which are drifted by the electric field towards an amplification and readout plane with 2D spatial segmentation. This plane records the amplitudes and transverse positions of the ionization electrons. The longitudinal coordinate is computed from the arrival time of the signals. Thus, the TPC provides a 3D measurement of the trajectory and energy deposition pattern ($\mathrm{d}E/\mathrm{d}x$) of a charged particle.

Achieving an excellent energy resolution requires a large photon collection area and single-photon sensitivity. On the other hand, the spatial reconstruction of events requires a dense sensor matrix. Designing one readout plane able to comply with both requirements is very hard. For this reason, the NEXT experiment uses two different sensor planes, each of them optimized for its function. This is known as the Separately-Optimized Functions TPC (SOFT) concept [101].

The design of NEXT detectors is an asymmetric TPC instrumented with photomultiplier tubes (PMTs) on one side to do precise calorimetry (the energy plane), and with an array of silicon photomultipliers

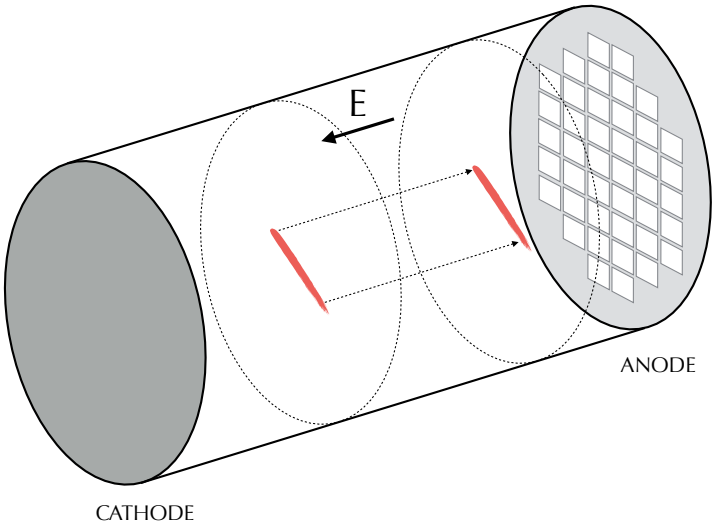

Figure 3.4: Working principle of a TPC [121]: the ionization electrons produced along the path of a charged particle (represented by the red trace) are drifted under the influence of an external electric field towards an amplification and readout plane that registers the signal amplitudes and transverse positions. The longitudinal coordinate is obtained from the arrival time of the signals.

(SiPMs) on the other side for topology reconstruction (the tracking plane). NEXT uses electroluminescence amplification as this is the most appropriate option to achieve an optimal energy resolution in xenon gas. This requires an additional electric field after the drift volume. A sketch showing how the detector works is shown in Figure 3.5.

The energy plane is located at the cathode plane of the TPC. PMTs are convenient for energy measurement since they can cover large areas at a reasonable cost and they have low noise and high gain, providing a very good energy resolution. On the other hand, PMT radioactivity levels are too high, so the detector must contain the minimum number of PMTs necessary to obtain a robust measurement.

The tracking plane is located at the anode plane, behind the EL region and can provide the transverse coordinates of the signals with high precision. The small signal coming from the primary scintillation

light of xenon can be read by the PMTs, providing the start time of the event, t_0. Taking the difference between t_0 and the time of arrival of the ionization signals to the tracking plane, the longitudinal coordinate can be obtained. Thus, the combination of signals from both planes yields a full and precise 3D reconstruction. The procedure is illustrated in Figure 3.5. To improve the resolution, the internal walls of the active volume are covered with a reflector, increasing the light collection efficiency.

A detector designed according to these principles would be able to reconstruct the track of each particle of an event. Given that the detection medium is xenon gas, a high energy electron would travel along several centimeters depositing energy. The pattern of those energy depositions is different for signal and background events, defining what we call the *topological signature* which can be used as an extra

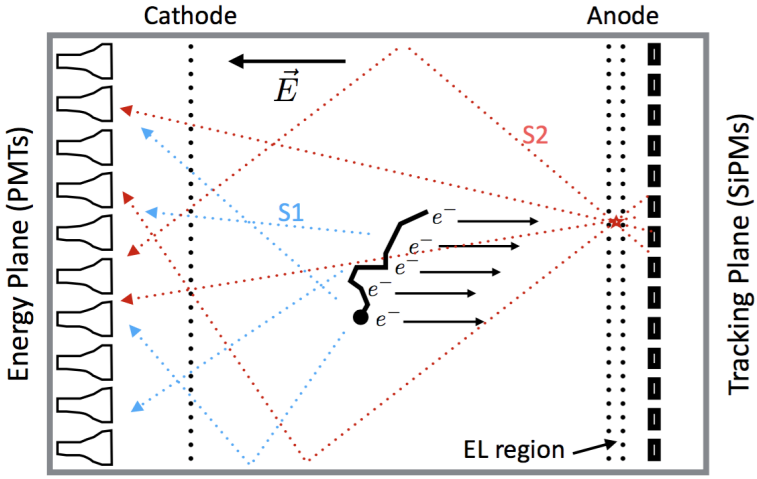

Figure 3.5: The SOFT concept [101]. EL light generated at the EL region is recorded in the photosensor plane right behind it and used for tracking. It is also recorded in the photosensor plane behind the transparent cathode and used for a precise energy measurement. The cathode is also used to detect primary scintillation light and provide t_0 information.

handle to separate signal and background events.

3.4 NEXT detectors

The goal of the NEXT experiment is to search for neutrinoless double beta decay of ^{136}Xe using a High Pressure Xenon gas TPC. During the first phase of the project (2009-2014) two small prototypes were developed: NEXT-DEMO and NEXT-DBDM. Their purpose was to demonstrate the detector concept and to gain technical expertise to design and build larger detectors.

Currently, the collaboration is operating NEXT-White (NEW), a medium-size detector running at the Laboratorio Subterraneo de Canfranc under low-background conditions. This detector is a demonstrator of the technological solutions that will be implemented in larger systems. Its physics goal is to measure the $2\nu\beta\beta$ decay half-life of ^{136}Xe.

NEXT-100, currently under construction, is the following step of the project. This detector will contain 100 kg of xenon gas at 15 bar, aiming to measure the $0\nu\beta\beta$ decay of ^{136}Xe. This detector will demonstrate the scalability of the technology and will serve as well as a test bench for technologies needed in a future tonne-scale detector.

3.4.1 R&D prototypes

NEXT-DEMO

Designed as a proof-of-concept of the NEXT technology, the NEXT-DEMO detector was a HPXe TPC that operated from 2009 to 2014 in a clean room at the Instituto de Física Corpuscular (IFIC), in Valencia, Spain. It consisted of a stainless steel vessel capable of withstanding up to 15 bar that contained a 30-cm drift length TPC with a 16-cm radius hexagonal cross section. The TPC included a 5 mm long EL amplification region delimited by stainless steel wire grids. A uniform electric field of 0.5 kV cm^{-1} was applied in the drift region, while the EL field had a higher intensity of 0.86 kV cm^{-1} bar^{-1}, above the excitation threshold of xenon. Inside the electric-field rings, six reflecting panels made of polytetrafluoroethylene (PTFE) are mounted forming an hexagonal tube. The panels were coated with tetraphenyl

butadiene (TPB), which shifts the VUV light emitted by xenon to blue light to improve the light collection efficiency. A schematic of NEXT-DEMO is shown in Figure 3.6.

The tracking plane, located at the anode, included 256 Hamamatsu S10362-11-050P SiPMs (1 mm^2 active area) arranged in a 1-cm-pitch square grid. The sensors were distributed in 4 boards, each of them housing an 8×8 matrix of SiPMs. Since they are not sensitive to VUV light, a TPB coating was added.

For calorimetry, the energy plane was instrumented with 19 1-inch Hamamatsu R7378A photomultiplier tubes [123]. These sensors resist a pressure up to 20 bar and have a quantum efficiency of $\sim$15% in the VUV region and $\sim$25% at the TPB emission wavelengths. The setup achieved a photocathode coverage of 39%. The gain was adjusted to about 5×10^6, so the sensors were able to distinguish a single photoelectron.

The detector was filled with natural xenon which was circulated through a gas system that included purifying filters to remove electronegative impurities. The DAQ was based on the Scalable Readout System developed by the RD51 Collaboration [124]. Further details of the detector can be found in several publications by the collaboration [103, 111, 125–127].

The detector was calibrated using a 1-μCi ^{22}Na source in a lateral port. A positron emitted via β^+ decay in the source annihilates resulting in two back-to-back 511-keV gammas. The readout was triggered detecting both gammas in coincidence using an external NaI scintillator coupled to a PMT.

NEXT-DEMO showed an energy resolution for the K_α peak of (5.691 ± 0.003)% FWHM, and (1.62 ± 0.01)% FWHM for the ^{22}Na photopeak [128]. These values can be extrapolated to the Q value of ^{136}Xe assuming an $E^{-1/2}$ dependence resulting in a predicted energy resolution of 0.63% FWHM and 0.74% FWHM, respectively.

The reconstruction of event topology was also studied using NEXT-DEMO data. Background was represented by single electrons resulting from the interactions of ^{22}Na 1275 keV gammas, while the signal was mimicked by electron-positron pairs produced by conversions of gammas from the ^{208}Tl decay chain. Track reconstruction and the identification of the energy deposited at the end-points yielded an extra rejection factor of 24.3 ± 1.4 %, while keeping an efficiency of

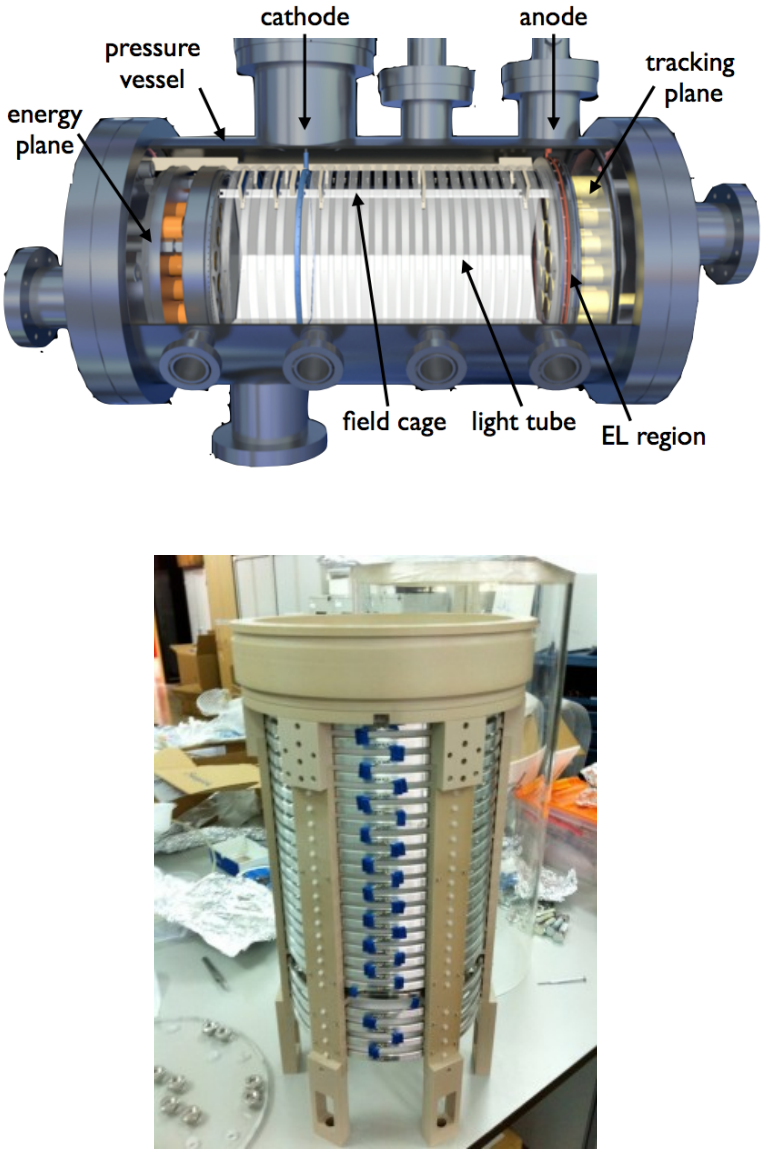

Figure 3.6: Cross-section drawing of the NEXT-DEMO prototype with major parts labelled (top), and image of the field cage standing upright (bottom).

66.7 ± 1.% for signal events [129].

NEXT-DBDM

Designed to demonstrate near-intrinsic energy resolution in HPXe, the NEXT-DBDM prototype was built and operated from 2009 to 2014 at the Lawrence Berkeley National Laboratory (USA). As in the case of NEXT-DEMO, the detector was made of a stainless steel cylindrical vessel (20 cm diameter, 33.5 cm length) containing a TPC with a hexagonal cross section. It had only one instrumented plane with 19 1-inch Hamamatsu 7378A PMTs [123] to measure the energy. The field cage was made of teflon panels supported by a plastic frame. The drift length was 8 cm and the EL region 5 mm long. The xenon was in constant recirculation through a gas system to remove electronegative impurities. A schematic of detector is shown in Figure 3.7.

The main result from this detector is the energy resolution study performed using 662 keV gammas from a ^{137}Cs source. The energy resolution achieved for those 662-keV gammas was 1.1% FWHM at 10 bar and 1.0% FWHM at 15 bar [130]. These results can be extrapolated to 0.5% FWHM at the $Q_{\beta\beta}$ value for ^{136}Xe, near the Fano limit of xenon gas.

3.4.2 NEXT-White

The NEXT-White[2] (NEW) detector is a 1:2-scale version of NEXT-100, currently running under low-background conditions at Laboratorio Subterráneo de Canfranc. NEW serves as a large scale validation of the technological solutions described in the NEXT-100 Technical Design Report [96]. From a physics point of view, the detector will provide an assessment of the background model, a characterization of the 2-electron tracks coming from signal events as well as a measurement of the $2\nu\beta\beta$-decay half-life of ^{136}Xe.

NEXT-White started operations at LSC in October 2016. After a short commissioning run (Run I), it was operating under stable conditions for over eight months (Run II) at 7.2 bar. Run III was short due to a technical problem, with operation being resumed at 10.2 bar in May 2018 for a low background run (Run IV). Since February 2019

[2]Named after Prof. James White

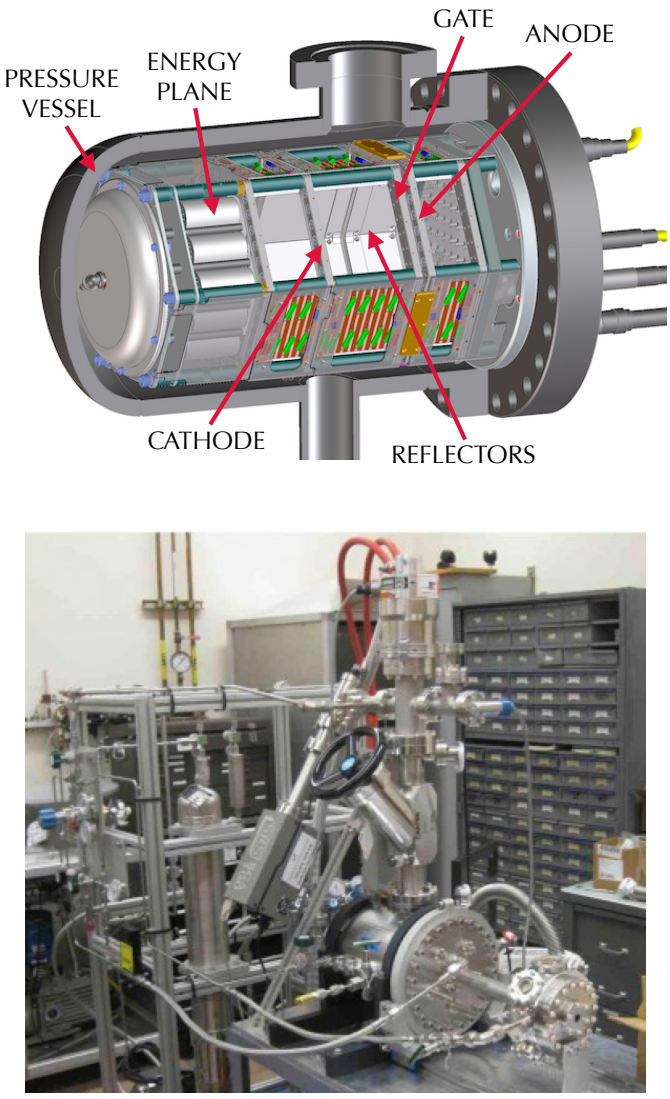

Figure 3.7: Cutaway drawing of the NEXT-DBDM detector with major parts labelled (top), and image of the complete setup of NEXT-DBDM in operation mode (bottom).

the detector has been running with xenon enriched in the ^{136}Xe isotope to take data for the $2\nu\beta\beta$ half-life measurement.

Detector operation during Run II established a calibration procedure based on ^{83m}Kr decays [131] and also provided the first measurement of the energy resolution [132], electron drift parameters such as drift velocity, and transverse and longitudinal diffusion [133] and a measurement of the impact of ^{222}Rn in the radioactive budget, which was found to be small [134].

Runs IV and V have shown an excellent stability, with negligible leaks and a very low spark rate. These two operational aspects were among the critical issues to be demonstrated by NEXT-White. Furthermore, an excellent electron lifetime has been achieved, in excess of 10 ms or 20 times the maximum drift length of the TPC.

The main results obtained so far with NEXT-White are:

- **Energy resolution at $Q_{\beta\beta}$ better than 1% FWHM**. For the high energy calibration, two ^{228}Th sources were placed in the upper ports of the detector and a ^{137}Cs source in the lateral one. The ^{137}Cs source provides a 661.6 keV gamma, while ^{228}Th decays into ^{208}Tl, which provides a 2614.5 keV gamma and also the double-escape peak resulting from e^+e^- pair production interactions of the gamma in which the two 511 gammas escape. The energy spectrum is shown in Figure 3.8. The resolutions obtained are 1.20 $\pm$ 0.02% FWHM at 662 keV, 0.98 $\pm$ 0.03% at 1592 keV and 0.91 $\pm$ 0.12% FWHM at 2615 keV [132, 135], the fits are shown in Figure 3.9. This means NEXT-White is the xenon-based detector with the best energy resolution in the world, less than 1% FWHM at $Q_{\beta\beta}$.

- **Performance of the topological signature**. Using events near the ^{208}Tl double escape peak at 1593 keV, it is possible to statistically separate a sample of signal-like, double-electron events (induced by pair production interactions) from a sample of background-like, single-electron events (induced by Compton interactions from the 2615 keV ^{208}Tl gammas with the same deposited energy as the double-escape peak). Applying a threshold on the energy of the ends of the tracks, most of the background can be removed while keeping the signal. This procedure can

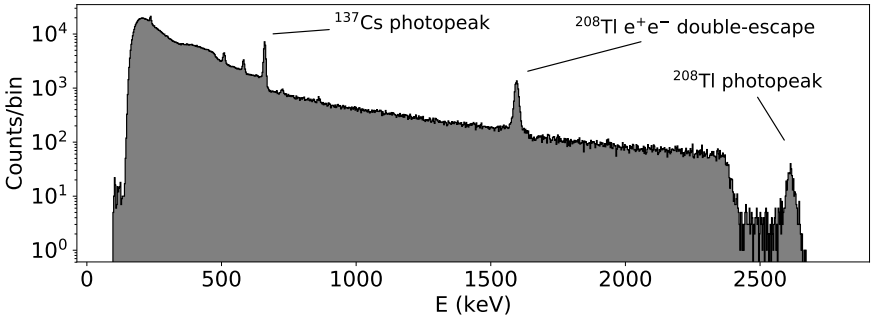

Figure 3.8: The full energy spectrum for calibration events from two ^{228}Th sources and a ^{137}Cs source. Taken from Ref. [135].

be applied both to data and Monte Carlo, allowing for a comparison between them. The optimal value for the threshold is $265.9 \pm 0.6_{\text{sys}}$ keV, giving an efficiency for signal-like events of $71.6 \pm 1.5_{\text{stat}} \pm 0.3_{\text{sys}}$% for a $22.3 \pm 0.4_{\text{stat}} \pm 0.5_{\text{sys}}$% background, compatible with the Monte Carlo result [136]. This represents an improvement over the results obtained with NEXT-DEMO [129].

- **Low background run**. During Run IV, using an exposure of 34.5 days, a comparison between the predicted and the measured background rate was carried out [137]. The expected rate was computed using a detailed background model including 4 isotopes (^{60}Co, ^{40}K, ^{214}Bi, ^{208}Tl) and 22 detector volumes. The model relies on the extensive radiopurity measurement campaign conducted by the NEXT collaboration [138–140]. Figure 3.10 shows that the background in NEXT-White can be well described with the model.

In the following, a detailed description of each part of NEXT-White is provided.

Electroluminescent TPC

One of the main technological challenges in building NEXT detectors is designing a large scale field cage. NEXT-White is an intermediate

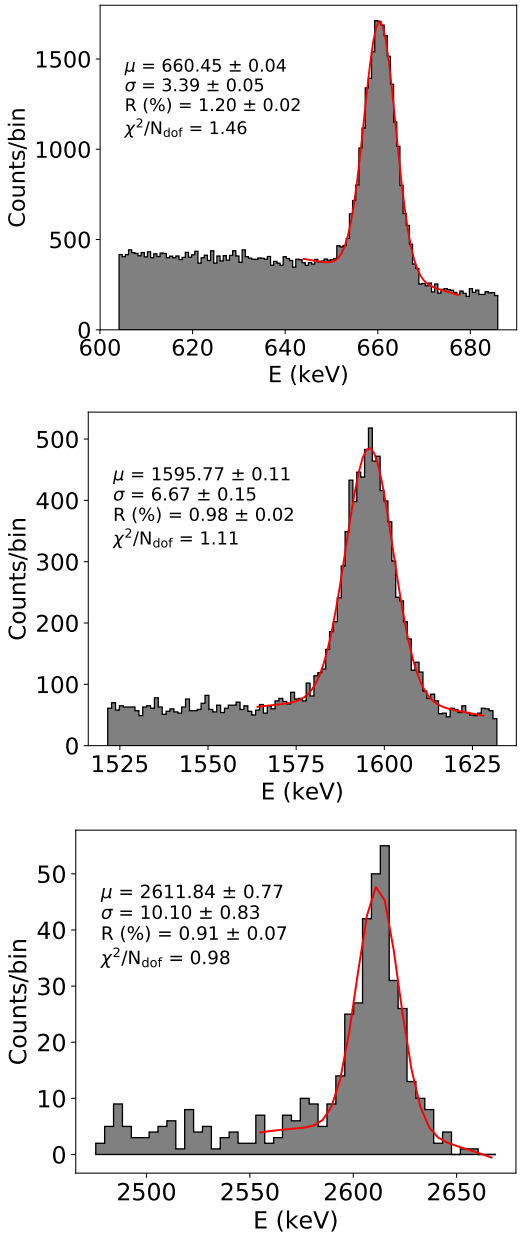

Figure 3.9: Energy spectra of three energy peaks from the ^{228}Th and ^{137}Cs sources (nominally at 662 keV, 1592 keV, and 2615 keV). Taken from Ref. [135].

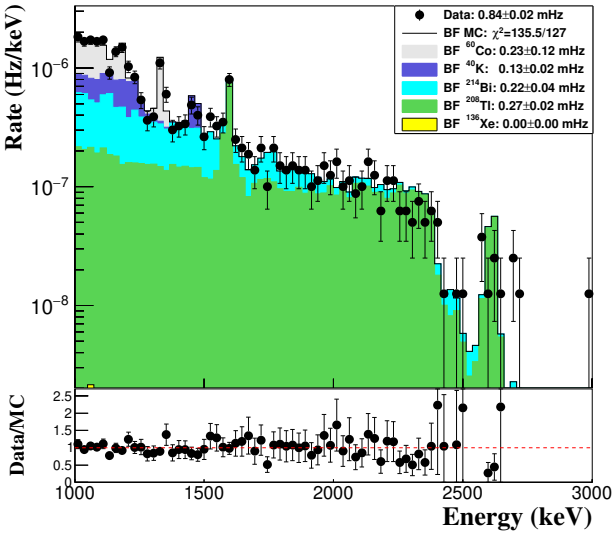

Figure 3.10: Run-IVc background fit. Data (black dots) are superimposed on the best-fit background model expectation (solid histograms), for which the different isotopes' contributions are shown. Taken from Ref. [137].

step between the NEXT-DEMO TPC, which was 16 cm in width and 40 cm long and NEXT-100, which will be 1 m width and 1.2 m long.

The main body of the TPC is an open-ended high-density polyethylene (HDPE) cylinder of 49 cm external diameter. The vessel provides structural support for other components, such as the copper rings, and it also electrically insulates the TPC from the vessel. The field cage is divided into three regions: the buffer, the drift region and the EL region.

The buffer extends from the PMTs to the cathode along 11.2 cm. Its purpose is to downgrade uniformly the high voltage from the cathode (50 kV) to zero, in order to protect the PMTs.

The drift region encloses the active volume of the detector, extending from the cathode to the gate along 52.7 cm. The cathode and the gate are made of 1-cm pitch stainless-steel wire meshes. A set of ultra pure copper [138] rings is placed in the inner side of the HDPE shell.

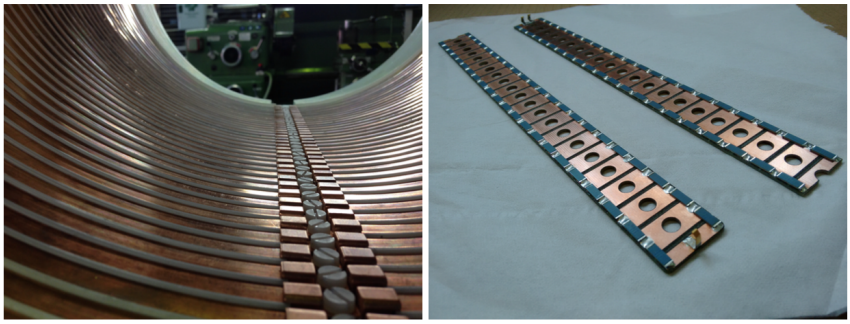

Figure 3.11: Detailed view of field cage copper rings (left) and resistor chain (right).

They are interconnected with low background 10 GOhm resistors (see Figure 3.11) to degrade the high voltage, providing a homogeneous and uniform electric field (300/600 V/cm). A teflon cylinder coated with tetraphenyl butadiene (TPB) is placed inside the HDPE shell to increase light collection efficiency.

The EL region, extending from the gate to the anode, is designed to hold up to 20 kV. The anode is a fused-silica rigid plate with a diameter of 52 cm. It is coated with Indium Tin Oxide (ITO) to make its surface conductive and with TPB to convert the VUV light to a range of wavelengths in the blue region, at which SiPMs have maximum photodetection efficiency and fused silica have excellent transparency.

The feedthroughs are designed to provide up to 50 kV between the cathode and the gate. They consist of an inner conductive rod surrounded by an HDPE insulator (see Figure 3.12).

Energy Plane

The first small prototypes, NEXT-DEMO and NEXT-DBDM, showed an outstanding energy resolution using electroluminescent TPCs with PMT readout. NEXT-White follows the same approach, performing the energy measurement with 12 Hamamatsu 3-inch R11410-10 PMTs [141]. They are arranged in two rings: 3 PMTs are placed in an inner ring and the other 9 in an outer ring, leading to a 35% photocathode coverage (see Figure 3.13). In order to protect them from the

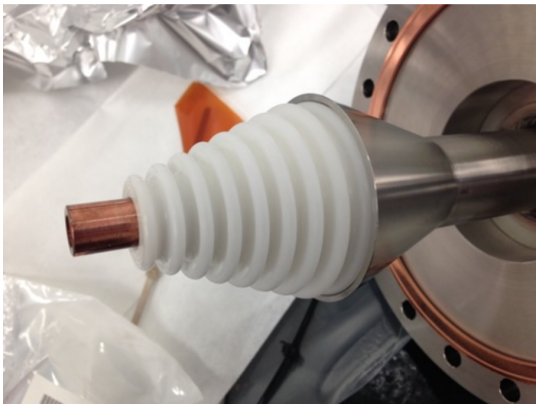

Figure 3.12: Detailed view of a NEW high voltage feedthrough.

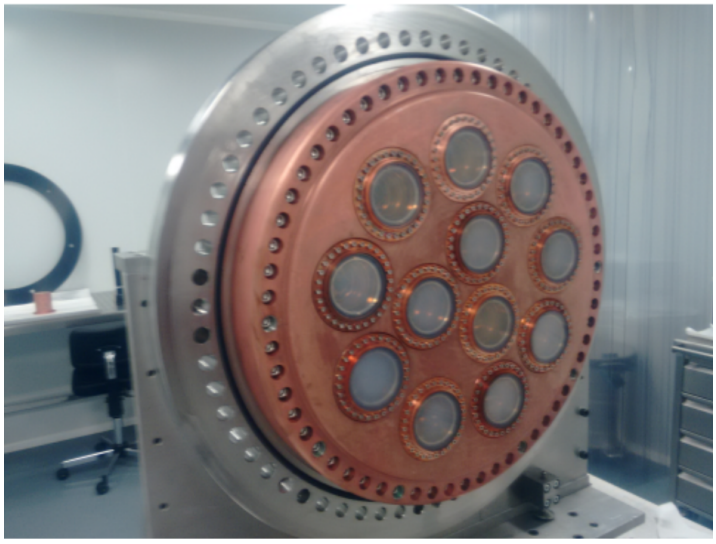

Figure 3.13: NEW energy plane with 12 PMTs coupled to sapphire windows, arranged in two concentric rings.

high voltage, the PMT plane is located 13 cm behind the cathode mesh, leaving enough space to downgrade the electric field.

PMTs cannot withstand the high pressure inside the vessel, so they need to be separated from the xenon. To achieve this, PMT windows are coupled to sapphire windows with optical gel (NyoGel

OCK-451) to match their refraction indices. The sapphire windows are also coated with TPB, to improve their transparency to scintillation photons. The shifted photon wavelengths also match the peak of the PMT quantum efficiency.

High voltage supply to the PMTs and signal extraction is done using shielded twisted pair cables. Each PMT is controlled with a Kapton circuit board, placed behind the PMT. They are mounted with heat dissipators connected to the copper shield.

Tracking Plane

One of the key advantages of NEXT detectors is the use of topological reconstruction as an extra handle to reject background events. In order to achieve a good reconstruction a high granularity of sensors is needed. However, extracting too many signals from the detector is challenging for the feedthrough designs as space for the cables is limited, and therefore a compromise is necessary.

NEXT-White uses SensL MicroFC-10035-SMT-GP SiPMs [142], with an active area of 1×1 mm^2. These sensors have a high quantum effiency for photons re-emitted by TPB ($\sim$ 50%), low dark count rate and they are very radiopure. Given that the charge diffusion in xenon gas is about 1 cm$/\sqrt{\text{m}}$ for electric fields around 0.5 kV/cm, the pitch was selected to be 1 cm [96]. A smaller pitch would worsen the background budget, increase the costs and would not contribute significantly to a better reconstruction, while a larger one would lead to worse results in the topological reconstruction.

SiPMs are arranged in Kapton Dice Boards (DBs) housing 8×8 sensors each. All the sensors in the same DB share the same bias voltage, and therefore they must have similar gains. To achieve this, all the SiPMs are selected after an automated characterization procedure [143]. Each DB also includes a blue LED for calibration and a NTC temperature sensor. To increase light collection efficiency, a teflon mask is placed on top of the DB, as shown in Figure 3.14.

The dice board material, Kapton, has been chosen due to its low radioactivity [139]. The design is a flexible circuit with a long tail, allowing one to put the SiPM connectors behind the copper plate and, therefore, shielding their background contribution [144].

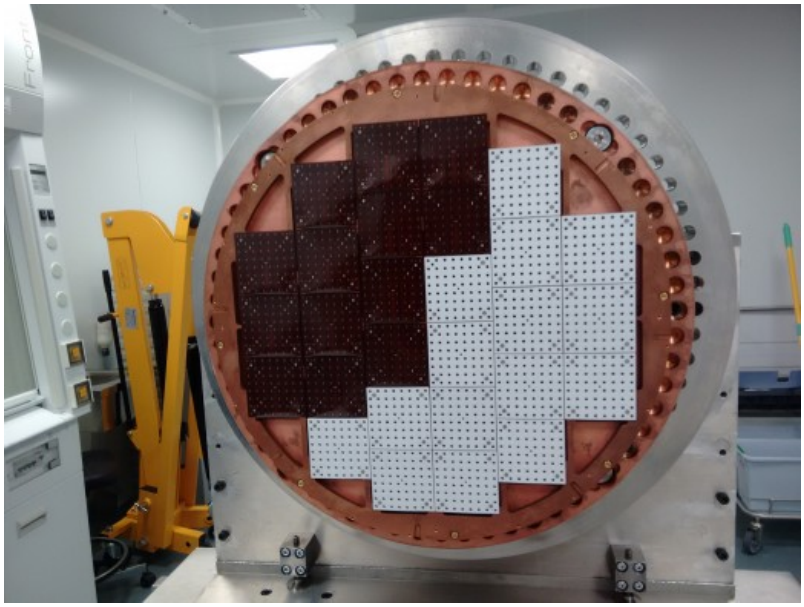

Figure 3.14: The NEW tracking plane during the assembly process. It is made of 28 dice boards, with 64 (1×1 mm^2 SensL) SiPMs each with a 1 cm pitch. The right half of boards is covered with reflective teflon masks. Once the assembly is finished, all DBs have a teflon mask in front of them.

Vessel

The NEW pressure vessel is made of a Ti-stainless steel alloy from *Nironit* [145, 146]. The dimensions are between those for NEXT-DEMO and NEXT-100, with an internal diameter of 64 cm and a length of 950 cm. The cylindrical body is enclosed by two 30 cm long endcaps (see Figure 3.15). The vessel is certified for up to 20 bar operation and it includes several ports for high-voltage feedthroughs, gas recirculation and calibration sources.

Inner Copper Shielding

The vessel material produces large amounts of background that must be shielded. For that purpose an ultra-pure copper shield has been installed inside the vessel. This Inner Copper Shielding (ICS) has

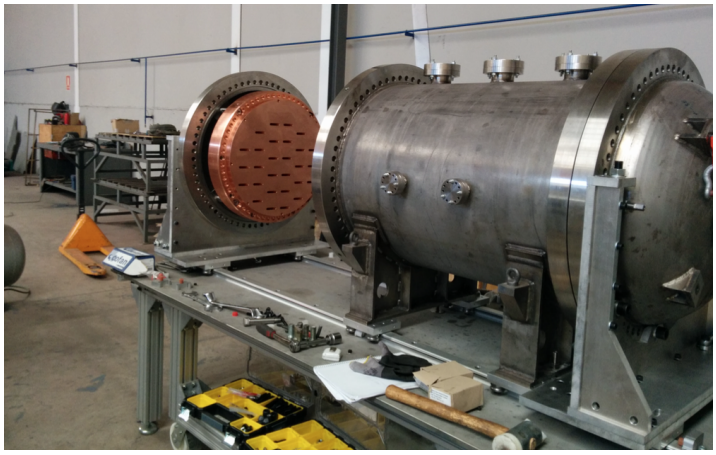

Figure 3.15: NEW vessel during its first assembly in its operational horizontal position. The tracking plane endcap is opened, showing the tracking plane copper shielding.

three sections. The cylindrical main body of the vessel is covered with 6 cm thick copper bars. The tracking plane endcap is shielded by the support plate, a 12 cm thick copper plate with rectangular holes for the Kapton cables from the dice boards. Similarly, the energy plane endcap is shielded by the carrier plate supporting the PMTs. The PMT holes are compensated with small copper caps 6-cm thick placed behind the sensors. The ICS is shown in Figure 3.16.

External shielding

To shield NEW from external backgrounds coming from the walls of the laboratory, the pressure vessel is placed inside a lead castle with a wall thickness of 20 cm, made of layers of staggered lead bricks supported by a steel structure. The bricks have an activity lower than 0.4 mBq/kg and they were bought by LSC from the OPERA experiment [147].

The lead castle dimensions are 195 cm in width, 265 cm in height and 293 cm in length. The lead bricks have a size of $200 \times 100 \times 50$ mm^3. The total weight is 65 tonnes. The lead castle is made of two separate halves that can move via a system of wheels and rails between two

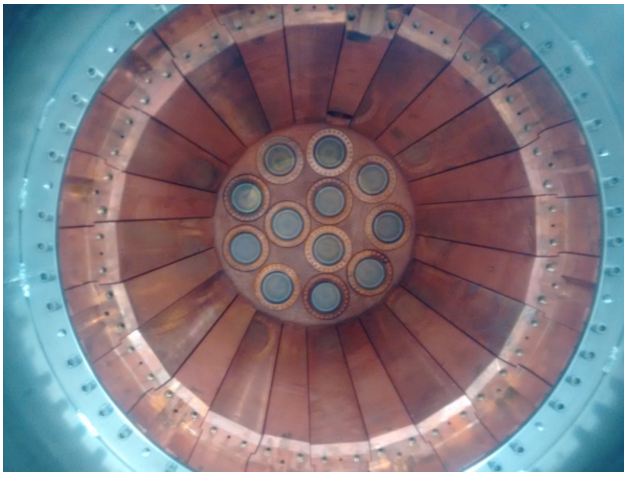

Figure 3.16: Detailed view of copper bars shielding the vessel body, with the energy plane viewed from the anode.

positions: open and closed. The former is used when some operation is needed on the detector and the latter is for regular operation of the detector, see Figure 3.17. A lock system fixes the castle to the floor in both configurations to avoid accidental displacements.

Due to the mild seismic activity of the part of the Pyrenees where the LSC is located, a seismic structure holds the vessel inside the castle. In this way, the system can be isolated from ground vibrations. All the electrical and gas connections are flexible to allow relative displacements between the vessel and the working platform in case of an earthquake.

Gas system

The gas system has several purposes: pressurization and depressurization of the detector, recirculation and cleaning of the gas, and evacuation of the detector. All these operations must be performed with maximum reliability since a loss of xenon, especially enriched xenon, would be too costly. For this reason, the gas system has been fully automated using an FPGA-based PLC (Programmable Logic Controller) from National Instruments named *Compact RIO*. This controller runs a real-time LabView-based monitoring of the different parts of the

Figure 3.17: Top: Detailed view of the NEXT shielding structure in its open position, with the NEW vessel placed on the anti-seismic platform. Bottom: View of the shielding structure in its closed position during installation.

system: valves, pressure gauges, compressor, chiller, etc. and operates them when needed to control the gas flow.

The different parts of the gas sytem are illustrated in Figure 3.18 and the three operation modes are detailed in the following:

- **Depressurization of the detector**: Before filling the detector with xenon, a vacuum level of 10^{-5} bar must be achieved to eliminate most of the impurities the detector could contain. To do this, several turbo-molecular pumps are used. In order to improve the efficiency of the process, the detector is heated to remove more easily the water vapor attached to the surfaces. This process is monitored using a Residual Gas Analyzer (RGA) that measures the level of impurities with a mass spectrometer.

- **Pressurization and recirculation**: After reaching the desired vacuum level, the vessel is filled with gas. To ensure everything works properly a cheaper gas, typically argon, is used before the enriched xenon. Once the detector is filled with xenon, the system starts to recirculate the gas to keep it clean and avoid electronegative impurities that could compromise the electron collection efficiency of the detector. To do this, a compressor from the SERA company keeps the gas flowing through a closed loop including two SAES MC4500-902 cold getters [148] and one SAES PS4-MT50-R-535 hot getter [149]. In the first days after the filling, cold getters allow for a faster purification, but at some point they have to be turned off given the large radon contamination they create. During a physics run, only the hot getter can be in operation.

- **Recovery**: There are two different cases in which all the xenon in the gas system must be evacuated: controlled evacuations and emergency recoveries. The first situation is addressed by a liquefaction process using a cryo-recovery bottle that is cooled using liquid nitrogen, creating a pressure gradient that slowly recovers the gas. After that, a vacuum pump is used to recover the residual gas from the vessel and the pipes. The emergency recovery is triggered automatically if a dangerous situation occurs, like an overpressure that could lead to an explosion or an underpressure indicating a leak. In these cases, the gas in the

(a) Cryo-recovery bottle

(b) NEXT-100 vessel used as emergency recovery tank

(c) Gas system frame with the getters

(d) Compressor

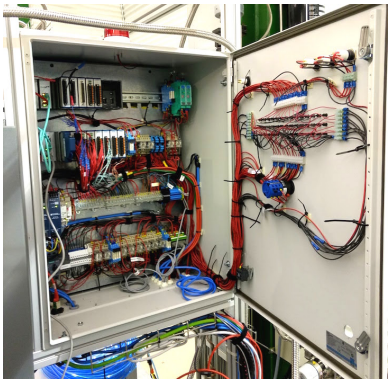

(e) Compact RIO cabinet

Figure 3.18: Different parts of the NEXT-White gas system.

system is moved to a large recovery tank which can store all the gas at a pressure of $\sim$ 1 bar. This expansion tank is connected to the system through a *Carten* valve which opens automatically.

Data acquisition

The NEXT-White Data Acquisition system (DAQ) uses the Scalable Readout System (SRS), developed by the RD51 Collaboration in 2011 [150], in an effort to which the NEXT collaboration also contributed.

To read out sensor signals, *front-end electronics* are connected to the PMTs and SiPMs. As the requirements for the two different sensor types are different, there is a specific front-end design for each. A detailed description of the front-end modules can be found in [144, 151].

The interfaces between application specific front-end modules and DAQ computers are called *Front-End Concentrator* (FEC) cards. NEXT uses three types of FEC cards: one for PMT readout digitization, another for SiPM readout digitization, and the last one to control the trigger of the system.

The last part of the DAQ is a two-level server farm running the DATE software [152]. A first level is made by the Local Data Concentrators (LDCs), which are servers directly connected to the DAQ electronics cards via Gigabit ethernet optical links. Each of these computers receives a sub-event with the information of the FECs connected to it. All of them are sent to the next level: Global Data Concentrators (GDCs). In this second step, the GDC will package all the information together, saving the entire event to disk for offline analysis. A detailed description of the system is given in Chapter § 4.

All the electronics (front-ends, power supplies, slow controls, etc.) are installed close to the detector, to reduce losses from signal transmission, but outside the shielding castle, so as to not contaminate the detector with their intrinsic radioactivity (see Figure 3.19). They are also connected to the LSC main power line via UPS units to increase protection and reliability.

Figure 3.19: NEW electronic racks and the Slow Control PC during installation.

Slow control

NEXT-White operation requires a set of advanced control systems. This type of system is called Slow Control (SC). An internal network connects all detector systems and several industrial computers running the SC software that monitors and controls the hardware. The control panel is shown in Figure 3.20.

There are six SC programs involved in the detector operation:

- **High voltage**: Monitors and controls the voltages set on the anode and cathode of the field cage. The system is able to detect sparks and performs an autorecovery process or shuts down the system depending on the configuration.
- **Gas sytem**: Monitors and controls all the parameters related to the gas system: valves, pressure gauges, vacuum pumps, compressor, chiller, RGA, etc. The software reacts automatically to anomalous values. If the current status is dangerous for the

Figure 3.20: The Slow Control for the NEXT-White detector.

setup, the program would trigger a change to a safe state. It also allows for manual activation of an emergency stop.

- **Power supplies**: Monitors and controls all the power supplies used by the electronics in the experiment.

- **PMT High Voltage**: Monitors and controls PMT power supplies and detects overcurrents.

- **Sensors**: Monitors the temperature and some other parameters of the electronics and DAQ computers.

- **Main**: Shows a summary of the more relevant parameters. It has a button to trigger an emergency stop of the system to prevent damage in case of any error, and it can remotely switch off the other slow control computers.

Since the behavior of a particular slow control can affect other subsystems, all of them are interconnected. They generate reports including all the events registered and also send alerts by email when any warning or alarm is triggered.

3.4.3 NEXT-100

The NEXT experiment was formally proposed to the *Laboratorio Subterráneo de Canfranc* (LSC) in 2009 in a *Letter of Intent* [153] that outlined the physics case and basic design concepts of an EL TPC for $0\nu\beta\beta$-decay searches with a source mass of the order of 100 kg of ^{136}Xe. The detector design was narrowed down in the NEXT-100 *Conceptual Design Report* [154] published in 2011, and fixed a year later in the *Technical Design Report* (TDR) [96]. The construction and comissioning of the detector is planned for 2021, although a delay of several months has been introduced by the COVID-19 crisis.

As mentioned before, the NEXT-White detector is a $\sim$1:2 scale version of the NEXT-100 detector. There are, though, some differences in their current designs. Therefore, some elements can be reused, but some others have to be scaled up or modified. In the following, the most relevant changes are explained.

Pressure vessel and shielding

The NEXT-100 pressure vessel has a cylindrical section of 160 cm length, 136 cm inner diameter and 1 cm wall thickness, enclosed by two torispherical heads of 35 cm height, 136 cm inner diameter and 1 cm wall thickness. As in the case of NEW, it has been fabricated with 316Ti stainless steel due to its radiopurity. A schematic of the detector is shown in Figure 3.21.

The vessel will be installed inside the same lead castle used currently by NEXT-White. The radioactivity coming from the vessel is shielded by 40 copper bars that are installed inside the vessel. This inner copper shield is analogous to that of NEXT-White, with a thickness of 12 cm.

Electroluminescent TPC

The NEXT-100 field cage has a design different from the one implemented in NEW. It has a nearly cylindrical shape, but it is made of 60 teflon reflector panels supported by a structure made of 20 HDPE struts with holes to house 45 copper rings. This design allows for less material usage, reducing the background produced near the active volume, with which it is in direct contact. There are 12 resistor chains

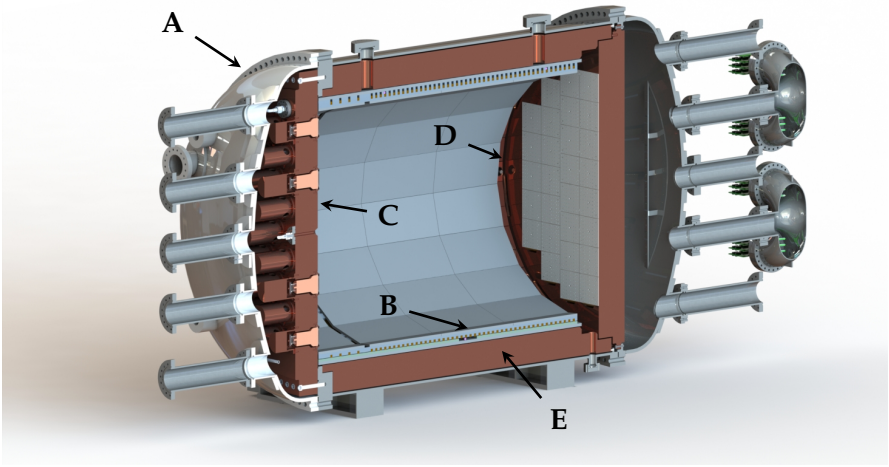

Figure 3.21: Cross-section view of the NEXT-100 detector. A stainless-steel pressure vessel (A) houses the electric-field cage (B) and the two sensor planes (energy plane, C; tracking plane, D) located at opposite ends of the chamber. The active volume is shielded from external radiation by at least 12 cm of copper (E) in all directions.

to degrade uniformly the electric field along the drift length. The inner diameter is 100.2 cm and the total length is 140.7 cm, with 26 cm of those being for the buffer region. The inner surface of the teflon reflector panels is coated with TPB to increase light collection efficiency. The design is illustrated in Figure 3.22.

Tracking plane

NEXT-100 will have 56 Dice Boards with 64 SiPMs each, leading to a total of 3584 sensors. To reduce background, in NEXT-100 the kapton dice boards will only have kapton on one side, leaving the PCB traces exposed. The design is an 8×8 SiPM matrix, as in NEW, but the pitch has been increased from 1 cm to 1.55 cm. Although the feedthroughs have been redesigned, keeping a 1 cm pitch is not possible because the amount of channels needed exceeds the maximum number of cables

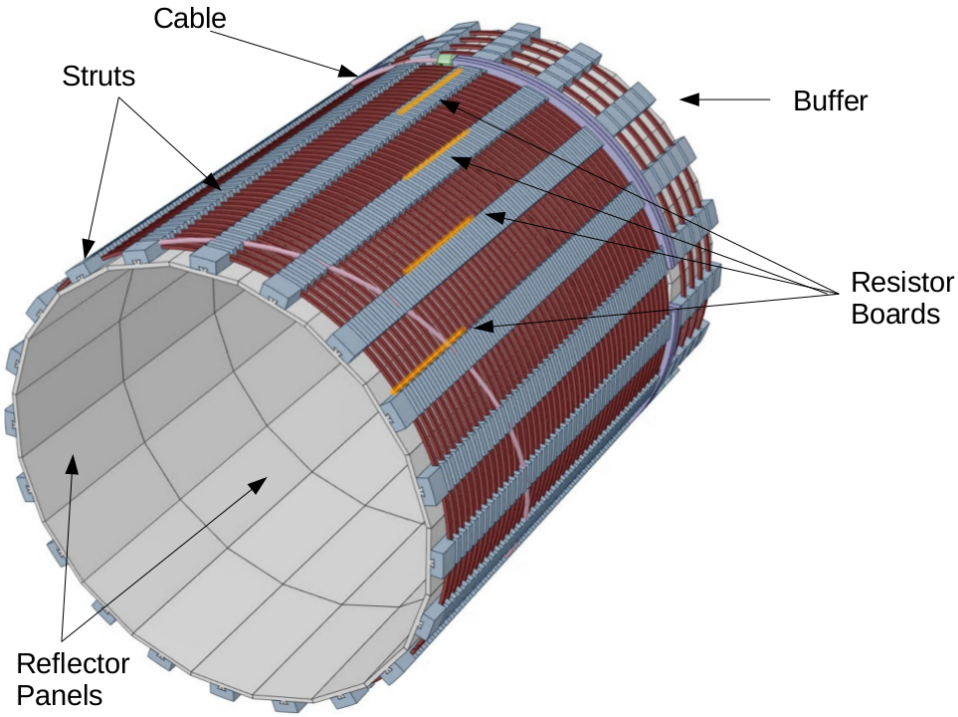

Figure 3.22: Drawing of the NEXT-100 field cage, including the teflon reflector panels, the HDPE struts for structural support and the resistor chains.

that the feedthroughs can accommodate. The increased pitch allows for a total coverage of the active volume.

Energy plane

The design of NEXT-100 has 60 Hamamatsu 3-inch R11410-10 PMTs (the same model used in NEW) [141], providing a coverage of approximately 37%. Given the fact that they are one of the main contributors to the background, a new design of the PMT base circuit with fewer capacitors is being tested out. The copper plate and the mechanical elements of the energy plane have the same structure as those of NEW, adapted to the bigger size.

Gas system

NEXT-White's gas system has proven to be a reliable gas recirculation, purification, pressurization, recovery, and storage setup, having passed three external safety reviews. To better serve NEXT-100 a few upgrades will be implemented.

To prevent dead spots with almost no flow inside the detector, a new piping system will allow for reversal of the gas flow without opening the detector. This change in the gas flow has proven very useful in NEW to increase gas purity. For the same reason, the gas input lines have been moved from the lateral side to the Energy Plane. Some extra pipes will be added to prevent excessive recovery times, given the larger size of NEXT-100. Finally, to better control the krypton calibration source, the manual valve will be replaced by a more precise metering valve.

Data acquisition

The design of the DAQ will remain without changes aside from the overall scaling. It will need more front-end cards to read all the sensors and, possibly, some more computer servers to deal with the extra load. A more detailed description is given in § 4.8.

3.5 Future generation detectors

To completely scan the inverted hierarchy of neutrino masses tonne-scale detectors will be needed. The NEXT Collaboration is intensely working in that direction with a two-phase approach [155]. In the first one, named NEXT-HD, incremental improvements over NEXT-100 will be done such as: replacing PMTs with SiPMs as they are the main background source, operating at lower temperatures to reduce dark noise and using a low diffusion gas mixture to improve the performance of the topological signature [156–158].

The second phase, NEXT-BOLD[3], will be a detector capable of performing barium tagging, that is, detecting with high efficiency the presence of the Ba^{++} ion produced in the ^{136}Xe $0\nu\beta\beta$ decay. Since natural radioactivity does not create Ba^{++} ions, if the barium ion

[3] Barium atOm Light Detector

could be detected in coincidence with the two-electron signal (and for events in the narrow ROI allowed by the good energy resolution), the expected background rate drops to zero.

In 2015, Nygren proposed a Ba^{++} sensor based on fluorescent molecular indicators that could be incorporated within a high-pressure gas xenon TPC (HPXe) [159], such as those developed by the NEXT collaboration. Fluorescent indicators are molecules whose response to optical stimulation changes when it forms a supramolecular complex with a specific ion. The concept was further developed in [160] and followed by an initial proof of concept [57] which resolved individual Ba^{++} ions on a scanning surface with more than 12 standard deviations.

After this seminal work, the NEXT collaboration launched an intense R&D program. Two complementary approaches are being pursued. The GodXilla R&D explores the possibility of a barium-tagging detector based on radio-frequency (RF) carpets whose goal is to focus the Ba^{++} ion in a small scanning region, while the SABAT (Single Atom BArium Tagging) R&D envisions a cathode fully equipped with sensors and scanned by a movable microscopy system. Both approaches use dry molecular indicators to capture the Ba^{++} ion. Those currently explored by GodXilla are of the type On-Off (light emission is greatly enhanced for molecules which have chelated an ion w.r.t. uncoordinated states). SABAT is based in a new type of fluorescent bicolor indicator (FBI) which responds to coordination with Ba^{++} enhancing the emission and shifting its color [58].

The NEXT collaboration is intensely working on these R&D programs to produce a technical design of a detector implementing a fully operative Ba^{++} tagging system.

The next-generation HPXe-EL experiment could deploy one or more modules based on the HD or BOLD approaches, depending on the status of the technologies. A sensible scenario would be to deploy first an HD module, followed by a second BOLD module. If the BOLD approach could be fulfilled, NEXT would be a background free experiment with a technology scalable to very large masses that would therefore potentially be able to scan the entire inverted hierarchy parameter space.

4 Data Acquisition System

4.1 NEXT-White Data Acquisition System

The NEXT collaboration, the RD51 Collaboration at CERN and IFIN-HH Bucharest co-developed SRS (Scalable Readout System) in 2011 [124, 150]. SRS was designed as general purpose multi-channel readout solution for small and medium scale experiments. The first SRS version used 6U Eurocard mechanics and had a generic FPGA-based readout card: the Front-End Concentrator card (FEC card). Several add-in cards were developed to read out popular ASICs in the RD51 community, to digitize analog channels (like PMTs) and to interface digital front ends.

In 2014, SRS was ported to the ATCA (Advanced Telecommunications Computing Architecture) standard which includes redundant power supplies and cooling, making it a more reliable solution for prolonged operation in experiments than the original SRS. NEXT-White DAQ system adopted the SRS-ATCA approach [161]. Each ATCA blade consists of two interconnected FPGAs (Xilinx Virtex-6 XC6VLX240T-1ff1156), two mezzanine slots, two event buffers, and I/O interfaces (Gigabit Ethernet and NIM trigger signals). Therefore, an ATCA blade is equivalent to two "classic" SRS FEC modules.

The DAQ system is divided into three parts: the energy plane (12 PMTs), the tracking plane (1792 SiPMs grouped in 28 Front-End Boards, FEBs) and the trigger. The PMTs are digitized at 40 MHz with 12 bits per sample and the SiPMs at 1 MHz and also 12 bits per sample. In raw mode at a 10 Hz trigger rate the PMTs generate 10 MB s^{-1} while the SiPMs produce 35 MB s^{-1}. The amount of data generated by the trigger is negligible.

A diagram of the system for NEXT-NEW is shown in Figure 4.1. It

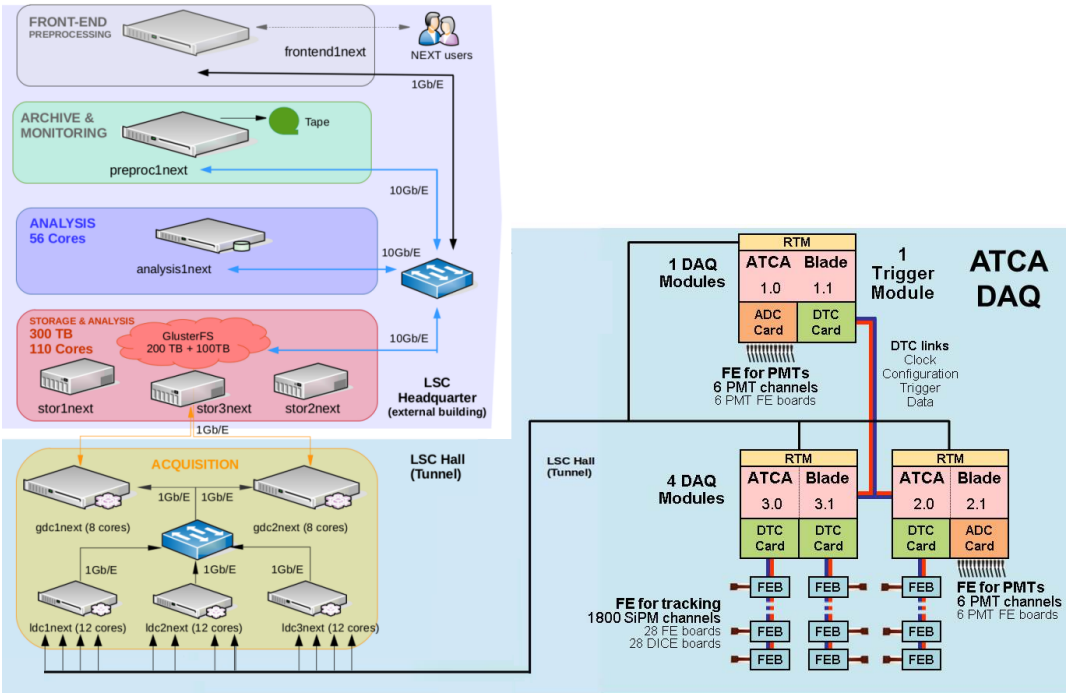

Figure 4.1: NEXT-White's DAQ structure including the server farm for online and offline event processing (left part) and the ATCA blade with the FEC cards for PMTs, SiPMs and trigger.

has 3 ATCA frames with 6 FECs boards: one for the trigger, two for the 12 PMTs and 3 for the 1729 SiPMs. They communicate through a DTC (Data, Trigger, Clock) link in order to be able to control and trigger the system.

The system is recording data continuously to a circular buffer until the trigger processor finds an event fulfilling all the conditions set in the configuration. Then data would be framed and sent to the different LDCs to be compounded later in a GDC.

4.2 DATE online system

The online system for the NEXT-White detector is using the DATE software from ALICE at CERN and the electronics developed within

the RD51 collaboration from CERN [152]. The main advantage of this option is the scalability of the system.

DATE is a software that runs on Scientific Linux and can handle parallel data streams produced by different subsystems from the detector. All these subevents would be later be combined into an event by the event builder. The system uses Gigabit ethernet and the UDP protocol [162] to communicate between the different computers involved in the data acquisition process.

The architecture of the system includes two levels of servers: Local Data Concentrators (LDC's) and Global Data Concentrators (GDC's), as they are named by DATE. The first level includes LDCs, that will receive the data from a subset of the sensors in the detector as subevents. From there, subevents are sent to the GDCs for the final event building process. In order to do so, LDC's are connected to the GDC's via network. GDCs can have load balancing mechanisms to improve the trigger rate of the system, the simplest of which is a round robin algorithm where events go to different GDCs following a circular order.

DATE has an internal database with all the IPs of the different nodes and their roles. A different software (see Section 4.4) written in Java by the NEXT collaboration configures the trigger and sends control commands to the FEC cards.

The DATE framework can work with Gigabit Ethernet networks using the User Datagram Protocol (UDP). This protocol allows communication over IP networks with commercial network cards. UDP is a standard for fast communications since the protocol imposes a very little overhead and only has an optional checksum mechanism. There are no ACK packets in response. The integrity and coherence of the message has to be checked at a higher level afterwards.

After the UDP header, DATE inserts a sequence counter (32 bits) to check for lost or duplicates packages, raising an error if any are found. The packet size is fixed to 9 KB to maximize throughput. This may be a problem for some old network equipment, but nowadays most networks cards and switches support jumbo frames (packets bigger than 1500 bytes).

The data collection is organized by *runs*. Using the DATE control program (Figure 4.2) a run can be started. Before starting a new run, the software checks whether all the equipment is reachable through

Figure 4.2: DATE run control panel.

the network and, then, a start command is sent. DATE takes control of the buffer of the network cards and maps part of the computer memory for its internal event building processes. Each LDC will get the subevents of the equipment connected to it and add some headers to them. These headers are defined by DATE and they are optimized for accelerator experiments. They contain important information for data quality monitoring, such as the origin equipment, machines involved, timestamps, sizes of the events and some words for error checking. Finally, each subevent (including DATE headers) is forwarded to a GDC where the whole event will be built and stored in disk in a binary file.

During data taking, DATE provides a monitoring utility (Figure 4.3) showing the trigger rate, byte rate, number of events, number of files written to disk and a few more relevant parameters. This information

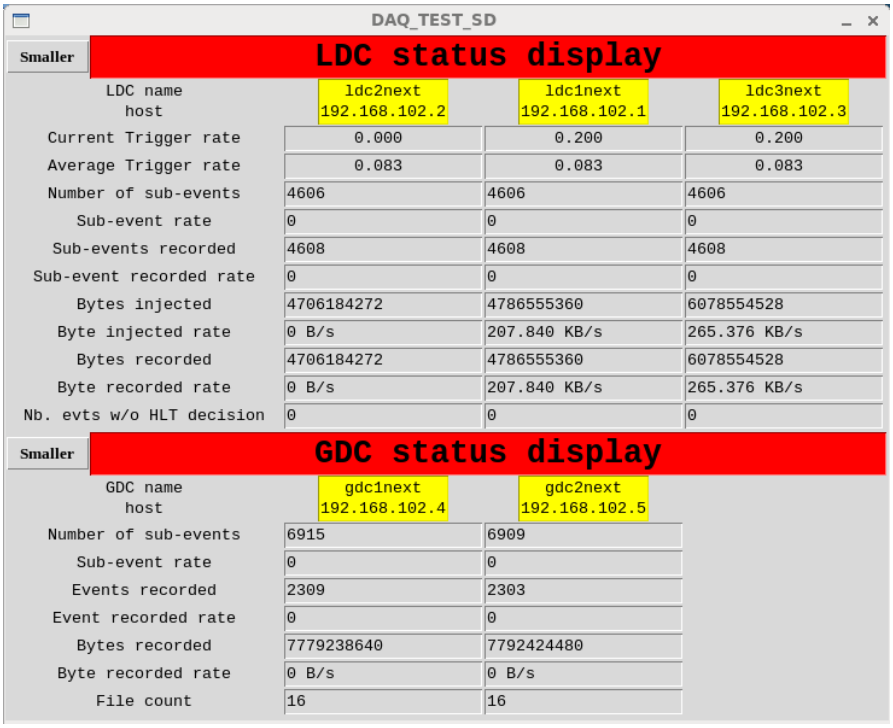

Figure 4.3: DATE monitoring window.

can be seen for each LDC and GDC.

An event is closed when a special packet is received with only the UDP header and a special word defined by the RD-51 collaboration: `0xFAFAFAFA`. The structure of the packets is shown in Figure 4.4. The information that comes after DATE's headers is the payload, whose format is defined by the NEXT collaboration according to the needs of the experiment. This part is totally transparent to DATE and will not be modified in any way during the transmission or event building procedures.

4.3 NEXT data format

The data generated by the detector must be written in a common format understood both by the FPGAs in the electronics and the com-

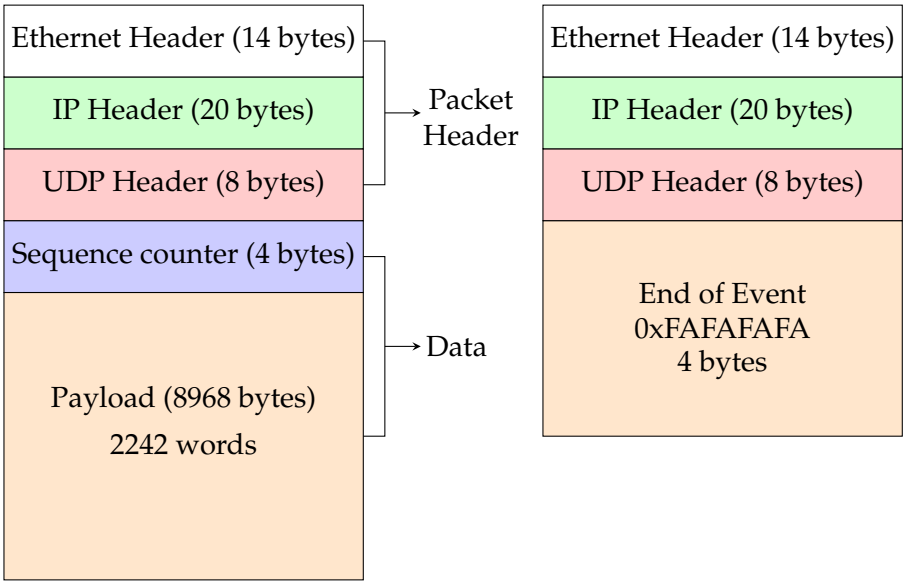

Figure 4.4: Structure of DATE packets (left). IP and UDP are used for communication and are not stored. A sequence counter is used to check the integrity of the data. A special datagram with the word `0xFAFAFAFA` is used to mark the end of an event (right).

puters that will run the analysis later. This format definition must include all the relevant information taken during the operation of the detector, from all PMTs, SiPMs and the trigger.

In the case of NEXT, the data format has evolved throughout time depending on the needs of the experiment. The different versions of the firmware are named according to the NATO phonetic alphabet, the current one, version 9, being India.

The firmware produces datagrams using 16-bit words while the DATE buffer has 32 bits, adding an extra requirement for the decoding software that will need to rearrange the words to interpret them properly. If 32-bit words are needed, they are split between the 16 Most Significant Bits (MSB) and the 16 Least Significant Bits (LSB) comprising two words.

There are different data formats defined for PMT, SiPM and Trigger

FECs. In the cases of PMTs and SiPMs the packet size is fixed to 9KB. If the last package is not filled with data, the remaining space would be padded with ones (`0xFFFF`) until the ending word (`0xFAFAFAFA`). Trigger packets are shorter, requiring only 48 bytes.

A detailed description of the format can be found in [163]. As a summary, the main fields defined in the headers are the following:

- **`Sequence counter`**: 32 bit counter used by DATE to check for missing or duplicate packets. If a packet arrives with a wrong sequence counter, there has been an error in the transmission and data has been lost.
- **`Format ID`**: Defines the type of data (PMT, SiPM or Trigger) and the firmware version. It also defines whether the data is in raw format or compressed/zero suppressed.
- **`Wordcount`**: 16-bit counter with the number of 16-bit words until the end of the frame.
- **`Event ID`**: Contains an absolute trigger counter for each run and the type of trigger for each event. In normal mode, trigger 1 has the code 1 and trigger 2 has code 9.
- **`Event conf`**: Information related to the system configuration including buffer size, pre-trigger size and channel mask. In the case of PMTs the channel mask indicates which channels are connected for a given FEC; for the SiPMs it indicates which FEBs are connected to each FEC.
- **`FEC-ID`**: FEC identifier. Each card has two links and therefore two identifiers. They are related to the IP address they have in the network.
- **`#Ch and #FE`**: Number of PMTs/FEBs connected.
- **`Coarse Timer (CT)`**: UNIX timestamp in milliseconds for each event in 42 bits. It is the number of milliseconds since 00:00:00 Thursday, 1 January 1970.
- **`Fine Timer (FT)`**: 17-bit timer with the sampling frequency of the PMTs (40 MHz). It indicates the position of data in the

circular buffer. Therefore, the timer goes up to the buffer size and then is reset to zero.

- `Data`: Charge values are concatenated in 16 bit-words, requiring 12-bit for each value. If operating in compression mode, then the length of each data value can be different. More details in Section § 4.6.
- `FEB ID and FEB info`: FEB identifier and error bit that signals synchronization errors between the FEB and the DAQ.
- `Channel mask`: For the SiPMs there are four 16-bit words, one bit per channel (64 in total) indicating which ones are sending data in that particular time bin.
- `Trg conf`: Contains information related to trigger configuration such as trigger code, auto-trigger, external trigger, dual trigger, etc.
- `Ch info`: Channel mask spanning four 16-bit words, indicating which PMT channels have triggered the system. Since NEXT100 is planned to have 60 PMTs, 64 bits are enough to address all of them.

Figure 4.5 shows the data format for PMTs in raw mode. The zero suppressed mode is shown in Figure 4.6. The SiPMs have the same data format both for raw and zero suppressed modes, illustrated in Figure 4.7. Finally, trigger information headers are shown in Figure 4.8.

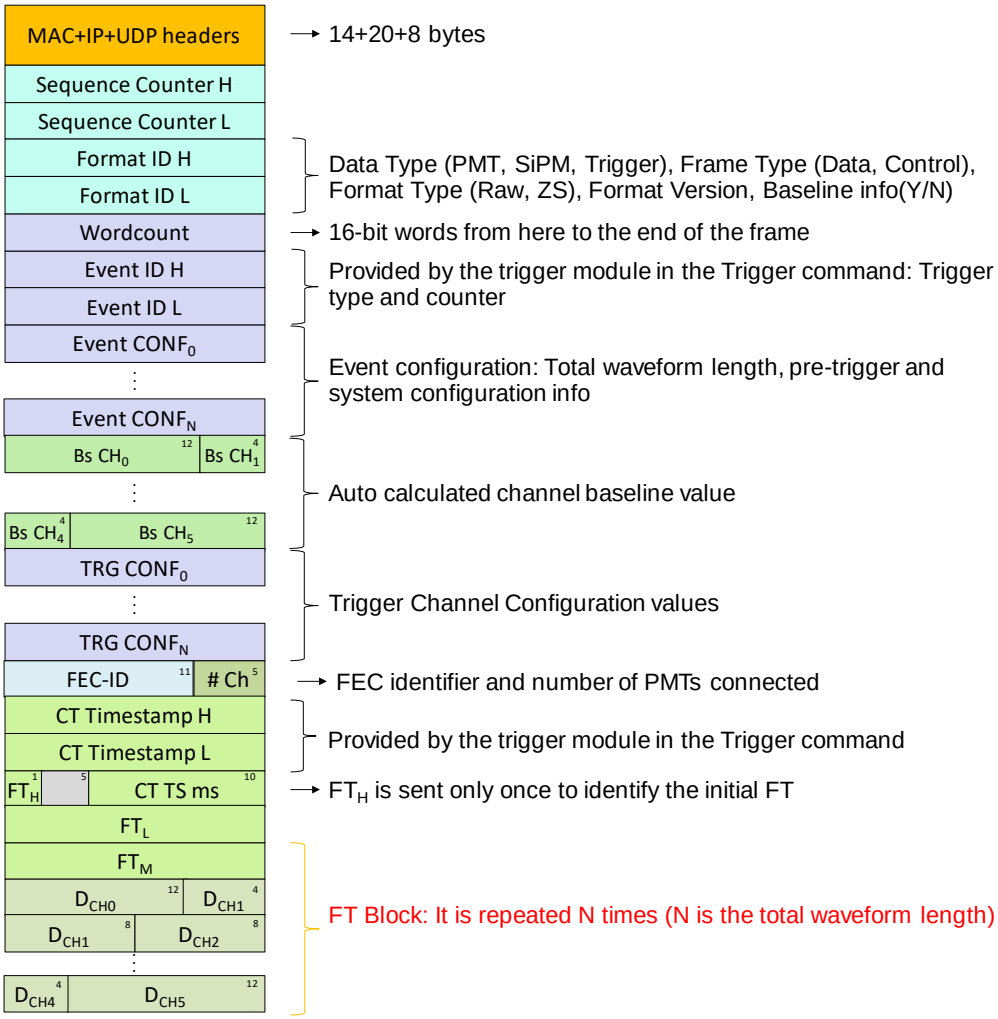

Figure 4.5: Data format for PMTs in raw mode.

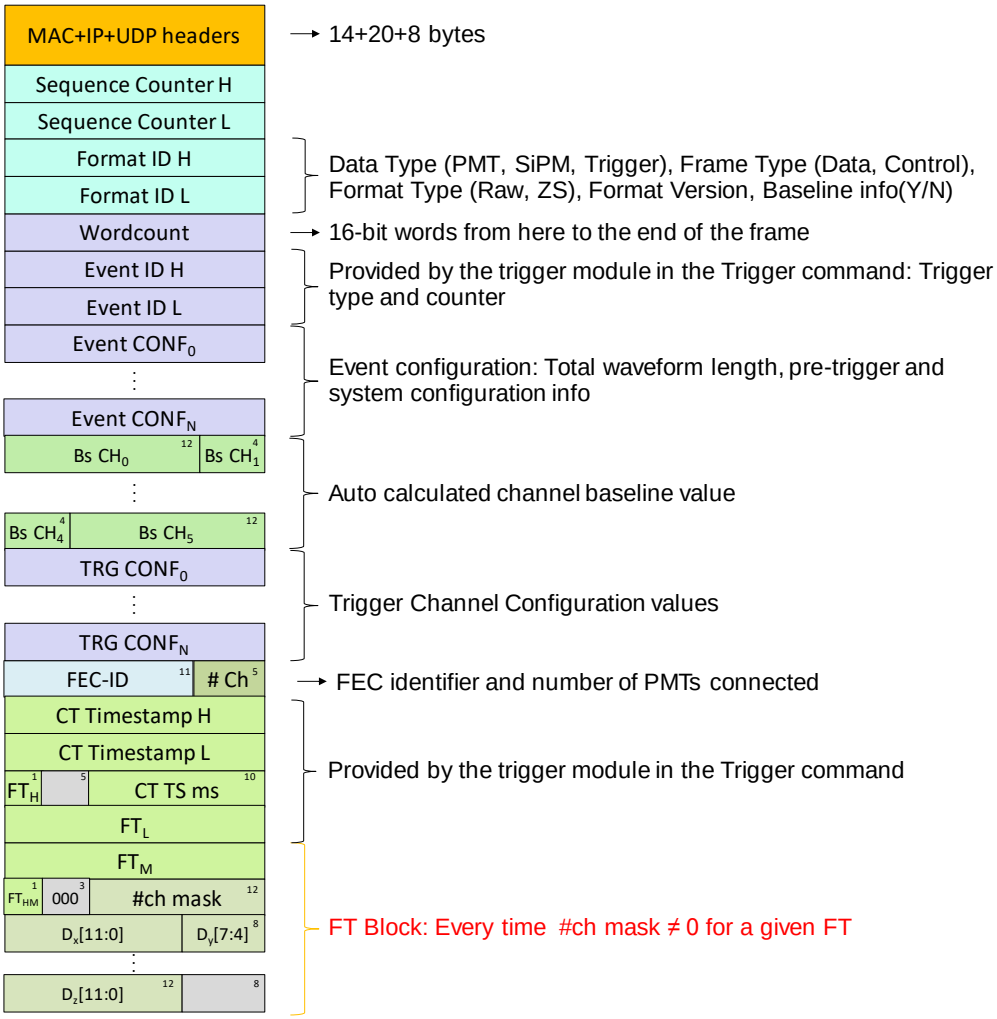

Figure 4.6: Data format for PMTs with zero suppression.

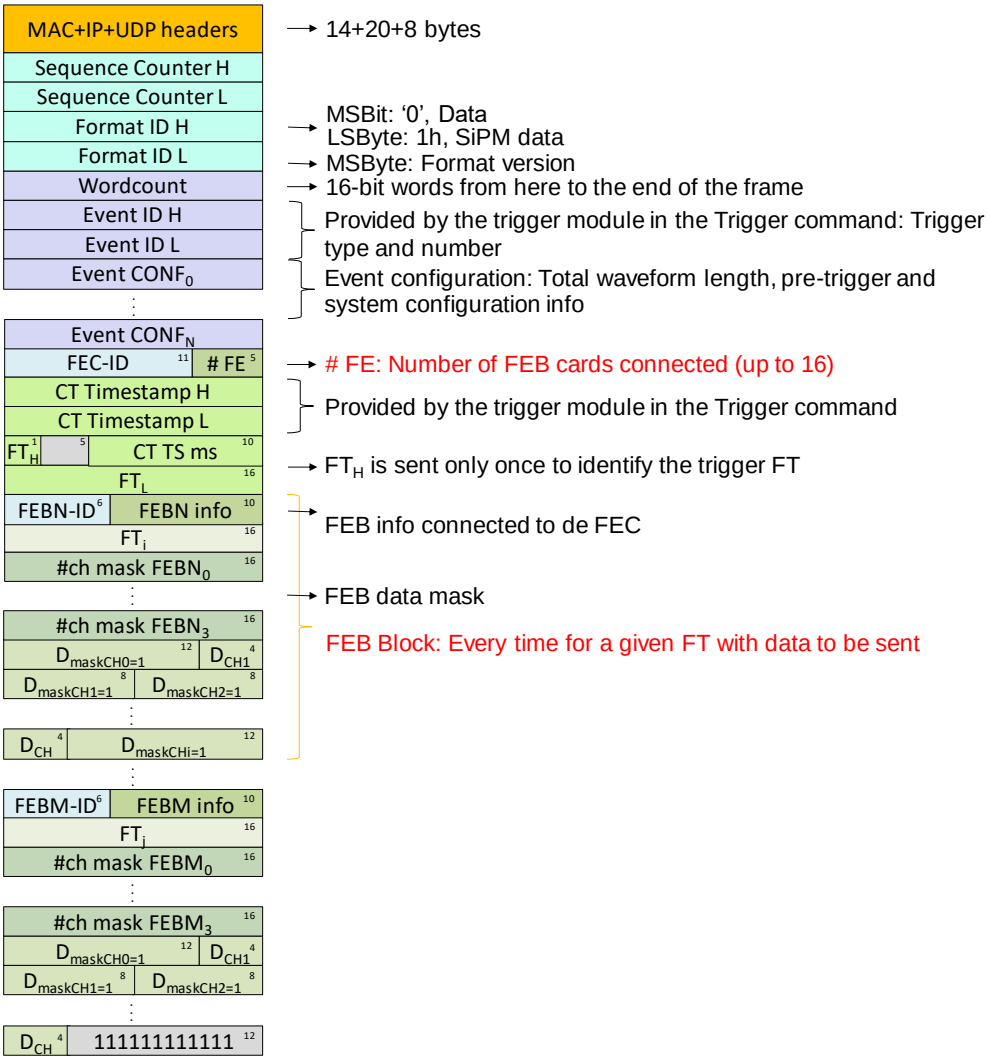

Figure 4.7: Data format for SiPMs both in raw mode and with zero suppression.

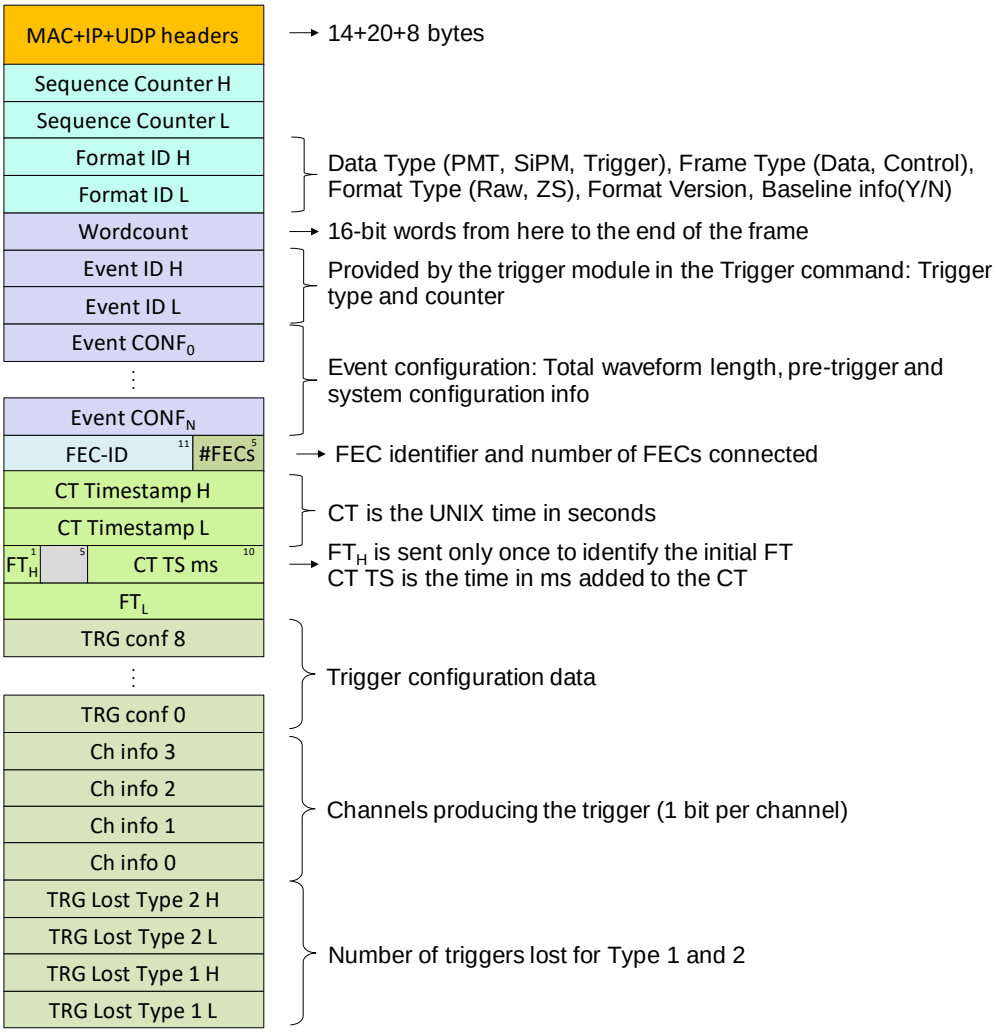

Figure 4.8: Data format for trigger information.

4.4 Trigger system

The event detection system for NEXT must be able to detect with high efficiency a wide variety of events. Low-energy calibration with a ^{83m}Kr source produces events with small signals, while high-energy sources (^{222}Rn, ^{232}Th), low-background runs or muons produce events with many different topologies depending on the direction of the particles in the gas.

The trigger in NEXT-White is an evolution of the trigger for NEXT-DEMO [164] that has a lot of flexibility for event selection. The maximum buffer size is 3.2 ms, about 6 times the maximum drift time for NEXT-White and 3 times the length of NEXT100.

The trigger implemented is a two-level system. In the first level, the Double Event Processor (DEP) generates one event candidate per each PMT sensor, based on an early energy measurement. From there, event candidates are sent to the second level, located in the Control Module. Then, the Coincidence Event Processor (CEP) produces an Event Accept signal that triggers a data download from the DAQ internal buffers to the online system's LDCs. A schematic is shown in Figure 4.9.

The system allows for a dual trigger to be configured. To do that, both the DEP and the CEP are each a double processor. Each processor can be configured with its own set of parameters to search for a different type of event. The default mode of operation during physics data-taking campaigns is to use the dual trigger. Trigger 1 is configured for low energy events (Kr calibration), while Trigger 2 is reserved for high energy events, usually near $Q_{\beta\beta}$. This is an important requirement as it allows the system to be calibrated at all times using low energy events. In order to minimize the probability of losing an interesting event, trigger 2 has priority over trigger 1, which is much more frequent than trigger 2. Additionally, to minimize the dead time, the DAQ is able to store two events using a double circular buffer.

When the system is running, PMTs are sampled every 25 ns and SiPMs every 1 µs. The Double Event Processor generates event candidates based on several configurable thresholds: baseline deviation, event energy and event duration. Although a different configuration can be set for each PMT, in standard physics operation all the PMTs have the same trigger parameters. Table 4.1 shows the configuration

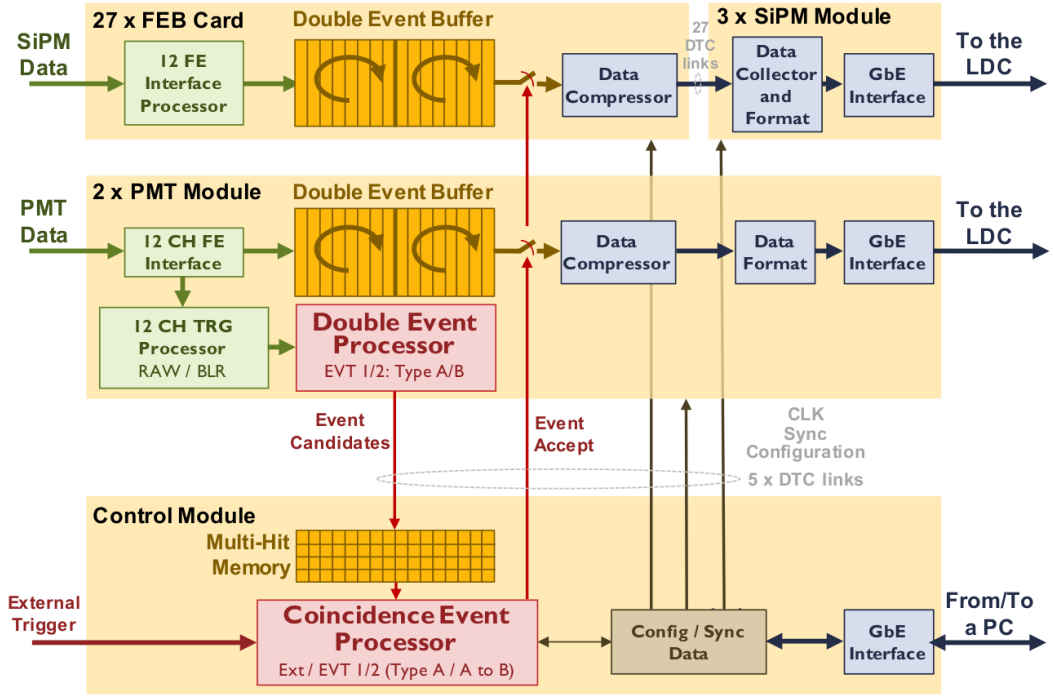

Figure 4.9: NEXT-White trigger scheme showing the Double Event Processor that generates event candidates and the Coincidence Event Processor that produces an *event accept* signal that triggers buffer data download to LDCs.

for different types of events. A JAVA program is used to set all the parameters for each run (see a screenshot in Figure 4.10).

PMT front-end electronics are designed with an AC coupling scheme. At first order, they produce an output signal that is the derivative of the input and it is characterized by a null total area. Since the energy estimation is done by computing the area of the input pulse, a baseline restoration (BLR) algorithm has to be applied [151]. To be able to include the event energy as a trigger configuration parameter, PMT FEC cards include an online implementation of a BLR algorithm.

Table 4.1: Trigger configuration parameters for different type of events. The same configuration is applied for all PMTs. In standard operation the buffer size is set to 1600 µs with a pre-trigger of 800 µs.

Event Type	Event Detection Parameters						Coincidence Event Processor Parameters	
	Energy Accumulation of ADC counts		Amplitude Relative to the baseline		Time µs		Time Coincidence Window µs	Coincident events Number of PMTs
	Min	Max	Min	Max	Min	Max		
$\beta\beta$	100000	16777215[a]	10	-	2	600	1.2	2
^{83m}Kr	5000	50000	10	1000	2	40	1.2	2
^{232}Th	220000	16777215	10	2000	10	250	0.5	2
Muons	100000	16777215	10	-	2	600	1.2	2

[a] Maximum possible value (24-bit parameter)

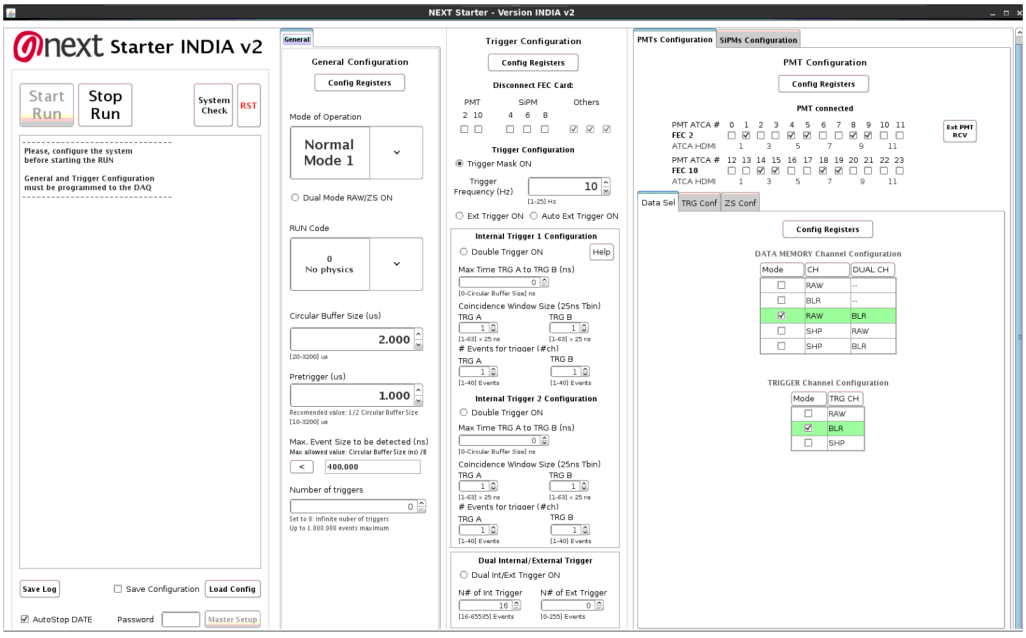

Figure 4.10: Trigger control program. Using this JAVA GUI it is possible to configure all the data taking parameters: buffer size, trigger configuration, active channels, etc.

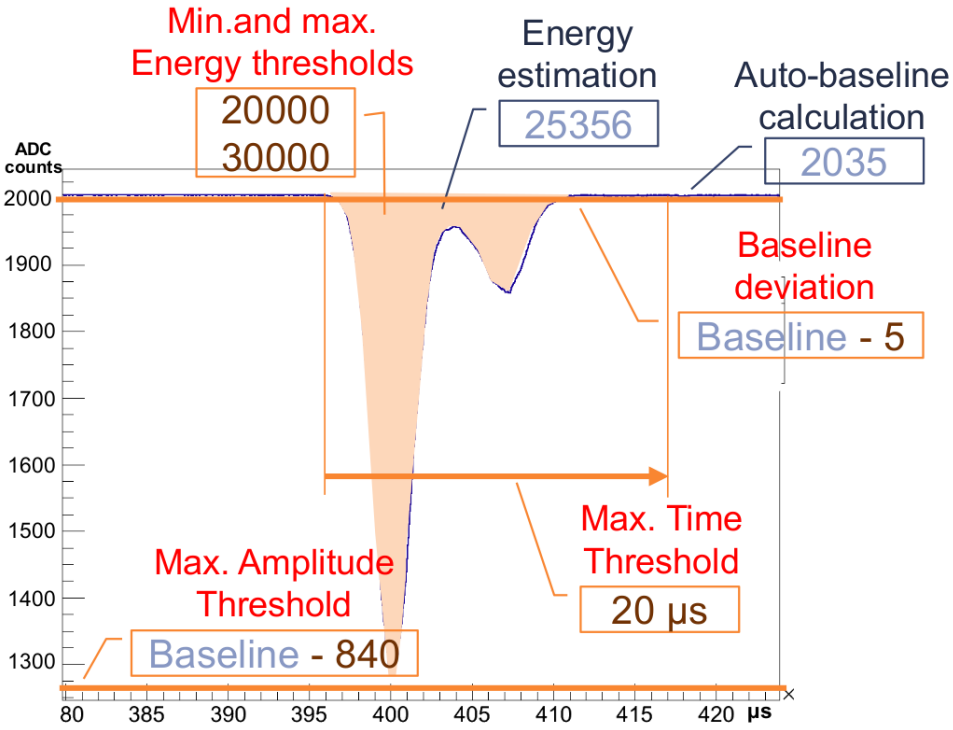

Figure 4.11: Sample waveform with the estimated parameters to be used by the Double Event Processor to generate event candidates. It includes measurements related to the signal amplitude, event energy and event duration.

The online system computes the baseline using a configurable moving average filter. Then, an energy estimation can be computed by integrating the difference between the signal and the baseline whenever the baseline deviation is higher than a configurable threshold. Figure 4.11 shows an example with a waveform.

Finally, after event candidates have been generated, the Coincidence Event Processor checks whether a minimum number of them are in a coincidence time window. If that is the case, an Event Accept signal is generated, triggering an event download and sending the buffer contents to the LDCs.

In addition to the modes described above, the system also has an external trigger mode in which an external signal is read to trigger the system. This mode is mainly used to calibrate the sensors using LEDs. The same square signal sent to the LEDs is used as external trigger, therefore saving waveforms containing LED pulses.

For debugging purposes, the system also has an autotrigger mode in which the trigger does not depend on neither sensors nor external signals but on an internal clock with a tunable frequency.

4.5 Decoding software

In order to read the information written in binary format by DATE, a decoder program is needed. This decoder has been my main contribution to the DAQ development. This tool translates the information sent by the DAQ to some higher-level format that would be the input for the event reconstruction framework. In our case, Invisible Cities is the software to run both reconstruction and analysis steps [165]. This software is written in python and uses the HDF5 file format [166] for persistency. Therefore, the decoder needs to translate the waveform information from DATE binary format to HDF5.

The software for this task is a program written in C++ that originally was integrated in the ART framework [167] that was used in the NEXT collaboration. When Invisible Cities was ready, the ART framework was deprecated and we took all the decoder functionality out of the ART module and implemented a new standalone program.

The decoder input is a JSON file [168] with all the relevant configuration parameters:

- `max_events`: Maximum number of events to be read from the input file. Default value: 100000.
- `verbosity`: Sets the level of information to be printed at execution time. Debug information will be printed to standard output while errors would go to standard error. Default value: 0.
- `ext_trigger`: Channel number for external PMT if used. Default value: 15.

- **two_files**: If true, the program will try to load at the same time the file from GDC1 and GDC2 and will read the events from them in chronological order (reading one event at a time alternating between files). Default: false.
- **file_in**: DATE input file. If two_files is true this file must be the one corresponding to GDC1.
- **file_out**: Path for the HDF5 output file. If split_trg is true, only events marked with trg_code1 will be saved in this file.
- **file_out2** If split_trg is true, only events marked with trg_code2 will be saved in this file.
- **split_trg**: If true, the output will be split between file_out and file_out2 according to trg_code1 and trg_code2. Default: false.
- **trg_code1**: If split_trg is true, events for file_out. Default: 1 (events with trigger 1 in normal mode).
- **trg_code2**: If split_trg is true, events for file_out2. Default: 9 (events with trigger 2 in normal mode).
- **discard**: If true, events with the error bit set are not decoded. If false, the program will try to decode them, but depending on the origin of the error segmentation faults are possible. Only to be used when debugging the DAQ. Default: true.
- **copy_evts**: If true, it will copy the events between skip and max_events in binary format into file_out. This mode is useful to extract particular events for testing purposes. Default: false.
- **skip**: Number of events to be skipped. Default: 0.
- **host**: Hostname of the MySQL server with the mapping between electronic and simulation channels.
- **dbname**: Database name in host. Must have a table named ChannelMapping. This table contains the mapping between electronic channels (ElecID) and the corresponding channels in the software simulation (SensorID).

- `user`: Username for `host` with read permission on `dbname`.
- `pass`: Password for `host`.
- `no_db`: If true, no channel mapping would be used, the waveforms would be written sorted by ElecID. If false, the program will read the mapping from `dbname` and sort them by SensorID. More details in Section § 4.5.2. Default: false.

4.5.1 File structure

The output of the decoder is one or two files in HDF5 format [166]. HDF5 stands for Hierarchical Data Format 5 and is a format designed to store large amounts of data. It was originally developed at the National Center for Supercomputing Applications and is supported by the HDF Group, a non-profit organization whose mission is to ensure continued development of HDF5 technologies and the continued accessibility of data stored in HDF. Therefore, libraries and APIs are available for many different programming languages and environments with open source licenses.

At a high level, HDF5 files are organized with three kinds of nodes arranged in a tree structure. The inner nodes of the tree are called *groups* and they behave like folders in a filesystem; the leaves are *datasets*, which can be multidimensional arrays and tables. The multidimensional arrays must have a unique datatype (integer, string, etc.) for all the elements in the dataset while the tables are like a $M \times N$ matrix where each of the different N columns can have different datatypes, including compound ones.

The structure of the files written by the decoder is the following:

- Group `RD`: All datasets within this node are three-dimensional arrays with dimension *Events* $\times$ *Sensors* $\times$ *Samples* and 16-bit integer elements. Since the DAQ is using 12 bits for each sample, 16-bit integer are enough to store those values. These integers are also a basic type both in HDF5 and in most programming languages.
  - `pmtrwf`: PMT waveforms. Only present if PMT data was sent by the DAQ. The order of the sensors is the same one as in the table `/Sensors/DataPMT`.

  - **pmtblr**: BLR waveforms. The DAQ can operate in a dual mode that sends both *real* channels and the output of the online BLR algorithm. This dataset will contain the BLR version of the PMT channels. The order of the sensors is the same one as in the table `/Sensors/DataBLR`.
  - **sipmrwf**: SiPM waveforms. If the DAQ is working in zero suppression mode, the time bins that are not sent will be zeros. Only present if SiPM data was sent by the DAQ. The order of the sensors is the same one as in the table `/Sensors/DataPMT`.
  - **extpmt**: External PMT waveform. In case an external PMT is used, usually to trigger in coincidence with a ^{22}Na source, a 2D-array (*Events* $\times$ *Samples*) with the waveform is written. The channel number is specified in the `ext_trigger` configuration parameter.

- Group **Run**:
  - **events**: Table with two columns: `evt_number` and `timestamp`. Event number is a 32 bit integer and event timestamp is a 64 bit integer with the UNIX timestamp in milliseconds. It has one entry per event.
  - **runinfo**: Table with one column: `run_number`. It has only one row with the run number of the files read from DATE.

- Group **Sensors**: In this group there are two-column tables containing the mapping between electronic channels and those configured in the simulation software. More details in Section § 4.5.2.
  - **DataPMT**: PMT sensor mapping. Only present if PMT data was sent by the DAQ.
  - **DataBLR**: PMT-BLR sensor mapping. Only present if PMT-BLR data was sent by the DAQ.
  - **DataSiPM**: SiPM sensor mapping. Only present if SiPM data was sent by the DAQ.

- Group `Trigger`:
  - `configuration`: Table with two columns: `param` and `value`. One row per parameter received in the `Trigger conf` words in the trigger headers.
  - `events`: Two dimensional array with dimension $Events \times \#PMTs$. Boolean array where the element $events_{ij}$ is 1 if pmt number j (according to `/Sensors/DataPMT`) has triggered on event i, 0 otherwise.
  - `trigger`: Table with one column: `trigger_type`. Contains one row per event with the trigger code sent by the DAQ for each event.

4.5.2 Database structure

Each sensor in the detector (both for PMTs and SiPMs) is identified by two numbers `SensorID` and `ElecID`. The former is the ID given to a sensor in a particular position in the simulation software and does not change over time, while the latter corresponds to the physical electronic channel to which each sensor is connected. This can be different for different runs depending on how the connections are made. For instance, if a channel is too noisy one may try to use another one that works better.

Since we need to compare simulations and real data, we need to store the relationship between those identifiers along different runs. There is a `ChannelMapping` table in the MySQL database of each detector with the mapping between `SensorID` and `ElecID`. The structure of the table and some sample rows can be found in Figure 4.12.

Due to the architecture of the software that will read the HDF5 waveform files, Invisible Cities, there is an extra constraint on the structure of the datasets. The number of sensors in `/RD/pmtrwf` and `/RD/sipmrwf` must be equal to the number of sensors defined for the detector in the database, regardless of how many sensors are actually sent by the DAQ. Missing channels will be filled with zeros. This does not create a storage issue because the datasets in the HDF5 file are compressed.

In the case of NEXT-White, the number of PMTs is 12 and the number of SiPMs is 1792. For NEXT-DEMO++ there are 3 PMTs and

```
mysql> select * from ChannelMapping where SensorID = 3;
+--------+--------+--------+----------+
| MinRun | MaxRun | ElecID | SensorID |
+--------+--------+--------+----------+
|      0 |   1273 |      3 |        3 |
|   1274 |   1754 |      6 |        3 |
|   1755 |   1765 |      3 |        3 |
|   1766 |   1978 |     19 |        3 |
|   1979 |   3292 |     19 |        3 |
|   3293 |   3913 |      0 |        3 |
|   3914 |   5024 |     23 |        3 |
|   5025 |   5203 |     13 |        3 |
|   5204 |   5366 |     17 |        3 |
|   5366 | 100000 |     13 |        3 |
+--------+--------+--------+----------+
10 rows in set (0,00 sec)
```

Figure 4.12: Sample data from `ChannelMapping` table. Shows the evolution of `SensorID=3` along different runs.

256 SiPMs. For this to work, there must be consistency between the state of the database and the actual connections between sensors and electronic channels in the detector. This will not always be the situation, especially when debugging the DAQ. For those occasions, there is an extra mode (activated with the `no_db` parameter) that does not use the database.

In `no_db` mode the decoder will write only the number of channels actually sent by the DAQ. For example, if there are only 11 PMTs and 512 SiPMs, that will be the size of the second dimension of the datasets in `/RD` and `/Sensors`. The waveforms would be sorted according to their ElecID and all SensorIDs would be set to -1, since they are not read from the database.

4.5.3 Automated testing and quality control

Given the complexity of the software needed to interpret binary files using the NEXT data format and its proper translation to HDF5 files,

we implemented an automated testing system to ensure the software works as expected. This is especially interesting for development purposes, as the developer can know easily whether the latest modification to the code base has broken or affected a part of the code that was previously working. It also avoids the need to manually check the program with a few files that may not catch a newly introduced bug.

The first type of test implemented are *unit tests*. They define a test case for a particular function consisting of a known input and its corresponding output. The test checks that running the tested function for the known input actually produces the expected output. These tests are useful for checking small parts of the code, but they do not ensure the proper function of the whole program.

Functions must be correctly connected to each other to obtain the expected HDF5 file for a given binary input file. To assess this, *integration tests* are used. They run the whole program with known input and configuration files and check the structure and contents of the HDF5 file given as output.

Given that the software is written in C++, a testing framework compatible with that language must be used. The one we chose is Catch2 [169], a simple framework that fulfills all the requirements for this project. There are many test cases to check the decoding of different headers. In some cases, a particular test generates automatically many different possible inputs (for instance, different numbers of sensors connected) and checks that the decoder reads them properly. Each check is called an *assertion*. Figure 4.13 shows the output after running the tests implemented with Catch2. Currently there are 36 tests cases that produce more than a million assertions.

For the integration tests, since they are higher level tests that do not involve calling particular C++ functions, the framework pytest [170] has been used. Some particular events have been extracted from different runs in binary format and they are used as input for several pytest tests. In this way, functionalities like splitting the output into two HDF5 files depending on the event trigger code can be tested easily.

Software testing is a complex discipline and achieving a good enough coverage takes time, especially if the tests are not defined as the software is being developed but afterwards, as has been the case for this code base. The current test suite provides a wide check

```
~~~~~~~~~~~~~~~~~~~~~~~~~~~~~~~~~~~~~~~~~~~~~~~~~~~~
tests is a Catch v1.10.0 host application.
Run with -? for options


===============================================
test cases:      36 |      36 passed | 0 failed
assertions: 1217808 | 1217806 passed | 0 failed
```

Figure 4.13: Sample output after running the automated tests implemented using Catch2.

of all software functionalities, but there may still be some untested features. More tests will be implemented in the future, especially when the software may need to be reviewed and updated for NEXT-100 operation. So far, the software has been working properly both for NEXT-White and NEXT-DEMO++ detectors.

4.6 Huffman compression

In order to improve the performance of the DAQ, we have implemented compression modes both for PMTs and SiPMs. If an event is triggered, there is some amount of time (called *dead time*) that the DAQ needs to send buffer data to the LDCs before it can write again in the circular buffer. Any event that occurs during that time would be lost. One way to reduce this time is sending less data by compressing the information.

There are two types of compression algorithms: lossless and lossy. The former allows for the recovery of all the original information from the reduced data while the latter only recovers part of the information. Zero suppression is a lossy compression mechanism where the system only sends the parts of the waveform that fulfill certain criteria (such as deviation from baseline). In this way the DAQ can send only S1 and S2 candidates with some pre/post-trigger information without sending the whole waveforms. Zero suppression is being used successfully in the operation of NEXT-NEW for SiPMs.

Table 4.2: Huffman codes obtained from real NEXT-White waveforms.

Value	Code	Value	Code
0	1		
1	001	-1	000
2	0111	-2	0110
3	010011	-3	010010
4	010001	-4	010000
5	0101011	-5	0101010
6	0101001	-6	0101000
7	0101101	-7	0101100
8	0101111	-8	0101110

For the PMTs, we also implemented zero suppression but it has not been used due to the BLR step that is run offline afterwards. This algorithm could be sensitive to missing parts of the waveform and has not been properly evaluated yet. Therefore the PMTs have to operate in raw mode. With this conditions of raw PMTs and ZS SiPMs the system can operate without errors at a rate of 35 Hz.

Using a lossless compression algorithm one could decrease further the dead time and/or increase the trigger rate without affecting in any way the BLR step that would come later, since it would have the whole waveform available as in raw mode. We implemented a mechanism along these lines and tested it in NEXT-DEMO++ before setting it up for NEXT-White in Canfranc.

The idea is to apply a Huffman code [171] to the differences between one sample and the previous one for each PMT. A Huffman code is a variable-length code where the most frequent words use the least bits and the less frequent ones use longer codes. In the case of NEXT, we obtained Table 4.2 using real data from NEXT-White waveforms.

With this scheme there would be two types of values: those whose difference with the previous one is included in the Huffman tree (now from -8 to 8) and those which are not. In the first case, a 1 would be sent, indicating the following code is a Huffman one, followed by the

Table 4.3: Comparison between raw data and Huffman compressed data using codes from Table 4.2. In the Huffman mode row, the first value is expressed in hexadecimal (with a 0 bit preceding it) and the rest of them are in binary.

Time	t_0	t_1	t_2	t_3	t_4
Value	2323	2322	2322	2321	2322
$t_i - t_{i-1}$	2323	-1	0	-1	1
Code in raw mode	0x913	0x912	0x912	0x911	0x912
Huffman mode	0-0x913	1000	11	1000	1001

code. In the second case, a 0 would be sent indicating the following code will be a 12-bit one, and then the code.

Therefore, the first value of each channel would always be sent with 13 bits (1+12) and then, the rest of the waveforms will depend on the differences between t_i and t_{i-1} and can have a different number of bits. A short example of how this work is shown in Table 4.3. A small waveform of 5 samples is shown. In raw mode it takes 60 bits while in Huffman mode the same data can be expressed with only 27 bits.

In a first step, we studied a simulation of the procedure using real NEXT-White waveforms (Kr, calibration sources, background...), showing that a compression rate of $\sim$ 85% was possible. We first implemented the system in NEXT-DEMO++ as a test bench, achieving an 87.8% compression level. Then, we deployed it at Canfranc for NEXT-White with similar results. Currently, this compression mode is part of the standard NEXT-White operation, running flawlessly with a smaller dead time than before thanks to the compression rates achieved.

Having this new strategy available, we considered whether Huffman compression could work better than zero suppression for SiPMs. Our current configuration for SiPMs sends only $\sim$ 15% of the waveforms, but the compression rate is $\sim$ 74%. The overhead is due to the rest of the headers sent (FEB-ID, channel mask, etc.). Using a Huffman tree with 16 codes the compression achieved in simulation is 64.4%, while for 32 codes it is 69.5%. Zero suppression is $6-7$% better.

With the aim of having a more flexible and robust system, Huffman

trees are saved in a MySQL database indexed by run number. Therefore, the decoding software can read each data file with the proper code table. Potentially, different tables could be used for different kinds of runs to optimize the compression as much as possible. The offline software is prepared for this.

4.7 NEXT-White setup in Canfranc

The DAQ and computing system deployed in Canfranc for NEXT-White is shown in Figure 4.14. There is one Cisco Catalyst 2960x switch with 48 1Gb ethernet ports and 2 SFP+ 10Gb ports for monitoring and remote access. The internal network for the computing cluster and distributed storage is connected via a Cisco SG350x switch with 24 10Gb ethernet ports.

There are 3 LDCs running in 3 DELL R320 servers, each of them with 6 CPU cores at 2.2 GHz, 16 GB of RAM and 2 network cards with 2 gigabit ethernet optical fibre ports connected to the ATCA cards. In total, there are 12 links to retrieve the data from the detector.

The two GDCs are running on 2 DELL R520 servers with an 8-core CPU at 2.2 GHz and 16 GB of RAM. Each GDC stores the events locally in $\sim$500 MB files before sending them to the distributed storage system used by the analysis cluster.

The storage and analysis cluster is composed of two Supermicro SSG-6048R-E1CR24N servers with 12 CPU cores at 2.6 GHz and 128 GB of RAM, one Supermicro SSG-6049P-E1CR36H server with 28 CPU cores at 2.6 GHz and 128 GB of RAM, and one Bull R421-E4 server with 28 CPU cores at 2.6 GHz and 128 GB of RAM. In total, there are 110 CPU threads available for event processing on-site at Canfranc and 300 TB of distributed storage space (DFS) using GlusterFS [172]. To store long-term data an IBM Library TS 2900 tape robot that can handle up to 8 tapes is used. By moving old data from the DFS to tape, free storage space can be obtained in the analysis cluster to continue with the data taking.

The system has performed very well over the years and has shown great stability taking data continuously. For documentation purposes, an electronic logbook software, ELOG [173] is used. A new entry is created automatically for each run, containing the related metadata

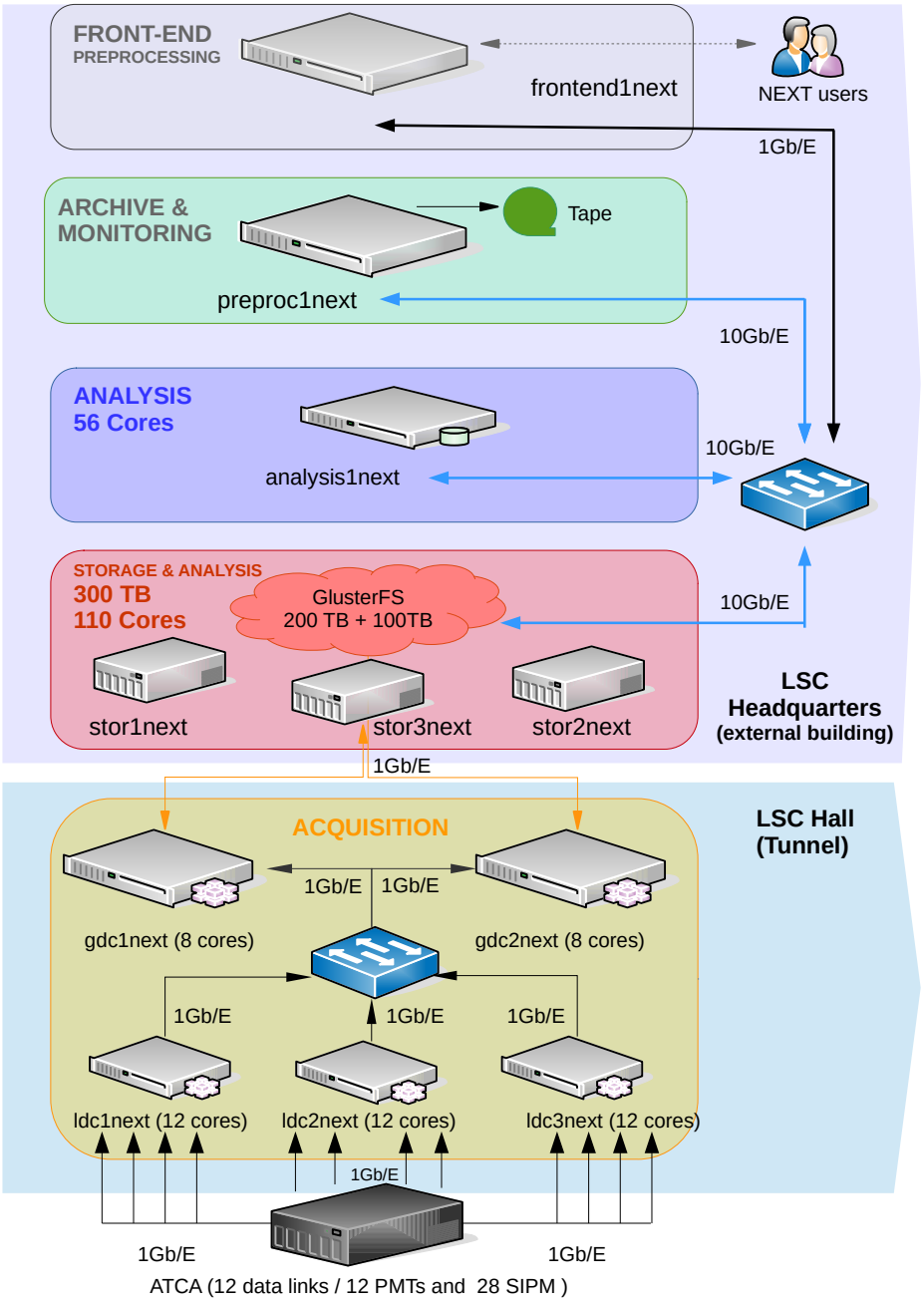

Figure 4.14: NEXT-White DAQ infrastructure in Canfranc.

such as type of run, trigger configuration parameters, number of events taken, etc. Up to August 2020, nearly 1.6 billion events have been recorded by the system.

Figure 4.15 shows the number of events taken over the years, with the different run periods shown in a different color. Run I was a short commissioning run that lasted from September to December 2016. After some hardware updates, mainly related to the field cage, Run II started on March 2017 with a pressure of 7.2 bar until October, when it was raised to 9 bar. Run II was stopped in November 2017 for some gas system updates to allow for higher pressures and some radiopurity updates in the field cage and PMT bases. Run III was started by the end of February 2017 but due to an issue with the EL voltage, it was stopped to allow for an upgrade in April 2017. Run IV lasted from June 2018 to the end of December 2018; it was a run devoted to calibration

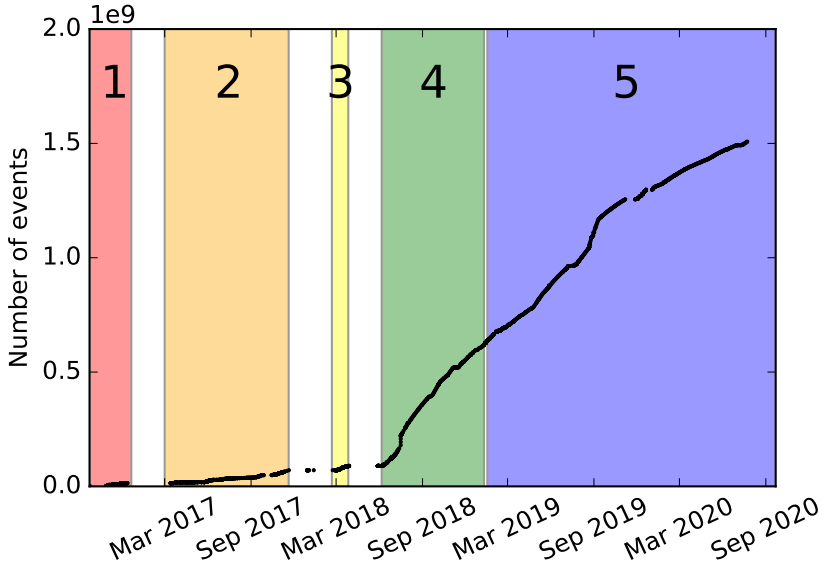

Figure 4.15: Number of events recorded as a function of time. Colors denote different run periods (details in the text). The system has shown to be extremely reliable, and has acquired so far nearly 1.6 billion events.

and background characterization. In February 2019 the detector was filled with enriched xenon, and Run V was started during that month. Run V lasted until July 2020, taking low background data for a lifetime measurement of the $2\beta2\nu$ decay of ^{136}Xe.

4.8 Towards NEXT-100's DAQ

The DAQ for NEXT-100 will be a scaled-up version of that in NEXT-White, at least in the first phase of the experiment. It will be based on DATE with the same NEXT-White FEC cards for PMTs and SiPMs. The first version of NEXT-100 will have 60 PMTs and 3584 SiPMs. Given the amount of data the detector will produce, the designed system includes three extra LDCs, each of them with 3 dual optical fiber 1GB ethernet network cards. Therefore, including NEXT-White LDCs, a total of 6 LDCs with 30 data links will be connected to the ATCA. LDCs will send subevents to 4 GDCs that will finish the event building and store the data to disk. There will be an extra node available that could take the role of an LDC or GDC if needed. One extra server will be added in the distributed storage to increase fault tolerance. The space available will be 300 TB. An outline of the system is shown in Figure 4.16.

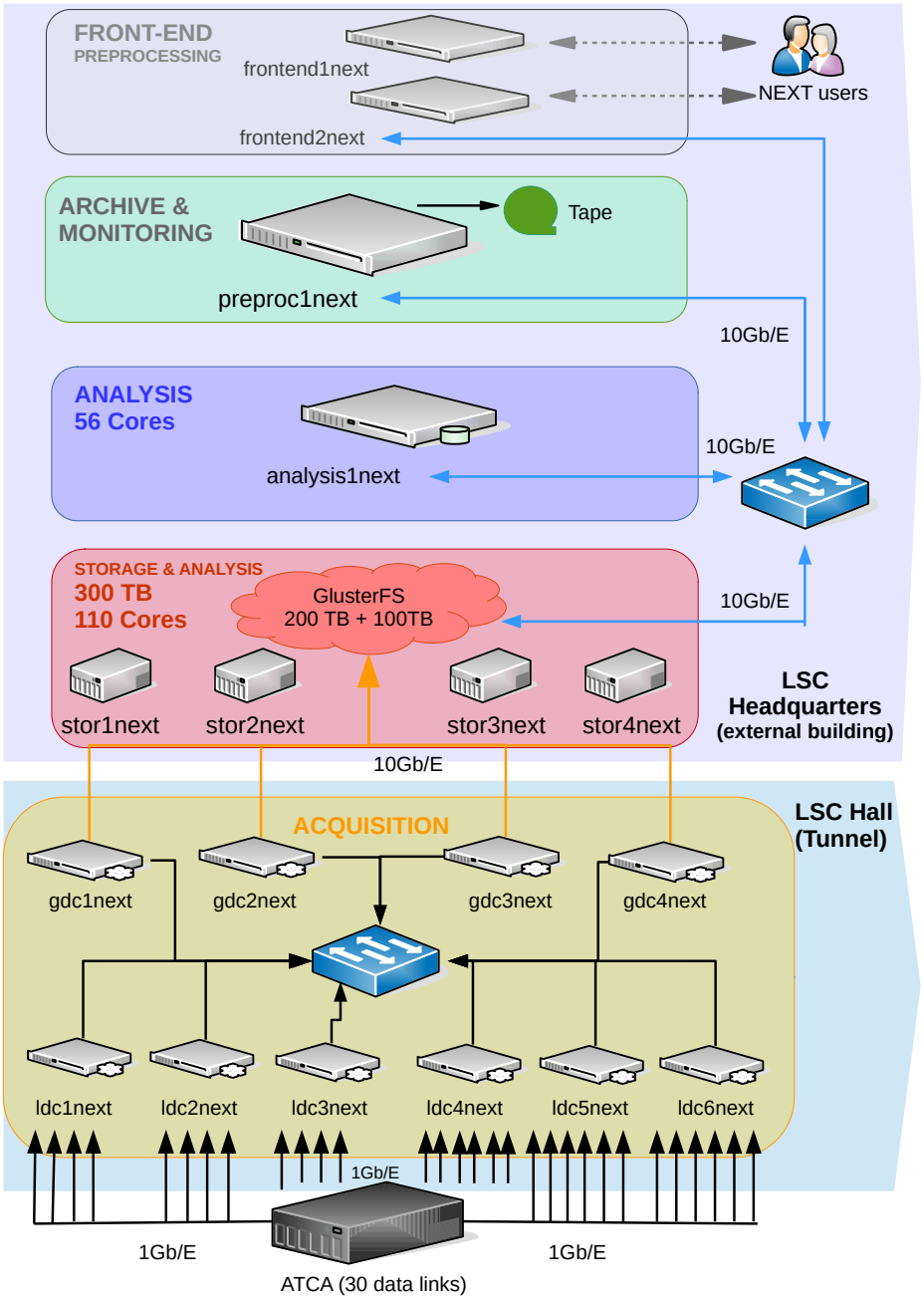

Figure 4.16: DAQ scheme for NEXT100.

5 Neutrinoless $\beta\beta$ searches with NEXT-100

NEXT-100 is a detector devoted to the search of ^{136}Xe $0\nu\beta\beta$ decays. As shown in previous chapters, a low background rate is critical to achieve that goal since different background sources can produce signal-like tracks in the detector.

Electrons propagating in xenon gas leave a characteristic energy deposition pattern. Below their critical energy (12.3 MeV in gaseous xenon [33]) they lose energy via ionization with a more or less constant $\mathrm{d}E/\mathrm{d}x$ until they become non-relativistic. Then, their effective energy deposition rate rises (see Figure 5.1), mainly due to the occurrence of strong multiple scattering, and the particles lose the remainder of their energy in a relatively short distance, generating a *blob*.

In neutrinoless double beta events, two electrons with a total energy of ^{136}Xe $Q_{\beta\beta}$ (2458 keV) are generated from the same vertex. Therefore, they will leave a single track with two blobs at both extremes (see Figure 5.2). The relevance of any potential background source depends on its probability to generate a signal-like track in the active volume with an energy around ^{136}Xe $Q_{\beta\beta}$. In principle, charged particles (muons, betas, etc.) entering the detector can be rejected with very high efficiency by defining a small veto region (a few centimeters) around the boundaries of the active volume. On the other hand, confined tracks produced by external neutral particles, like high-energy gammas or internal contamination in the xenon gas, could lead to a single-track with $Q_{\beta\beta}$ energy. These events, however, could be rejected by analyzing the topology of their energy deposition. Since most of them are single electrons, they will create a track with only one blob in one of the extremes, as shown in Figure 5.2.

In 2015 the NEXT Collaboration published the estimated sensitivity of the detector [174]; later some updates were included in the

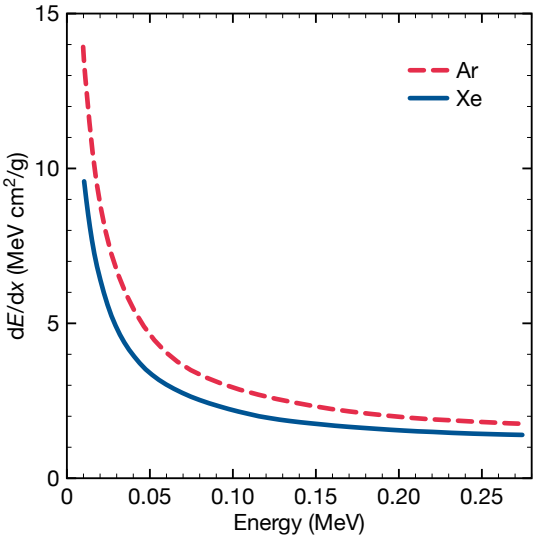

Figure 5.1: Stopping power for electrons in argon and xenon as a function of energy. Note the steep increase in $\mathrm{d}E/\mathrm{d}x$ below 50 keV that results in the end-of-track blobs. Taken from Ref. [59].

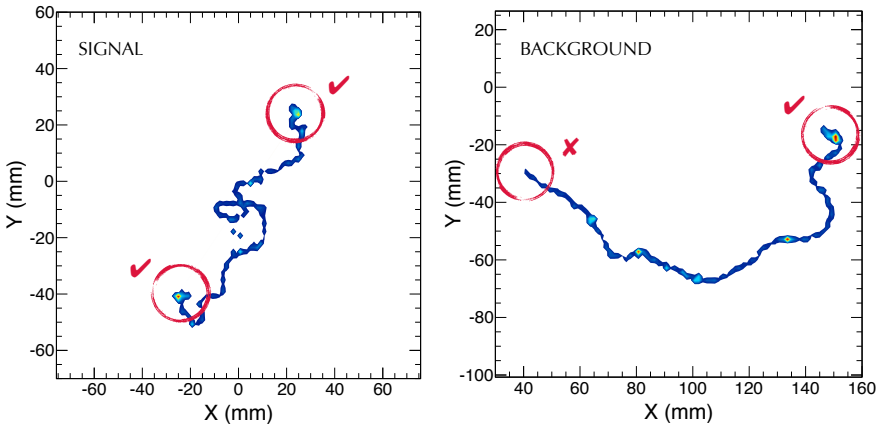

Figure 5.2: Monte Carlo simulation of signal ($0\nu\beta\beta$ decay of ^{136}Xe) and background (single electron of energy equal to the Q value of ^{136}Xe) events in gaseous xenon at 15 bar. The ionization tracks left by signal events feature large energy deposits, or *blobs*, at both ends.

study done in Ref. [175]. Those studies were based on a simplified fast Monte Carlo simulation. In this chapter we assess the precision of those results using a detailed simulation software very similar to the one used for the NEXT-White detector. That software can be validated with data-Monte Carlo comparisons, leading to a more realistic extrapolation for the possible NEXT-100 results.

There are several sources of background for the NEXT experiment, such as radiogenic backgrounds from material contamination, cosmogenic muons, ^{222}Rn activity or neutrons from lab walls. Among them, the radiogenic backgrounds represent 97% of the whole background activity, according to previous studies [175]. Therefore, the analyses in this chapter are focused only on backgrounds of radiogenic origins.

5.1 Radiogenic backgrounds in NEXT-100

Natural radioactivity in detector components is the main source of background in NEXT, as in many other $0\nu\beta\beta$ decay experiments. The $0\nu\beta\beta$ peak of ^{136}Xe ($Q_{\beta\beta} = 2458.1 \pm 0.3$ keV [176, 177]) is between the photopeak of high-energy gammas from ^{214}Bi and ^{208}Tl decays.

From the uranium chain (see Figure 5.3), the daughter of ^{214}Po, ^{214}Bi, has a line at 2447 keV with 1.57% intensity [178] that overlaps with the signal peak even with resolutions as good as 0.5% FWHM [174]. The rest of the lines have very low intensity and are negligible.

From the thorium chain (see Figure 5.4), the decay product of ^{208}Tl, ^{208}Pb, emits a de-excitation photon of 2615 keV with an intensity of 99.75% [178]. Electrons from the photo-peak can lose energy via bremsstrahlung and fall into the region of interest (ROI) around $Q_{\beta\beta}$. Additionally, even though the Compton edge of the 2.6 MeV gamma is well below $Q_{\beta\beta}$ at 2382 keV, the Compton-scattered photon can generate other electron tracks close enough to the initial Compton electron to be reconstructed as a single track with energy around $Q_{\beta\beta}$.

Lower-energy gammas from long-lived radionuclides like ^{60}Co and ^{40}K dominate at energies below 1.5 MeV, well below ^{136}Xe $Q_{\beta\beta}$. Although they are significant for the $2\nu\beta\beta$ measurement, they do not represent a relevant contribution to the $0\nu\beta\beta$ background.

^{214}Bi and ^{208}Tl are present at some level in almost any material. The NEXT Collaboration has done an extensive campaign of material

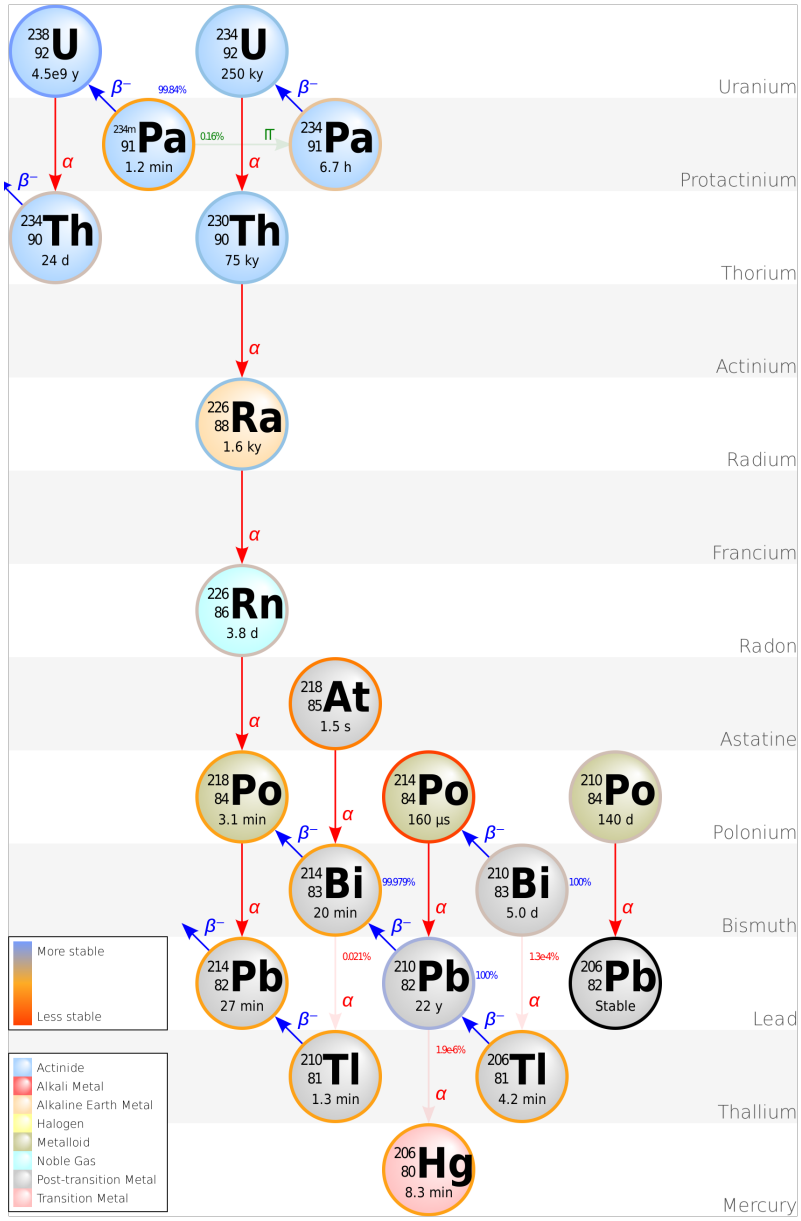

Figure 5.3: Uranium decay series, from ^{238}U to ^{206}Pb [179].

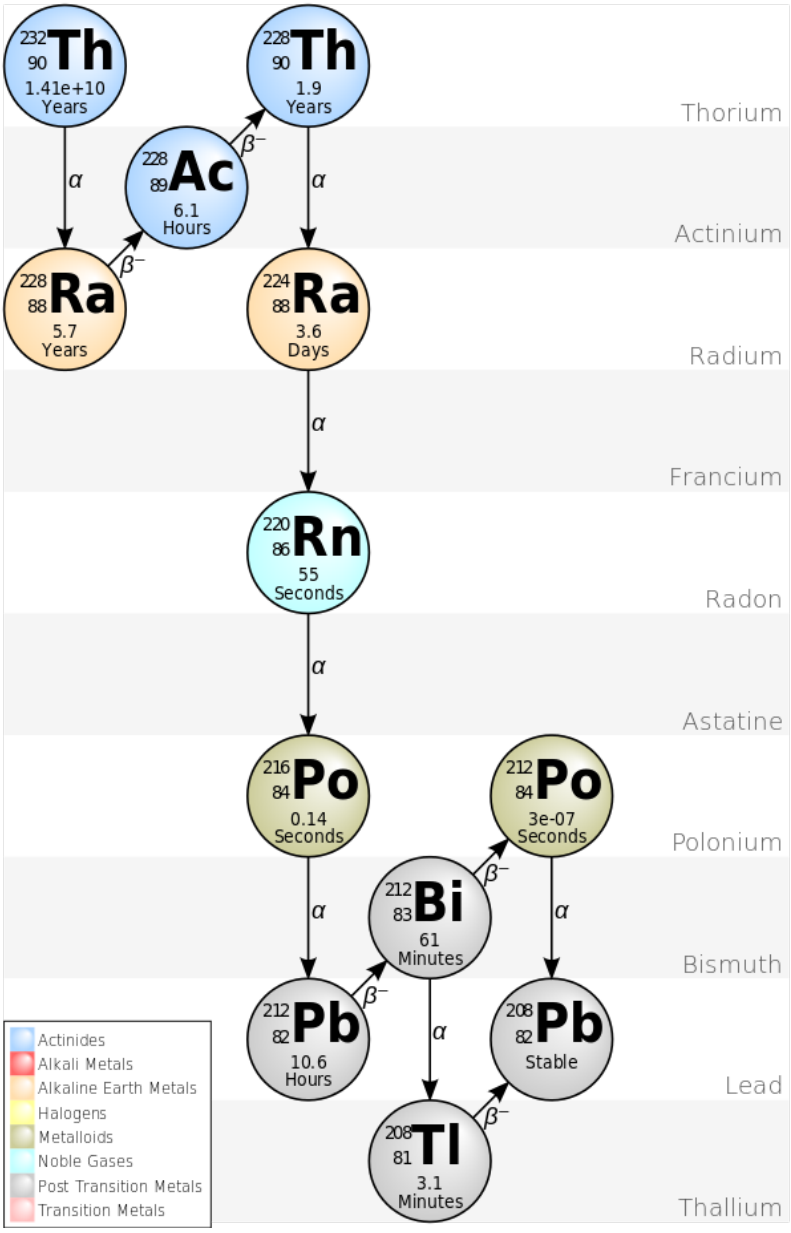

Figure 5.4: Thorium decay series, from ^{232}Th to ^{208}Pb [179].

screening and characterization [138–140, 180–183]. Many activities have been determined using gamma-ray spectroscopy with ultra-low background high purity germanium (HPGE) detectors of the LSC's Radiopurity Service [138]. In some cases, where only upper limits could be set, other techniques like Glow Discharge Mass Spectrometry (GDMS) and Inductively Coupled Plasma Mass Spectrometry (ICPMS) have been used to improve limits of materials, samples of which could be destroyed.

The results of those measurements are presented in the following tables: Table 5.1 shows the ^{214}Bi and ^{208}Tl activities for the materials used in the NEXT100 detector; Table 5.2 includes the total activity for each detector component; and Table 5.3 contains the NEXT100 radioactive budget for each detector subsystem.

In previous studies [174, 175], the radioactivity assumptions used were different from the ones used now. Figure 5.5 shows a comparison between the older version [184] and the current one [185]. The latter has updated materials and measurements taken from NEXT-White components, and some upper limits have been improved to central values as well. In particular, the main differences are in the PMT bases, the Dice Board connectors and the vessel. To achieve better readability, Figure 5.5 does not include the shielding castle activity since it is much higher than the other activities shown. Its activity is now $\sim$10 times higher than its value in the previous analysis: it changed from the previous 530 mBq (5460 mBq) Tl (Bi) to the current 7339.55 mBq (73743.0 mBq) Tl (Bi). This difference is due the inclusion in the model of the steel structure that supports the lead bricks and the anti-corrosion painting on its surface.

Finally, the rock walls of the underground laboratory are an intense source of high-energy gammas due to the presence of radioactive contaminants in their composition. The total gamma flux in Hall A at LSC is 1.06 ± 0.24 cm^{-2} s^{-1}, with contributions from ^{40}K (0.52 ± 0.23 cm^{-2} s^{-1}), ^{238}U (0.35 ± 0.03 cm^{-2} s^{-1}) and ^{232}Th (0.19 ± 0.04 cm^{-2} s^{-1}) [186]. Nonetheless, the external lead shield of NEXT (see Section § 3.4.2) will attenuate this flux by more than 4 orders of magnitude, making its contribution negligible in comparison to that of the detector components.

Material	**Provider**	^{214}**Bi**	^{208}**Tl**	**Units**
Antioxidant	HEMPEL	5.23×10^{4}	4.71×10^{3}	mBq/kg
Connectors FX11LA	Hirose	2.76	2.11	mBq/unit
Copper	Lugand Aciers	1.26×10^{-3}	4.31×10^{-4}	mBq/kg
Dice Boards	Flexiblecircuit	7.00×10^{-2}	1.04×10^{-2}	mBq/unit
Foam joint EDPM	Artein Gaskets	4.30	1.08	mBq/m
Fused silica	Kvartzsteklo	2.10×10^{-1}	3.40×10^{-2}	mBq/kg
HDPE	Simona	$< 6.20 \times 10^{-2}$	$< 7.55 \times 10^{-3}$	mBq/kg
Lead	Britannia, OPERA exp.	3.50×10^{-1}	3.38×10^{-2}	mBq/kg
Optical Gel	Nye Lubricants Inc.	$< 2.20 \times 10$	<6.47	mBq/kg
PMT	Hamamatsu	3.50×10^{-1}	1.90×10^{-1}	mBq/unit
PMT base		7.00×10^{-1}	8.91×10^{-1}	mBq/unit
Resistor HVF 2512 1G	Ohmite	1.79×10^{-2}	3.09×10^{-3}	mBq/unit
Sapphire	Swiss Jewel Company	$< 3.10 \times 10^{-1}$	4.40×10^{-2}	mBq/kg
SiPM	SensL	$< 8.89 \times 10^{-5}$	$< 2.80 \times 10^{-5}$	mBq/unit
Stainless Steel 316L	Radon-free air tubes	< 3.00	< 1.29	mBq/kg
Stainless Steel 316Ti	Nironit	$< 4.60 \times 10^{-1}$	$< 4.31 \times 10^{-2}$	mBq/kg
Steel S275	PRYCON	1.20	1.69	mBq/kg

Table 5.1: ^{214}Bi and ^{208}Tl activities measured for each material used in NEXT-100. Some values are upper limits, and the rest of them are central values.

Detector Subsystem	Material	Provider	Quantity	^{214}Bi (mBq)	^{208}Tl (mBq)
Trk Support	Copper	Lugand Aciers	158 kg	$\mathbf{1.99 \times 10^{-1}}$	$\mathbf{6.81 \times 10^{-2}}$
DB Plug	Connectors FX11LA	Hirose	107 units	$\mathbf{2.95 \times 10^{2}}$	$\mathbf{2.26 \times 10^{2}}$
Dice Board	Dice Boards	Flexiblecircuit	107 units	7.49	1.11
	SiPM	SensL	6848 units	$< 6.09 \times 10^{-1}$	$< 1.92 \times 10^{-1}$
	Total			$\mathbf{< 8.10}$	$\mathbf{< 1.30}$
Carrier Plate	Copper	Lugand Aciers	511.6 kg	$\mathbf{6.45 \times 10^{-1}}$	$\mathbf{2.20 \times 10^{-1}}$
Enclosure Window	Sapphire	Swiss Jewel Company	8.1 kg	< 2.51	3.56×10^{-1}
	Optical Gel	Nye Lubricants Inc	0.1284 kg	< 2.82	$< 8.31 \times 10^{-1}$
	Total			$\mathbf{< 5.34}$	$\mathbf{< 1.19}$
PMT	PMT	Hamamatsu	60 units	$\mathbf{2.10 \times 10}$	$\mathbf{1.14 \times 10}$
PMT Base	PMT base		60 units	$\mathbf{4.20 \times 10}$	$\mathbf{5.35 \times 10}$
Field Cage	Copper	Lugand Aciers	80.4 kg	1.01×10^{-1}	3.47×10^{-2}
	HDPE	Simona	122.7 kg	< 7.61	$< 9.26 \times 10^{-1}$
	Resistor HVF 2512 1G	Ohmite	178 units	3.19	5.50×10^{-1}
	Total			$\mathbf{< 1.09 \times 10}$	$\mathbf{< 1.51}$
Anode Quartz	Fused Silica	Kvartzsteklo	6.85 kg	**1.44**	$\mathbf{2.33 \times 10^{-1}}$
ICS	Copper	Lugand Aciers	8310.1 kg	$\mathbf{1.05 \times 10}$	**3.58**
Vessel	Stainless Steel 316Ti	Nironit	1310 kg	$\mathbf{< 6.03 \times 10^{2}}$	$\mathbf{< 5.65 \times 10}$
Shielding Lead	Lead	Britannia & OPERA	15600 kg	$\mathbf{5.46 \times 10^{3}}$	$\mathbf{5.27 \times 10^{2}}$
Shielding Struct	Antioxidant	HEMPEL	1.296 kg	6.78×10^{4}	6.10×10^{3}
	Steel S275	PRYCON	419 kg	5.03×10^{2}	7.08×10^{2}
	Total			$\mathbf{6.83 \times 10^{4}}$	$\mathbf{6.81 \times 10^{3}}$

Table 5.2: ^{214}Bi and ^{208}Tl activities for each detector component. Some components are made of several materials, and in those cases the total is computed in the final row for each group. Some values are upper limits due to the uncertainties in the measurements.

Table 5.3: ^{214}Bi and ^{208}Tl activities for each detector subsystem. Some values are upper limits.

Volume	^{214} Bi (mBq)	^{208}Tl (mBq)	Total (mBq)
TRACKING PLANE	$\mathbf{< 3.03 \times 10^2}$	$\mathbf{< 2.27 \times 10^2}$	$\mathbf{< 5.30 \times 10^2}$
DB Plug	2.95×10^2	2.26×10^2	5.21×10^2
Dice Board	< 8.10	< 1.30	< 9.40
ENERGY PLANE	$\mathbf{< 6.83 \times 10}$	$\mathbf{< 6.60 \times 10}$	$\mathbf{< 1.34 \times 10^2}$
Enclosure Window	< 5.34	< 1.19	< 6.52
PMT	2.10×10	1.14×10	3.24×10
PMT Base	4.20×10	5.35×10	9.55×10
FIELD CAGE	$\mathbf{< 1.23 \times 10}$	$\mathbf{< 1.74}$	$\mathbf{< 1.41 \times 10}$
Field Cage	$< 1.09 \times 10$	< 1.51	$< 1.24 \times 10$
Anode Quartz	1.44	2.33×10^{-1}	1.67
COPPER SHIELD	$\mathbf{1.13 \times 10}$	**3.87**	$\mathbf{1.52 \times 10}$
ICS	1.05×10	3.58	1.41×10
Tracking Support	1.99×10^{-1}	6.81×10^2	2.67×10^{-1}
Carrier Plate	6.45×10^{-1}	2.20×10^{-1}	8.65×10^{-1}
VESSEL	$\mathbf{< 6.03 \times 10^2}$	$\mathbf{< 5.65 \times 10}$	$\mathbf{< 6.59 \times 10^2}$
SHIELDING	$\mathbf{7.37 \times 10^4}$	$\mathbf{7.34 \times 10^3}$	$\mathbf{8.11 \times 10^4}$
Shielding Lead	5.46×10^3	5.27×10^2	5.99×10^3
Shielding Struct	6.83×10^4	6.81×10^3	7.51×10^4

5.2 The NEXT-100 detector simulation

The detector geometry is implemented in *nexus* [54], a Geant4-based [187] software developed by the NEXT Collaboration. For a variety of reasons, there are some differences between the current design of NEXT-100 and the one originally proposed in the TDR [96]. At the time of this study, the design of NEXT-100 was the one proposed in the TDR [96]. At a later time, some parts of it have been updated, as described in Section § 3.4.3, and therefore there are some differences between these simulations and the current design of the detector. However, preliminary studies of the updated geometry show that a comparable performance can be achieved. In the following, a brief description of the simulation used is described. A schematic of the detector is shown in Figure 5.6.

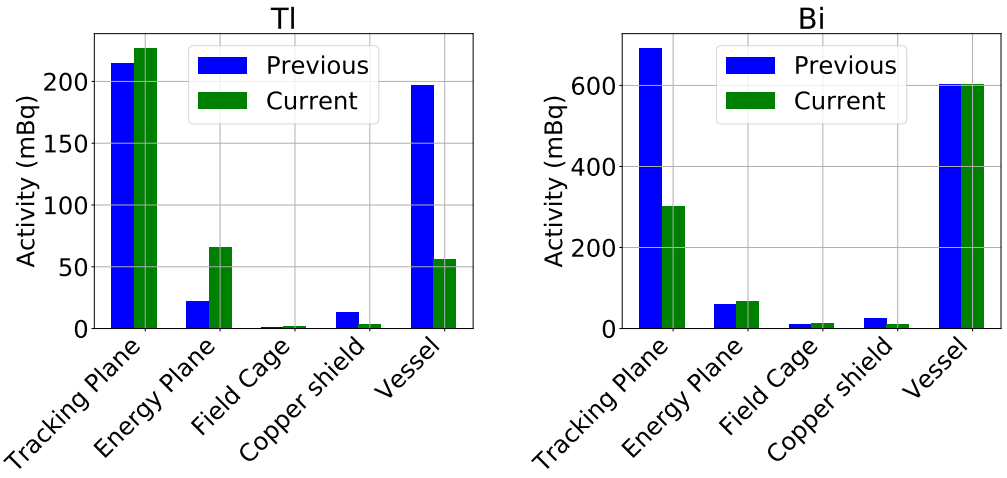

Figure 5.5: Comparison between the activities used in this study (green) and those used in [175] (blue). Shielding is omitted in the plot to improve readability of the remaining volumes.

The active volume is a cylinder of about 1.15 m^3 and can hold around 100 kg of Xe gas at 15 bar. It is surrounded by the field cage, which is a high density polyethylene (HDPE) cylinder of 148 cm length, 107.5 cm inner diameter and 2.5 cm wall thickness that provides electric insulation and supports, in its inner surface, copper rings for electric field shaping. One end of the field cage, the TPC anode, is closed by a 1-cm thick fused-silica window coated with indium tin oxide (ITO) and tetraphenyl-butadiene (TPB). The two other electrodes, EL gate and cathode, are positioned 0.5 cm and 106.5 cm away from the anode, respectively. They are built with a highly transparent stainless steel wire mesh.

The energy plane of NEXT-100 is composed of 60 Hamamatsu R11410-10 PMTs, the same model used in NEXT-White. They are located behind the cathode and offer a 37% coverage. Since they do not withstand the pressure, they have to be sealed into individual pressure-resistant, vacuum-tight copper enclosures coupled to sapphire windows. PMTs and enclosure windows are optically coupled using an optical gel with a refractive index between those of fused

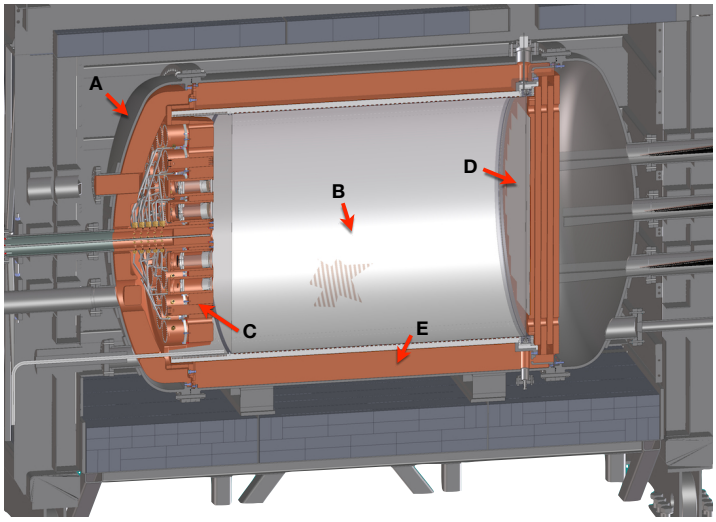

Figure 5.6: Cross-section view of the NEXT-100 detector inside its lead castle shield. A stainless-steel pressure vessel (A) houses the electric-field cage (B) and the two sensor planes (energy plane, C; tracking plane, D) located at opposite ends of the chamber. The active volume is shielded from external radiation by at least 12 cm of copper (E) in all directions.

silica and sapphire. All the copper enclosures are mounted into a carrier plate made of radio-pure copper.

The tracking plane is made of an array of 6848 SiPMs mounted in 107 Kapton boards with 8×8 sensors each, placed at a pitch of 1 cm. They are positioned behind the fused-silica window closing the EL gap. The boards have long tails following a zigzagging path through the copper plate to avoid a straight path for external gammas, and to allow for the placement of the SiPM connectors behind the plate.

The pressure vessel consists of a cylindrical section of 160 cm length, 136 cm inner diameter and 1 cm wall thickness, and two identical torispherical heads of 35 cm height, 136 cm inner diameter and 1 cm wall thickness. It is made of stainless steel Type 316Ti due to its radiopurity. Inside the vessel, surrounding the field cage, there is a set of 12 cm thick copper bars along the drift axis, as well as one 12 cm copper plate for each sensor plane. Finally, the vessel is placed inside

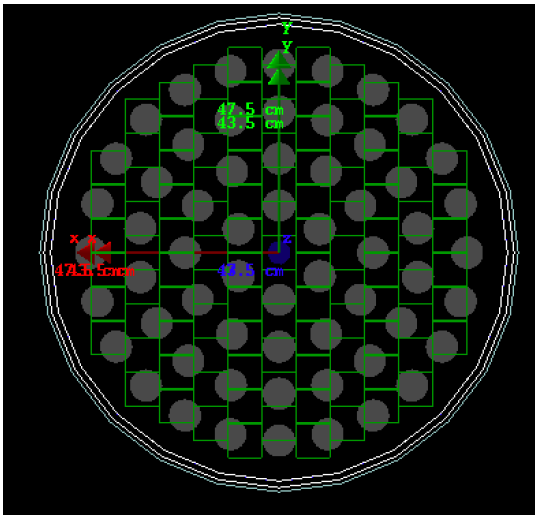

Figure 5.7: Section of the NEXT-100 geometry implemented in nexus. The outer rings represent the vessel and field cage. The 60 gray circles are PMTs and the green-square pattern is the tracking plane. Each green square represents a Dice Board with 64 SiPMs. Notice how the tracking plane does not reach the edge of the vessel.

a 20 cm thick lead shield.

There is an important caveat in this design: the tracking plane does not cover a complete section of the active volume, so many events cannot be reconstructed. Figure 5.7 shows a section of the detector as it is implemented in nexus. As seen, depending on the direction, there are up to 10cm not instrumented with tracking sensors. This limitation has implications for the analysis procedure to be used, as will be shown in the following sections.

5.3 Simulation and classical reconstruction

The simulation for this study includes $\sim 10^{10}$ events generated with nexus from all detector volumes, weighted according to the activity of each component. Nexus simulates the propagation of the particles produced in each event through the different volumes of the detector and calculates the energy deposited in the xenon gas. The simulation

of the sensor response to primary and secondary scintillation are done by the *detsim* package, within the Art framework [167], using a parametrization of the charge recorded by the sensors, extracted from look-up tables [131]. Detsim includes the effects of transverse and longitudinal diffusion in the electron cloud, as well as the EL gain. The values of these parameters have been extrapolated from NEW measurements and are shown in Table 5.4. Detsim also simulates electron attachment, which describes how many electrons are captured by the impurities in the gas along the drift region. This can be modeled as an exponential distribution with a given lifetime, 10 ms in this study, several times the drift time for the whole chamber.

The output of detsim is an HDF5 file with PMT and SiPM waveforms with photoelectrons without any noise. PMT waveforms are binned at 25 ns and SiPM waveforms at 1 μs. Those photoelectron files will be the input for Invisible Cities [165] which will simulate the sensor responses. It adds the effect of single photoelectron resolution for PMTs and SiPM noise using PDFs taken from NEXT-White.

Starting from the PMT and SiPM waveforms, the event reconstruction takes place. The reference system is the natural one for a TPC, with z axis along the drift direction and x and y perpendicular to z creating a right-handed reference frame. Charged particles moving through xenon gas will deposit energy via scintillation and ionization processes. The primary scintillation light (S1) is detected by the PMTs, measuring the initial time of the event (t_0). The ionization charge is drifted by an electric field to the EL region, which is 5 mm wide, where a more intense electric field amplifies the signal, creating the secondary scintillation (S2) signal. The S2 light is read by both PMTs

Table 5.4: Simulation parameters.

Pressure	15 bar
Lifetime	10 ms
EL gain	410 photons/ie
Transverse diffusion	1.072 mm/$\sqrt{\text{cm}}$
Longitudinal diffusion	0.237 mm/$\sqrt{\text{cm}}$

and SiPMs. The PMTs provide a precise measurement of the energy while the SiPMs, placed $\sim$5 mm away from the EL region, reconstruct the position.

S1 and S2 signals are searched for using a peak finder algorithm over the sum of all individual PMT waveforms. Events with one S1 and one or more S2s are selected for track reconstruction.

To eliminate dark current and electronic noise a cut on SiPM charge is applied. Time bins with less than 1 photoelectron (pe) are eliminated, after which the total integrated charge of a SiPM must be at least 5 pe to be considered in the reconstruction. After this cut, SiPM charges are rebinned to 2 µs time slices. A 3D hit is created for each SiPM with a charge larger than 30 pe, with x and y positions set to the position of the SiPM and z equal to the difference between the time of the slice and the time of S1, multiplied by the drift velocity of the electrons in the gas. The purpose of this cut is to alleviate the effect of diffusion by eliminating the charge far from the center of the hit while keeping the information about the position of the source of light.

The energy measured by the PMTs is divided among the reconstructed hits, proportionally to the charge of the SiPMs used to create the hits. In the case of a slice where no SiPM charge is above the minimum threshold, the energy of that slice will be assigned to the closest slice of the same S2.

Once all the hits of a given event are reconstructed, they have to be grouped into tracks. To achieve that, the gas volume is divided into 3D pixels (voxels) with a fixed dimension and with the energy corresponding to the sum of the hits inside each particular voxel. Adjacent voxels are grouped into separated sets using a Breadth First Search (BFS) algorithm. These sets are the particle tracks of each event. The end-point voxels of each track are also identified by the BFS algorithm as the pair of voxels with longest distance between them along the track. A maximum size of the voxels is fixed, but the actual voxel size varies event by event, being optimized according to the distribution of the hits in space. This optimization tries to avoid having voxels with only one hit on a border, as the position of that voxel would not be representative of the charge distribution used to build the voxel. Figure 5.8 shows the hits produced by a ^{208}Tl event and the subsequent voxelization of that event.

The next step is finding two *blobs* for each track. They are defined

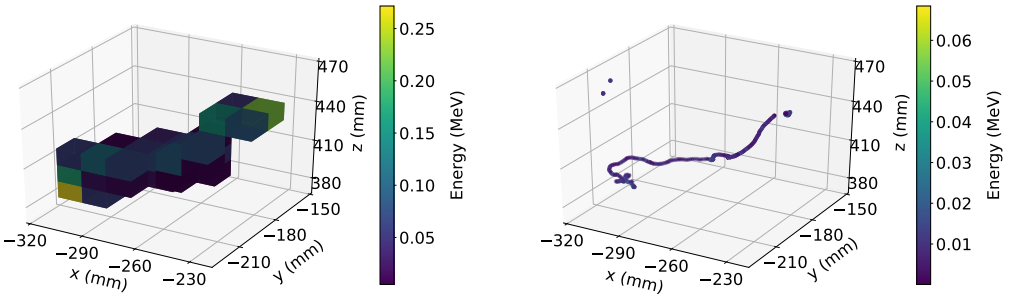

Figure 5.8: Sample event from the simulation. The left panel shows the voxels obtained after the procedure described in the text. The right panel shows the true energy depositions generated in the simulation for the same event.

by summing the energy of the hits contained in a sphere of fixed radius centered on the end-points previously identified with the BFS algorithm. It can happen that hits are included in the blob candidate that are far away from the extreme in terms of distance measured along the track, but have a short Euclidean distance from it (as, for example, in the case of a winding track). In order to avoid this, only the hits belonging to the voxels that have a distance along the track shorter than the radius plus an allowance are considered. The allowance is needed because the voxel position is discretized, and therefore an extra distance equivalent to the size of the voxel diagonal is added to the radius, only for the purpose of selecting the voxels, to ensure that all the hits within the spheres are taken into account correctly. Once the voxel candidates are selected, only the hits belonging to those voxels and that have a Euclidean distance shorter than the radius from the end-points of the tracks are considered for the blob candidates.

Figure 5.9 shows the blob energy distributions for signal and background events. It can be seen that they defined two different populations that, up to a certain level, can be discriminated by setting an energy threshold for the lowest-energy blob. Improving the reconstruction algorithm can lead to a better separation between signal and background events, as will be shown in Section § 5.7.

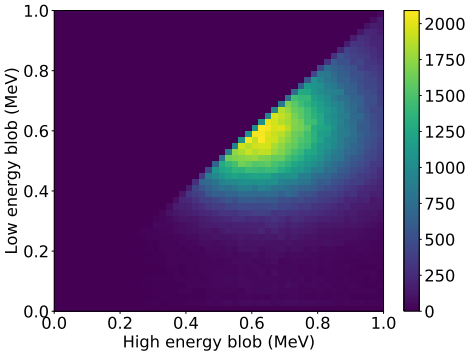

(a) ^{136}Xe $0\nu\beta\beta$ events.

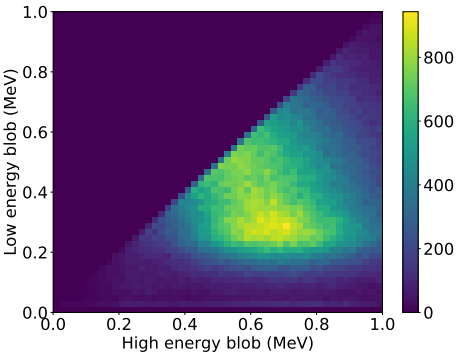

(b) ^{208}Tl events.

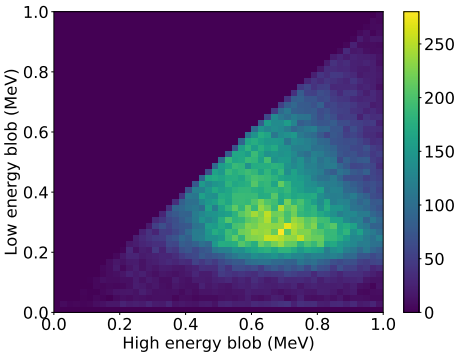

(c) ^{214}Bi events.

Figure 5.9: Distribution of $0\nu\beta\beta$ (top panel), ^{208}Tl (left) and ^{214}Bi (right) events in terms of the energies of the end-of-track blob candidates.

5.3.1 Geometrical and lifetime corrections

The first corrections that must be performed on the data are the geometrical and electron attachment (lifetime) corrections. The geometrical one is related to the fact that PMTs will see a different amount of light depending on where the event has occurred due to factors such as the solid angle or the reflectivity of different surfaces. Electron attachment can be obtained by fitting an exponential to the S2 energy along the z axis and, then, computing normalization factors for each z value according to the curve.

The procedure used in NEXT-White to apply those corrections is to put a ^{83m}Kr source in the gas system to produce low-energy events. These events produce a gamma of 41.5 keV that can be considered as a point-like event, giving us a perfect tool to characterize the behavior of the chamber. After reconstructing them, an XY-map can be produced with the geometrical correction factors and the corresponding lifetime for each bin [131]. In principle, the same procedure is expected to be used in NEXT-100, therefore a simulation of several millions of ^{83m}Kr has been done to compute the correction maps in the same way.

Figure 5.10 shows the geometrical and lifetime Kr maps, as well as a fit of the ^{83m}Kr peak with a resolution of 3.11% FWHM. The precision of these maps is high ($\sim$0.13% for the geometrical map and $\sim$1.5% for the lifetime map). The areas with larger uncertainties are those on the borders of the active volume, where the light collection varies more abruptly and the lower number of events in those areas affects the lifetime fit. Since a fiducial cut is imposed, these larger uncertainties do not pose a problem.

5.3.2 Analysis cuts

Once the reconstruction is done, the analysis includes the following steps:

1. **Fiducial cut**: Select events with no hits outside a fiducial region, defined as $z_{\text{min}} > 20$ mm, $z_{\text{max}} < 1280$ mm and $r_{\text{max}} < 400$ mm. The tight fiducial cut in r is due to the tracking problem explained in Section § 3.4.2.

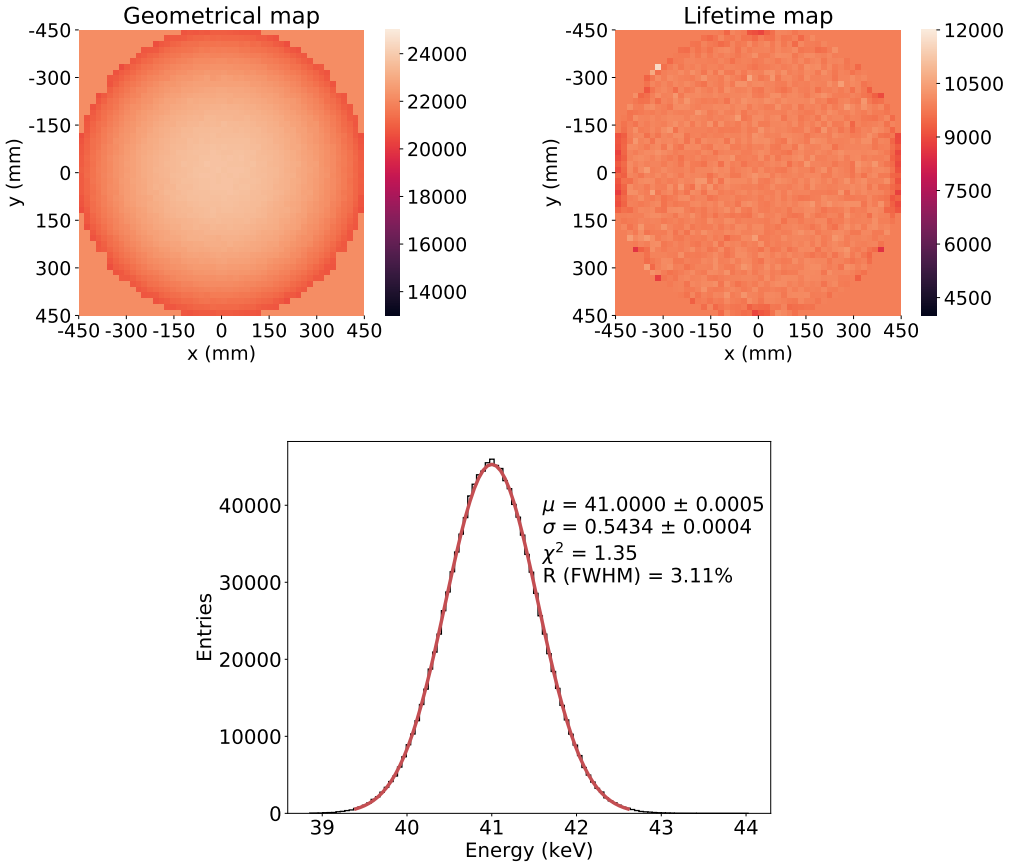

Figure 5.10: Upper left: geometrical map of detector response. Upper right: lifetime map in μs. Down: fit of the ^{83m}Kr peak with a resolution of 3.11% FWHM.

2. **Broad energy cut**: Select events whose energy is between 2.4 and 2.5 MeV.

3. **1-track filter**: Select events with only one reconstructed track.

4. **Region of Interest (ROI)**: Select events in a narrow region of interest near $Q_{\beta\beta}$, whose energy is in: $E \in [2.448, 2.477]$ MeV.

5. **Blob 2 cut**: Select events having more energy than a given threshold in the lowest-energy blob.

The efficiency ε of each of those steps is defined as the fraction of events that fulfill the conditions impose by each filter. Therefore, for signal events the aim is to achieve the highest efficiency possible, while for background events the objective is to minimize the efficiencies.

Figure 5.11 shows the energy resolution for the ^{136}Xe peak after fiducial and 1-track cuts. The obtained value (0.42%) is close to the intrinsic resolution achievable in a xenon gas detector.

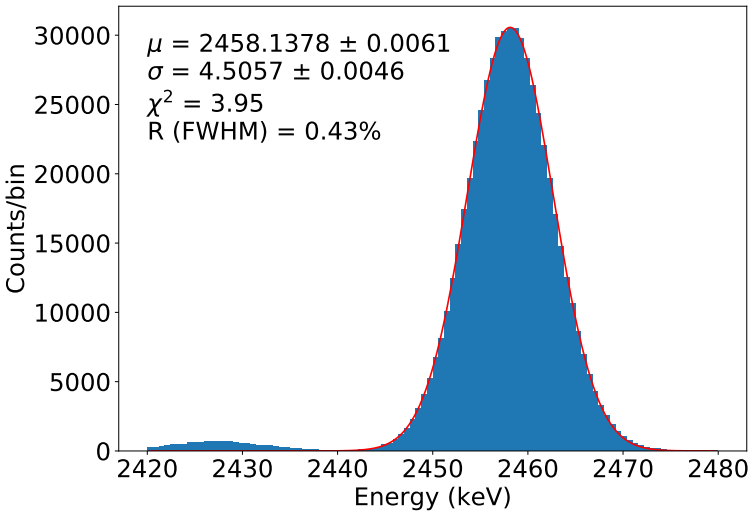

Figure 5.11: Energy resolution for $0\nu\beta\beta$ events from ^{136}Xe after fiducial and single-track cuts have been applied.

5.3.3 Topological optimization

The blob cut has several parameters to be optimized. Taking the NEXT-White analysis as a reference, the voxel sizes used are 10, 12 and 15 mm, while the blob radius varies between 15 and 33 mm with a step of 3 mm. According to Eq. 2.9, the maximization of the ratio $s/\sqrt{b}$ —where s is the signal efficiency and b is the background efficiency—optimizes the experimental sensitivity to $m_{\beta\beta}$. Therefore, the figure of merit defined to evaluate the performance of each configuration is defined as f.o.m. $= s/\sqrt{b}$ and is computed varying the energy threshold for the second blob. Figure 5.12 shows the maximum of the f.o.m. for each pair of values, showing that the best are 15 mm voxel size and 27 mm

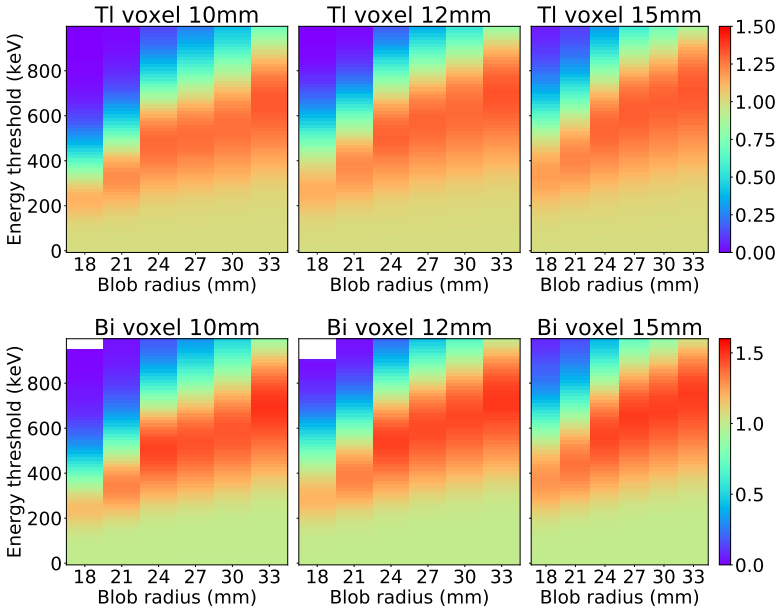

Figure 5.12: Blob energy cut optimization for the classical algorithm. Each plot shows the figure of merit ($s/\sqrt{b}$) of the blob cut for a given configuration. On the x axis different blob radii are shown, and on the y axis the energy threshold for the lower-energy blob is shown. The first row is for ^{214}Bi events, and the second row for ^{208}Tl events. Each column corresponds to a voxel size of 10, 12 and 15 mm, respectively.

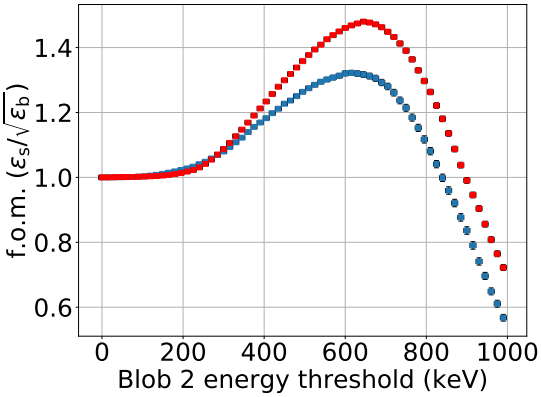

Figure 5.13: Figure of merit using classical reconstruction for ^{214}Bi (red) and ^{208}Tl (blue) events with 15 mm voxels and a blob radius of 27 mm.

blob radius. Figure 5.13 displays the f.o.m. curves for those selected values. Setting the threshold at 675 keV (near the f.o.m. peak) a signal efficiency of 72.0% is achieved for a background acceptance of 20.4% in ^{214}Bi events and 30.4 in ^{208}Tl events. The figure of merit for NEXT-100 with this algorithm is 1.47 in ^{214}Bi and 1.30 in ^{208}Tl, indicating there is some problem with the latter reconstruction and analysis.

In a previous study performed with NEXT-White, a comparison between data and Monte Carlo was done using events from the ^{208}Tl double escape peak. The energy of the blobs was rescaled in the simulation by a constant factor, to match the distribution found in the data. Having calibrated the Monte Carlo with the data, an extrapolation to the $0\nu\beta\beta$ region was carried out using ^{208}Tl events generated from the light tube that surrounds the active volume and $0\nu\beta\beta$ decays of ^{136}Xe in the active volume. Using the same classical analysis described in this section, a signal efficiency of 71.5% with a background acceptance of 13.6% were found, corresponding to a figure of merit of 1.58 [136]. Figure 5.14 shows the signal efficiency as a function of background rejection for both detectors. It can be clearly seen that NEXT-White is working better as for the same background level it has a higher signal efficiency.

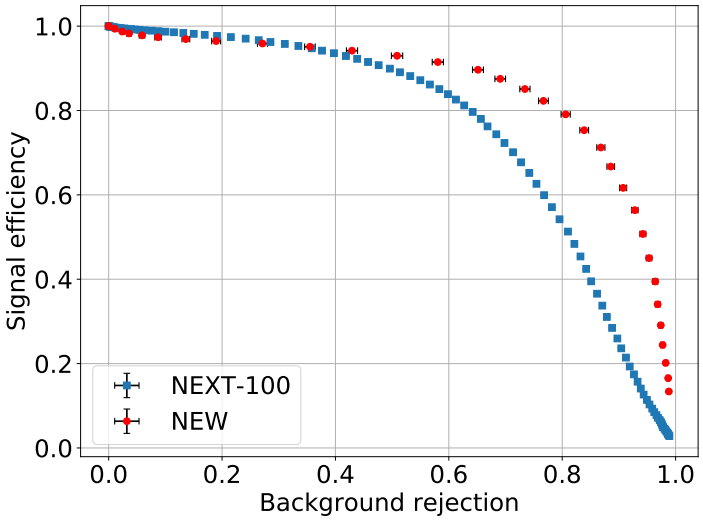

Figure 5.14: Signal efficiency as a function of background rejection. This plot is obtained by varying the required minimum energy of the *blob candidate 2* for events in the $0\nu\beta\beta$ region.

5.4 FANAL

The software used in previous studies [174, 175] is FANAL, which stands for Fast Analysis and is a simplified way of estimating the performance of a detector. In the fast analysis, the sensor response is not simulated, and therefore it is not analyzed to provide a reconstruction, but the true MC information of the deposited energy is used, with some smearing to make it more realistic. The same files produced for the current study have been run through FANAL to get a performance baseline to which the new results can be compared. The FANAL analysis flow is the following:

1. **Read MC hits**: Read all energy depositions (hits) stored in the Monte Carlo files. This information is the truth from the nexus simulation, and no noise has been added nor effects of electron drifting or diffusion.

2. **Fluctuate energy**: Each event energy is varied following a gaussian distribution with a sigma corresponding to the energy resolution of the detector.

3. **Voxelize hits**: The energy depositions are voxelized with a given voxel size. This step simulates the effect of position resolution.

4. **Track reconstruction**: Voxels are grouped into separated sets using a BFS algorithm. These sets of voxels are regarded as the particle tracks of the event.

The same optimization procedure has been applied to obtain the best topological parameters for this algorithm. Figure 5.15 shows the figure of merit for each voxel size, blob radius and energy threshold.

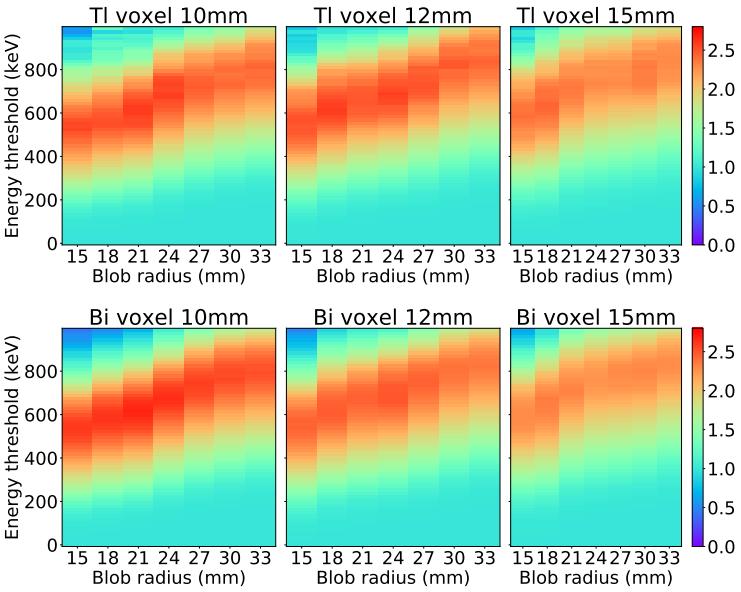

Figure 5.15: Blob energy cut optimization for the FANAL algorithm. Each plot shows the figure of merit ($s/\sqrt{b}$) of the blob cut for a given configuration. On the x axis different blob radii are shown, and on the y axis the energy threshold for the lowest-energy blob is shown. The first row is for ^{214}Bi events, and the second row for ^{208}Tl events. Each column corresponds to a voxel size of 10, 12 and 15 mm, respectively.

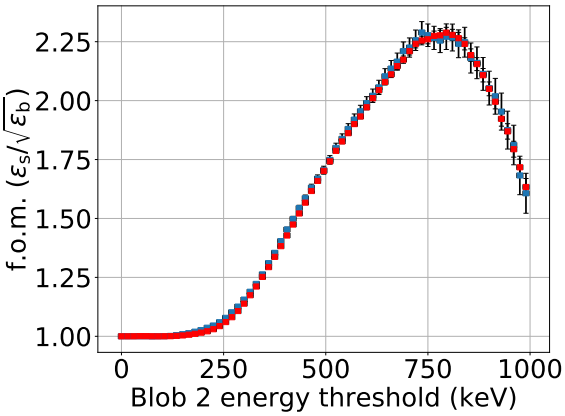

Figure 5.16: Figure of merit using FANAL for ^{214}Bi (red) and ^{208}Tl (blue) events with 10 mm voxels and a blob radius of 21 mm.

In this case, values obtained for the f.o.m. are much higher than those seen in Section § 5.2 for the classical reconstruction. Figure 5.15 shows the maximum value of the f.o.m. for each pair of values. Within the space of parameters, FANAL works best with 10 mm voxels and a blob radius of 21 mm. Figure 5.16 displays the f.o.m. curves for those values as a function of the energy cut of the lowest-energy blob. Setting the threshold at 735 keV, a signal efficiency of 85.2% is achieved for a background acceptance of 16.6% yielding a f.o.m of 2.09.

5.5 The problem of diffusion

Most of the difference between the results obtained with FANAL and the classical algorithm is explained by the inclusion of diffusion in the latter. Diffusion spreads the charge in three dimensions as it drifts towards the anode, creating several problems for the reconstruction and analysis of events. The most important of them is that the 30 pe cut applied to each individual SiPM, for long-drift events, can remove completely secondary tracks created by lower-energy particles, giving a false positive in the one-track filter. This effect is expected to be more important in ^{208}Tl events, as they frequently contain lower-energy

secondary gammas, which are rare for ^{214}Bi events.

Figure 5.17 shows the efficiency of the one-track cut for ^{208}Tl events from different volumes. The first three volumes are the enclosure windows (the sapphire windows that separate the high pressure region from the PMTs), the PMTs, placed just behind them, and the PMT bases, which are behind the PMTs. These volumes are all sources of background events occurring at high drift (high z). The fourth volume contains the dice boards, which produce background events very close to the anode (low z).

We are also comparing three different analyses in Figure 5.17: 1) FANAL, which does not simulate diffusion, 2) Full simulation including diffusion (with the values in Table 5.4), and 3) Full simulation without diffusion. The effect that is clearly shown is that the 1-track cut efficiency is quite similar for the two cases without diffusion but very different for high-drift volumes when diffusion is simulated, in which case it is significantly higher.

To understand that difference we have to take into account how

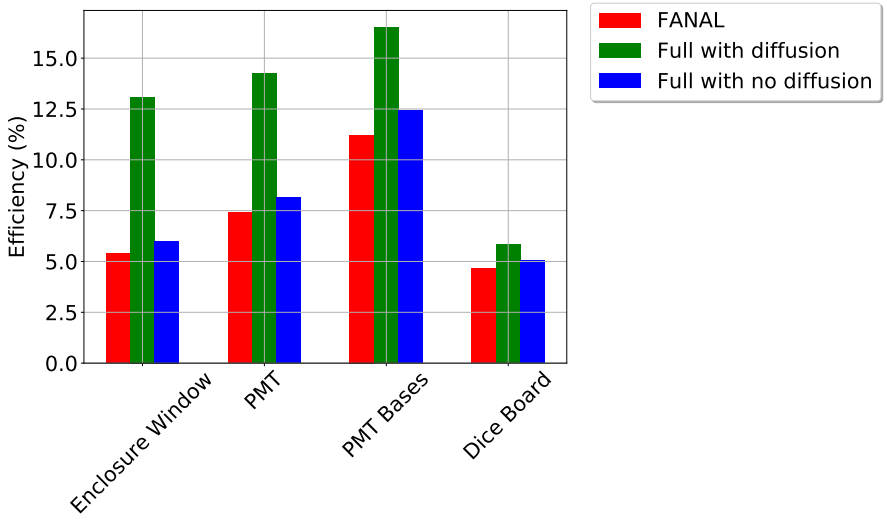

Figure 5.17: Efficiency of 1-track cut for ^{208}Tl events originating in different volumes. Enclosure Window, PMT and PMT Base are high-drift volumes situated in the Energy Plane, while Dice Board is a low-drift volume in the Tracking Plane.

^{208}Tl decays: it has a 2615 keV gamma, accompanied by a 511 keV gamma in 20% of the cases and a 585 keV gamma in 85% of the cases. If a ^{208}Tl decay occurs near the anode (low drift), diffusion does not come into play and the 30 pe cut per SiPM in the reconstruction is low enough not to remove any secondary particle, which is why the efficiency of the 1-track cut is very similar for the three simulations in the Dice Board volume. The opposite happens in the volumes from the Energy Plane (high drift), where diffusion strongly affects the spatial charge distribution, and the 30 pe per SiPM cut can remove secondary particles as if they were noise, giving the false impression that the event contains a single track while it does not.

It can be seen as well in Figure 5.17 that the 1-track cut efficiency follows also this additional pattern: Enclosure Window < PMT < PMT Bases, being lower for volumes closer to the active region. This fact can be understood since gammas produced farther from the active volume have to cross more materials, and therefore secondary gammas have a higher probability of being absorbed before reaching the gas. Thus, farther volumes produce a higher proportion of single-track events. Also, the higher the efficiency, the more similar the three simulations are, because for genuine 1-track events diffusion does not play a role.

False positives in the single-track cut are not the only (negative) effect that diffusion has in the analysis. It blurs the whole event and makes it more difficult to find the ends of the track and measure properly their energy. This can be seen in Figure 5.18, where the same event is shown after full simulation with and without diffusion as well as the FANAL version. The version with diffusion has lost secondary tracks, while the one without it has preserved them, being more similar to the FANAL result. Among the three versions, FANAL offers the sharpest track.

There are two possible strategies to mitigate the effect of diffusion, which lead to two additional analyses:

- Lower the threshold for the individual SiPM charge cut. The purpose of such a high cut was to improve the efficiency of the lowest-energy blob cut, since a *cleaner* track makes it easier to find the extremes. This strategy creates the need for a dual cut analysis, since a lower-energy cut is needed for the single-track cut while a higher-energy cut is needed for the blob energy cut.

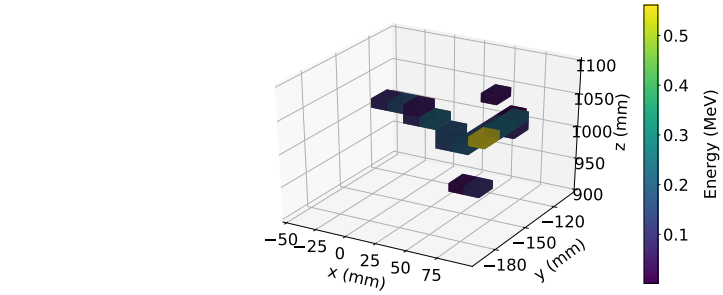

(a) FANAL

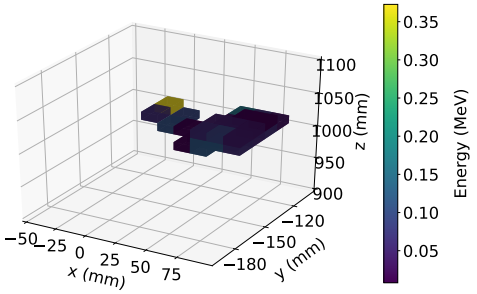

(b) Full simulation with diffusion

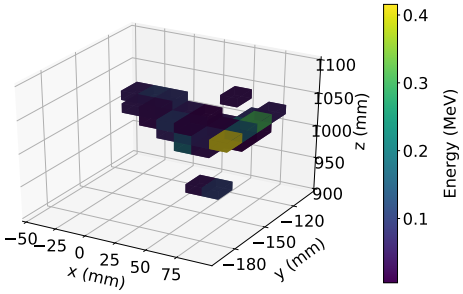

(c) Full simulation without diffusion

Figure 5.18: All panels show the same event, the top one reconstructed with FANAL, without diffusion; the bottom ones using the full simulation with and without diffusion. Notice how the secondary tracks disappear when the diffusion is added.

- Try to deconvolve diffusion using a Richardson-Lucy algorithm. This requires the generation of a Point Spread Function (PSF) to describe the effect of diffusion.

5.6 Dual cut analysis

We start this Section examining the effect of the 30 pe SiPM charge cut on the single-track cut in the presence of diffusion. We thus evaluate how the signal efficiency of the single-track cut changes with different SiPM energy thresholds between 0 and 30 pe.

For a low-drift volume (near the anode), such as Dice Board, there

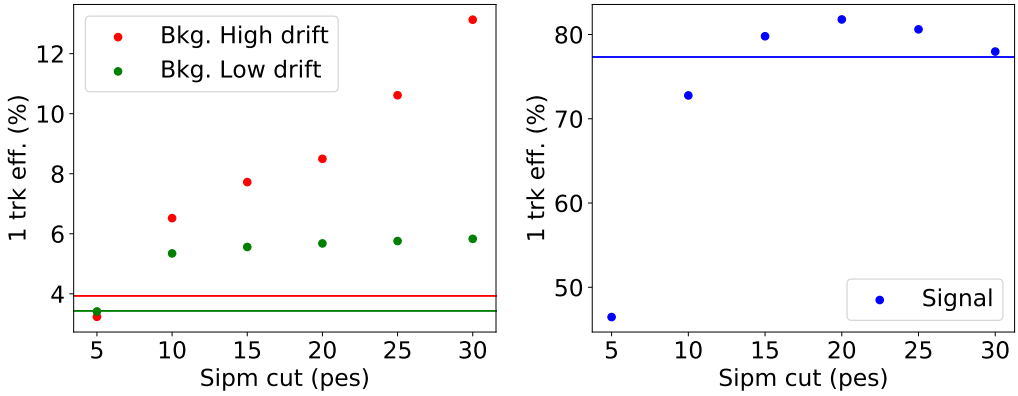

Figure 5.19: Efficiency of single-track cut for different individual SiPM charge thresholds. Horizontal lines are the efficiency in FANAL while the dots corresponds to the full simulation. Left panel: ^{208}Tl events generated in both high-drift (Enclosure Window, red) and low-drift (Dice Board, blue) regions. Right panel: signal events of ^{136}Xe generated in the active volume.

should not be a strong dependence between the charge threshold and the cut efficiency: the signal produced in the SiPMs by secondary gammas is high enough that even high SiPM charge thresholds would not affect their reconstruction. On the other hand, for a high-drift volume (near the cathode), such as Enclosure Window, the efficiency should be higher for higher thresholds as a multi-track event would lose its secondary tracks, passing as a false-positive single-track event. Those effects are shown in Figure 5.19, where the efficiency is flat for low-drift events and grows with the charge cut for high-drift events. In the case of signal events, the efficiency stays around 75-80% for all thresholds except 5 pes. The lowest cut is not enough to remove all the noise and spurious depositions, leading to false negatives in the 1-track filter that decrease the efficiency.

Lowering the SiPM charge threshold can also have an effect on the efficiency of the second blob energy cut. At the topology level, a higher cut can lead to cleaner tracks, where finding the extremes is easier. Figure 5.20 shows the signal efficiency of the cut for different

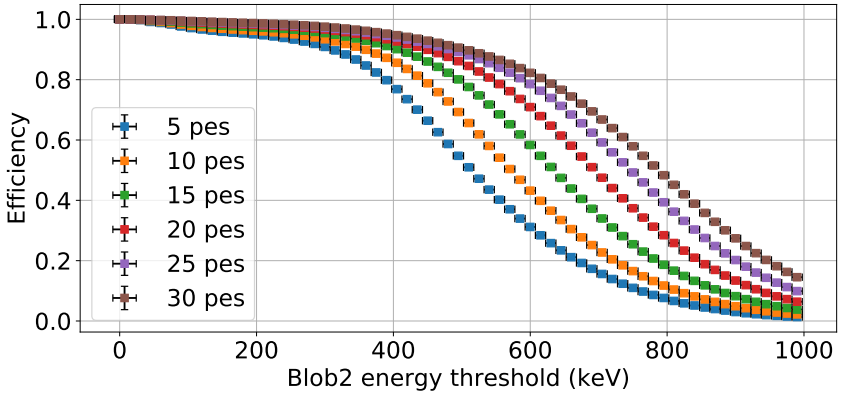

Figure 5.20: Second blob energy threshold cut efficiency for signal events.

charge thresholds. As can be seen, the efficiency is higher for higher cuts, proving that a higher SiPM charge cut increases the efficiency of the second blob energy cut.

These facts lead to a strategy in which a first low charge threshold is used to assess the single-track cut and, then, a higher one for the blob cut. According to Figure 5.19, the optimal value for the first cut should be between ∼10 to 15 pe. This procedure raises some concerns, as it could happen that some events pass the single-track filter with a low SiPM charge threshold, but a higher one could disconnect the track and break it into a multi-track event. Figure 5.21 shows the proportion of events under each of these circumstances. In general, a large proportion of events (30-50% depending on the volume for background and 20% for signal) become single-track events with the lower cut but not with the higher one. In this study, only those events that are single-track with both cuts are considered for the rest of the analysis.

Having seen that the optimal cut for the single-track filter seems to be in the 10 to 15 pes range, we have evaluated the performance of different cut levels: 8, 10, 12 and 15 pes. To do this, the final step is to compute the figure of merit of the single-track and blob cuts, both separately and combined, to assess which is the best combination of

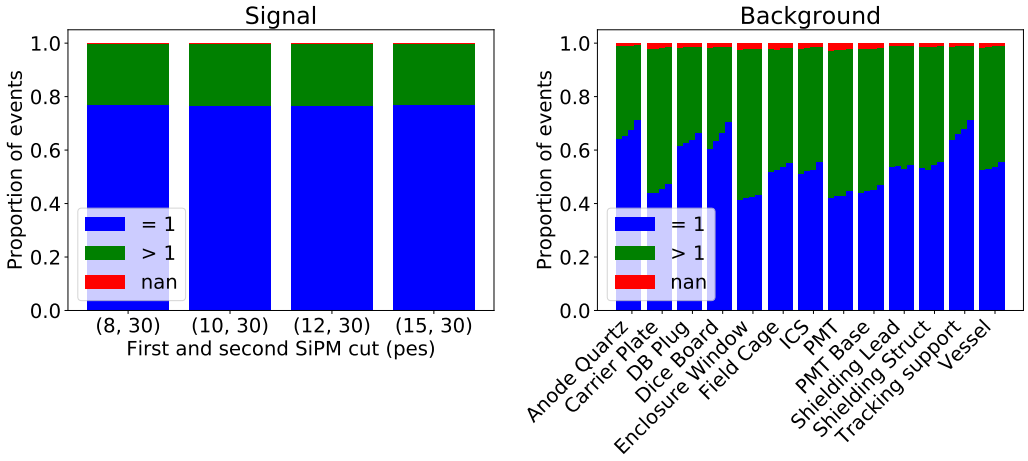

Figure 5.21: Left panel: proportion of signal events that are single-track for different first low cuts (8, 10, 12 and 15 pe) and single or multi-track for a second higher cut of 30 pe (in blue and in green respectively). Right plot: the same for background events (Tl) shown for different origin volumes. Each volume displays 4 subcolumns corresponding to a first cut of 8, 10, 12 and 15 pe, from left to right. Events that are filtered out by the energy filter after passing the single-track cut are shown in red.

thresholds for individual SiPM charge. Figure 5.22 shows how the figure of merit for the single-track cut slightly increases for higher SiPM charge threshold values. The variation is much more subtle for the blob cut, as shown in Figure 5.23, which is expected, taking into account that this cut depends mostly on the second, higher SiPM charge cut, which is constant at 30 pe. Combining both the single-track and blob cuts, a stronger difference can be seen in the f.o.m., as shown in Figure 5.24. The optimal set values for the dual cut strategy are a first cut at 15 pe and a second one at 30 pe.

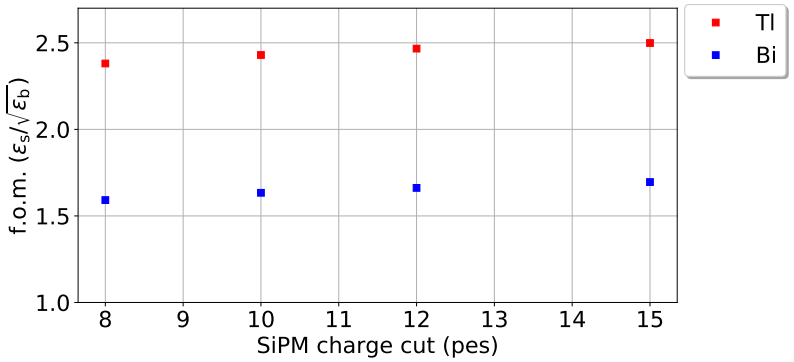

Figure 5.22: Figure of merit ($s/\sqrt{b}$) of the single track cut for different individual SiPM charge thresholds. The red points correspond to ^{208}Tl events and the blue points to ^{214}Bi events.

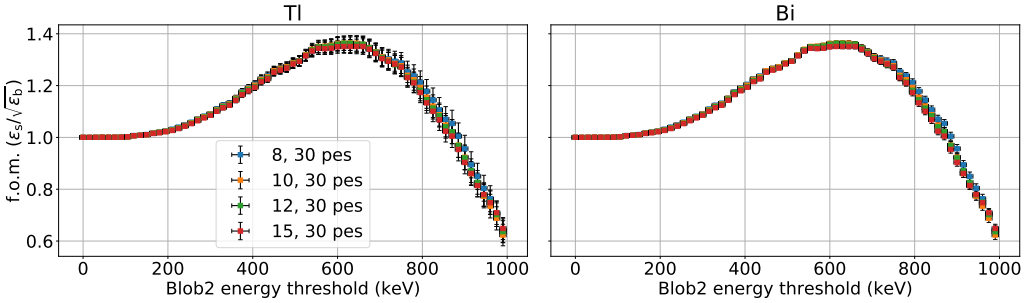

Figure 5.23: Figure of merit ($s/\sqrt{b}$) of the second blob energy cut for different pairs of thresholds for SiPM charge. The first value (8, 10, 12, 15 pe) is used to assess the single-track filter and the second one, fixed to 30 pe, for the blob cut. The left panel corresponds to ^{208}Tl events and the right panel to ^{214}Bi events.

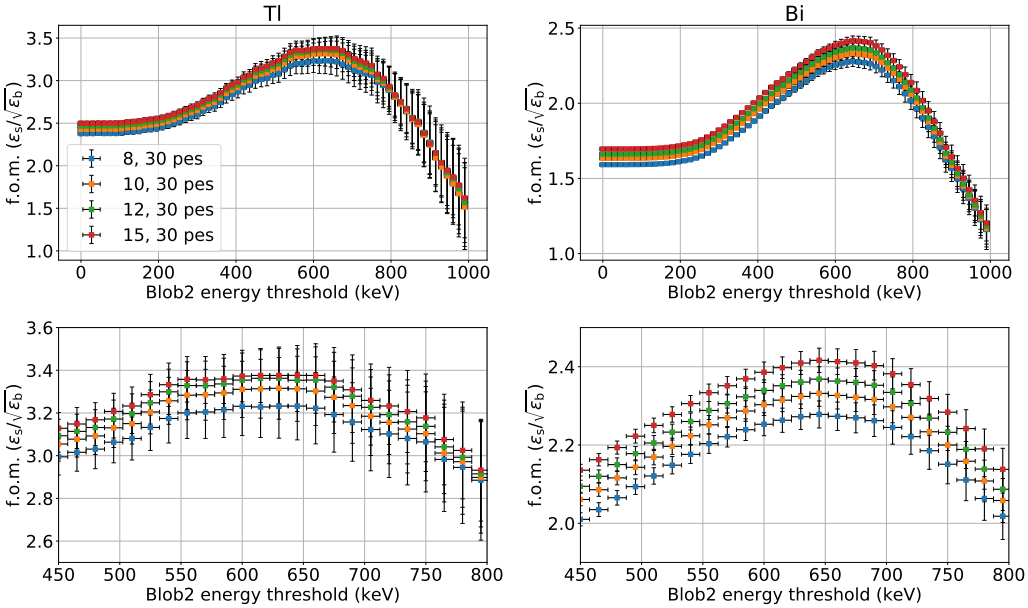

Figure 5.24: Figure of merit ($s/\sqrt{b}$) of single-track and second blob energy cuts combined for different pairs of thresholds for SiPM charge. The first value (8, 10, 12, 15 pe) is used to assess the single-track filter and the second one, fixed to 30 pe, for the blob cut. The left panels correspond to ^{208}Tl events and the right panels to ^{214}Bi events. The second row is a zoom of the peak region.

5.7 Richardson-Lucy deconvolution

The Richardson-Lucy algorithm is an iterative procedure with the aim of recovering an underlining image that has been blurred by a known Point Spread Function (PSF) [188, 189]. It can be expressed as

$$\hat{f}_0(x,y) = g(x,y)\,, \tag{5.1a}$$

$$\hat{f}_{k+1}(x,y) = \hat{f}_k(x,y)\left[h(x,y) \otimes \frac{g(x,y)}{h(x,y) \otimes \hat{f}_k(x,y)}\right]\,, \tag{5.1b}$$

where g is the observed image (the SiPM response), f is the ideal image (reconstructed image) and h is the PSF.

One fundamental input for this algorithm is the PSF, which can be computed using ^{83m}Kr events. The procedure consists of reconstructing the ^{83m}Kr as a point-like event and then computing a 2D map with the XY-distances from each SiPM to the event position and the fraction of total charge read by each sensor.

One way of modeling the diffusion with PSFs is dividing the detector in z-bins and computing one PSF for each bin. Therefore, only ^{83m}Kr events within each particular bin are taken into account for each PSF. Later, upon reconstruction, depending on the z position of each particular hit, a different PSF would be used. In this study 52 z-bins have been computed, each one with its own PSF. Figure 5.25 shows two of them, one near the anode, rather focused, and the other one near the cathode, much wider, showing clearly the effect of diffusion

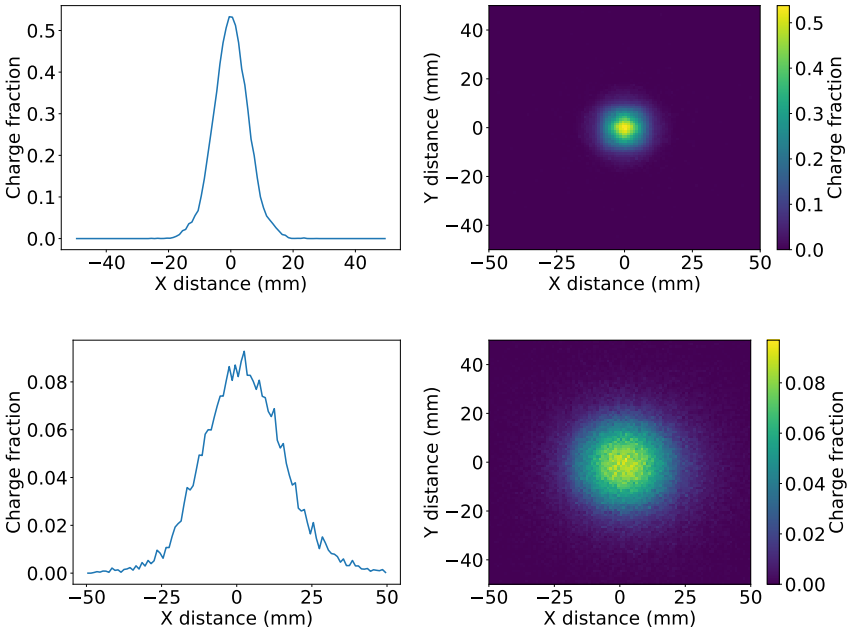

Figure 5.25: PSFs for two different z bins. The upper row plots are for a bin centered at z=37.5 mm and the lower row at z=1037.5 mm. The left column shows the X projection of the 2D maps and the right column shows the maps themselves.

along the chamber.

This algorithm allows for a smaller voxel size, since it can better reconstruct the energy depositions. For this study a voxel size of 5 mm has been used. An example of the finer reconstruction achieved with the Richardson-Lucy algorithm with respect to the classical reconstruction is shown in Figure 5.26.

Figure 5.27 shows the blob energy distributions for signal and background. The populations are much different than the ones obtained with the classical analysis (see Figure 5.9), suggesting that the reconstruction method is working better than the classical one. This is

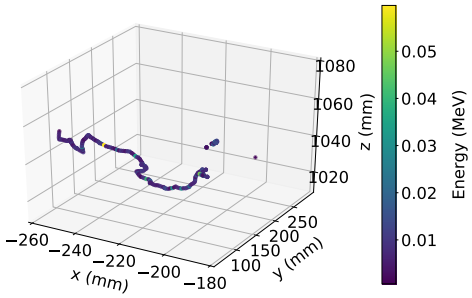

(a) Monte Carlo energy depositions.

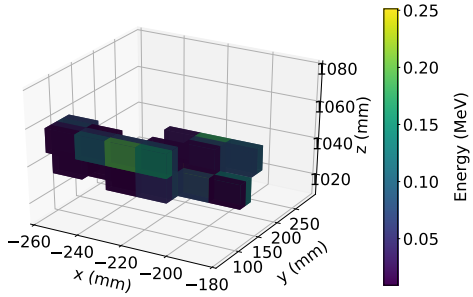

(b) Classical reconstruction

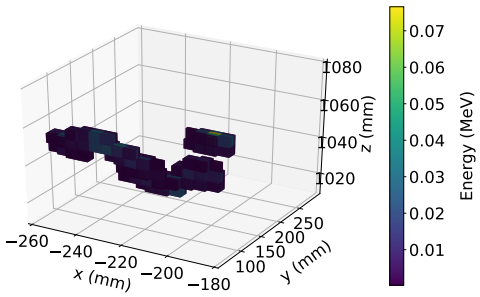

(c) R-L reconstruction

Figure 5.26: All panels show the same ^{208}Tl event. The top panel shows the Monte Carlo energy depositions, and the bottom row shows a comparison of the voxels obtained with the classical analyis and with the Richardson-Lucy reconstruction.

reflected as well in the figure of merit of the second blob energy cut for ^{208}Tl and ^{214}Bi events, shown in Figure 5.28. The maximum value of the f.o.m., around 2.25, is larger than that achieved by the other reconstruction methods.

The best value of the threshold is chosen with the requirement that it lies in an interval for which the figure of merit is within 10% of the maximum and that the minimum amount of signal is lost. Following this criterium, the energy threshold chosen is 480 keV.

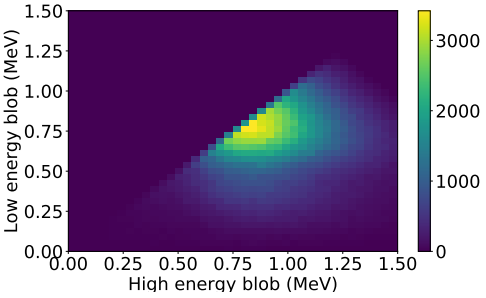

(a) ^{136}Xe $0\nu\beta\beta$ events.

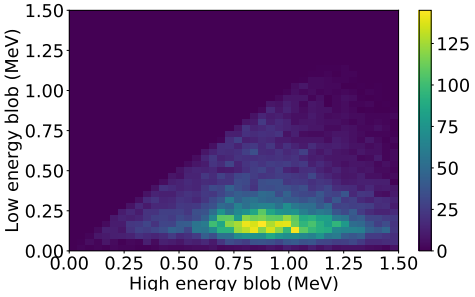

(b) ^{208}Tl events.

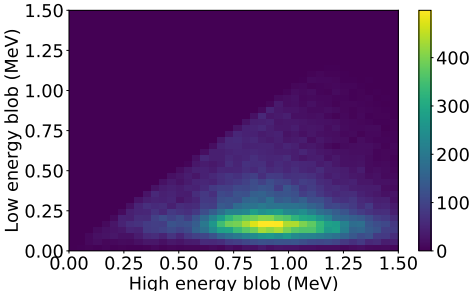

(c) ^{214}Bi events.

Figure 5.27: Distribution of $0\nu\beta\beta$ (top panel), ^{208}Tl (left) and ^{214}Bi (right) events in terms of the energies of the end-of-track blob candidates using the Richardson-Lucy reconstruction.

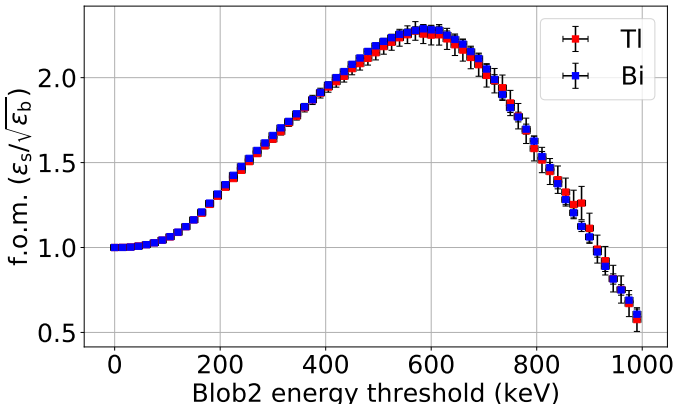

Figure 5.28: Figure of merit of second blob energy cut for ^{208}Tl and ^{214}Bi events using 5 mm voxels with Richardson-Lucy reconstruction.

5.8 Results

This section shows how all the different methods described above compare to each other. For this purpose, FANAL has also been run with the same voxel size used with the R-L algorithm (5 mm). The first relevant comparison is the efficiency of the single-track filter for all methods. As seen in Figure 5.29, diffusion has a very strong effect on high-drift volumes, with the biggest difference between FANAL with 10 mm voxels and the classical reconstruction coming from the Energy Plane. This effect is more important for ^{208}Tl events than ^{214}Bi due to the different decay mode, as ^{208}Tl events usually have secondary tracks that could be lost in the reconstruction due to the effect of diffusion. A dual cut strategy can fix the problem for the single-track cut, but using a Richardson-Lucy deconvolution further improves the result. The best possible result is obtained using FANAL with 5 mm voxels.

Figure 5.30 shows the efficiency of the blob energy cut, where again FANAL performs better than both the classical and dual cut procedures. Diffusion has also a strong effect here, as is evident in the fact that the Energy Plane is the volume with the largest difference in the efficiency with respect to FANAL. This is reasonable since for high-drift events it is harder to locate the extremes of the tracks and measure

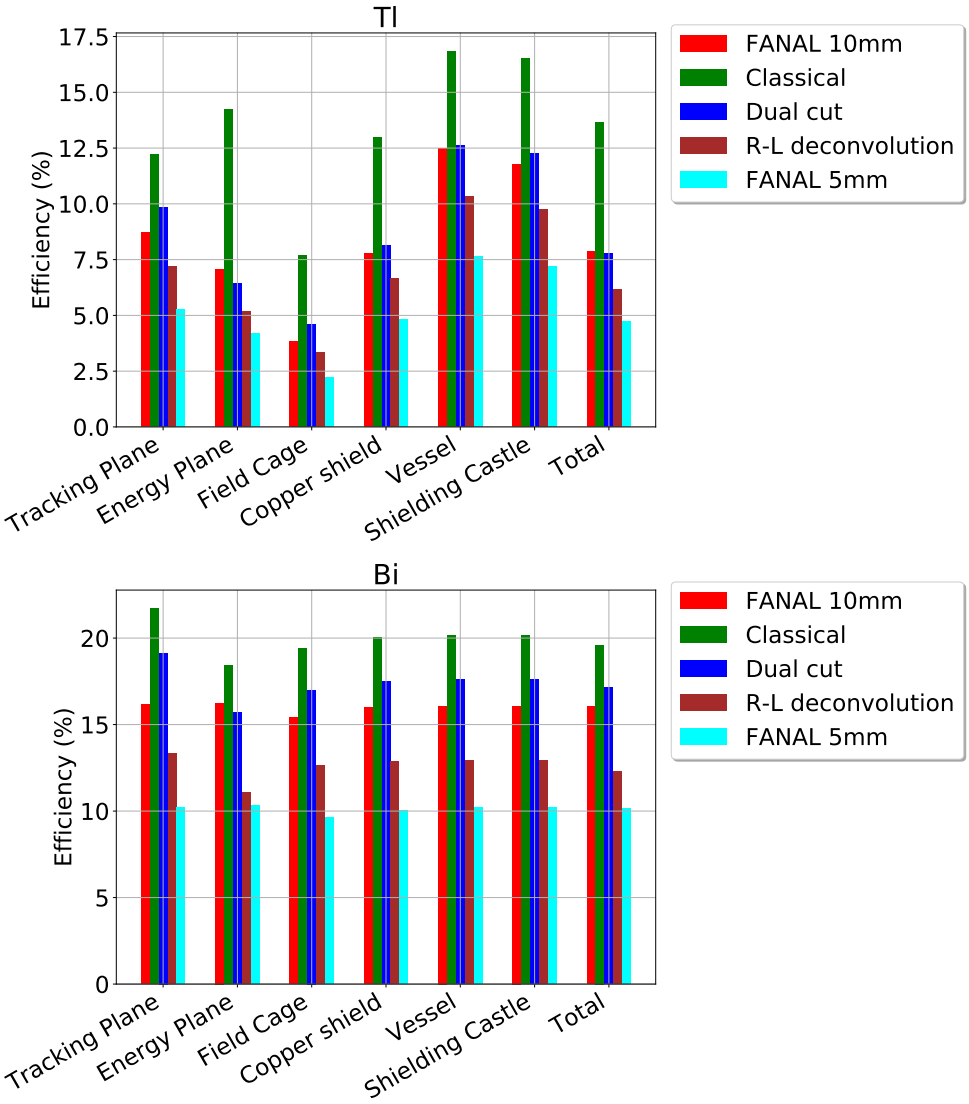

Figure 5.29: Single-track cut efficiency by volumes for all reconstructions.

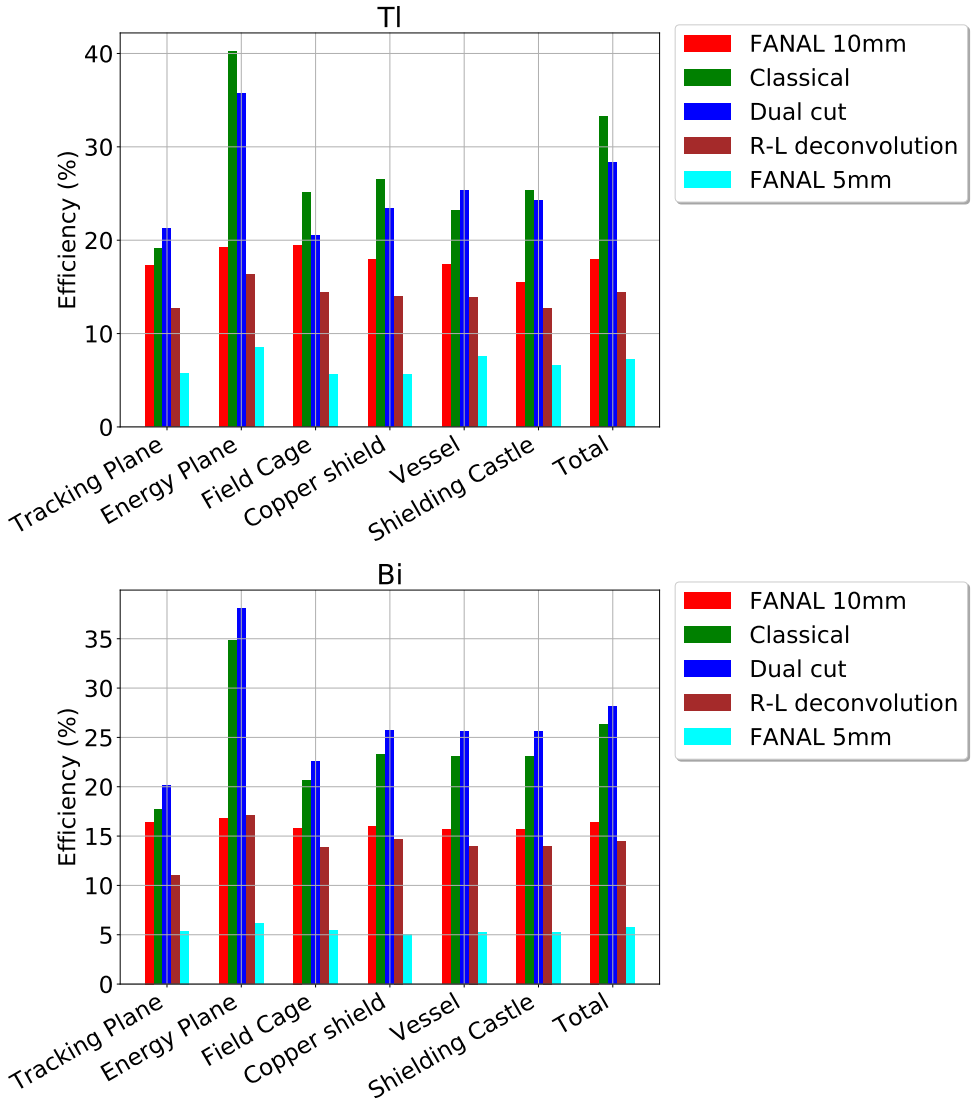

Figure 5.30: Blob energy cut efficiency by volumes for all reconstructions.

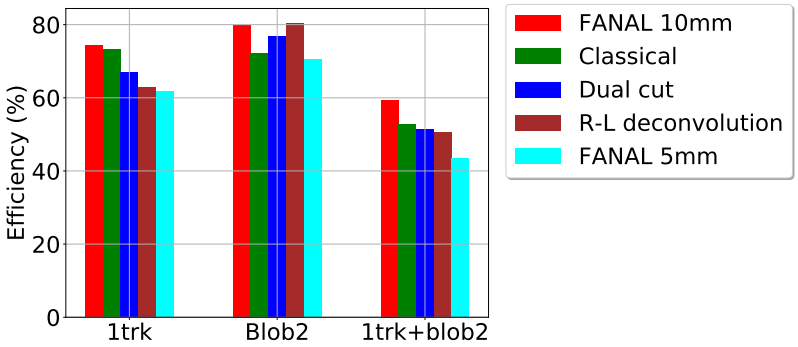

Figure 5.31: Single-track and blob energy cuts efficiencies for signal events using different reconstructions.

their energy properly. Richardson-Lucy deconvolution removes the diffusion effect and achieves results better than FANAL with 10 mm voxels. This is a very good result, because it proves that deconvolution algorithms provide a performance comparable with the one of an ideal reconstruction. An ideal reconstruction with the same voxel size as R-L (5 mm) gives even better results, as expected. In the case of signal events (Figure 5.31), all results are more similar, and there is no significant difference as events are spread uniformly along the active volume.

Figure 5.32 shows the background index for each detector subsystem. It has been computed assuming a fiducial mass of 90 kg and the radioactivities from Section 5.1. In order to compare with Refs. [174, 175] a ROI of 29 keV has been used (from 2448 keV to 2477 keV). Energy Plane is the biggest contributor, especially in the case of ^{208}Tl with the classical analysis. As expected from this study, a dual cut strategy can palliate the effect of diffusion, in particular for Tl events, where there are lower-energy secondary gammas. This is not the case for Bi events, where the main problem is not related to missing secondary tracks, but with the difficulty of finding the extremes of the tracks and their energies since diffusion makes them more blurry.

Figure 5.33 shows the contribution to the background index of each detector subsystem for each isotope, using the R-L deconvolution reconstruction. The Energy Plane is still the greatest background source. Table 5.5 contains the final contribution of each detector component

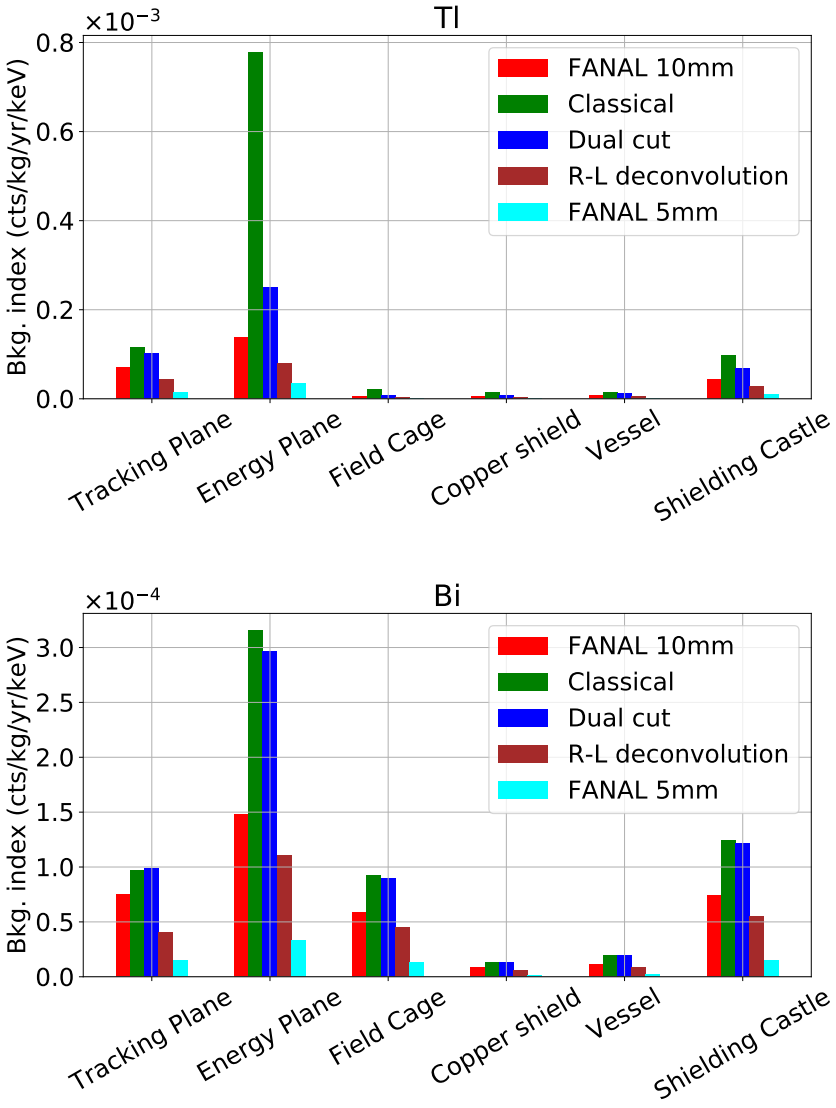

Figure 5.32: Background index by isotope for different reconstruction algorithms. The top panel corresponds to ^{208}Tl events and the bottom panel to ^{214}Bi events.

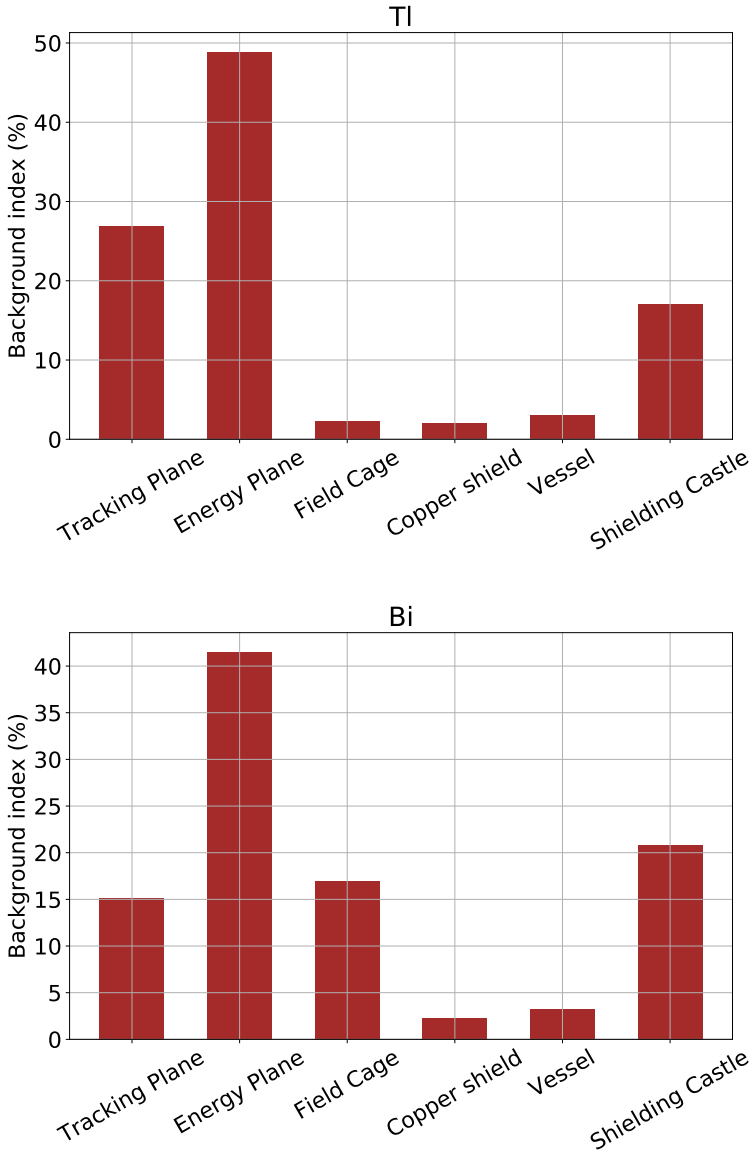

Figure 5.33: Percentage of background index induced by each detector subsystem using Richardson-Lucy deconvolution. The top panel corresponds to ^{208}Tl events and the bottom panel to ^{214}Bi events.

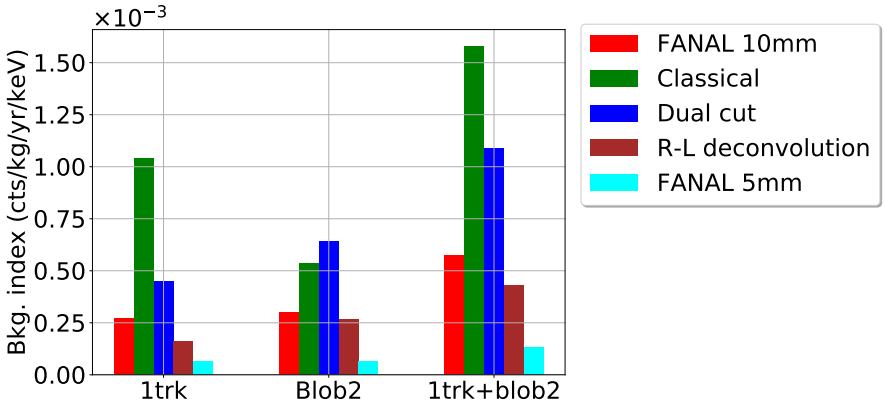

Figure 5.34: Total background index computed with all the algorithms described. Richardson-Lucy deconvolution is the best performing among the realistic simulations.

after all the analysis cuts. PMT bases are the largest contributors to the ^{208}Tl background and PMTs themselves have the greatest ^{214}Bi activity.

Putting everything together, Figure 5.34 and Table 5.6 show the total background index for each reconstruction method. Classical reconstruction is much worse than FANAL even after the improvements due to the dual cut strategy. Richardson-Lucy offers a performance similar to that of FANAL.

All of the above results are obtained with a very tight fiducial cut of 400 mm due to the limitation of the simulation explained in Section § 5.2. Since FANAL does not depend on the sensors it is possible to make an extrapolation to looser fiducial cuts. The idea is to compute the efficiency of different fiducial cuts, considering that the efficiency of the remaining steps does not depend on the fiducial cut. In that way, the FANAL efficiency can be combined with the efficiencies found for later cuts in different algorithms. This extrapolation is shown in Figure 5.35. Using a fiducial cut of 2 cm in every border the background index obtained is 7.16×10^{-4} cts keV^{-1} kg^{-1} yr^{-1}, with a global signal efficiency of 27.14%.

Volume	^{214}Bi		^{208}Tl		Total	
	mBq	%	mBq	%	mBq	%
TRACKING PLANE	**$<3.61 \times 10^{-6}$**	**27.41 %**	**$<3.34 \times 10^{-6}$**	**16.62 %**	**$<6.94 \times 10^{-6}$**	**9.11 %**
DB Plug	3.26×10^{-6}	24.76 %	6.58×10^{-7}	3.28 %	3.92×10^{-6}	11.78 %
Dice Board	$<3.50 \times 10^{-7}$	2.66 %	$<2.68 \times 10^{-6}$	13.34 %	$< 3.03 \times 10^{-6}$	20.89 %
ENERGY PLANE	**$<6.57 \times 10^{-6}$**	**49.97 %**	**$<9.16 \times 10^{-6}$**	**45.61 %**	**$<1.57 \times 10^{-5}$**	**47.34 %**
Enclosure Window	$<2.97 \times 10^{-7}$	2.26 %	$<1.98 \times 10^{-6}$	9.86 %	$<2.28 \times 10^{-6}$	6.85 %
PMT	2.01×10^{-6}	15.24 %	4.79×10^{-6}	23.84 %	6.79×10^{-6}	20.43 %
PMT Base	4.27×10^{-6}	32.47 %	2.39×10^{-6}	11.92 %	6.66×10^{-6}	20.05 %
FIELD CAGE	**$<3.02 \times 10^{-7}$**	**2.30 %**	**$<3.76 \times 10^{-6}$**	**18.71 %**	**$<4.06 \times 10^{-6}$**	**12.21 %**
Field Cage	$<2.33 \times 10^{-7}$	1.77 %	$<3.30 \times 10^{-6}$	16.44 %	$<3.53 \times 10^{-6}$	10.63 %
Anode Quartz	6.90×10^{-8}	0.52 %	4.55×10^{-7}	2.27 %	5.24×10^{-7}	1.58 %
COPPER SHIELD	**2.67×10^{-7}**	**2.03 %**	**3.61×10^{-7}**	**2.50 %**	**7.70×10^{-7}**	**2.32 %**
ICS	2.35×10^{-7}	1.79 %	4.04×10^{-7}	2.01 %	6.39×10^{-7}	1.92 %
Tracking Support	1.22×10^{-9}	0.01 %	3.52×10^{-8}	0.18 %	3.64×10^{-8}	0.11 %
Carrier Plate	3.07×10^{-8}	0.23 %	6.38×10^{-8}	0.32 %	9.45×10^{-8}	0.28 %
VESSEL	**$<4.03 \times 10^{-7}$**	**3.07 %**	**$<7.24 \times 10^{-7}$**	**3.61 %**	**$<1.13 \times 10^{-6}$**	**3.39 %**
SHIELDING	**2.30×10^{-6}**	**17.48 %**	**4.58×10^{-6}**	**22.81 %**	**6.88×10^{-6}**	**20.70 %**
Shielding Lead	5.87×10^{-7}	4.46 %	6.98×10^{-7}	3.48 %	1.28×10^{-6}	3.87 %
Shielding Struct	1.71×10^{-6}	13.02 %	3.88×10^{-6}	19.34 %	5.60×10^{-6}	20.70 %
Total (mBq)	**$<1.35 \times 10^{-5}$**		**$<2.21 \times 10^{-5}$**		**$<3.55 \times 10^{-5}$**	
Total (cts keV^{-1} kg^{-1} yr^{-1})	**$<1.63 \times 10^{-4}$**		**$<2.67 \times 10^{-4}$**		**$<4.29 \times 10^{-4}$**	

Table 5.5: Final contribution from natural radioactivity contamination for each NEXT-100 detector subsystem to overall background model after R-L reconstruction. Note some activities are derived from measurements of upper limits.

Table 5.6: Background index (cts/keV/kg/yr) for each analysis. Richardson-Lucy has the best result among the realistic simulations and is comparable to the latest result from Ref. [175].

Bkg. (cts/keV/kg/yr)	**^{208}Tl**	**^{214}Bi**	**Total**
Ref. [175]	1.30×10^{-4}	2.78×10^{-4}	4.09×10^{-4}
FANAL 10mm	2.72×10^{-4}	3.02×10^{-4}	5.74×10^{-4}
Classical	1.04×10^{-3}	5.38×10^{-4}	1.58×10^{-3}
Dual cut	4.48×10^{-4}	6.40×10^{-4}	1.09×10^{-3}
Richardson-Lucy	1.63×10^{-4}	2.67×10^{-4}	4.29×10^{-4}
FANAL 5mm	6.43×10^{-5}	6.60×10^{-5}	1.30×10^{-4}

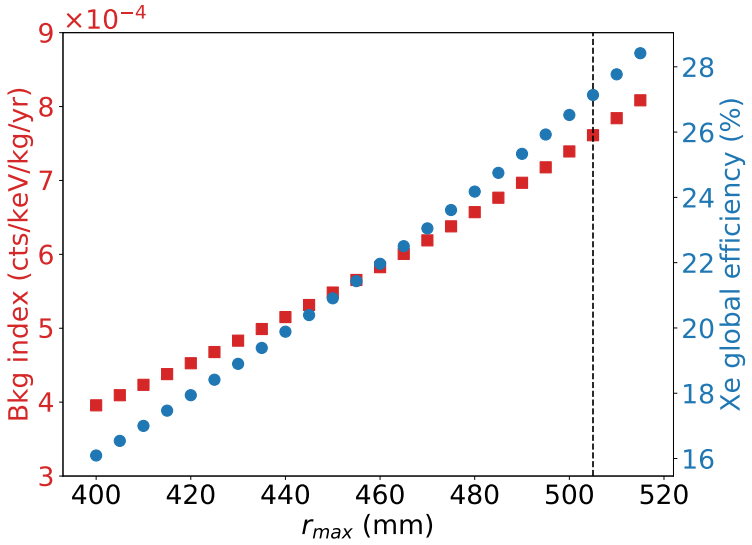

Figure 5.35: Extrapolation to higher fiducial cuts. The left axis (red) is the total background index (cts/keV/kg/yr). The right axis (blue) is the global efficiency for signal events. The dotted vertical line corresponds to a fiducial cut of 2 cm in each border.

5.9 Conclusions

The analysis presented is an update of previous NEXT-100 sensitivity studies to neutrinoless double beta decay [174, 175]. A new detailed software simulation has been used, similar to the one in use in the already operating NEXT-White detector. The materials used in the detector and their radioactivities have been updated, too, and, although the geometry implemented in the simulation does not follow exactly the current design, it is an important step to understand the sensitivity of NEXT-100.

The most important finding of this analysis is that diffusion of the electron cloud in the TPC has an important effect on the classical reconstruction algorithm, especially since NEXT-100 has twice the drift length of NEXT-White. An ideal reconstruction is provided by the fast analysis, which does not account for diffusion and is not completely realistic, but can be used as a baseline to compare with. The realistic classical analysis can be modified to improve its performance, until reaching similar levels to those of FANAL. One option is to split the charge cut per SiPM into two, a first low cut to assess the single-track filter and a second, higher one, for the blob cut. This strategy improves the result by a factor 1.44, but presents some problems, since a substantial fraction of the events that pass the one-track cut are multi-track after applying the higher threshold. Another option is to include a Richardson-Lucy deconvolution step with different Point Spread Functions for different z bins. In this way the diffusion effect is accounted for in the model and can be factored out during the reconstruction.

The background index obtained with the R-L deconvolution is 4.29×10^{-4} cts/keV/kg/yr, in between FANAL 5 mm, 1.30×10^{-4} cts/keV/kg/yr and FANAL 10 mm, 5.74×10^{-4} cts/keV/kg/yr, and much better than the 1.58×10^{-3} cts/keV/kg/yr obtained with the classical analysis. These results are compatible with previous studies [174, 175] and show how electron cloud diffusion is an important issue for next generation high pressure xenon gas detectors that needs to be taken care of, probably via both software and hardware.

At the reconstruction level, a Richardson-Lucy deconvolution seems to be able to palliate the effect of diffusion, but other methods like deep neural networks can potentially offer further improve-

ments [190].

From a detector design perspective, the NEXT collaboration is studying different gas mixtures that could reduce the effect while still providing enough light to measure precisely S1 and S2 signals [156–158]. Besides that, to achieve a lower radioactive budget, future detectors or NEXT-100 upgrades will replace PMTs (which are the leading source of background in NEXT-100) with SiPMs, which are more radiopure, resistant to pressure and able to provide better light collection. For further improvements, the kapton circuit boards, which are the dominant background source in the tracking plane, could be replaced by ultra-low-background quartz circuits.

6 *Medical applications of NEXT technology*

Particle physics has made important contributions to the development of instrumentation for biomedical research, diagnosis and therapy. Among these applications one can find X-rays, radiotherapy, Computational Tomography (CT) and Positron Emission Tomography (PET) [191]. Medical imagining has especially benefited from developments in particle detectors, including new scintillators, pixel detectors, high performance electronics and reconstruction algorithms.

The technology and expertise developed for NEXT can also have uses beyond basic research on the nature of neutrinos. The material used for the detector, xenon, is a scintillator that could be used to design new detectors for medical uses. The SiPMs used for the precise tracking of NEXT could be applied to reconstruct with high precision the origin of particles coming from the body of a patient, as is done in a PET scan. This chapter discusses one of the possible advantages of a new concept for PET scanners: PETALO[1], a PET scanner based on liquid xenon (LXe) with SiPM readout.

6.1 Positron Emission Tomography

Positron Emission Tomography is a non-invasive functional imaging technique used to observe metabolic processes in the body. It does not show anatomic features like an MRI[2] or a CT scan, but the activity of the cells. PET scanners are used both in clinical and pre-clinical research to study the molecular bases and treatments of disease.

The principle of operation consists of injecting into the patient a biologically active molecule, modified to include a radioactive iso-

[1] Positron Emission TOF Apparatus with Liquid xenOn

[2] Magnetic Resonance Imaging

tope called a *tracer*. One common tracer is fluorodeoxyglucose, which is a glucose molecule where one oxygen is replaced by a β^+ emitter ^{18}F. The radionuclide decays within the patient and the positron annihilates with one electron after traveling a short distance in the neighboring tissues. This annihilation produces two back-to-back 511 keV photons. The trajectory of the photons defines a line of response (LOR) that can be reconstructed by measuring the direction of both particles observing their interaction in a detector surrounding the body of the patient. The intersection of many LORs shows the emission point of the radiotracer. An illustration of the technology is shown in Figure 6.1.

A LOR can be produced in three different situations:

- **True coincidence**: Both photons from an annihilation event are detected without any other prior interaction.
- **Scattered coincidence**: One of the photons has at least one Compton interaction before reaching the detector, changing its direction and creating an erroneous LOR. To minimize the background produced by this type events a good energy resolution is needed, as those photons will have less than 511 keV.
- **Random coincidence**: Two photons from different events are detected in the same time window. Improving the time resolution of the electronics can palliate the effect of this kind of events.

The sensitivity of a PET scanner is defined as the number of counts per unit time detected by the detector for each unit of activity present in a source. It can be defined as $S = E_g \times E_i$, where E_g is the geometrical efficiency (solid angle covered by the detector), and E_i is the intrinsic coincidence detection efficiency. The latter depends on the thickness of the detector along the gamma path, packing fraction and the capacity to set narrow windows for energy and time.

The measurement of the time difference between the arrival of the two photons (time-of-flight, or TOF) improves the scanner sensitivity and signal to noise ratio. A sketch is shown in Figure 6.2. The resolution in TOF (proportional to the commonly used coincidence resolving time or CRT) depends on: (a) the physical properties of the radiator (e.g, the yield and the emission time of the photons); (b) the

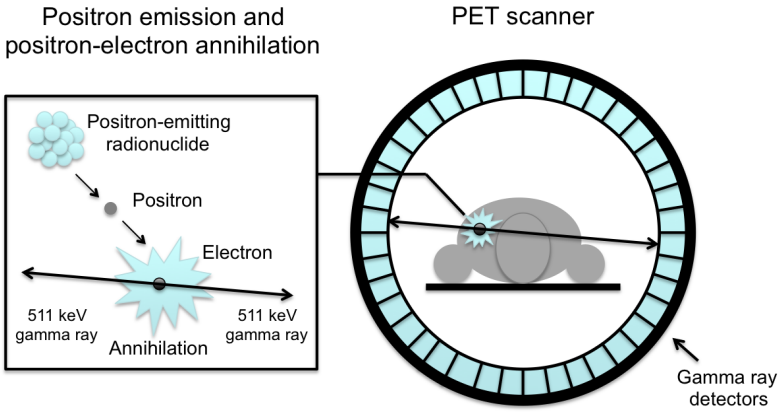

Figure 6.1: Schematic of a PET scanner showing the positron emission, annihilation and subsequent detection. Taken from Ref. [192].

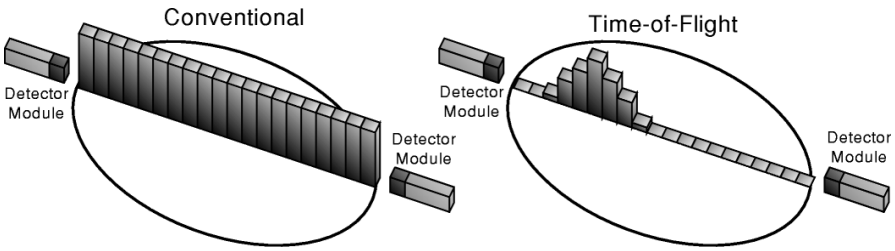

Figure 6.2: TOF reconstruction. With conventional reconstruction (left), all pixels along the LOR have the same probability. The location of the source can be constrained with the TOF measurement (right). Taken from Ref. [193].

time resolution (time jitter) introduced by the photosensors and the readout electronics.

Current commercial PET scanners use inorganic scintillating crystals as detectors, such as LYSO (lutetium yttrium oxyorthosilicate), which enables TOF measurements, resulting in a CRT of $300 - 600$ ps FWHM [194, 195]. The most recent investigations performed in small laboratory systems, deploying detectors of a few tens of mm^3 volume, obtain a CRT of $\sim 80 - 120$ ps FWHM [196, 197].

6.2 The PETALO concept

Relying on the knowledge and experience gathered from NEXT, we proposed in 2016 a new scintillator detector called PETALO based on liquid xenon cells read out by silicon photomultipliers (SiPM) [198]. The excellent properties of liquid xenon as scintillator are clearly established in the literature [199–203]. The main advantages are:

1. **A high scintillation yield** ($\sim$ 30 000 photons per 511 keV gamma).
2. **Fast scintillation** which can be parametrized as the sum of two exponentials with decay times of 2.2 and 27 ns [204].
3. **LXe is a continuous medium with uniform response**. Therefore, the design of a compact system is much simpler than in the case of solid detectors of fixed shape. It is also possible to provide a 3D measurement of the interaction point, and, thus, a high resolution measurement of the depth of interaction (DOI).
4. **In principle, in LXe it is possible to identify Compton events** depositing all their energy in the detector as separate-site interactions, due to its relatively large interaction length. Once an event in the region of interest (around 511 keV of total deposited energy) is identified, the pattern of recorded light on the SiPMs can be inspected to find one or more depositions, using, for instance, neural networks [205]. Compton events can commonly lead to incorrect LORs as the interaction point reconstructed can be misplaced, contributing to the noise of the image. Identifying correctly the first interaction of a Compton event would improve the sensitivity of the system.
5. **The temperature at which xenon can be liquefied at a pressure very close to the atmospheric pressure** is high enough ($\sim$161 K) as to be reached using a basic cryostat. Also, at this temperature SiPMs can be operated normally, and their dark count rate is essentially negligible (see, for instance Ref. [206]).

An initial Monte Carlo study was carried out to assess the TOF measurement performance of such a detector, using xenon scintillation light. If the scanner is equipped with (currently available) VUV-

sensitive SiPMs, an excellent CRT of 70 ps can be obtained [198]. This chapter shows a possible improvement for PETALO using Cherenkov radiation published in [207].

6.3 The Cherenkov radiation

A charged particle propagating in a dielectric medium, at a speed higher than the speed of light in the medium, excites the surrounding molecules, which subsequently relax, emitting radiation. If a particle travels at a speed lower than that of light, the light emitted by the molecules of the medium at different points along its trajectory never interferes (see Fig. 6.3-*top*). However, if the particle speed is higher than that of light, the electromagnetic waves emitted at different points interfere constructively and emit a glow sufficiently intense as to be detected. The wave front propagates at an angle θ with the direction of the particle such that:

$$\cos\theta = \frac{v_{\text{light}}}{v} \tag{6.1}$$

where v_{light} is the speed of light in the medium and v is the speed of the particle (see Fig. 6.3-*bottom*). Cherenkov photons are emitted with wavelengths following the distribution:

$$\frac{\partial N}{\partial x \partial \lambda} = \frac{2\pi\alpha}{\lambda^2}\left(1 - \frac{1}{\beta^2 n^2(\lambda)}\right) \tag{6.2}$$

where α is the fine-structure constant, $\beta \equiv v/c$, n is the refraction index of the medium, λ is the photon wavelength and x is the distance travelled by the charged particle. Eq. (6.2) does not diverge for high photon energy, because $n(\lambda) \to 1$ for short wavelengths (or high wave frequencies). Most Cherenkov radiation is emitted in the blue and ultraviolet range. Emission stops when the speed of the particle drops below that of light in the medium, thus resulting in a threshold for light emission at a given wavelength of

$$v > \frac{c}{n(\lambda)} \tag{6.3}$$

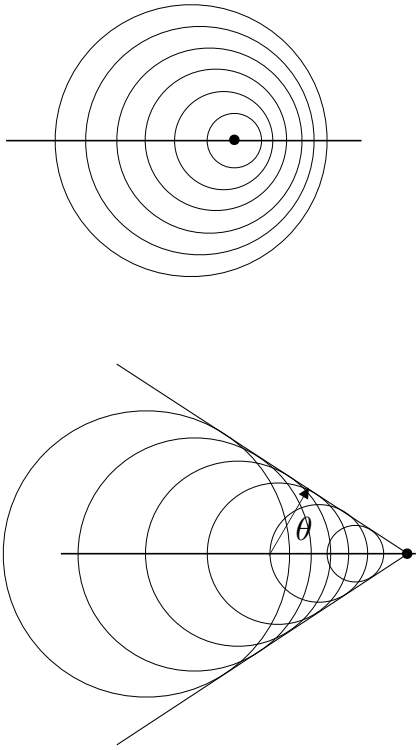

Figure 6.3: Schematic of light emission when a particle travels at a speed lower (top), or higher (bottom) than that of light in the medium.

6.3.1 *Using Cherenkov light in PET scanners*

The promptness of Cherenkov light (few picoseconds, to be compared with tens of nanoseconds for scintillation light, see Fig. 6.4) is a very attractive feature for TOF applications of PET scanners, since it could lead to a dramatic improvement of the CRT, provided that: a) the yield of Cherenkov photons is sufficiently high and b) the noise introduced by photosensors and electronics is sufficiently low.

In the last decade, the idea of using Cherenkov light for TOF-PET in scintillation crystals has been vigorously pursued and numerous measurements as well as Monte Carlo studies have been carried out.

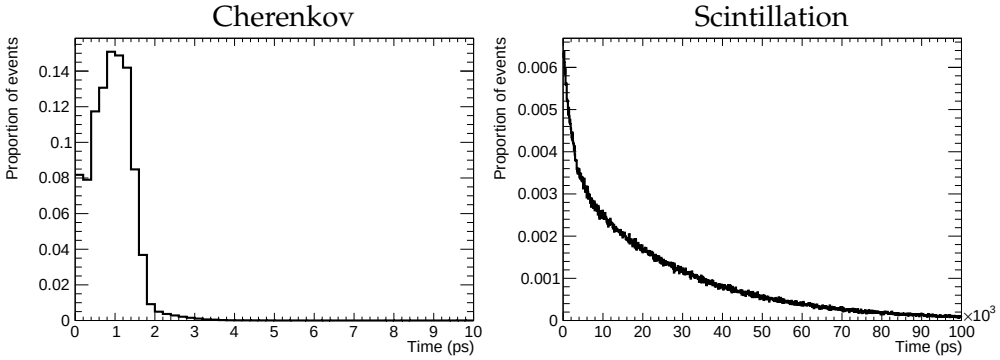

Figure 6.4: Emission time of Cherenkov (left) and scintillation (right) photons in liquid xenon. Notice that the range of time axis for scintillation is 10^3 times larger than that of Cherenkov radiation.

The main difficulty found is the very low efficiency of detecting two photons in coincidence, due to the high absorption of UV and blue light in conventional PET detectors, such as LYSO [208]. The best results so far have been obtained with PbF_2 scintillator crystals read out by microchannel plate photomultipliers [209], which give a CRT of 71 and 95 ps FWHM in small setups (5 and 15 mm long respectively).

Liquid xenon, on the other hand, is transparent to UV and blue light. Furthermore, scintillation and Cherenkov light separate naturally, as will be shown below. Last but not least, operation at moderate cryogenic temperatures may be an advantage (e.g, negligible dark count rate in sensors such as SiPMs [206]). Therefore, liquid xenon appears to be an optimal candidate for TOF measurements using Cherenkov radiation.

6.4 Monte Carlo simulation

To study the performance of a Cherenkov radiation TOF-PET based on liquid xenon, we have simulated a two-cell set-up using the Geant4 toolkit with version number 10.01.p01 [187,210]. Our set-up is the same as the one described in Ref. [198] and consists of two cells of 2.4 $\times$ 2.4 $\times$ 5 cm^3 filled with liquid xenon, at a distance of 20 cm along the z axis, on the opposite sides of a back-to-back 511 keV gamma source. The

cells are instrumented in their entry and exit faces with a dense array of 8×8 photosensors with an active area of 3×3 mm^2 and configurable photodetection efficiency. The photosensors are placed at a pitch of 3 mm, thus they cover the whole box face. The uninstrumented faces are covered by polytetrafluoroethylene (PTFE), which reflect optical photons according to a lambertian distribution with an efficiency of 97%. This value for the reflectivity has been chosen following Ref. [211] and references therein. A reflectivity higher than 99% is reported for the spectral range 350–1800 nm, and slightly lower values from 350 nm down to 200 nm. A simple extrapolation to 175 nm would give 95%. For the scintillation spectrum of LXe (155–200 nm) values between 88% and 95% are found to produce a good fit of Monte Carlo to data, varying the absorption length of LXe to UV light from 1 m to infinity. We have chosen to use 97% for all wavelengths as an average value and an absorption length > 1 m, which is virtually the same as infinity, given the dimensions of our cells. The physical properties used in the simulation which are relevant for the generation and propagation of optical photons are summarized in Table 6.1, together with the main characteristics of the geometry.

The coverage of the instrumented faces is assumed to be 100%. We

Table 6.1: Summary of the Monte Carlo set-up specifications and the LXe relevant properties used in the simulation.

Geometry	
Cell dimensions	$2.4 \times 2.4 \times 5$ cm^3
Distance between cell entry faces	20 cm
Sensor pitch	3 mm
Number of sensors per face	64
Physics properties	
LXe density	2.98 g/cm^3 [212]
LXe attenuation length for 511 keV gammas	4 cm [213]
LXe Rayleigh scattering length	36.4 cm [214]
Refraction index of sensor entrance window	1.54
Reflectivity of PTFE walls	0.97

take into account the effect of a non-perfect coverage in a global detection efficiency (GDE), which encloses the probability of the photon to fall within the active area of a sensor and its photodetection efficiency.

Back-to-back 511 keV gammas are shot isotropically, at $t = 0$ from a vertex at equal distance from both boxes. The photons can interact in the liquid xenon via photoelectric absorption or Compton scattering. In this study we focus on photoelectric events, only, in which all the available kinetic energy (511 keV) is deposited in one point. The Cherenkov radiation emitted by the electrons produced in such processes is simulated, with a wavelength distribution that follows Eq. (6.2) and is shown in Fig. 6.5–*left*. A cut is set at 155 nm, because no reliable measurements of the refraction index of liquid xenon exist for energies higher than ~ 8 eV, which corresponds to $\sim$ 155 nm (see, for instance, Ref. [215]). This assumption will not affect our results, since the fastest photons (which dominate the CRT, as will be demonstrated below) have much higher wavelengths (Fig. 6.5–*right*), mainly in the blue and near UV region. The upper cut at 1200 nm is conservative, being well beyond the typical sensitivity of the photosensors proposed.

The Cherenkov photons are propagated inside the box and eventually either reach a photosensor where they may produce a photoelectron, depending on the GDE, or are absorbed by the uninstrumented

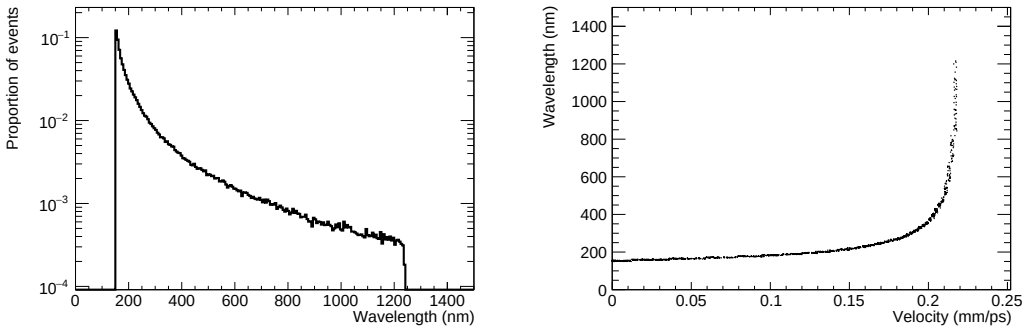

Figure 6.5: (Left) Distribution of the Cherenkov radiation wavelength used in the simulation. (Right) Cherenkov radiation wavelength as a function of the group velocity of the photons. The plot shows that in the 350–600 nm range the photon velocity has very little variation.

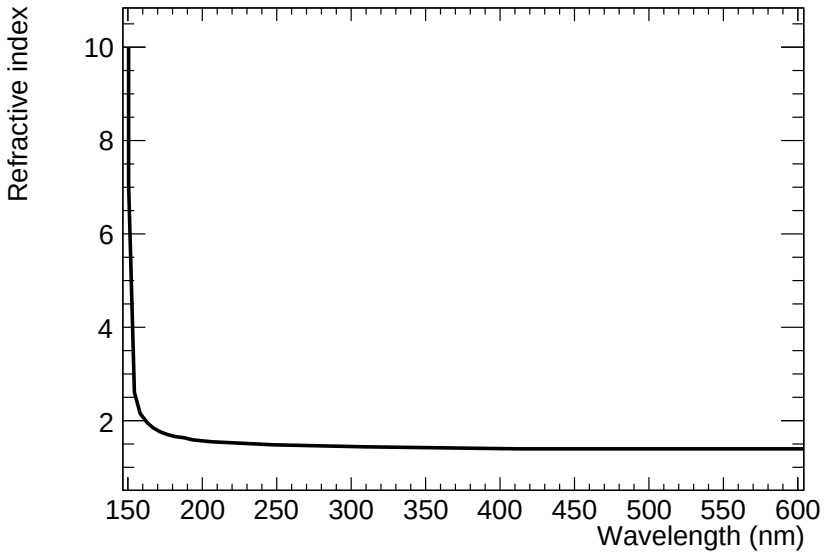

Figure 6.6: LXe refraction index as a function of the wavelength of the optical photon, as results from the parametrization in Ref. [215]. For wavelengths above 300 nm the refraction index is practically flat, and has a value of around 1.4.

faces. The LXe refraction index dependence on the energy of photons is simulated according to the Lorentz-Lorenz equation [215]

$$\frac{n^2-1}{n^2+2} = -A(E)\cdot d_M \tag{6.4}$$

where n is the LXe refraction index, d_M is the molar density and $A(E)$ is the first refractivity virial coefficient:

$$A(E) = \sum_i^3 \frac{P_i}{E^2 - E_i^2} \tag{6.5}$$

with $P_i(\text{eV}^2\cdot\ \text{cm}^3/\text{mole}) = (71.23, 77.75, 1384.89)$ and $E_i(\text{eV}) = (8.4, 8.81, 13.2)$. This dependence is illustrated in Fig. 6.6 in terms of the wavelength.

In Table 6.2 the properties of Cherenkov radiation production in liquid xenon are summarized for the wavelengths of relevance in

Table 6.2: Properties of Cherenkov light simulation in liquid xenon.

Bin range (nm)	Refraction index	Energy threshold (keV)	# photons for 511–keV e-
155–250	2.58–1.46	43–189	41
250–350	1.46–1.41	189–214	10
350–450	1.41–1.39	214–224	5
450–550	1.39 –1.38	224–229	3
550–650	1.38	229–232	2

this study. The kinetic energy threshold E_{thr} for electrons to produce Cherenkov radiation at a fixed wavelength λ is calculated by

$$E_{\text{thr}}(\lambda) = \left(\frac{1}{\sqrt{1 - \frac{v^2}{c^2}}} - 1 \right) m_e c^2 \tag{6.6}$$

where $v = c/n(\lambda)$ according to Eq. (6.3) and m_e is the electron mass. The range of a 511–keV electron in liquid xenon is of a few mm, which is enough to produce ∼60 Cherenkov photons on average, as can be seen in Fig. 6.7. The same figure shows that in the ideal case of a perfect GDE the distribution of the detected photons is almost coincident with that of produced photons. This is due to the high collection efficiency of the PETALO set-up, made possible thanks to the transparency of liquid xenon to all the wavelengths involved and the almost perfect reflectivity of PTFE.

6.4.1 CRT calculation

We denote d_g as the distance from the centre of the LOR to the interaction vertex of each 511 keV gamma, d_d as the displacement of the gamma emission vertex from the centre of the LOR and d_p as the distance from the interaction vertex to the detection vertex (i.e., the position of the sensor), as illustrated in Fig. 6.8. If t_1, t_2 are the times of the first photoelectron recorded in each one of the cells, the time difference between them can be written as:

$$t_1 - t_2 = 2\frac{d_d}{c} + \frac{\Delta d_g}{c} + \frac{\Delta d_p}{v} \tag{6.7}$$

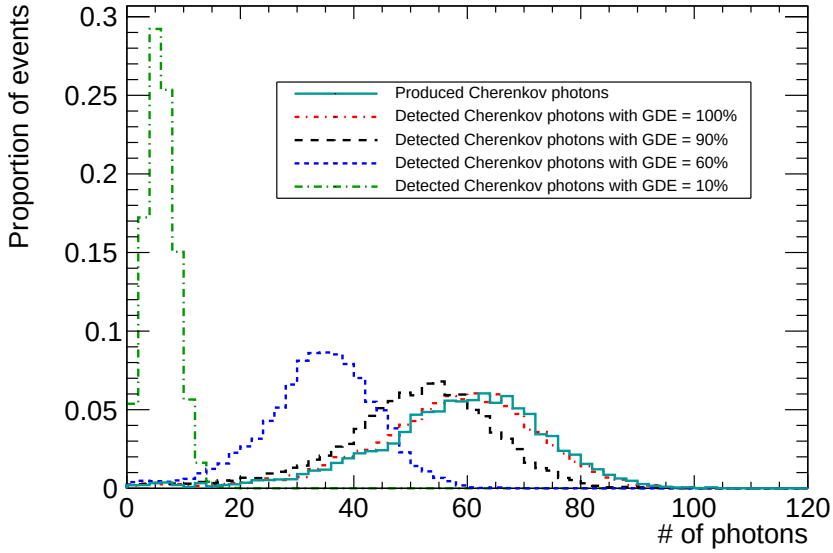

Figure 6.7: Distribution of the number of Cherenkov photons produced and detected in one photoelectric interaction of a 511–keV gamma in our set-up, varying the GDE of the sensors between 10% and 100%.

where v is the velocity of the Cherenkov photon and c is the speed of light in vacuum. Therefore, the difference in time between the gamma emission vertex and the centre of the LOR can be expressed as:

$$\Delta t \equiv \frac{d_d}{c} = \frac{1}{2}(t_1 - t_2 - \frac{\Delta d_g}{c} - \frac{\Delta d_p}{v}) \tag{6.8}$$

The CRT, $\delta\Delta t$, is defined as the variance, expressed in FWHM, of the Δt distribution. Therefore, the factors that affect the fluctuation of Δt are: a) the number of detected Cherenkov photons; b) the fluctuations in the velocity of propagation of Cherenkov photons in liquid xenon; c) the precision in the measurement of the recorded time of photoelectrons, which is driven by the time jitter of the sensors and the front-end electronics; and d) the determination of the interaction point of the 511-keV gammas, which depends on the spatial resolution of the detector.

Notice that the velocity of propagation of optical photons in Geant4 is the group velocity, which depends on the refraction index of the

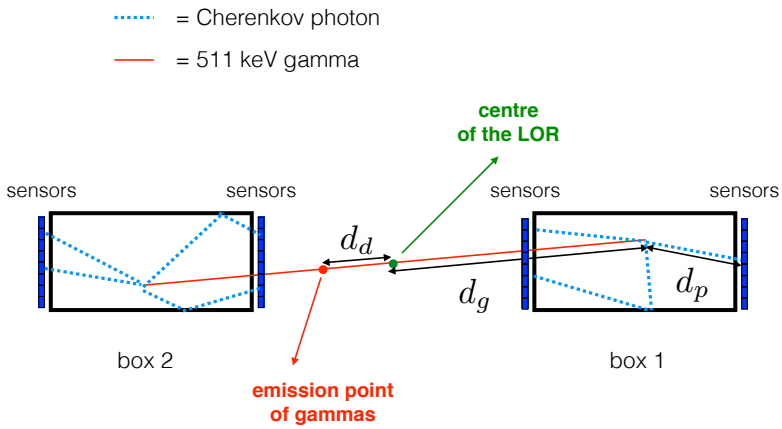

Figure 6.8: Schematic of the Monte Carlo simulation set-up, where d_g is the distance between the centre of the LOR and the interaction point of the 511-keV gamma, d_d is the distance between the centre of the LOR and the emission point of gammas and d_p is the distance that a Cherenkov photon covers between its emission and detection point.

medium in the following way:

$$v = c \times \left(n(E) + \frac{\mathrm{d}n}{\mathrm{d}(\log(E))} \right)^{-1} \tag{6.9}$$

where E is the energy of the photon and n is the refraction index of the medium.

6.5 Analysis and results

6.5.1 Speed of Cherenkov photons

The calculation of the CRT depends on the speed of the Cherenkov photons in liquid xenon (Eq. 6.9), which, in turn, depends on the wavelength of the photon. Since the wavelength of a detected photon is not known, it is necessary to use an average value $\bar{v}$ in the calculation of the CRT, thus introducing a fluctuation.

Fig. 6.9 shows the CRT as a function of $\bar{v}$, assuming the ideal case of perfect spatial resolution and no jitter in the sensor response and

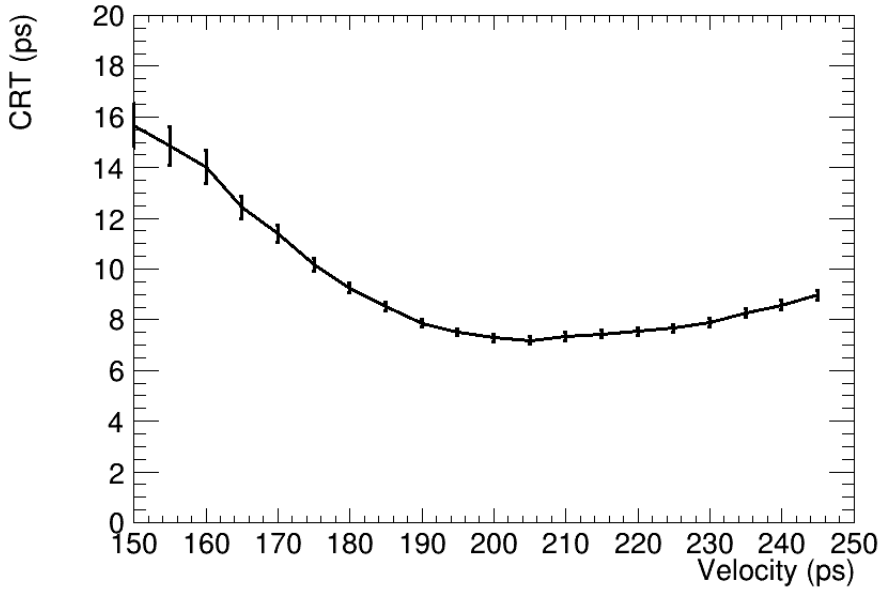

Figure 6.9: Variation of the CRT as a function of the value of the optical photon speed used for the calculation.

in the front-end electronics. The CRT has a minimum around 200–210 mm/ns, as expected, since most of the radiation is emitted in the blue and near-UV range, where the photon speed varies very little (Fig. 6.5-*right*.) In the rest of the paper, a value of 210 mm/ns will be used for the speed of all photons, regardless of their wavelength.

6.5.2 Intrinsic CRT

Our initial calculation assumes an ideal sensor with no time jitter or fluctuations introduced by the electronics. The uncertainty in the determination of the 511–keV gamma interaction position in the cell is simulated as a gaussian fluctuation with 2–mm r.m.s., as in Ref. [198]. In this case, the CRT is dominated by the GDE. Fig. 6.10 shows that the variation of the CRT with the GDE is small: using the time of the first photoelectron detected in each cell to compute the CRT, a perfect sensor with 100% GDE exhibits a CRT of 12 ps, while a sensor with a GDE of 10%, shows a CRT of some 17 ps. This result demonstrates

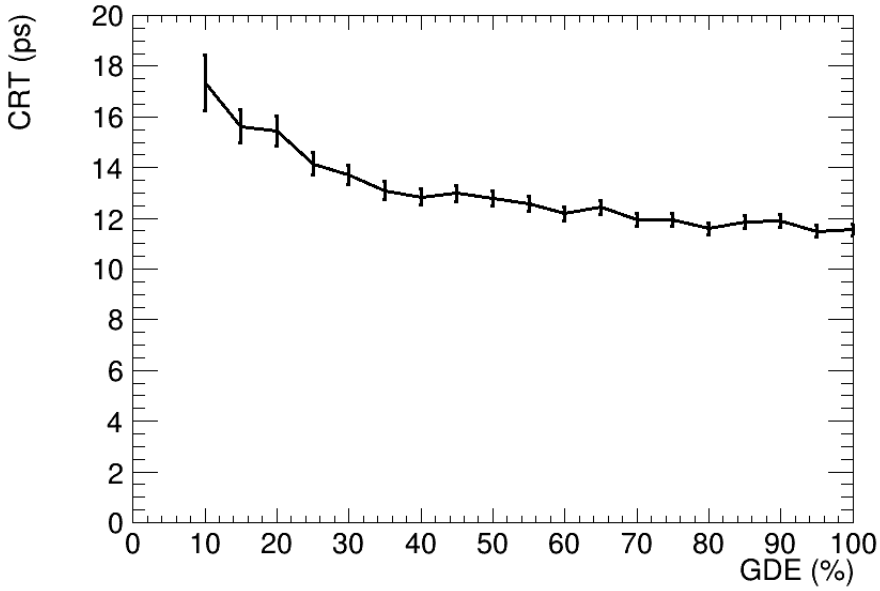

Figure 6.10: Dependence of the CRT on the sensor photodetection efficiency assuming all wavelengths are detected with the same efficiency.

that, in spite of the low average number of detected photons in the case of low GDEs, the CRT is not affected sizeably, since it depends only on the arrival time of the first detected pair of photons.

On the other hand, Fig. 6.5-*right* shows that the speed of photons in liquid xenon varies very little for wavelengths above 300 nm. It follows that the CRT can improve using sensors with a detection threshold above 300 nm (e.g, detectors sensitive to the near UV and blue light), provided that the number of detected photons is high enough. Fig. 6.11 shows that, indeed, limiting the sensitivity of the sensors down to soft UV wavelengths improves the CRT to some 10 ps almost independent of GDE. As shown in Table 6.2, the number of emitted Cherenkov photons that survive this cut is around 15–20, large enough to ensure that the CRT is not spoiled. This result has very relevant implications for our study, since it shows that: a) an intrinsic CRT of near 10 ps can be reached in a LXe detector; b) the required sensors do not need to be sensitive to hard VUV light (as is the case to detect scintillation light,

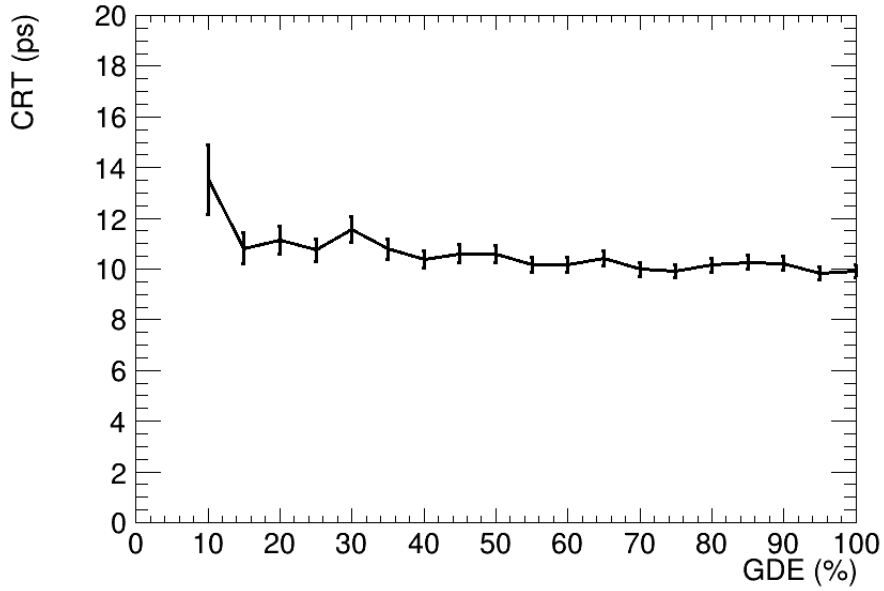

Figure 6.11: Dependence of the CRT on the PDE with a threshold of 300 nm on the detected wavelengths.

where 170-nm sensitive SiPMs must be used for optimal results, as discussed in Ref. [198]); and c) it is possible to decouple the detection of scintillation light and Cherenkov light (which can be done, for example, using micro-channel plate PMTs sensitive to the near UV and optical spectrum). This decoupling allows one to optimize separately sensors dedicated to energy and position measurement and those dedicated to time measurement.

6.5.3 Effect of the sensor and front-end electronics jitter

Given that the intrinsic CRT achievable with Cherenkov light in LXe approaches 10 ps, the obvious requirement for the sensors and associated electronics is to achieve a time uncertainty of the same order. With a time jitter of around 80 ps current SiPMs are far from satisfying this requirement. On the other hand, state-of-the-art fast electronics introduce a time fluctuation in the vicinity of 30 ps [216]. When combined with very fast sensors such as single photon avalanche diodes

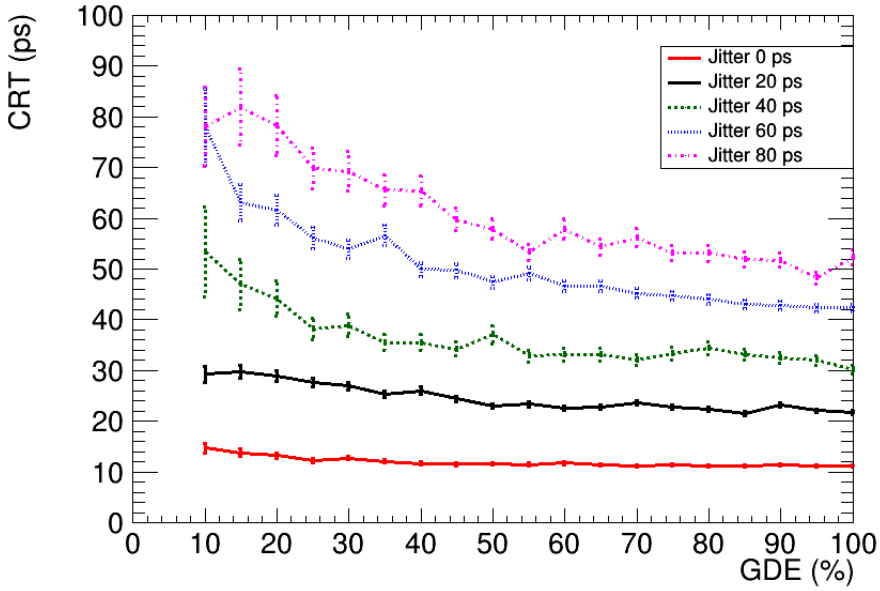

Figure 6.12: Dependence of the CRT on the total jitter (sensor + electronics) with a threshold of 300 nm on the detected wavelengths.

or micro-channel plate photomultipliers, featuring time jitters of about the same order (see, for instance, Ref. [217] for the latter sensors), it appears that an overall time uncertainty of some 40 ps may be possible with today's technology.

To quantify the effect, we have simulated gaussian noise (corresponding to the combined time jitter of sensors and front-end electronics) for sensors with a minimum detection wavelength of 300 nm. The results, shown in Fig. 6.12 as a function of the GDE, show that the worst case (time jitter of 80 ps corresponding to SiPMs) yields a CRT between 50 and 80 ps (which is still better than the state-of-the-art), while jitters around 40 ps, which appear reachable with fast detectors and electronics, result in a CRT between 30 and 55 ps, depending on the GDE. In the case of micro-channel plates, their quantum efficiency nowadays reaches 20–25% [218].

6.6 Summary and outlook

In this work we have shown the potential of liquid xenon, and in particular for a detector along the lines of the recently proposed PETALO scanner, of using Cherenkov light to provide an excellent CRT. The intrinsic CRT of LXe (using detectors sensitive to near UV and blue light) approaches 10 ps. In a PETALO cell, designed to cover two of the faces (entry and exit along the line of flight of the gammas) with VUV-sensitive SiPMs, one can cover the up to four additional faces with fast detectors (e.g., single photon avalanche diodes or micro-channel plate photomultipliers) sensitive to near-UV and blue light. While the CRT achieved reading scintillation light with SiPMs can be as good as 70 ps, the corresponding Cherenkov CRT may be up to a factor of two better, and the combined CRT may approach 30 ps for sufficiently fast sensors and electronics. Thus, the PETALO technology may truly result in a break-through for TOF-PET scanners.

7 Conclusions and prospects

The observation of neutrino oscillations in the past few decades implied the first evidence of physics beyond the Standard Model (§1.1): this phenomenon confirmed that neutrinos have masses and opened the door to a new possible explanation of the neutrino nature (§1.2).

Once neutrino masses are added to the Standard Model lagrangian, the gauge symmetry allows for a Majorana mass term to be added. The Majorana nature of the neutrinos could explain the smallness of the neutrino masses as well as the baryon asymmetry observed in the universe (§1.3).

Furthermore, the Majorana mass term would introduce violation of total lepton number, which is otherwise conserved in the Standard Model. Such a term allows for processes that were forbidden in the SM, with neutrinoless double beta decay being the best experimental method to confirm whether the neutrino is a Majorana particle (§2.1).

A positive measurement of $0\nu\beta\beta$ decay would give a half-life measurement and, from there, a neutrino mass value (§2.2). The search for $0\nu\beta\beta$ decays has become an attractive field, with different techniques (§2.4) and experiments running all over the world (§2.5).

The NEXT collaboration proposes a high pressure xenon Time Projection Chamber (TPC) to search for $0\nu\beta\beta$ decays of ^{136}Xe at Laboratorio Subterráneo de Canfranc (§3.1). NEXT has two salient features: an excellent energy resolution and topological reconstruction to suppress backgrounds. The NEXT collaboration designed and operated two R&D detectors (DEMO and DBDM, §3.4.1) before installing NEXT-White at LSC. NEXT-White has been operating under radiopure conditions since October 2016. The NEXT-White detector has been used to characterize the backgrounds at LSC and to test the technologies and designs for NEXT-100 (§3.4.2).

In this work we have presented the Data Acquisition system (DAQ) of NEXT-White (§4.1). The DAQ is an upgrade of that of NEXT-DEMO. It is based on the ATCA-SRS architecture designed by NEXT, CERN and IFIN-HH Bucharest within the RD51 collaboration. The DAQ has three subsystems: the energy plane (12 PMTs), the tracking plane (1792 SiPMs grouped in 28 Front-End Boards) and the trigger. The online system used is DATE, from the ALICE experiment at CERN (§4.2). To transfer efficiently and store all the relevant information regarding the events detected, a specific-purpose binary format has been defined by the NEXT collaboration (§4.3). A decoding software that translates those binary files to higher-level HDF5 files has been implemented and described in detail (§4.5). The output of this software is the input for the analysis and reconstruction software. To ensure quality, an automated testing system has been implemented.

The performance of the system has been improved by adding the possibility of using a Huffman compression algorithm, already implemented in NEXT-White (§4.6). The results achieved show a compression rate of $\sim$ 85%, allowing for a significant reduction in the dead time of the detector. NEXT-White has successfully taken more than 1.6 billion events, showing the robustness of the system implemented (§4.7). The same architecture with few changes will be employed for the NEXT-100 detector (§4.8).

Chapter 5 presented an upgrade on the sensitivity studies for the NEXT-100 detector using the latest radiopurity measurements (§5.1). Previous studies relied on a fast Monte Carlo simulation that lacked the details of the latest software used by the NEXT collaboration. The study presented in this thesis includes a detailed simulation of the drift, the effect of the electronics and the reconstruction (§5.2, §5.3).

The standard cut-based analysis (*classical analysis*) includes geometrical and lifetime corrections. The topological cuts have been optimized as well. The classical analysis leads to significantly worse results than those from an *ideal* reconstruction (FANAL): the background index found is a factor of 2.75 larger than the one yielded by FANAL (§5.4). The main effect responsible for this performance difference is the diffusion of the electron cloud along the drift in the TPC (§5.5).

A modified cut-based analysis was evaluated, showing it can improve the situation but not as much as needed (§5.6). The solution to

the problem came in the form of a Richardson-Lucy algorithm (§5.7). This iterative procedure can recover an underlying image blurred by a known Point Spread Function (PSF). In the case of NEXT, these PSFs can be produced by analyzing point-like ^{83m}Kr events. Using different PSFs along the z axis allows for a deconvolution of the electron cloud diffusion effect. This algorithm achieves a large improvement in the results making it comparable to the ideal reconstruction (§5.8). The total background index found using the R-L deconvolution is 4.29×10^{-4} cts keV^{-1} kg^{-1} yr^{-1}.

The results found highlight the critical importance of dealing with the electron cloud diffusion in larger detectors (§5.9). Algorithms such as Richardson-Lucy can be used for this purpose. Beyond improved reconstruction techniques, the R&D on low-diffusion gas mixtures could potentially be very useful too. Another strategy to improve the detector would be to replace the PMTs by SiPMs, as the energy plane is the main source of background.

Lastly, the technology developed for the NEXT detectors can also be applied to medical imaging (§6.1). PETALO is a PET scanner based on liquid xenon (LXe) with SiPM readout (§6.2). This technology offers several advantages: a very fast scintillation with a high light yield; LXe is a continuous medium with uniform response; and, potentially, identification and reconstruction of Compton events. LXe produces Cherenkov radiation that could be used to achieve a very fast Coincidence Resolving Time (CRT) in a TOF-PET (§6.3). A Geant4-based Monte Carlo simulation was carried out to assess the performance of such a detector (§6.4). The study presented is a proof-of-concept showing that a CRT of $\sim$ 30 ps could be achieved with sufficiently fast sensors and electronics (§6.5).

Bibliography

[1] C. D. Ellis and W. A. Wooster, *The average energy of disintegration of radium e*, Proceedings of the Royal Society of London A: Mathematical, Physical and Engineering Sciences **117** (1927), no. 776, 109–123.
doi: 10.1098/rspa.1927.0168.

[2] v. W. W. Ornstein, L.S., *Untersuchungen über das negative stickstoff bandenspektrum*, Zeitschrift für Physik (1928), no. 49, 315–322.
doi: 10.1007/BF01337921.

[3] N. Bohr, *Atomic stability and conservation laws*, Atti del convegno di fisica nucleare, ottobre 1931-IX (1932) 119–130.
doi: 10.1016/S1876-0503(08)70456-0.

[4] W. Pauli, *Dear radioactive ladies and gentlemen*, Phys. Today **31N9** (1978) 27.

[5] E. Fermi, *An attempt of a theory of beta radiation. 1.*, Z. Phys. **88** (1934) 161–177.
doi: 10.1007/BF01351864.

[6] J. Chadwick, *Possible Existence of a Neutron*, Nature **129** (1932) 312.
doi: 10.1038/129312a0.

[7] E. Majorana, *Theory of the symmetry of electrons and positrons*, Nuovo Cim. **14** (1937) 171–184.
doi: 10.1007/BF02961314.

[8] H. Bethe and R. Peierls, *The 'neutrino'*, Nature **133** (1934) 532.
doi: 10.1038/133532a0.

[9] B. Pontecorvo, *Inverse beta processes and nonconservation of lepton charge*, Sov. Phys. JETP **7** (1958) 172–173. [Zh. Eksp. Teor. Fiz.34,247(1957)].

[10] F. Reines, C. L. Cowan, F. B. Harrison, A. D. McGuire, and H. W. Kruse, *Detection of the free anti-neutrino*, Phys. Rev. **117** (1960) 159–173.
doi: 10.1103/PhysRev.117.159.

[11] G. Danby, J. M. Gaillard, K. A. Goulianos, L. M. Lederman, N. B. Mistry, M. Schwartz, and J. Steinberger, *Observation of High-Energy Neutrino Reactions and the Existence of Two Kinds of Neutrinos*, Phys. Rev. Lett. **9** (1962) 36–44.
doi: 10.1103/PhysRevLett.9.36.

[12] DONUT Collaboration, J. Sielaff, *Observation of tau neutrino charged current interactions*, in *36th Rencontres de Moriond on Electroweak Interactions and Unified Theories*, 2001.
arXiv: hep-ex/0105042.

[13] J. N. Bahcall and R. Davis, *Solar Neutrinos - a Scientific Puzzle*, Science **191** (1976) 264–267.
doi: 10.1126/science.191.4224.264.

[14] GALLEX Collaboration, P. Anselmann et al., *GALLEX results from the first 30 solar neutrino runs*, Phys. Lett. **B327** (1994) 377–385.
doi: 10.1016/0370-2693(94)90744-7.

[15] SAGE Collaboration, D. Abdurashitov et al., *Results from SAGE*, Phys. Lett. **B328** (1994) 234–248.
doi: 10.1016/0370-2693(94)90454-5.

[16] Super-Kamiokande, *Neutrinos and Neutrino Oscillation*, accessed 6 June, 2020.
URL: http://www.hyper-k.org/en/neutrino.html.

[17] SNO Collaboration, Q. R. Ahmad et al., *Direct evidence for neutrino flavor transformation from neutral current interactions in the Sudbury Neutrino Observatory*, Phys. Rev. Lett. **89** (2002) 011301.

doi: 10.1103/PhysRevLett.89.011301,
arXiv: nucl-ex/0204008.

[18] KamLAND Collaboration, S. Abe et al., *Precision Measurement of Neutrino Oscillation Parameters with KamLAND,* Phys. Rev. Lett. **100** (2008) 221803.
doi: 10.1103/PhysRevLett.100.221803,
arXiv: 0801.4589.

[19] K2K Collaboration, M. Ahn et al., *Measurement of Neutrino Oscillation by the K2K Experiment,* Phys. Rev. D **74** (2006) 072003.
doi: 10.1103/PhysRevD.74.072003,
arXiv: hep-ex/0606032.

[20] Wikipedia, *Standard Model*, accessed 15 June 2020.
URL: http://en.wikipedia.org/w/index.php?title=Standard_Model.

[21] S. F. King, *Models of Neutrino Mass, Mixing and CP Violation,* J. Phys. G **42** (2015) 123001.
doi: 10.1088/0954-3899/42/12/123001,
arXiv: 1510.02091.

[22] P. de Salas, D. Forero, S. Gariazzo, P. Martínez-Miravé, O. Mena, C. Ternes, M. Tórtola, and J. Valle, *2020 Global reassessment of the neutrino oscillation picture,* (6, 2020).
arXiv: 2006.11237.

[23] A. Segarra, *Breaking of Discrete Symmetries and Global Lepton Number in Neutrino Physics*. PhD thesis, IFIC, 2019.

[24] KATRIN, M. Aker et al., *Improved Upper Limit on the Neutrino Mass from a Direct Kinematic Method by KATRIN,* Phys. Rev. Lett. **123** (2019), no. 22, 221802.
doi: 10.1103/PhysRevLett.123.221802,
arXiv: 1909.06048.

[25] D. Lorca Galindo, *SiPM based tracking for detector calibration in NEXT*. PhD thesis, U. Valencia, 2015.

[26] J. Lesgourgues and S. Pastor, *Massive neutrinos and cosmology*, Phys. Rept. **429** (2006) 307–379.
doi: 10.1016/j.physrep.2006.04.001,
arXiv: astro-ph/0603494.

[27] Planck Collaboration, N. Aghanim et al., *Planck 2018 results. VI. Cosmological parameters*, (7, 2018).
arXiv: 1807.06209.

[28] C. Giunti and C. W. Kim, *Fundamentals of Neutrino Physics and Astrophysics*, 2007
ISBN: 978-0198508717.

[29] P. Hernandez, *Neutrino physics*, (2010).
arXiv: 1010.4131.

[30] M. Fukugita and T. Yanagida, *Baryogenesis without Grand Unification*, Phys. Lett. B **174** (1986) 45.
doi: 10.1016/0370-2693(86)91126-3.

[31] S. Davidson, E. Nardi, and Y. Nir, *Leptogenesis*, Phys. Rept. **466** (2008) 105–177.
doi: 10.1016/j.physrep.2008.06.002,
arXiv: 0802.2962.

[32] A. Sakharov, *Violation of CP Invariance, C asymmetry, and baryon asymmetry of the universe*, Sov. Phys. Usp. **34** (1991), no. 5, 392–393.
doi: 10.1070/PU1991v034n05ABEH002497.

[33] Particle Data Group, P. A. Zyla et al., *Review of Particle Physics*, Progress of Theoretical and Experimental Physics **2020** (08, 2020).
doi: 10.1093/ptep/ptaa104. 083C01.

[34] A. Atre, V. Barger, and T. Han, *Upper bounds on lepton-number violating processes*, Phys. Rev. D **71** (2005) 113014.
doi: 10.1103/PhysRevD.71.113014,
arXiv: hep-ph/0502163.

[35] M. Goeppert-Mayer, *Double beta-disintegration*, Phys. Rev. **48** (1935) 512–516.
doi: 10.1103/PhysRev.48.512.

[36] M. Inghram and J. Reynolds, *Double beta-decay of Te-130*, Phys. Rev. **78** (1950) 822–823.
doi: 10.1103/PhysRev.78.822.2.

[37] S. Elliott, A. Hahn, and M. Moe, *Direct Evidence for Two Neutrino Double Beta Decay in ^{82}Se*, Phys. Rev. Lett. **59** (1987) 2020–2023.
doi: 10.1103/PhysRevLett.59.2020.

[38] K. S. Krane, D. Halliday, et al., *Introductory nuclear physics*, 1987 ISBN: 978-0471805533.

[39] W. H. Furry, *On transition probabilities in double beta disintegration*, Phys. Rev. **56** (1939) 1184–1193.
doi: 10.1103/PhysRev.56.1184.

[40] M. Doi, T. Kotani, and E. Takasugi, *Double beta decay and Majorana neutrino*, Prog. Theor. Phys. Suppl. **83** (1985) 1.
doi: 10.1143/PTPS.83.1.

[41] M. Mirea, T. Pahomi, and S. Stoica, *Values of the phase space factors involved in double beta decay*, Rom. Rep. Phys. **67** (2015), no. 3, 872.

[42] J. Kotila and F. Iachello, *Phase space factors for double-β decay*, Phys. Rev. C **85** (2012) 034316.
doi: 10.1103/PhysRevC.85.034316,
arXiv: 1209.5722.

[43] KamLAND-Zen Collaboration, A. Gando et al., *Search for Majorana Neutrinos near the Inverted Mass Hierarchy Region with KamLAND-Zen*, Phys. Rev. Lett. **117** (2016), no. 8, 082503.
doi: 10.1103/PhysRevLett.117.082503,
arXiv: 1605.02889.

[44] J. Schechter and J. Valle, *Neutrinoless Double beta Decay in SU(2) x U(1) Theories*, Phys. Rev. D **25** (1982) 2951.
doi: 10.1103/PhysRevD.25.2951.

[45] M. Duerr, M. Lindner, and A. Merle, *On the Quantitative Impact of the Schechter-Valle Theorem,* JHEP **06** (2011) 091.
doi: 10.1007/JHEP06(2011)091,
arXiv: 1105.0901.

[46] W. Rodejohann, *Neutrino-less Double Beta Decay and Particle Physics,* Int. J. Mod. Phys. E **20** (2011) 1833–1930.
doi: 10.1142/S0218301311020186,
arXiv: 1106.1334.

[47] J. Menéndez, A. Poves, E. Caurier, and F. Nowacki, *Disassembling the nuclear matrix elements of the neutrinoless $\beta\beta$ decay,* Nucl. Phys. A **818** (2009) 139–151.
doi: 10.1016/j.nuclphysa.2008.12.005,
arXiv: 0801.3760.

[48] F. Šimkovic, V. Rodin, A. Faessler, and P. Vogel, *$0\nu\beta\beta$ and $2\nu\beta\beta$ nuclear matrix elements, quasiparticle random-phase approximation, and isospin symmetry restoration,* Phys. Rev. **C87** (2013), no. 4, 045501.
doi: 10.1103/PhysRevC.87.045501,
arXiv: 1302.1509.

[49] J. Hyvärinen and J. Suhonen, *Nuclear matrix elements for $0\nu\beta\beta$ decays with light or heavy Majorana-neutrino exchange,* Phys. Rev. **C91** (2015), no. 2, 024613.
doi: 10.1103/PhysRevC.91.024613.

[50] J. Barea, J. Kotila, and F. Iachello, *$0\nu\beta\beta$ and $2\nu\beta\beta$ nuclear matrix elements in the interacting boson model with isospin restoration,* Phys. Rev. **C91** (2015), no. 3, 034304.
doi: 10.1103/PhysRevC.91.034304,
arXiv: 1506.08530.

[51] N. Vaquero López, T. R. Rodríguez, and J. L. Egido, *Shape and pairing fluctuations effects on neutrinoless double beta decay nuclear matrix elements,* Phys. Rev. Lett. **111** (2013) 142501.
doi: 10.1103/PhysRevLett.111.142501,
arXiv: 1401.0650.

[52] L. S. Song, J. M. Yao, P. Ring, and J. Meng, *Nuclear matrix element of neutrinoless double-β decay: Relativity and short-range correlations,* Phys. Rev. **C95** (2017), no. 2, 024305. doi: 10.1103/PhysRevC.95.024305, arXiv: 1702.02448.

[53] J. Menendez., *Double-beta decay.nuclear matrix elements*, Talk at Neutrino 2020. URL: https://indico.fnal.gov/event/43209/contributions/187855/attachments/130618/159476/menendez_Neutrino20.pdf.

[54] J. Martín-Albo, *The NEXT experiment for neutrinoless double beta decay searches*. PhD thesis, Valencia U., IFIC, 2015.

[55] A. Bettini, *Underground laboratories,* Nucl. Instrum. Meth. A **626-627** (2011) S64–S68. doi: 10.1016/j.nima.2010.05.017.

[56] M. Moe, *New approach to the detection of neutrinoless double beta decay,* Phys. Rev. C **44** (1991) 931–934. doi: 10.1103/PhysRevC.44.R931.

[57] A. McDonald et al., *Demonstration of Single Barium Ion Sensitivity for Neutrinoless Double Beta Decay using Single Molecule Fluorescence Imaging,* Phys. Rev. Lett. **120** (2018), no. 13, 132504. doi: 10.1103/PhysRevLett.120.132504, arXiv: 1711.04782.

[58] I. Rivilla et al., *Fluorescent bicolour sensor for low-background neutrinoless double β decay experiments,* Nature **583** (2020), no. 7814, 48–54. doi: 10.1038/s41586-020-2431-5.

[59] J. Thomas, D. A. Imel, and S. Biller, *Statistics of charge collection in liquid argon and liquid xenon,* Phys. Rev. A **38** (1988) 5793. doi: 10.1103/PhysRevA.38.5793.

[60] A. V. Tikhomirov, *Centrifugal enrichment of stable isotopes and modern physical experiments,* Czech. J. Phys. **50** (2000) 577–580. doi: 10.1023/A:1022809128791.

[61] A. Giuliani and A. Poves, *Neutrinoless double-beta decay*, Adv. High Energy Phys. **2012** (2012) 857016. doi: 10.1155/2012/857016.

[62] R. S. Raghavan, *New approach to the search for neutrinoless double beta decay*, Phys. Rev. Lett. **72** (1994) 1411–1414. doi: 10.1103/PhysRevLett.72.1411.

[63] S. Dell'Oro, S. Marcocci, M. Viel, and F. Vissani, *Neutrinoless double beta decay: 2015 review*, Adv. High Energy Phys. **2016** (2016) 2162659. doi: 10.1155/2016/2162659, arXiv: 1601.07512.

[64] KamLAND-Zen Collaboration, K. Asakura et al., *Results from KamLAND-Zen*, AIP Conf. Proc. **1666** (2015), no. 1, 170003. doi: 10.1063/1.4915593, arXiv: 1409.0077.

[65] KamLAND-Zen Collaboration, A. Gando et al., *Limit on Neutrinoless $\beta\beta$ Decay of ^{136}Xe from the First Phase of KamLAND-Zen and Comparison with the Positive Claim in ^{76}Ge*, Phys. Rev. Lett. **110** (2013), no. 6, 062502. doi: 10.1103/PhysRevLett.110.062502, arXiv: 1211.3863.

[66] KamLAND-Zen Collaboration, A. Gando et al., *Measurement of the double-beta decay half-life of 136Xe with the KamLAND-Zen experiment*, Phys. Rev. C **85** (2012) 045504. doi: 10.1103/PhysRevC.85.045504, arXiv: 1201.4664.

[67] M. Auger et al., *The EXO-200 detector, part I: Detector design and construction*, JINST **7** (2012) P05010. doi: 10.1088/1748-0221/7/05/P05010, arXiv: 1202.2192.

[68] EXO-200 Collaboration, E. Conti et al., *Correlated fluctuations between luminescence and ionization in liquid xenon*, Phys. Rev. B **68** (2003) 054201.

doi: 10.1103/PhysRevB.68.054201,
arXiv: hep-ex/0303008.

[69] EXO-200 Collaboration, J. Albert et al., *Search for Majorana neutrinos with the first two years of EXO-200 data,* Nature **510** (2014) 229–234.
doi: 10.1038/nature13432,
arXiv: 1402.6956.

[70] EXO-200 Collaboration, J. Albert et al., *Improved measurement of the $2\nu\beta\beta$ half-life of ^{136}Xe with the EXO-200 detector,* Phys. Rev. C **89** (2014), no. 1, 015502.
doi: 10.1103/PhysRevC.89.015502,
arXiv: 1306.6106.

[71] EXO-200 Collaboration, G. Anton et al., *Search for Neutrinoless Double-β Decay with the Complete EXO-200 Dataset,* Phys. Rev. Lett. **123** (2019), no. 16, 161802.
doi: 10.1103/PhysRevLett.123.161802,
arXiv: 1906.02723.

[72] EXO-200 Collaboration, J. Albert et al., *Searches for double beta decay of ^{134}Xe with EXO-200,* Phys. Rev. D **96** (2017), no. 9, 092001.
doi: 10.1103/PhysRevD.96.092001,
arXiv: 1704.05042.

[73] GERDA Collaboration, M. Agostini et al., *Results on Neutrinoless Double-β Decay of ^{76}Ge from Phase I of the GERDA Experiment,* Phys. Rev. Lett. **111** (2013), no. 12, 122503.
doi: 10.1103/PhysRevLett.111.122503,
arXiv: 1307.4720.

[74] M. Agostini et al., *Background-free search for neutrinoless double-β decay of ^{76}Ge with GERDA,* Nature **544** (2017) 47.
doi: 10.1038/nature21717,
arXiv: 1703.00570.

[75] GERDA Collaboration, C. Macolino, *Search for neutrinoless double beta decay with the GERDA experiment,* Nuovo Cim. C **36** (2013), no. 6, 13–20.

doi: 10.1393/ncc/i2014-11611-0.

[76] M. Agostini et al., *Results on $\beta\beta$ decay with emission of two neutrinos or Majorons in ^{76}Ge from GERDA Phase I*, Eur. Phys. J. C **75** (2015), no. 9, 416.
doi: 10.1140/epjc/s10052-015-3627-y,
arXiv: 1501.02345.

[77] Yoann Kermaidic, *GERDA, MAJORANA and LEGEND, towards a background-free ton-scale Ge-76 experiment*, Talk at Neutrino 2020.
URL: https://indico.fnal.gov/event/43209/contributions/187846/attachments/129106/159515/20200701_Nu2020_Ge76_YoannKermaidic.pdf.

[78] CUORE Collaboration, C. Alduino et al., *Analysis techniques for the evaluation of the neutrinoless double-β decay lifetime in ^{130}Te with the CUORE-0 detector*, Phys. Rev. C **93** (2016), no. 4, 045503.
doi: 10.1103/PhysRevC.93.045503,
arXiv: 1601.01334.

[79] CUORE Collaboration, D. Adams et al., *Improved Limit on Neutrinoless Double-Beta Decay in ^{130}Te with CUORE*, Phys. Rev. Lett. **124** (2020), no. 12, 122501.
doi: 10.1103/PhysRevLett.124.122501,
arXiv: 1912.10966.

[80] CUORE Collaboration, D. Chiesa, *The CUORE experiment at LNGS*, in *18th Lomonosov Conference on Elementary Particle Physics*, pp. 90–93, 2019.
doi: 10.1142/9789811202339_0015,
arXiv: 1712.07995.

[81] SNO Collaboration, J. Boger et al., *The Sudbury neutrino observatory*, Nucl. Instrum. Meth. A **449** (2000) 172–207.
doi: 10.1016/S0168-9002(99)01469-2,
arXiv: nucl-ex/9910016.

[82] SNO+ Collaboration, S. Biller, *SNO+ with Tellurium*, Phys. Procedia **61** (2015) 205–210.
doi: 10.1016/j.phpro.2014.12.033,
arXiv: 1405.3401.

[83] SNO+ Collaboration, J. Paton, *Neutrinoless Double Beta Decay in the SNO+ Experiment*, in *Prospects in Neutrino Physics*, 3, 2019. arXiv: 1904.01418.

[84] APPEC Committee, A. Giuliani, J. Gomez Cadenas, S. Pascoli, E. Previtali, R. Saakyan, K. Schäffner, and S. Schönert, *Double Beta Decay APPEC Committee Report*, (10, 2019). arXiv: 1910.04688.

[85] I. Phillips, D.G. et al., *The Majorana experiment: an ultra-low background search for neutrinoless double-beta decay*, J. Phys. Conf. Ser. **381** (2012) 012044. doi: 10.1088/1742-6596/381/1/012044, arXiv: 1111.5578.

[86] LEGEND Collaboration, N. Abgrall et al., *The Large Enriched Germanium Experiment for Neutrinoless Double Beta Decay (LEGEND)*, AIP Conf. Proc. **1894** (2017), no. 1, 020027. doi: 10.1063/1.5007652, arXiv: 1709.01980.

[87] nEXO Collaboration, J. Albert et al., *Sensitivity and Discovery Potential of nEXO to Neutrinoless Double Beta Decay*, Phys. Rev. C **97** (2018), no. 6, 065503. doi: 10.1103/PhysRevC.97.065503, arXiv: 1710.05075.

[88] CUPID Collaboration, W. Armstrong et al., *CUPID pre-CDR*, (7, 2019). arXiv: 1907.09376.

[89] CUPID Collaboration, O. Azzolini et al., *Final result of CUPID-0 phase-I in the search for the ^{82}Se Neutrinoless Double-β Decay*, Phys. Rev. Lett. **123** (2019), no. 3, 032501. doi: 10.1103/PhysRevLett.123.032501, arXiv: 1906.05001.

[90] E. Armengaud et al., *The CUPID-Mo experiment for neutrinoless double-beta decay: performance and prospects*, Eur. Phys. J. C **80** (2020), no. 1, 44.

doi: 10.1140/epjc/s10052-019-7578-6,
arXiv: 1909.02994.

[91] A. Bettini, *The Canfranc Underground Laboratory (LSC),* Eur. Phys. J. Plus **127** (2012) 112.
doi: 10.1140/epjp/i2012-12112-1.

[92] J. Gomez-Cadenas, J. Benlloch-Rodríguez, P. Ferrario, F. Monrabal, J. Rodríguez, and J. Toledo, *Investigation of the coincidence resolving time performance of a PET scanner based on liquid xenon: a monte carlo study,* Journal of Instrumentation **11** (sep, 2016) P09011–P09011.
doi: 10.1088/1748-0221/11/09/p09011.

[93] C. Iacobaeus, T. Francke, B. Lund-Jensen, J. Ostling, P. Pavlopoulos, et al., *A High position resolution X-ray detector: An 'Edge on' illuminated capillary plate combined with a gas amplification structure,* IEEE Trans. Nucl. Sci. **53** (2006) 554–561.
doi: 10.1109/TNS.2006.872635,
arXiv: physics/0411082.

[94] LUX Collaboration, D. Akerib et al., *The Large Underground Xenon (LUX) Experiment,* Nucl. Instrum. Meth. **A704** (2013) 111–126.
doi: 10.1016/j.nima.2012.11.135,
arXiv: 1211.3788.

[95] T. Ohashi, K. Ebisawa, Y. Fukazawa, K. Hiyoshi, M. Horii, et al., *The Gas Imaging Spectrometer on Board ASCA,* Publ. Astron. Soc. Jap. **48** (1996) 157–170.
doi: 10.1093/pasj/48.2.157.

[96] NEXT Collaboration, V. Alvarez et al., *NEXT-100 Technical Design Report (TDR): Executive Summary,* JINST **7** (2012) T06001.
doi: 10.1088/1748-0221/7/06/T06001,
arXiv: 1202.0721.

[97] J. J. Gomez-Cadenas, F. Monrabal Capilla, and P. Ferrario, *High Pressure Gas Xenon TPCs for Double Beta Decay Searches,* Front. in Phys. **7** (2019) 51.

doi: 10.3389/fphy.2019.00051,
arXiv: 1903.02435.

[98] E. Bellotti, O. Cremonesi, E. Fiorini, et al., *The Milano experiment on double beta decay of Xe-136,* J. Phys. G **17** (1991) S231–S241.
doi: 10.1088/0954-3899/17/S/025.

[99] J. C. Vuilleumier et al., *Search for neutrinoless double beta decay in Xe-136 with a time projection chamber,* Phys. Rev. D **48** (1993) 1009–1020.
doi: 10.1103/PhysRevD.48.1009.

[100] R. Luescher et al., *Search for $\beta\beta$ decay in Xe-136: New results from the Gotthard experiment,* Phys. Lett. B **434** (1998) 407–414.
doi: 10.1016/S0370-2693(98)00906-X.

[101] D. Nygren, *High-pressure xenon gas electroluminescent TPC for 0-ν $\beta\beta$-decay search,* Nucl. Instrum. Meth. A **603** (2009) 337–348.
doi: 10.1016/j.nima.2009.01.222.

[102] R. L. Platzman, *Total ionization in gases by high-energy particles: An appraisal of our understanding,* Int. J. Appl. Radiat. Isot. **10** (1961) 116–127.
doi: 10.1016/0020-708X(61)90108-9.

[103] NEXT Collaboration, V. Alvarez et al., *Ionization and scintillation response of high-pressure xenon gas to alpha particles,* JINST **8** (2013) P05025.
doi: 10.1088/1748-0221/8/05/P05025,
arXiv: 1211.4508.

[104] C. A. B. Oliveira, M. Sorel, J. Martín-Albo, et al., *Energy Resolution studies for NEXT,* JINST **6** (2011) P05007.
doi: 10.1088/1748-0221/6/05/P05007,
arXiv: 1105.2954.

[105] T. Takahashi, S. Konno, T. Hamada, M. Miyajima, S. Kubota, A. Nakamoto, A. Hitachi, E. Shibamura, and T. Doke, *Average energy expended per ion pair in liquid xenon,* Phys. Rev. **A12** (1975) 1771–1775.
doi: 10.1103/PhysRevA.12.1771.

[106] A. J. P. L. Policarpo, *Light production and gaseous detectors,* Phys. Scripta **23** (1981) 539–549.
doi: 10.1088/0031-8949/23/4A/029.

[107] E. Aprile, A. E. Bolotnikov, A. I. Bolozdynya, and T. Doke, *Noble gas detectors*, Weinheim (Germany), 2006
ISBN: 978-3527405978.

[108] A. Parsons et al., *High pressure gas scintillation drift chambers with wave shifter fiber readout,* IEEE Trans. Nucl. Sci. **37** (1990) 541–546.
doi: 10.1109/23.106674.

[109] S. J. C. do Carmo, F. I. G. M. Borges, F. P. Santos, T. H. V. T. Dias, and C. A. N. Conde, *Absolute primary scintillation yield of gaseous xenon under low drift electric fields for 5.9 keV X-rays*, JINST **3** (2008) P07004.
doi: 10.1088/1748-0221/3/07/P07004.

[110] L. M. P. Fernandes et al., *Primary and secondary scintillation measurements in a xenon Gas Proportional Scintillation Counter,* JINST **5** (2010) P09006.
doi: 10.1088/1748-0221/5/09/P09006,
arXiv: 1009.2719.

[111] NEXT Collaboration, L. Serra et al., *An improved measurement of electron-ion recombination in high-pressure xenon gas,* JINST **10** (2015), no. 03, P03025.
doi: 10.1088/1748-0221/10/03/P03025,
arXiv: 1412.3573.

[112] C. M. B. Monteiro et al., *Secondary scintillation yield in pure xenon,* JINST **2** (2007) P05001.
doi: 10.1088/1748-0221/2/05/P05001,
arXiv: physics/0702142.

[113] U. Fano, *Ionization Yield of Radiations. 2. The Fluctuations of the Number of Ions,* Phys. Rev. **72** (1947) 26–29.
doi: 10.1103/PhysRev.72.26.

[114] A. J. P. L. Policarpo, M. A. F. Alves, M. Salete, S. C. P. Leite, and M. C. M. dos Santos, *Detection of soft x-rays with a xenon*

proportional scintillation counter, Nucl. Instrum. Meth. **118** (1974) 221–226.
doi: 10.1016/0029-554X(74)90706-X.

[115] H. Sipilä, *Energy resolution of the proportional counter*, Nucl. Instrum. Meth. A **133** (1976) 251.
doi: 10.1016/0029-554X(76)90616-9.

[116] D. F. Anderson, T. T. Hamilton, W. H.-M. Ku, and R. Novick, *A large area, gas scintillation proportional counter*, Nucl. Instrum. Meth. **163** (1979) 125–134.
doi: 10.1016/0029-554X(79)90040-5.

[117] T. H. V. T. Dias, J. M. F. dos Santos, P. J. B. M. Rachinhas, F. P. Santos, C. A. N. Conde, and A. D. Stauffer, *Full-energy absorption of x-ray energies near the xe l- and k-photoionization thresholds in xenon gas detectors: Simulation and experimental results*, Journal of Applied Physics **82** (1997), no. 6, 2742–2753.
doi: 10.1063/1.366105,
arXiv: https://doi.org/10.1063/1.366105.

[118] T. Doke, A. Hitachi, S. Kubota, A. Nakamoto, and T. Takahashi, *Estimation of Fano factors in liquid argon, krypton, xenon and xenon-doped liquid argon*, Nucl. Instrum. Meth. **134** (1976) 353–357.
doi: 10.1016/0029-554X(76)90292-5.

[119] A. Bolotnikov and B. Ramsey, *The spectroscopic properties of high-pressure xenon*, Nucl. Instrum. Meth. A **396** (1997) 360–370.
doi: 10.1016/S0168-9002(97)00784-5.

[120] A. Bolozdynya, V. Egorov, A. Koutchenkov, G. Safronov, G. Smirnov, S. Medved, and V. Morgunov, *A high pressure xenon self-triggered scintillation drift chamber with 3d sensitivity in the range of 20–140 kev deposited energy*, Nuclear Instruments and Methods in Physics Research Section A: Accelerators, Spectrometers, Detectors and Associated Equipment **385** (1997), no. 2, 225 – 238.
doi: 10.1016/S0168-9002(96)01035-2.

[121] D. R. Nygren, *A time projection chamber*. PEP-198, 1975.

[122] J. N. Marx and D. R. Nygren, *The Time Projection Chamber,* Phys. Today **31N10** (1978) 46–53.
doi: 10.1063/1.2994775.

[123] Hamamatsu Photonics, *Photomultiplier tube R7378A*, Datasheet. 2004.
URL: https://www.hamamatsu.com/resources/pdf/etd/R7378A_TPMH1288E.pdf.

[124] J. Toledo, H. Muller, R. Esteve, J. M. Monzo, A. Tarazona, and S. Martoiu, *The Front-End Concentrator card for the RD51 Scalable Readout System,* JINST **6** (2011) C11028.
doi: 10.1088/1748-0221/6/11/C11028.

[125] NEXT Collaboration, V. Álvarez et al., *Initial results of NEXT-DEMO, a large-scale prototype of the NEXT-100 experiment,* JINST **8** (2013) P04002.
doi: 10.1088/1748-0221/8/04/P04002,
arXiv: 1211.4838.

[126] NEXT Collaboration, V. Álvarez et al., *Operation and first results of the NEXT-DEMO prototype using a silicon photomultiplier tracking array,* JINST **8** (2013) P09011.
doi: 10.1088/1748-0221/8/09/P09011,
arXiv: 1306.0471.

[127] NEXT Collaboration, D. Lorca et al., *Characterisation of NEXT-DEMO using xenon K_α X-rays,* JINST **9** (2014) P10007.
doi: 10.1088/1748-0221/9/10/P10007,
arXiv: 1407.3966.

[128] NEXT Collaboration, L. Serra, D. Lorca, J. Martin-Albo, M. Sorel, and J. J. Gomez-Cadenas, *Latest results of NEXT-DEMO, the prototype of the NEXT 100 double beta decay experiment*, in *Proceedings, 37th International Conference on High Energy Physics (ICHEP 2014)*, 2014.
arXiv: 1410.6700.

[129] NEXT Collaboration, P. Ferrario et al., *First proof of topological signature in the high pressure xenon gas TPC with electroluminescence amplification for the NEXT experiment*, JHEP **01** (2016) 104.
doi: 10.1007/JHEP01(2016)104,
arXiv: 1507.05902.

[130] NEXT Collaboration, V. Alvarez et al., *Near-Intrinsic Energy Resolution for 30 to 662 keV Gamma Rays in a High Pressure Xenon Electroluminescent TPC*, Nucl. Instrum. Meth. **A708** (2013) 101–114.
doi: 10.1016/j.nima.2012.12.123,
arXiv: 1211.4474.

[131] NEXT Collaboration, G. Martínez-Lema et al., *Calibration of the NEXT-White detector using ^{83m}Kr decays*, JINST **13** (2018), no. 10, P10014.
doi: 10.1088/1748-0221/13/10/P10014,
arXiv: 1804.01780.

[132] NEXT Collaboration, J. Renner et al., *Initial results on energy resolution of the NEXT-White detector*, JINST **13** (2018), no. 10, P10020.
doi: 10.1088/1748-0221/13/10/P10020,
arXiv: 1808.01804.

[133] NEXT Collaboration, A. Simón et al., *Electron drift properties in high pressure gaseous xenon*, JINST **13** (2018), no. 07, P07013.
doi: 10.1088/1748-0221/13/07/P07013,
arXiv: 1804.01680.

[134] NEXT Collaboration, P. Novella et al., *Measurement of radon-induced backgrounds in the NEXT double beta decay experiment*, JHEP **10** (2018) 112.
doi: 10.1007/JHEP10(2018)112,
arXiv: 1804.00471.

[135] NEXT Collaboration, J. Renner et al., *Energy calibration of the NEXT-White detector with 1% resolution near $Q_{\beta\beta}$ of ^{136}Xe*, JHEP **10** (2019) 230.

doi: 10.1007/JHEP10(2019)230,
arXiv: 1905.13110.

[136] NEXT Collaboration, P. Ferrario et al., *Demonstration of the event identification capabilities of the NEXT-White detector*, JHEP **10** (2019) 052.
doi: 10.1007/JHEP10(2019)052,
arXiv: 1905.13141.

[137] NEXT Collaboration, P. Novella et al., *Radiogenic Backgrounds in the NEXT Double Beta Decay Experiment*, JHEP **10** (2019) 051.
doi: 10.1007/JHEP10(2019)051,
arXiv: 1905.13625.

[138] V. Alvarez et al., *Radiopurity control in the NEXT-100 double beta decay experiment: procedures and initial measurements*, JINST **8** (2013) T01002.
doi: 10.1088/1748-0221/8/01/T01002,
arXiv: 1211.3961.

[139] NEXT Collaboration, S. Cebrián et al., *Radiopurity assessment of the tracking readout for the NEXT double beta decay experiment*, JINST **10** (2015), no. 05, P05006.
doi: 10.1088/1748-0221/10/05/P05006,
arXiv: 1411.1433.

[140] NEXT Collaboration, S. Cebrián et al., *Radiopurity assessment of the energy readout for the NEXT double beta decay experiment*, JINST **12** (2017), no. 08, T08003.
doi: 10.1088/1748-0221/12/08/T08003,
arXiv: 1706.06012.

[141] K. Lung et al., *Characterization of the Hamamatsu R11410-10 3-Inch Photomultiplier Tube for Liquid Xenon Dark Matter Direct Detection Experiments*, Nucl. Instrum. Meth. **A696** (2012) 32–39.
doi: 10.1016/j.nima.2012.08.052,
arXiv: 1202.2628.

[142] SensL, *SensL MicroFC-10035-SMT-GP*, Datasheet. 2014.
URL: http://www.sensl.com/downloads/ds/DS-MicroCseries.pdf.

[143] J. Rodriguez, M. Querol, J. Diaz, J. J. Gomez-Cadenas, D. Lorca, V. Alvarez, A. Martinez, and A. Gil, *Mass production automated test system for the NEXT SiPM tracking plane*, in *Proceedings IEEE Nuclear Science Symposium and Medical Imaging Conference (NSS/MIC 2012)*, pp. 1106–1108, 2012. doi: 10.1109/NSSMIC.2012.6551277.

[144] J. Rodríguez, J. Toledo, R. Esteve, D. Lorca, and F. Monrabal, *The front-end electronics for the 1.8-kchannel SiPM tracking plane in the NEW detector*, JINST **10** (2015), no. 01, C01025. doi: 10.1088/1748-0221/10/01/C01025.

[145] W. Maneschg, M. Laubenstein, D. Budjas, W. Hampel, G. Heusser, K. Knopfle, B. Schwingenheuer, and H. Simgen, *Measurements of extremely low radioactivity levels in stainless steel for GERDA*, Nucl. Instrum. Meth. A **593** (2008) 448–453. doi: 10.1016/j.nima.2008.05.036.

[146] E. Aprile et al., *Material screening and selection for XENON100*, Astropart. Phys. **35** (2011) 43–49. doi: 10.1016/j.astropartphys.2011.06.001, arXiv: 1103.5831.

[147] OPERA Collaboration, M. Guler et al., *OPERA: An appearance experiment to search for nu/mu <–> nu/tau oscillations in the CNGS beam. Experimental proposal*, (2000).

[148] SAES Pure Gas Inc., *Microtorr purifiers*, Datasheet. 2020. URL: http://www.saespuregas.com/Library/specifications-brochures/MC4500_spec.pdf.

[149] SAES Pure Gas Inc., *Rare gas / nitrogen / hydrogen gas purification ps4-mt50*, Datasheet. 2020. URL: http://www.saespuregas.com/Products/Gas-Purifier/PS4-MT50.html.

[150] S. Martoiu, H. Muller, A. Tarazona, and J. Toledo, *Development of the scalable readout system for micro-pattern gas detectors and other applications*, Journal of Instrumentation **8** (mar, 2013) C03015–C03015. doi: 10.1088/1748-0221/8/03/c03015.

[151] V. Álvarez, V. Herrero-Bosch, R. Esteve, A. Laing, J. Rodríguez, M. Querol, F. Monrabal, J. Toledo, and J. Gómez-Cadenas, *The electronics of the energy plane of the NEXT-White detector,* Nucl. Instrum. Meth. A **917** (2019) 68–76. doi: 10.1016/j.nima.2018.11.126, arXiv: 1805.08636.

[152] F. Carena, W. Carena, S. Chapeland, V. C. Barroso, F. Costa, E. Dénes, R. Divià, U. Fuchs, A. Grigore, T. Kiss, G. Simonetti, C. Soós, A. Telesca, P. V. Vyvre, and B. von Haller, *The alice data acquisition system,* Nuclear Instruments and Methods in Physics Research Section A: Accelerators, Spectrometers, Detectors and Associated Equipment **741** (2014) 130 – 162. doi: 10.1016/j.nima.2013.12.015.

[153] NEXT Collaboration, F. Grañena et al., *NEXT, a HPGXe TPC for neutrinoless double beta decay searches (Letter of Intent),* (2009). arXiv: 0907.4054.

[154] NEXT Collaboration, V. Álvarez et al., *The NEXT-100 experiment for neutrinoless double beta decay searches (Conceptual Design Report),* (2011). arXiv: 1106.3630.

[155] J. Gomez-Cadenas, *Status and prospects of the NEXT experiment for neutrinoless double beta decay searches*, in *54th Rencontres de Moriond on Electroweak Interactions and Unified Theories*, pp. 201–206, 2019. arXiv: 1906.01743.

[156] NEXT Collaboration, C. Henriques et al., *Secondary scintillation yield of xenon with sub-percent levels of CO_2 additive for rare-event detection,* Phys. Lett. B **773** (2017) 663–671. doi: 10.1016/j.physletb.2017.09.017, arXiv: 1704.01623.

[157] NEXT Collaboration, R. Felkai et al., *Helium–Xenon mixtures to improve the topological signature in high pressure gas xenon TPCs,* Nucl. Instrum. Meth. A **905** (2018) 82–90. doi: 10.1016/j.nima.2018.07.013,

arXiv: 1710.05600.

[158] NEXT Collaboration, A. McDonald et al., *Electron Drift and Longitudinal Diffusion in High Pressure Xenon-Helium Gas Mixtures,* JINST **14** (2019), no. 08, P08009. doi: 10.1088/1748-0221/14/08/P08009, arXiv: 1902.05544.

[159] D. R. Nygren, *Detecting the barium daughter in ^{136}Xe 0-$\nu\beta\beta$ decay using single-molecule fluorescence imaging techniques,* J. Phys. Conf. Ser. **650** (2015), no. 1, 012002. doi: 10.1088/1742-6596/650/1/012002.

[160] B. Jones, A. McDonald, and D. Nygren, *Single Molecule Fluorescence Imaging as a Technique for Barium Tagging in Neutrinoless Double Beta Decay,* JINST **11** (2016), no. 12, P12011. doi: 10.1088/1748-0221/11/12/P12011, arXiv: 1609.04019.

[161] R. Esteve, J. Toledo, J. Rodríguez, M. Querol, and V. Álvarez, *Readout and data acquisition in the NEXT-NEW detector based on SRS-ATCA,* Journal of Instrumentation **11** (jan, 2016) C01008–C01008. doi: 10.1088/1748-0221/11/01/c01008.

[162] J. Postel, *User Datagram Protocol. RFC 768*, 1980. URL: https://tools.ietf.org/html/rfc768.

[163] R. Esteve, *Data format and gui. version india,* (June, 2019).

[164] R. Esteve, J. Toledo, F. Monrabal, D. Lorca, L. Serra, A. Marí, J. J. Gómez-Cadenas, I. Liubarsky, and F. Mora, *The trigger system in the NEXT-DEMO detector,* Journal of Instrumentation **7** (dec, 2012) C12001–C12001. doi: 10.1088/1748-0221/7/12/c12001.

[165] G. Martínez Lema, *Low-energy calibration, reconstruction software and light-collection efficiency parametrization of the NEXT-White detector*. PhD thesis, Santiago de Compostela U., 7, 2018.

[166] The HDF Group, *Hierarchical Data Format, version 5*, 1997-2020. URL: https://www.hdfgroup.org/HDF5.

[167] C. Green, J. Kowalkowski, M. Paterno, M. Fischler, L. Garren, and Q. Lu, *The Art Framework*, J. Phys. Conf. Ser. **396** (2012) 022020. doi: 10.1088/1742-6596/396/2/022020.

[168] ECMA, *404: The json data interchange format*, 2013. URL: http://www.ecma-international.org/publications/files/ECMA-ST/ECMA-404.pdf.

[169] P. Nash, *Catch2*, 2010-2020. URL: https://github.com/catchorg/Catch2.

[170] H. Krekel, B. Oliveira, R. Pfannschmidt, nd F. Bruynooghe, B. Laugher and F. Bruhin, *pytest 3.8*, 2004-2020. URL: https://github.com/pytest-dev/pytest.

[171] D. A. Huffman, *A method for the construction of minimum-redundancy codes*, Proceedings of the IRE **40** (1952), no. 9, 1098–1101. doi: 10.1109/JRPROC.1952.273898.

[172] Gluster, *Gluster File System*, 2005-2020. URL: https://www.gluster.org.

[173] S. Ritt, *ELOG*, 2002-2020. URL: https://elog.psi.ch/elog/.

[174] NEXT Collaboration, J. Martín-Albo et al., *Sensitivity of NEXT-100 to Neutrinoless Double Beta Decay*, JHEP **05** (2016) 159. doi: 10.1007/JHEP05(2016)159, arXiv: 1511.09246.

[175] J. I. Muñoz Vidal, *The NEXT path to neutrino inverse hierarchy*. PhD thesis, U. Valencia (main), 2018.

[176] M. Redshaw, E. Wingfield, J. McDaniel, and E. Myers, *Mass and double-beta-decay Q value of Xe-136*, Phys. Rev. Lett. **98** (2007) 053003. doi: 10.1103/PhysRevLett.98.053003.

[177] P. McCowan and R. Barber, *Q value for the double-beta decay of Xe-136,* Phys. Rev. C **82** (2010) 024603.
doi: 10.1103/PhysRevC.82.024603.

[178] National Nuclear Data Center, *NuDat database, version 2.8*, 2008-2020.
URL: http://www.nndc.bnl.gov/nudat2/.

[179] Wikipedia, *Natural decay chain*, accessed 16 June, 2020.
URL: https://en.wikipedia.org/wiki/Decay_chain.

[180] V. Álvarez et al., *Radiopurity control in the NEXT-100 double beta decay experiment,* AIP Conf. Proc. **1549** (2013) 46–49.
doi: 10.1063/1.4818073.

[181] NEXT Collaboration, P. J. Pérez, *The NEXT-100 experiment for Neutrino-less Double Beta decay: Main features, Results from Prototypes and Radiopurity issues,* PoS **EPS-HEP2013** (2013) 528.
doi: 10.22323/1.180.0528.

[182] NEXT Collaboration, T. Dafni et al., *Results of the material screening program of the NEXT experiment,* Nucl. Part. Phys. Proc. **273-275** (2016) 2666–2668.
doi: 10.1016/j.nuclphysbps.2015.10.024,
arXiv: 1411.1222.

[183] NEXT Collaboration, S. Cebrián et al., *Radon and material radiopurity assessment for the NEXT double beta decay experiment*, AIP Conf. Proc. **1672** (2015) 060002.
doi: 10.1063/1.4927990,
arXiv: 1505.07052.

[184] NEXT, *Activity assumptions for NEW and NEXT-100 detector simulations. Version 6.* NEXT-doc-182-v6.

[185] NEXT, *Activity assumptions for NEW and NEXT-100 detector simulations. Version 9.* NEXT-doc-182-v9.

[186] I. Bandac, *Gamma flux at the LSC*. Private communication, 2013.

[187] GEANT4, S. Agostinelli et al., *GEANT4–a simulation toolkit,* Nucl. Instrum. Meth. A **506** (2003) 250–303. doi: 10.1016/S0168-9002(03)01368-8.

[188] W. H. Richardson, *Bayesian-based iterative method of image restoration,* JoSA **62** (1972), no. 1, 55–59. doi: 10.1364/JOSA.62.000055.

[189] L. B. Lucy, *An iterative technique for the rectification of observed distributions,* The astronomical journal **79** (1974) 745. doi: 10.1086/111605.

[190] NEXT Collaboration, J. Renner et al., *Background rejection in NEXT using deep neural networks,* JINST **12** (2017), no. 01, T01004. doi: 10.1088/1748-0221/12/01/T01004, arXiv: 1609.06202.

[191] M. Dosanjh, *From Particle Physics to Medical Applications*, 2017 ISBN: 978-0750314442.

[192] A. Van Der Veldt, E. Smit, and A. A. Lammertsma, *Positron emission tomography as a method for measuring drug delivery to tumors in vivo: the example of [11c] docetaxel,* Frontiers in oncology **3** (2013) 208. doi: 10.3389/fonc.2013.00208.

[193] W. Moses, *Time of flight in pet revisited,* IEEE Transactions on Nuclear Science **50** (2003), no. 5, 1325–1330. doi: 10.1109/TNS.2003.817319.

[194] S. Surti, A. Kuhn, M. E. Werner, A. E. Perkins, J. Kolthammer, and J. S. Karp, *Performance of philips gemini tf pet/ct scanner with special consideration for its time-of-flight imaging capabilities,* Journal of Nuclear Medicine **48** (2007), no. 3, 471–480.

[195] M. Miller, J. Zhang, K. Binzel, J. Griesmer, T. Laurence, M. Narayanan, D. Natarajamani, S. Wang, and M. Knopp, *Characterization of the vereos digital photon counting pet system,* Journal of Nuclear Medicine **56** (2015), no. supplement 3, 434–434.

[196] M. V. Nemallapudi, S. Gundacker, P. Lecoq, E. Auffray, A. Ferri, A. Gola, and C. Piemonte, *Sub-100 ps coincidence time resolution for positron emission tomography with lso: Ce codoped with ca,* Physics in Medicine & Biology **60** (2015), no. 12, 4635. doi: 10.1088/0031-9155/60/12/4635.

[197] A. Ferri, A. Gola, N. Serra, A. Tarolli, N. Zorzi, and C. Piemonte, *Performance of fbk high-density sipm technology coupled to ce: Lyso and ce: Gagg for tof-pet,* Physics in Medicine & Biology **59** (2014), no. 4, 869. doi: 10.1088/0031-9155/59/4/869.

[198] J. J. Gomez-Cadenas, J. Benlloch-Rodríguez, P. Ferrario, F. Monrabal, J. Rodríguez, and J. Toledo, *Investigation of the Coincidence Resolving Time performance of a PET scanner based on liquid xenon: A Monte Carlo study,* JINST **11** (2016), no. 09, P09011. doi: 10.1088/1748-0221/11/09/P09011, arXiv: 1604.04106.

[199] E. Aprile and T. Doke, *Liquid Xenon Detectors for Particle Physics and Astrophysics,* Rev. Mod. Phys. **82** (2010) 2053–2097. doi: 10.1103/RevModPhys.82.2053, arXiv: 0910.4956.

[200] V. Chepel and H. Araujo, *Liquid noble gas detectors for low energy particle physics,* JINST **8** (2013) R04001. doi: 10.1088/1748-0221/8/04/R04001, arXiv: 1207.2292.

[201] T. Doke, J. Kikuchi, and F. Nishikido, *Time-of-flight positron emission tomography using liquid xenon scintillation,* Nuclear Instruments and Methods in Physics Research Section A: Accelerators, Spectrometers, Detectors and Associated Equipment **569** (2006), no. 3, 863–871. doi: 10.1016/j.nima.2006.07.067.

[202] L. Gallego Manzano et al., *XEMIS: A liquid xenon detector for medical imaging,* Nucl. Instrum. Meth. A **787** (2015) 89–93. doi: 10.1016/j.nima.2014.11.040.

[203] F. Nishikido, T. Doke, J. Kikuchi, T. Mori, H. Murayama, T. Ooshita, and H. Takahashi, *Performance of prototype liquid xenon scintillation detector system for time-of-flight type positron emission tomography with improved photomultipliers,* Japanese journal of applied physics **44** (2005), no. 7R, 5193. doi: 10.1143/JJAP.44.5193.

[204] S. Kubota, M. Hishida, M. Suzuki, and J.-z. Ruan(Gen, *Dynamical behavior of free electrons in the recombination process in liquid argon, krypton, and xenon,* Phys. Rev. B **20** (1979), no. 8, 3486. doi: 10.1103/PhysRevB.20.3486.

[205] J. Renner, J. Benlloch-Rodríguez, J. Carrión, R. Gadea, V. Herrero-Bosch, M. Kekic, C. Romo-Luque, P. Ferrario, and J. Gómez-Cadenas, *Processing of Compton events in the PETALO readout system*, in *IEEE Nuclear Science Symposium (NSS) and Medical Imaging Conference (MIC)*, pp. 1–7, 2019. doi: 10.1109/NSS/MIC42101.2019.9059979, arXiv: 2001.04724.

[206] SensL, *Introduction to SiPM*, accessed 17 August, 2020. URL: https://www.sensl.com/downloads/ds/TN-IntrotoSPMTech.pdf.

[207] J. J. Gomez-Cadenas, J. M. Benlloch-Rodríguez, and P. Ferrario, *Monte Carlo study of the Coincidence Resolving Time of a liquid xenon PET scanner, using Cherenkov radiation,* JINST **12** (2017), no. 08, P08023. doi: 10.1088/1748-0221/12/08/P08023, arXiv: 1706.07629.

[208] S. Brunner, L. Gruber, J. Marton, K. Suzuki, and A. Hirtl, *Studies on the cherenkov effect for improved time resolution of tof-pet,* IEEE Transactions on Nuclear Science **61** (2013), no. 1, 443–447. doi: 10.1109/TNS.2013.2281667.

[209] S. Korpar, R. Dolenec, P. Kriˇ zan, R. Pestotnik, and A. Stanovnik, *Study of TOF PET using Cherenkov light,* Phys. Procedia **37** (2012) 1531–1536.

doi: 10.1016/j.phpro.2012.03.750.

[210] J. Allison, K. Amako, J. Apostolakis, H. Araujo, P. A. Dubois, M. Asai, G. Barrand, R. Capra, S. Chauvie, R. Chytracek, et al., *Geant4 developments and applications,* IEEE Transactions on nuclear science **53** (2006), no. 1, 270–278. doi: 10.1109/TNS.2006.869826.

[211] M. Yamashita, T. Doke, K. Kawasaki, J. Kikuchi, and S. Suzuki, *Scintillation response of liquid xe surrounded by ptfe reflector for gamma rays,* Nuclear Instruments and Methods in Physics Research Section A: Accelerators, Spectrometers, Detectors and Associated Equipment **535** (2004), no. 3, 692–698. doi: 10.1016/j.nima.2004.06.168.

[212] A. Sinnock and B. Smith, *Refractive indices of the condensed inert gases,* Physical Review **181** (1969), no. 3, 1297. doi: 10.1103/PhysRev.181.1297.

[213] U. Oberlack, E. Aprile, A. Curioni, and K.-L. Giboni, *Performance of the light trigger system in the liquid xenon gamma-ray imaging telescope lxegrit*, in *IEEE Nuclear Science Symposium*, vol. 1, pp. 4–76, IEEE, 2000. doi: 10.1109/23.958720.

[214] V. Solovov, V. Chepel, M. Lopes, A. Hitachi, R. F. Marques, and A. Policarpo, *Measurement of the refractive index and attenuation length of liquid xenon for its scintillation light,* Nuclear Instruments and Methods in Physics Research Section A: Accelerators, Spectrometers, Detectors and Associated Equipment **516** (2004), no. 2-3, 462–474. doi: 10.1016/j.nima.2003.08.117.

[215] A. Baldini, C. Bemporad, F. Cei, T. Doke, M. Grassi, T. Haruyama, S. Mihara, T. Mori, D. Nicolo, H. Nishiguchi, et al., *Liquid xenon scintillation calorimetry and xe optical properties,* IEEE transactions on dielectrics and electrical insulation **13** (2006), no. 3, 547–555. doi: 10.1109/TDEI.2006.1657967.

[216] PETsys electronics, *PETsys TOFPET2 ASIC*, accessed 17 August, 2020.
URL: https://www.petsyselectronics.com/web/public/products/1.

[217] L. C. García, L.-R. Collaboration, et al., *Testing micro-channel plate detectors for the particle identification upgrade of lhcb*, Nuclear Instruments and Methods in Physics Research Section A: Accelerators, Spectrometers, Detectors and Associated Equipment **695** (2012) 398–402.
doi: 10.1016/j.nima.2011.12.021.

[218] H. Kim, H. Frisch, C.-T. Chen, J.-F. Genat, F. Tang, W. Moses, W. Choong, and C.-M. Kao, *A design of a pet detector using micro-channel plate photomultipliers with transmission-line readout*, Nuclear Instruments and Methods in Physics Research Section A: Accelerators, Spectrometers, Detectors and Associated Equipment **622** (2010), no. 3, 628–636.
doi: 10.1016/j.nima.2010.07.083.